Rojava Journal of Science and Technology

2026, VOL. 3, No 1, [1-11]

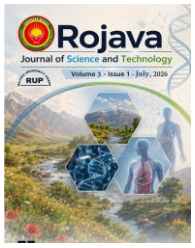

A Perspective on Scientific Resilience, Open Science, and International Cooperation in Conflict-Affected and Resource-Limited Regions

Haidar Saify Nabiabad*[1],[2]

1-Department of Clinical Laboratory, Institute of Science and Modern Technology, Rojava University, Qamişlo, Syria

2-Editor-in- chief, Rojava Journal of Science and Technology

ABSTRACT

Scientific progress increasingly depends on openness, collaboration, and the free exchange of knowledge across disciplines and national boundaries. However, researchers working in conflict-affected and resource-limited regions continue to face substantial barriers, including inadequate infrastructure, limited funding, restricted access to scientific resources, and geopolitical constraints. This perspective examines how scientific resilience, international collaboration, science diplomacy, and open science can strengthen research capacity and innovation under challenging conditions. It highlights examples of scientific achievements from conflict-affected and developing regions, demonstrating that adversity can stimulate innovation, adaptability, and locally relevant solutions with global significance. The article further emphasizes the importance of interdisciplinary partnerships, equitable international collaborations, responsible research practices, and FAIR data principles in improving research quality, reproducibility, and societal impact. In addition, it discusses the critical role of regional scientific journals in promoting local research, strengthening scientific capacity, and connecting underrepresented researchers with the global scientific community. Ultimately, the paper argues that investing in inclusive scientific ecosystems and sustained international cooperation is essential for addressing shared global challenges and advancing sustainable development, peace, and scientific excellence worldwide.

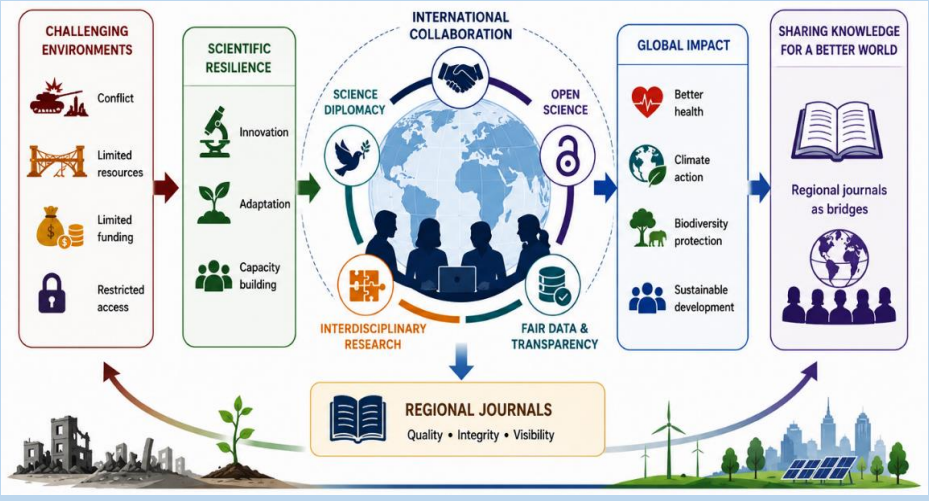

ARTICLE HISTORY

Received: 14 Jan. 2026

Revised: 10 Apr 2026

Accepted: 28 Jul. 2026

Keywords: Science diplomacy, Open science, Scientific resilience, Conflict-affected and resource-limited regions.

*Corresponding author: Dr. Haidar Saify Nabiabad: homan_saify@Yahoo.com

1. Introduction: Science Has No Borders

We are fundamentally linked to one another and to our surroundings. These connections are evident in our daily observations and experiences. Our interconnectedness provides us with numerous benefits each day. Nevertheless, the effects and consequences of human actions on these connections are clearly apparent to those of us involved in environmental science, engineering, health research, and the endeavors associated with safeguarding public health and the environment. Historically, scientific advancement has thrived when ideas transcended borders more easily than political divisions. From worldwide initiatives aimed at tackling infectious diseases to collaborative international efforts focused on climate change and the loss of biodiversity, science shows that addressing humanity's most significant challenges requires shared knowledge rather than solitary endeavors (Rezaei 2021). Significantly, there is an increasing global awareness of the human-induced pressures on the biosphere, as demonstrated by international initiatives like the Intergovernmental Panel on Climate Change, the Intergovernmental Science-Policy Platform on Biodiversity and Ecosystem Services, and ongoing efforts to establish an Intergovernmental Science-Policy Panel on Chemicals and Waste. In addition to the fundamental moral and ethical responsibilities we hold toward people and the planet, our varied and extensive connections should foster the creation and preservation of links in environmental science and technology, ensuring continued support for these initiatives. Establishing connections across different fields within environmental science and technology remains crucial, especially as we adopt systems-oriented methods to tackle significant environmental challenges (Sarmento et al., 2016). Fedoroff (2009) views science diplomacy as a strategic approach to manage intricate global issues through international scientific collaboration, asserting that science serves as a universal language that can bypass political, cultural, and ideological divides. To effectively address challenges like food insecurity, climate change, infectious diseases, and energy shortages, there is a need for interdisciplinary research and enduring partnerships between developed and developing countries. A key point of this paper advocates for a transition from conventional aid-based models to fair scientific collaborations that enhance local research capabilities, higher education, and innovation ecosystems. This viewpoint is especially pertinent for regions affected by conflict and resource limitations, where scientific infrastructure and human resources are often compromised by ongoing instability. Nevertheless, despite the hopeful outlook on science diplomacy, there is insufficient focus on the structural obstacles that commonly hinder collaboration in fragile contexts. These include political unrest, restricted funding, sanctions, damaged infrastructure, and limited access to advanced technologies, all of which present significant challenges. These circumstances indicate that effective science diplomacy necessitates not only international goodwill but also ongoing investment in institutional resilience, researcher mobility, digital connectivity, and locally driven research priorities. Fon et al. (2023) contend that international scientific collaboration has become a crucial method for addressing complex developmental issues, especially in areas facing resource limitations, institutional obstacles, and shared socio-environmental challenges. Problems like infectious diseases, climate change, loss of biodiversity, and technological inequality cannot be effectively resolved by individual national actions alone, underscoring the need for integrated research collaborations and cross-border knowledge sharing. However, effective collaboration is frequently hindered by issues such as regulatory inconsistencies, disparities in funding, institutional limitations, cultural differences, and geopolitical conflicts. These obstacles can restrict the fair distribution of resources and research opportunities, especially for institutions situated in difficult environments. Therefore, we stress the necessity of aligned policies, inclusive governance frameworks, sustainable funding strategies, and capacity-building efforts to foster enduring scientific collaborations. Nonetheless, our appeal continues to be a fundamental contribution, highlighting that scientific collaboration serves not just as a means for generating

knowledge, but also as a catalyst for peacebuilding, enhancing capacities, and fostering sustainable socioeconomic advancement. We emphasize that science acts as a universal language. No matter the geographical, political, or economic circumstances, scientific inquiry is fueled by curiosity, evidence, and teamwork. Historically, significant scientific breakthroughs have relied on the global exchange of knowledge, data, and expertise.

2. Science in Challenging Environments

Throughout history, scientific research has thrived in contexts marked by political stability, ongoing investment, and robust research infrastructure. Nonetheless, a growing collection of evidence reveals that significant scientific advancements can also originate from areas affected by armed conflict, economic turmoil, natural disasters, and persistent resource shortages. Scholars operating in these challenging environments often face disrupted education systems, impaired laboratory facilities, shortages of necessary equipment and supplies, limited access to scientific publications, restricted funding options, unreliable electricity and internet connectivity, and fewer chances for international collaboration (Al-Worafi, 2024). Despite these obstacles, we persist in producing important scientific insights that tackle both local and global issues. Research carried out in demanding circumstances is often marked by impressive resilience, flexibility, and creativity. Researchers frequently create cost-efficient techniques, make the most of restricted laboratory resources, forge local partnerships, and utilize open-source technologies to navigate infrastructural challenges. These adaptive strategies have resulted in significant progress in areas like public health monitoring, biodiversity preservation, agricultural sustainability, environmental stewardship, and community-focused healthcare. Instead of simply being a reaction to challenges, these innovations often offer scalable and economical solutions that can assist other low- and middle-income nations, as well as resource-sensitive research settings globally (AAAS & The Royal Society, 2025). Regions affected by conflict serve as powerful examples of scientific resilience. In Northeast Syria (Rojava), years of warfare and political turmoil have severely disrupted higher education, healthcare systems, and research infrastructure. Despite these challenges, universities, independent research centers, and healthcare professionals have continued their work in areas such as public health, clinical medicine, microbiology, ethnobotany, agriculture, environmental science, and biotechnology. These research initiatives not only meet urgent regional requirements but also provide valuable insights from populations and ecosystems that are often overlooked in global scientific publications. A similar trend has been noted in Ukraine, where researchers have sustained their scientific output in spite of extensive infrastructure damage and the displacement of academic personnel. The swift adaptation of Ukrainian institutions through digital collaboration, international partnerships, and remote research efforts demonstrates that scientific communities can maintain research continuity even amidst prolonged conflict. Numerous nations in Sub-Saharan Africa showcase the ability of scientific communities to generate significant research even in the face of ongoing financial and infrastructural challenges. Researchers from Africa have made notable contributions that are recognized worldwide in areas such as infectious disease monitoring, genomics, vaccine creation, malaria management, antimicrobial resistance, biodiversity preservation, climate adaptation, and advancements in agriculture. The development of regional research collaborations, genomic sequencing facilities, and public health labs during outbreaks of Ebola, COVID-19, and other emerging infectious diseases underscores the continent's growing scientific leadership. These accomplishments illustrate that continuous investment in local scientific capabilities can yield considerable global advantages. Similarly, researchers across Latin America have made significant contributions to scientific knowledge despite facing ongoing economic downturns, political chaos, and inconsistent funding for research. Institutions in countries like Argentina, Brazil, Colombia, Peru, and Mexico have established research

programs in environmental sciences, biodiversity, tropical medicine, renewable energy, biotechnology, and public health that are competitive on an international scale. Strong academic collaborations and regional networks have allowed these researchers to sustain their scientific output while tackling pressing global issues such as biodiversity in the Amazon, and sustainable farming practices. In addition to conflicts and economic struggles, natural disasters and climate-related challenges also represent significant hurdles for scientific inquiry. Scientists based in disaster-prone areas provide crucial data for risk assessment, disaster preparedness, and climate adaptation strategies that are increasingly important on a global scale. A key feature of fruitful research in difficult settings is collaboration. Global scientific partnerships grant access to state-of-the-art laboratories, funding sources, mentorship opportunities, data-sharing platforms, and specialized skills that may be lacking on a local level. Similarly significant are South–South collaborations, regional research networks, and partnerships within communities that foster tailored solutions and enhance local scientific capabilities. Furthermore, digital technologies, open-access publishing, cloud-based data storage, virtual conferences, and online training have diminished geographical barriers, enabling researchers in resource-constrained environments to engage more actively in the worldwide scientific community (Morgan et al., 2023). Even with these promising advancements, considerable structural inequalities persist, hindering scientific progress in difficult conditions. Researchers often encounter obstacles such as insufficient research funding, high publication fees, lack of access to subscription-based journals, poor laboratory facilities, challenges in acquiring research materials and equipment, limited chances for advanced training, and underrepresentation in global collaborations and decision-making institutions. To address these disparities, it is essential to make ongoing investments in research infrastructure, implement equitable funding approaches, promote open science efforts, develop capacity-building programs, and establish policies that acknowledge the importance of research led by local entities (Quak 2025). In the end, science pursued in difficult circumstances shouldn't simply be seen as a tale of struggle. Rather, it showcases remarkable scientific resilience, innovation, and dedication to society. Researchers operating in areas impacted by conflict, disasters, or limited resources persist in producing knowledge that enhances health, safeguards biodiversity, promotes sustainable development, and guides evidence-based policy. It is vital to bolster these scientific communities through fair international collaboration and sustained institutional support, as this is crucial not just for local growth but also for tackling various intricate global challenges that cross national boundaries.

3. Innovation Through Collaboration

Scientific innovation is becoming more reliant on collaboration that crosses boundaries of disciplines, institutions, and countries. The intricate nature of modern scientific issues like sustainable energy transitions cannot be sufficiently undertake through isolated research or single-discipline efforts. Instead, these global problems necessitate the merging of various scientific viewpoints, cutting-edge technologies, and shared research facilities. As a result, interdisciplinary and international collaboration has become a fundamental aspect of contemporary scientific advancement and innovation (Luo et al., 2025). Interdisciplinary research brings together expertise from different scientific domains to create new methodologies, improve problem-solving abilities, and speed up knowledge generation. For instance, progress in genomics increasingly depends on partnerships among molecular biologists, bioinformaticians, statisticians, clinicians, and computer scientists, working together to analyze extensive genomic datasets and apply findings to precision medicine. Likewise, the swift evolution of artificial intelligence (AI) has revolutionized scientific research by facilitating automated data analysis, predictive modeling, and decision support across various fields, from biomedical sciences to environmental monitoring. The combination of AI with biotechnology and healthcare has greatly accelerated drug

discovery, disease diagnosis, and the development of personalized treatment approaches (Shao et al., 2026). The realm of biotechnology clearly illustrates the importance of collaboration across various disciplines. Breakthroughs such as CRISPR-based genome editing, synthetic biology, vaccine creation, and regenerative medicine necessitate the combined efforts of experts from genetics, molecular biology, engineering, computational science, chemistry, and clinical medicine. The rapid development of COVID-19 vaccines showcased how cooperative international research networks can significantly speed up the process from fundamental scientific findings to their clinical implementation. In a similar way, managing climate change requires teamwork among climatologists, ecologists, engineers, economists, geographers, and social scientists. Effective climate modeling, strategies for mitigation, adaptation planning, and the creation of environmental policies all rely on the integration of data collected globally and analyzed via multidisciplinary methods. Research in renewable energy also thrives on collaboration among materials scientists, physicists, chemists, electrical engineers, economists, and environmental scientists in order to enhance solar panels, wind technologies, energy storage solutions, and sustainable hydrogen generation. Global collaboration has become essential in public health, where the monitoring of infectious diseases, genomic tracking of pathogens, epidemiological modeling, and coordinated responses to pandemics necessitate quick international data sharing and collaborative research frameworks. The COVID-19 pandemic underscored the significance of global scientific partnerships through open-access databases, multinational clinical trials, and joint vaccine development efforts that sped up scientific breakthroughs and guided evidence-based public health strategies. In the realm of biodiversity conservation, interdisciplinary teamwork combines ecology, genetics, remote sensing, conservation biology, environmental policy, and local ecological insights to create effective approaches for safeguarding ecosystems and endangered species. International collaborations promote standardized biodiversity monitoring, enhance species distribution modeling, and reinforce conservation planning across political borders, acknowledging that ecological systems seldom adhere to national limits. Working together on research projects grants access to specialized tools, advanced computing resources, extensive databases, and unique research locations that might not be available to individual institutions or countries. This shared infrastructure minimizes redundancy, boosts research efficiency, and allows scientists from resource-constrained areas to engage in state-of-the-art scientific investigations. Furthermore, international cooperation promotes the sharing of knowledge, technologies, and best practices, thereby enhancing scientific capabilities on a global scale. Another important advantage of international collaboration is the integration of a wide range of expertise and viewpoints. Research teams made up of individuals from various cultural, educational, and disciplinary backgrounds are likely to develop more innovative solutions, as they handle problems using varied methodologies and theoretical perspectives. This kind of diversity fosters creativity, enriches the critical assessment of research outcomes, and mitigates disciplinary biases. Collaborative research enhances both reproducibility and scientific rigor. When findings are independently validated across various laboratories and populations, it boosts confidence in research results and supports the creation of standardized methods. Utilizing shared protocols, adopting transparent data-sharing practices, and conducting multicenter studies are essential for tackling the ongoing reproducibility issues faced by many scientific fields (Nature Editorial, 2025). Bibliometric analyses consistently show that publications co-authored internationally receive more citations, are featured in higher-impact journals, and gain wider scientific exposure compared to those from a single institution. These collaborations broaden research networks, increase funding opportunities, and promote the global spread of scientific knowledge. Furthermore, multinational research consortia often have the capabilities to pursue large-scale, ambitious projects that would be beyond the reach of individual laboratories. Collaboration in science has shifted from being

a commendable practice to a crucial element of research excellence. As scientific inquiries grow more intricate and interconnected on a global scale, interdisciplinary and international collaborations will be vital for speeding up innovation, improving research quality, bolstering scientific resilience, and devising solutions to the urgent challenges confronting humanity.

4. Science Diplomacy

Science diplomacy has become a crucial tool for enhancing global collaboration, enabling the exchange of knowledge, and tackling intricate international issues that cannot be resolved by single nations alone. In a practical context, science diplomacy goes beyond official political discussions; it involves utilizing scientific collaboration to foster relationships, encourage mutual understanding, and back decisions based on evidence. Scientific partnerships frequently endure even amid political strains, illustrating that common scientific objectives can create reliable avenues for dialogue and collaboration (Rüland et al., 2025). One of the key contributions of science diplomacy is its capacity to foster trust among researchers, institutions, and countries. Scientific collaboration is built on the principles of transparency, reproducibility, peer review, and the open sharing of knowledge. These common values cultivate an environment where researchers from various cultural, social, and political backgrounds can collaborate on shared goals. Long-term partnerships, joint publications, and global research networks enhance professional connections and promote mutual trust that lasts beyond single projects (Fähnrich, 2017). Additionally, science diplomacy is vital in promoting evidence-based policymaking. International scientific collaboration empowers governments and organizations to obtain trustworthy data, unify research methods, and formulate coordinated strategies informed by the best available evidence. In this manner, science acts as a conduit between research and policy, ensuring that decisions are based on objective information rather than immediate interests. Another key feature of science diplomacy is its ability to remain steadfast during times of political or economic instability. While diplomatic ties between nations may vary, scientific collaborations often persist through universities, research organizations, professional associations, and international bodies. Scientists pursue shared research goals, engage through established academic networks, and sustain collaborative projects that enhance global understanding. This continuity is crucial for tackling cross-border issues, such as pandemic readiness, environmental protection, disaster risk mitigation, and sustainable resource management, where ongoing scientific cooperation is vital. The effectiveness of science diplomacy is also bolstered by the common ethical standards that guide scientific research around the globe. Regardless of their country of origin, researchers typically follow internationally accepted principles of research integrity, which include honesty, transparency, accountability, consideration for human participants and biodiversity, responsible data management, and ethical standards in publication (Lips et al., 2025). These standard practices promote collaboration by setting shared expectations for research quality, reproducibility, and ethical conduct. Global ethical guidelines and peer-review processes further enhance trust in collaborative research and boost the reliability of scientific findings. Contemporary scientific organizations are increasingly acknowledging science diplomacy as a vital element of global research management. International efforts are promoting collaborative research infrastructures, researcher mobility, open science initiatives, and fair access to scientific information. These initiatives foster skill development, narrow the gap in research resources, and empower scientists from both advanced and developing countries to play a significant role in addressing global issues. In areas affected by conflict or lacking resources, science diplomacy can also help sustain academic progress by linking local researchers with global expertise, training opportunities, and research facilities (Kaltofen 2018). In the end, science diplomacy illustrates that science serves not just as a source of knowledge but also as a significant tool for promoting international discussion, trust, and collaboration. By

supporting evidence-driven policymaking, maintaining partnerships across political divides, and upholding common ethical standards, science diplomacy bolsters the international scientific community and improves our collective ability to overcome the complex challenges of the twenty-first century. As scientific issues grow more global in scope, effective science diplomacy will continue to be essential for progressing research, innovation, and sustainable development.

5. Open Science and Research Integrity

Open science has become a crucial framework for enhancing the quality, transparency, accessibility, and societal impact of scientific research. By encouraging open access to scientific knowledge, research data, methodologies, and software, open science allows researchers across the globe to validate findings, replicate experiments, and build on previous work more effectively. This approach is especially beneficial in areas with limited resources or those affected by conflict, where access to scientific infrastructure and subscription-based journals can be constrained. Consequently, open science not only aids in scientific progress but also promotes greater equity in participation in global research (UNESCO, 2021). Maintaining transparency during the research process is vital for upholding scientific integrity. Researchers must provide detailed descriptions of study designs, sampling techniques, experimental protocols, statistical methods, and computational approaches to enable independent verification of their results (Limongi et al., 2026). Transparent reporting helps to reduce selective reporting, mitigate methodological bias, and bolster trust in published findings. The growing adoption of reporting guidelines like CONSORT, PRISMA, STROBE, and ARRIVE highlights the increasing recognition that methodological transparency is essential to research quality and informed decision-making based on evidence (Khan et al., 2025). The principle of reproducibility is closely tied to transparency and has emerged as a fundamental aspect of contemporary scientific integrity. Reproducibility enables independent researchers to achieve consistent results using identical methods and data, thus validating scientific assertions and uncovering possible errors or biases. Concerns about the widespread "reproducibility crisis" in various fields—including psychology, biomedical sciences, and preclinical research—have underscored the necessity for better experimental design, sufficient statistical power, thorough data reporting, and the open sharing of research materials. By reinforcing reproducibility, we ultimately foster public confidence in science and promote dependable scientific advancements. The FAIR data principles—Findable, Accessible, Interoperable, and Reusable—offer globally accepted guidelines for effective management of research data. Datasets that comply with FAIR standards are given persistent identifiers, include standardized metadata, are kept in readily accessible repositories, and are formatted using interoperable standards that enable reuse by both people and automated systems. Following FAIR principles enhances research productivity, encourages collaboration across disciplines, and maximizes the enduring value of scientific data. As large-scale, data-centric research becomes ever more prevalent, adopting FAIR practices is crucial for ensuring that scientific datasets remain discoverable and reusable across different institutions and countries. The swift incorporation of artificial intelligence (AI) into scientific research has opened up unique avenues for data analysis, literature synthesis, drug discovery, genomics, climate modeling, and personalized medicine. Nonetheless, responsible AI usage demands transparency, accountability, fairness, and human oversight. Researchers must carefully assess the outputs generated by AI, disclose their use of AI tools when applicable, safeguard confidential data, and make sure that algorithms do not introduce hidden biases or undermine scientific objectivity. International bodies are increasingly advocating that AI should support, not replace, essential scientific reasoning and ethical decision-making (UNESCO, 2021). Ethical publishing serves as a crucial foundation of research integrity. Scientific articles must accurately present methods and findings, free from fabrication, falsification, plagiarism,

inappropriate authorship, or duplicate publication. Researchers are also required to reveal any conflicts of interest, secure the necessary ethical approvals for studies involving human or animal subjects, and comply with established publication ethics as set forth by groups like the Committee on Publication Ethics (COPE). Upholding ethical publishing practices is vital for maintaining the trustworthiness of the scientific record and sustaining public confidence in academic research. Thorough peer review is a key mechanism for ensuring the quality and reliability of scientific publications. Independent expert assessments help uncover methodological flaws, statistical inaccuracies, unsupported claims, and ethical issues before research is published. While peer review has its limitations, enhancements such as open peer review, reviewer training, clear editorial policies, and post-publication evaluations have improved its overall effectiveness. It is essential to recognize constructive peer review not just as a process of gatekeeping, but as a vital element in the enhancement of scientific quality. In the end, maintaining scientific integrity is much more important than simply focusing on the number of publications. The increasing reliance on publication metrics, citation numbers, and journal impact factors can sometimes lead to practices that favor productivity over the quality of research. These pressures can result in questionable research methods, disjointed publications, and a decrease in reproducibility. On the other hand, research carried out with honesty, sound methodology, transparency, and ethical responsibility holds significant scientific value, regardless of the volume of publications. Institutions, funding bodies, and journals are progressively acknowledging that research excellence should be assessed not only by how much is published but also by the reliability, reproducibility, transparency, and societal impact of scientific work. Upholding these standards is crucial for maintaining public trust, promoting international collaboration, and ensuring that science continues to effectively benefit humanity.

6. The Role of Regional Journals

Regional scientific journals are crucial in bolstering research ecosystems, especially in developing areas and regions affected by conflict, where researchers often encounter challenges such as limited funding, inadequate infrastructure, and restricted opportunities for international publication. These journals do more than just serve as venues for publication; they offer an important platform for emerging scientists to share original research, hone their academic writing abilities, and achieve recognition within the wider scientific community. By providing accessible channels for scholarly exchange, regional journals foster the development of the next generation of researchers and aid in establishing long-term scientific capabilities. Additionally, regional journals act as significant links between local and international research communities. They promote the dissemination of scientific knowledge by publishing work focused on issues specific to their regions, ensuring that these findings reach a global audience. This exchange of information encourages collaboration among researchers from various disciplines and countries, facilitates the sharing of methodologies and data, and opens doors for collaborative research efforts. Such partnerships are especially important for considering intricate global challenges that require coordinated international responses. Another crucial role played by regional journals is fostering interdisciplinary research. Many of the scientific issues we face today transcend individual disciplines, necessitating knowledge from various fields. By inviting submissions from a wide range of scientific areas, regional journals promote collaboration among experts in biology, medicine, engineering, environmental science, information technology, and the physical sciences. This interdisciplinary strategy sparks innovation and aids in creating comprehensive solutions to societal and environmental challenges. Additionally, regional journals help enhance the integrity and credibility of scientific research by advocating for ethical publishing practices. Through peer review, compliance with international publication standards, transparency in reporting research, and strict policies against plagiarism and scientific misconduct, these journals

work to guarantee the quality and dependability of the findings published. Maintaining high ethical standards builds public trust in science and supports the reproducibility and long-term significance of scientific research. Furthermore, regional journals serve as important repositories of scientific knowledge that is pertinent to local contexts. They safeguard significant research that focuses on issues such as regional biodiversity, indigenous expertise, public health, agriculture, natural resources, environmental conservation, and technological advancements—subjects that may not receive adequate focus in more expansive international publications. By documenting scientific progress within specific geographical and cultural frameworks, regional journals produce evidence that supports policy-making, directs sustainable development efforts, and meets local community needs, all while enriching the global pool of scientific knowledge. The Rojava Journal of Science and Technology was established with these purposes in mind. The journal is dedicated to offering a high-quality, peer-reviewed, and globally accessible platform for sharing original scientific research that aids both regional advancements and worldwide scientific development. It aspires to enhance scientific capabilities, encourage international collaboration, and support research excellence across various disciplines. The journal is open to original research articles, reviews, short communications, and interdisciplinary studies across a wide array of scientific domains, such as biotechnology, medicine, environmental science, engineering, agriculture, computer science, mathematics, physics, chemistry, and other related fields. By fostering collaboration among researchers from various backgrounds and institutions, the journal aims to promote scientific advancement, encourage innovation, and tackle the urgent scientific and technological issues that confront both the region and the global community.

7. Looking Forward

Scientific discovery has historically advanced through openness, collaboration, and the unrestricted exchange of ideas across different fields, institutions, and countries. Over the ages, significant breakthroughs in areas such as medicine, agriculture, engineering, environmental science, and technology have occurred when researchers unified their knowledge, resources, and viewpoints to tackle common challenges. In our increasingly interconnected world, scientific advancement relies not only on individual brilliance but also on the collective ability of the global research community to collaborate towards shared objectives. The issues facing humanity—including climate change, loss of biodiversity, emerging infectious diseases, food and water insecurity, antimicrobial resistance, sustainable energy, and rapid technological change—cross political borders and demand coordinated international efforts. No single entity or country has all the knowledge, infrastructure, or resources necessary to independently address these intricate challenges. Therefore, enhancing international scientific collaborations, fostering interdisciplinary research, and ensuring fair access to scientific information have become essential for achieving sustainable development and strengthening global resilience. It is equally vital to establish an inclusive global scientific environment where researchers from low- and middle-income countries, conflict-affected areas, and resource-constrained institutions can actively engage in the creation of new knowledge. Investing in research capabilities, enhancing access to funding and modern scientific tools, fostering researcher mobility, and promoting open and responsible science initiatives can help bridge the gaps in scientific opportunities while enriching the diversity of viewpoints that fuel innovation. Scientific excellence thrives when talent is acknowledged irrespective of geographical location or political context. Digital technologies, open-access publishing, international data-sharing platforms, and collaborative research networks are transforming the conduct of science, allowing for quicker dissemination of findings and fostering more transparent, reproducible, and inclusive research practices. These advancements offer unparalleled opportunities to boost innovation and build greater trust among scientists,

policymakers, and society. However, to fully realize these advantages, continuous investment in research infrastructure, ethical governance, data integrity, and international collaboration is essential. As we look ahead, the advancement of science will rely not only on technological innovations but also on our united dedication to cooperation, inclusiveness, and shared responsibility. Assisting scientists across all regions of the globe goes beyond an academic goal; it represents a strategic investment in global health, environmental sustainability, economic progress, and social stability. By fostering equitable partnerships, enhancing scientific diplomacy, and encouraging the free flow of ideas, the international research community can develop innovative solutions to the world's most urgent issues and help create a more resilient, peaceful, and sustainable future for everyone. We stay interconnected. In light of geopolitical tensions, the importance of mutually beneficial scientific dialogue and broader science diplomacy initiatives is greater than ever for the community focused on environmental science and technology, especially as the world starts to recover from the various effects of the global COVID-19 pandemic. Indeed, dismantling barriers and fostering collaboration across borders and disciplines is crucial for tackling significant environmental issues of global relevance and achieving the United Nations' Sustainable Development Goals, which are designed to benefit everyone, irrespective of race, gender, religion, or national origin. In simple terms, our collective well-being relies on our mutually beneficial relationships. It's time to intensify our efforts to build these bridges. In support of this mission, the Rojava Journal of Science and Technology team is broadening our global initiatives in environmental science, engineering, and health, with a particular focus on regions that have been historically underrepresented. We enthusiastically invite your urgent, timely, and valuable contributions to enhance cross-disciplinary research in environmental science and technology, no matter where you are located.

Reference

1. AAAS (American Association for the Advancement of Science) and The Royal Society. 2025. Science Diplomacy in an Era of Disruption.
2. Al-Worafi, Yaser Mohammed. 2024. "Research and Development in Developing Countries: Achievements and Challenges." In Handbook of Medical and Health Sciences in Developing Countries: Education, Practice, and Research, 1–23.
3. Fähnrich, Birte. 2017. "Science Diplomacy: Investigating the Perspective of Scholars on Politics–Science Collaboration in International Affairs." Public Understanding of Science.
4. Fedoroff, Nina V. 2009. "Science Diplomacy in the 21st Century." Cell 136 (1): 9–11.
5. Fon, Elvis Tata, Kenneth A. Yongabi, Alhaji U. N'jai, Oly Alawuba, A. W. Verla, C. N. Ezenwa, J. C. Uwaezuoke, and C. N. Nwadike. 2023. "Bridging Academic Borders: Unleashing the Power of Transborder Scientific Collaboration for Africa Development." Research and Reviews on Healthcare: Open Access Journal 8 (4).
6. Kaltofen, Carolin, and Michele Acuto. 2018. "Science Diplomacy: Introduction to a Boundary Problem." Global Policy.
7. Khan, Adam, Tim Smith, Asaad Chaudhry, Caleb A. Smith, Danya Nees, Griffin Hughes, Kaylyn Rowsey, and Matt Vassar. 2025. "A Cross-Sectional Study on the Endorsement of Reporting Guidelines and Clinical Trial Registration among Immunology and Allergy Journals." PLOS ONE 20 (5): e0322003.
8. Limongi, Ricardo, Carina Munhoz de Lima, and Patricia da Silva Costa Gross. 2026.

"Scientific Integrity in the Digital Age: Challenges and Responsibilities for Oncology Research." Revista Brasileira de Cancerologia 72: e-005712.

9. Lips, Karen R., and Meredith L. Gore. 2025. "Science Diplomacy: Using Global Environmental Change as an Opportunity for Public Diplomacy." In Handbook on Public Diplomacy, 310–322. Cheltenham, UK: Edward Elgar Publishing.
10. Luo, Qingfeng, and Jingyuan Wang. 2025. "Cross-Regional Collaborative Innovation in the Era of Data Openness: A Factor Mobility Perspective." Technology in Society 83: 102989.
11. Morgan, Ruth, and Rees Kassen. 2023. "Global Science for Global Challenges: The Landscape of International Scientific Collaboration." Frontiers Policy Labs.
12. Nature Editorial. 2025. "Science Diplomacy Can Help to Heal Global Rifts—If Research Is Respected." Nature.
13. Quak, Evert-Jan. 2025. "Contributions of International Partnerships in Science & Technology to Economic Growth."
14. Rezaei, Nima, ed. 2021. Integrated Science: Science without Borders. Vol. 1. Cham, Switzerland: Springer Nature.
15. Rüland, Anna-Lena, Lise H. Andersen, Alan Kai Hassen, Carringtone Kinyanjui, Annika Ralfs, and Bruno Iochins Grisci. 2025. "Science Diplomacy: A Global Research Field? Findings from a Bibliometric Analysis of the Science Diplomacy Scholarship of the Past Twenty Years." Scientometrics 130 (8): 4697–4722.
16. Sarmento, Simone, and Vanessa Oliveira Andreotti. 2016. "Science without Borders: An Alternative Framework for Evaluation." Interfaces Brasil/Canadá 16 (1): 40–71.
17. Shao, Erzhuo, Yifang Wang, Yifan Qian, Zhenyu Pan, Han Liu, and Dashun Wang. 2026. "SciSciGPT: Advancing Human–AI Collaboration in the Science of Science." Nature Computational Science 6 (3): 301–315.
18. UNESCO. 2021. UNESCO Recommendation on Open Science. Paris: UNESCO.

Rojava Journal of Science and Technology

2026, VOL. 3, No 1, [12-30]

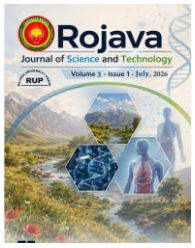

An Integrative Review and Conceptual Framework for Flood Resilience in Brazil: SWAT+GWFlow, Rock Dust, and Socio-Hydrological Governance

Cristiano Trindade De Angelis[1]*

[1]Skema Business School, Lille, France.

ABSTRACT

Flood risk in Brazil is intensifying under the combined pressures of climate change, land-use transformation, urban expansion, and institutional fragility. Although hydrodynamic flood models, watershed-scale hydrological models, and governance studies have each advanced substantially, they are often examined independently. This study presents an integrative literature review and conceptual framework that links current knowledge on watershed modelling, soil-management interventions, sustainable land management, and socio-hydrological governance, with particular emphasis on the complementary roles of HydroPol2D and SWAT+GWFlow and rock dust soil amendments. The review draws on peer-reviewed literature published between 2000 and 2025 to examine advances in flood modelling, surface–groundwater interactions, agricultural land management, and institutional approaches to flood-risk reduction. The analysis indicates that HydroPol2D is valuable for high-resolution flood inundation and impact assessment, while SWAT+GWFlow provides a stronger representation of long-term watershed processes, including land use, soil-water interactions, and groundwater dynamics. The analysis further suggests that rock dust amendments may improve soil structure, infiltration, and water retention under certain conditions, potentially contributing to runoff attenuation. However, the review does not claim that rock dust has been empirically demonstrated to reduce flood damage at the watershed scale; rather, it identifies this as an important hypothesis for future modelling and field validation. A central contribution of this study is the development of an integrated socio-hydrological governance framework that connects hydrological modelling with adaptive decision-making, emergency planning, land-management strategies, and stakeholder participation. The findings suggest that effective flood resilience in Brazil requires not only improved simulation tools, but also stronger hydrometeorological monitoring, interdisciplinary collaboration, and closer integration between science, policy, and society. The proposed framework advances interdisciplinary understanding of flood resilience by integrating hydrological modelling, sustainable land management, and governance into a unified conceptual approach applicable to climate adaptation and watershed management in Brazil.

ARTICLE HISTORY

Received: 14 Jan. 2026

Revised: 10 Jul. 2026

Accepted: 28 Aug. 2026

Keywords: Flood resilience; SWAT+GWFlow; HydroPol2D; rock dust; socio-hydrology; watershed management; governance.

* Corresponding Author: cristianotrindade@protonmail.com

1. Introduction

Flooding has become a persistent and increasingly severe challenge across Brazil, particularly in Rio Grande do Sul, which has emerged as one of the most vulnerable states, and recent extreme events have exposed the fragility of both structural protection systems and emergency response arrangements. In Porto Alegre, the May 2024 floods revealed serious operational weaknesses in the city's existing protection infrastructure. Although pumps and floodgates were designed to reduce inundation risk, their effectiveness depends on proper maintenance, operation, and resilience under extreme conditions. The failure of key system components contributed to a cascading breakdown that significantly intensified flood impacts. Short-lead flood forecasting substantially improves evacuation planning, emergency response, and infrastructure protection. However, forecasting alone cannot reduce disaster risk without adequate monitoring networks, hydrometeorological observations, technical capacity, land-use planning, and institutional coordination. An integrated strategy combining accurate monitoring and rapid forecasting is essential for effective flood management. A recent technical note by Paiva et al. (2024), titled Hydrological Criteria for Adaptation to Climate Change: Extreme Rainfall and Floods in the Southern Region of Brazil, emphasises that large-scale infrastructure projects must be designed to withstand extreme hydrometeorological conditions rather than relying solely on historical return periods. Traditionally, urban drainage infrastructure has been dimensioned according to return periods ranging from 10 to 25 years for micro-drainage systems and 50 to 100 years for macro-drainage systems. However, climate change and the alteration of vegetation cover in urban basins are increasing both the frequency and intensity of flood events, making these assumptions increasingly less reliable under non-stationary climatic conditions. As a result, the concept of tolerable risk in urban drainage planning must therefore be redefined in light of growing climate uncertainty.

Addressing current and future flood risks in Rio Grande do Sul requires more than isolated structural interventions. The 2024 flood disaster demonstrated that even well-established flood-protection infrastructure can be overwhelmed by unprecedented hydrometeorological conditions, exposing weaknesses in drainage systems, dams, and emergency management. Extreme rainfall, rapid runoff generation, and complex watershed interactions highlighted the need for integrated hydrological and hydraulic assessments that consider both catchment-scale processes and urban flood dynamics. While structural measures remain important, their effectiveness during extreme events is inherently limited without complementary non-structural approaches, including land-use planning, early warning systems, risk communication, and coordinated governance. These lessons emphasise the importance of combining advanced hydrological modelling with adaptive watershed management to strengthen long-term flood resilience under a changing climate. Although small reservoirs and related structural measures can help regulate runoff and reduce pollutant transport under moderate conditions, their effectiveness is limited during extreme hydrometeorological events because discharge volumes exceed capacity. Under such circumstances, structural measures alone may offer limited protection. Non-structural approaches, including land-use planning, risk communication, early warning systems, and institutional coordination, often provide more flexible and cost-effective pathways for reducing flood risk. Where structural interventions remain necessary, they must be supported by detailed technical, hydrological, and environmental studies to minimise unintended consequences and improve long-term resilience. In this context, integrated modelling frameworks are essential for linking physical hydrological processes with socio-institutional decision-making. Flood generation is shaped not only by rainfall intensity and hydraulic routing, but also by soil conditions, land use, groundwater behaviour, watershed management, and governance capacity. Accordingly, this study is structured into four analytical components: (1) a comparative

assessment of HydroPol2D and SWAT+GWFlow for flood simulation and forecasting; (2) a review of hydrodynamic and coupled hydrological modelling approaches in flood-risk management; (3) an examination of emergency planning, and social participation mechanisms within flood governance systems; and (4) the development of a socio-hydrological governance framework aimed at improving adaptive capacity and resilience in flood-prone regions.

2. Research Gap and Study Contribution

Substantial advances have been made in flood modelling, agricultural soil management, and governance studies. Yet these areas are often addressed as separate research agendas. Urban flood models frequently provide detailed inundation maps but do not adequately represent groundwater behaviour, longer-term watershed responses, or the cumulative effects of land-management change. Conversely, agricultural studies on soil amendments rarely explore implications for flood resilience, runoff generation, or catchment hydrology. Governance studies, meanwhile, often acknowledge environmental uncertainty but do not consistently incorporate hydrological model outputs into institutional decision-making frameworks. This paper addresses that gap by integrating three traditionally separate research domains:

1. hydrodynamic and hydrological modelling for flood analysis;

2. sustainable soil management through rock dust applications; and

3. socio-hydrological governance systems.

The main contribution of this study is the development of an interdisciplinary framework for assessing the potential links between rock dust application, catchment hydrology, and flood resilience. Rather than establishing a direct causal relationship, the paper provides an integrative conceptual review with practical relevance for watershed management and flood resilience planning in Brazil.

3. Methodology

3.1. Review Design

This study adopts an integrative literature review to synthesise current knowledge on flood modelling, sustainable soil management, and socio-hydrological governance. Unlike systematic reviews that primarily evaluate evidence within a narrowly defined research question, an integrative review enables the combination of theoretical, empirical, and methodological studies from multiple disciplines to develop new conceptual understanding. This approach is particularly appropriate because flood resilience is influenced by interacting hydrological, environmental, agricultural, and institutional processes that cannot be adequately examined within a single disciplinary framework. The review therefore seeks to identify conceptual linkages between hydrodynamic flood modelling, watershed-scale hydrological processes, sustainable soil-management practices, and adaptive governance. These relationships are synthesised into an interdisciplinary framework intended to support future research and flood-management planning in Brazil.

3.2. Literature Search Strategy

The literature search was conducted using four major scientific databases: Scopus, Web of Science, ScienceDirect, and Google Scholar. Publications published between 2000 and 2025 were considered to capture both foundational developments in hydrological modelling and recent advances in integrated watershed management.

Searches combined keywords related to five principal themes:

- hydrodynamic modelling;
- flood forecasting;
- SWAT+GWFlow;
- HydroPol2D;
- rock dust, soil management, and socio-hydrology.

- Representative search strings included combinations such as:
- "HydroPol2D AND flood modelling";
- "SWAT+GWFlow";
- "rock dust AND soil hydrology";
- "flood resilience AND Brazil";
- "socio-hydrology AND governance".

Reference lists of highly cited review papers and recent journal articles were also examined to identify additional relevant studies.

3.3. Study Selection

Studies were included when they:

- were published in peer-reviewed journals or authoritative technical reports;
- addressed flood modelling, watershed hydrology, groundwater interactions, sustainable soil management, or flood governance;
- presented empirical results, numerical modelling, conceptual developments, or methodological innovations relevant to flood resilience.

Studies were excluded when they:

- lacked methodological transparency;
- focused exclusively on engineering applications unrelated to flood management;
- provided insufficient information for evaluating hydrological or governance implications.

3.4. Data Synthesis

The selected literature was analysed using a qualitative thematic synthesis to identify recurring concepts, methodological developments, and knowledge gaps across the fields of hydrological modelling, sustainable land management, and socio-hydrological governance. The review did not follow a formal systematic review protocol (e.g., PRISMA), as its primary objective was conceptual integration rather than quantitative evidence synthesis. Rather than statistically combining results, the review synthesised evidence from multiple disciplines to develop an interdisciplinary framework linking hydrological modelling, rock dust applications, and adaptive governance for flood-resilience planning.

The synthesis was organised into three interconnected themes:

1. hydrodynamic and hydrological modelling for flood analysis;

2. sustainable soil management and the potential hydrological effects of rock dust applications; and

3. socio-hydrological governance and adaptive flood-risk management.

These themes provided the basis for developing the interdisciplinary conceptual framework proposed in this study, which integrates physical watershed processes, land-management practices, numerical modelling, and institutional decision-making into a unified approach for improving flood resilience.

4. Hydrological and Hydrodynamic Modelling for Flood Management

4.1. Fundamentals of Hydrological and Hydrodynamic Modelling

According to Rennó and Soares (2022), hydrological models are mathematical representations of the movement and storage of water and its constituents within the Earth's surface and subsurface systems. These models provide a quantitative framework for simulating watershed processes and understanding the interactions among precipitation, infiltration, evapotranspiration, groundwater recharge, and streamflow across spatial and temporal scales. Hydrodynamic models, by contrast, solve the fundamental equations of fluid flow to simulate flood propagation, water levels, flow velocities, and inundation dynamics under different hydrological conditions. Whereas hydrological models primarily

describe rainfall–runoff processes at the catchment scale, hydrodynamic models simulate the movement of floodwaters through river channels and floodplains, making them indispensable for flood forecasting, hazard assessment, infrastructure planning, and emergency management. Hydrological and hydrodynamic processes are closely interconnected with ecological systems and land-management practices because changes in vegetation cover, soil properties, agricultural activities, and groundwater conditions directly influence runoff generation, sediment transport, and river flow dynamics. Consequently, modern flood-risk assessments increasingly adopt integrated modelling approaches that combine physical hydrological processes with environmental and land-use information to better represent watershed behaviour under changing climatic conditions. Environmental hydrodynamic models play a central role in flood-risk assessment and water-resources management by simulating the movement of water, sediments, and dissolved substances throughout river systems. Beyond predicting flood extent and water depth, these models provide valuable insights into three key processes (Rossman, 2001):

- Hydrodynamic circulation, which describes variations in water levels, flow velocities, and current patterns resulting from changes in momentum.

- Water-quality processes, which simulate the transport, dispersion, and transformation of chemical and biological constituents within aquatic environments.

- Sediment transport, which evaluates erosion, transport, deposition, and channel morphodynamics that shape river morphology and floodplain evolution.

Together, these processes provide a comprehensive representation of river-basin dynamics and support integrated assessments of flood hazards, environmental quality, and watershed management.

4.2. Data Requirements for Hydrological and Hydrodynamic Modelling

The reliability of hydrological and hydrodynamic models depends largely on the quality, spatial resolution, and temporal availability of input data. Accurate datasets are essential for model calibration, validation, and the reliable simulation of flood processes across different spatial scales. Although recent advances in remote sensing and geospatial technologies have improved data accessibility, many river basins continue to experience significant data limitations, particularly in developing countries such as Brazil. According to Stokes Oceanography (2023), the modelling process typically involves the following steps:

1. Build a conceptual model of the phenomenon.

2. Gather relevant input data.

3. Define the numerical domain boundaries.

4. Digitize coastlines or use Digital Elevation Models (DEMs) for river basins.

5. Create a numerical grid to discretize the study area for solving the governing conservation equations.

6. Generate bathymetry (riverbed and reservoir depths).

7. Define simulation scenarios and boundary conditions.

8. Configure and execute the model runs.

9. Analyse simulation results.

10. Iterate the process until simulated results closely reproduce observed conditions.

In Brazil, one of the most widely used data sources for hydrological and hydrodynamic modelling is the HidroWeb Portal, operated by the National Water Agency (ANA). It provides access to historical river-flow records, bathymetric information, and other hydrological observations collected through the National Hydrometeorological Network (RHN). These datasets constitute an important foundation for model development, calibration, and operational flood forecasting. However, flow observations alone are insufficient for reliable flood simulations. More comprehensive modelling approaches require additional datasets, including:

- Soil moisture conditions;
- Topographic characteristics (Digital Elevation Models);
- Land-use and land-cover information;
- Temporal and spatial rainfall distribution; and
- Groundwater observations, where available.

The integration of these datasets enables a more realistic representation of watershed processes, although it also increases computational complexity and data requirements. In countries such as the United States, nationwide availability of high-resolution topographic and hydrometeorological datasets has substantially facilitated hydrological modelling. In contrast, Brazil continues to face important monitoring limitations. Smaller rivers frequently lack direct observations within the ANA monitoring network, requiring indirect estimation methods such as regionalisation techniques or area-proportional calculations from neighbouring catchments. Although these approaches provide practical alternatives where observations are unavailable, they may introduce considerable uncertainty during extreme flood events, when local hydrological responses differ substantially from regional averages.

4.3. Sources of Uncertainty in Flood Modelling

Despite significant advances in hydrological and hydrodynamic modelling, the accuracy of flood simulations remains highly dependent on the quality of input data and the representation of key physical processes. Uncertainties associated with topography, river geometry, boundary conditions, and hydrometeorological observations can substantially influence model performance, particularly during extreme flood events when small errors may propagate through the simulation and affect flood-depth and inundation estimates. Getirana et al. (2012) emphasize that open water surface extent is heavily influenced by river geometry and topography. While geometry determines whether a river will overflow, topography defines the shape of the floodplain and therefore the extent of flooding for a given overflow volume. Yet, both parameters are often affected by limitations in available input data, which remain one of the principal sources of uncertainty in hydrodynamic modelling. Errors in Digital Elevation Models (DEMs) remain a major source of uncertainty in modeling the interactions between rivers and floodplains,commonly known as várzeas. Current satellite, derived DEMs often lack the resolution and accuracy needed to represent floodplain elevation profiles with sufficient precision. This poses significant challenges, especially when modeling flood dynamics in flat, low-lying regions, where even small elevation errors can substantially alter predicted inundation extent and flow pathways. To address this limitation, the "floodplain burning" technique, which modifies elevation pixels using river and floodplain map data, has been proposed as a method to better reflect actual terrain features. This gradual adjustment of elevations improves model

performance in many cases. However, in extreme flood events, such simplified approaches may fail to capture the full complexity of hydrological behaviour, particularly where floodplain storage, groundwater interactions, and rapidly changing hydraulic conditions occur simultaneously. According to Getirana et al. (2012), the extent of open water surfaces depends closely on both river geometry and topography. While geometry influences whether river overflow will occur, topography determines how floodwaters spread across the floodplain. Unfortunately, limitations in input data, especially elevation data, can undermine the accuracy of such models, particularly in the simulation of overflow and inundation areas. These findings highlight the importance of high-quality topographic information and continuous improvements in remote-sensing technologies to reduce uncertainty in flood-risk assessments.

4.4. Major Hydrodynamic Models for Flood Simulation

Hydrological and hydrodynamic models for flood and water-quality management have become essential tools for supporting flood forecasting, emergency planning, and river-basin management. Different models have been developed to address specific hydrological processes, spatial scales, and management objectives, ranging from rapid urban flood simulations to large-scale watershed analyses. As noted by Gomes Junior et al. (2023), hydrological, hydrodynamic, and pollutant transport models are essential tools for decision-making in flood mitigation and water-quality management. A variety of models exist to quantify hydrodynamic processes across different temporal and spatial scales. At finer scales, such as urban watersheds and rapid-response events, the WCA2D model (Guidolin et al., 2016) applies a cellular automata approach to simulate surface runoff and generate flood maps efficiently. This model offers high computational performance and low memory requirements, enabling large-scale two-dimensional simulations with minimal loss of accuracy, making it particularly suitable for real-time flood forecasting and scenario analysis in urban environments. The WCA2D model can also be integrated with the CADDIES 1D model (Austin et al., 2014), which simulates sewer-network behaviour, resulting in a simplified yet effective approach for urban drainage modelling. However, during large flood events, the impact of micro-drainage systems becomes negligible compared with the overwhelming volume of surface runoff and precipitation. Consequently, additional hydrodynamic processes must be represented to accurately simulate large-scale flood propagation. The HEC-RAS software, developed by the United States Army Corps of Engineers, allows the simulation of two-dimensional flows through the numerical solution of the shallow-water equations. It explicitly represents inertia, pressure gradients, gravitational forces, friction, turbulence, and Coriolis effects. These capabilities have made HEC-RAS one of the most widely adopted hydrodynamic models for floodplain mapping, river engineering, and hydraulic infrastructure assessment. However, the model's major limitation is its high computational cost when high-resolution flood simulations are required. Details of the formulations and numerical schemes implemented in Version 6.1 are presented by Brunner (2016). Recent advances have also introduced artificial intelligence (AI) techniques into flood modelling. Lago et al. (2024) evaluated the performance of the cGAN-Flood model, demonstrating that AI-based approaches can substantially reduce computational time compared with conventional hydrodynamic models. The study reported that cGAN-Flood was approximately 50 times faster than WCA2D and 250 times faster than HEC-RAS, highlighting its potential for rapid flood prediction. Despite these computational advantages, cGAN-Flood presents important limitations. The model cannot predict flow velocities, which are essential for producing reliable flood-risk maps, and it was trained

primarily on flood-expansion datasets. Consequently, its applicability remains limited in situations involving varying spatial resolutions or where detailed hydraulic information is required. Furthermore, AI models depend on extensive high-quality observational datasets for training and validation, which remain unavailable in many river basins, particularly within developing countries. Large-scale implementation of AI-based flood models therefore requires extensive hydrometeorological monitoring networks capable of providing reliable observations of watershed behaviour. Without sufficient observational data, physically based hydrodynamic models continue to provide the most robust framework for understanding flood processes and supporting flood-risk management.

4.5. HydroPol2D: Capabilities and Limitations

Gomes Junior et al. (2023) emphasize the potential of the HydroPol2D model, which advances flood modelling by enabling two-dimensional simulations of both flood dynamics and water-quality processes. Unlike conventional hydrodynamic models that focus primarily on flood extent, HydroPol2D integrates hydraulic and environmental processes within a single modelling framework, allowing a more comprehensive assessment of watershed behaviour during flood events. HydroPol2D incorporates key features such as:

- Simulation of floodplain momentum transfer;
- Spatially distributed infiltration and evapotranspiration; and
- Modelling of pollutant transport and fate.

This integrated approach allows for a more comprehensive assessment of watershed hydrological behaviour, especially in scenarios involving both high runoff and contamination risks. By combining flood prediction with water-quality analysis, such models support more effective, cross-disciplinary decision-making for river-basin management and disaster resilience. The ability to simultaneously evaluate hydraulic processes and pollutant transport represents an important advantage for urban flood management, where floodwaters often mobilise contaminants from industrial, agricultural, and residential areas. Given the wide availability of models and numerical solutions, models capable of handling the often-recurring lack of data in large basins could provide a practical solution for flood forecasting. In this sense, De Angelis and Gomes Júnior (2024) found that the HydroPol2D model provides a cost-effective solution for predicting the hydrological–hydraulic behaviour of river basins, particularly for estimating flood maps containing water depths in streets, blocks, neighbourhoods, canals, and, consequently, throughout the entire river basin. Its computational efficiency makes the model particularly attractive for operational flood forecasting, especially where computational resources are limited. Furthermore, recent research uses the HydroPol2D model to assess the risk of human entrapment, generating flood-risk maps at 15-minute intervals that can be used to support emergency decision-making. These high-temporal-resolution simulations provide emergency managers with timely information that can improve evacuation planning, infrastructure protection, and disaster response during rapidly evolving flood events. However, the quality of the model outputs depends strongly on the availability of accurate hydrometeorological observations. Currently, Rio Grande do Sul has approximately 1,700 pluviometric stations, which measure rainfall, and fluviometric stations, which measure river level and discharge. However, only about 25% transmit data in real time. Only in this way can hydrodynamic models be effectively updated, if they do not rely on supplementary information provided by the population through photographs and videos (De Angelis & Gomes Júnior, 2024). This limitation highlights that improvements in monitoring infrastructure are as

important as advances in numerical modelling for increasing the reliability of flood forecasts. Despite its considerable advantages, HydroPol2D provides a simplified representation of groundwater dynamics and long-term watershed processes. The model is primarily designed to simulate surface-water dynamics during flood events and therefore does not explicitly represent groundwater recharge, subsurface flow, agricultural drainage, or long-term land-management effects. These limitations justify the integration of HydroPol2D with watershed-scale hydrological models capable of representing coupled surface–groundwater interactions.

4.6. SWAT+GWFlow: Integrating Surface and Groundwater Processes

With ongoing climate change, most experts predict an increase in the frequency and intensity of extreme weather events (IPCC, 2014). These changes are expected to alter watershed hydrology through shifts in precipitation patterns, increased surface runoff, modified groundwater recharge, and changes in soil-moisture dynamics. Consequently, hydrological models capable of representing both surface-water and groundwater processes have become increasingly important for long-term flood-risk assessment and watershed management. Because land use and agricultural management strongly influence watershed hydrology, process-based models capable of representing these interactions have become increasingly important. Le Li et al. (2021) highlight the complex, nonlinear relationships between hydrological processes and environmental change, emphasising the need for modelling approaches that integrate both natural watershed dynamics and human activities. Among the most widely applied process-based models is the Soil and Water Assessment Tool (SWAT), developed by the United States Department of Agriculture (USDA). SWAT simulates the daily dynamics of streamflow, sediment transport, nutrients, and other watershed processes across meso- to macro-scale river basins (Arnold et al., 1998). Its process-based structure enables the assessment of natural hydrological processes together with the impacts of land-use change, agricultural management, and climate variability on watershed behaviour. The SWAT model is particularly valuable for identifying the key hydrological processes affecting sediment and nutrient transport within river basins, especially during dry seasons. Unlike purely hydrodynamic models, SWAT represents long-term watershed behaviour by simulating precipitation, evapotranspiration, infiltration, surface runoff, groundwater recharge, lateral flow, and river discharge within an integrated framework. Key inputs for SWAT modelling include Digital Elevation Models (DEMs), land-use and land-cover data, soil characteristics, and meteorological observations. Although SWAT has been widely applied for watershed management and water-quality assessment, its traditional groundwater component represents aquifer processes using simplified conceptual approaches. This limitation has led to the development of SWAT+GWFlow, which couples SWAT with a physically based groundwater-flow model to improve the representation of groundwater dynamics and surface–groundwater interactions.

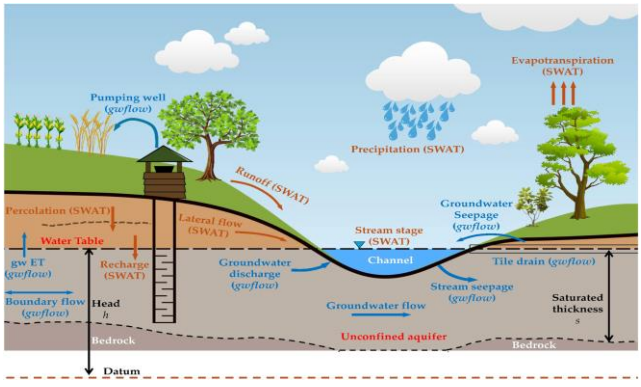

Figure 1: Conceptual representation of the coupled SWAT+GWFlow model illustrating the interactions among precipitation, surface runoff, infiltration, groundwater recharge, lateral flow, evapotranspiration, and groundwater–surface water exchanges within a watershed. The coupled framework enables explicit simulation of surface–groundwater interactions and

agricultural drainage processes, providing a comprehensive representation of watershed hydrology.

As illustrated in Figure 1, SWAT+GWFlow explicitly represents the major hydrological pathways controlling watershed behaviour. Unlike conventional watershed models, the coupled framework simulates groundwater flow and river–aquifer interactions, allowing a more realistic assessment of long-term hydrological responses to land-use change and soil-management practices. SWAT+GWFlow explicitly simulates groundwater recharge, groundwater flow, river–aquifer exchanges, and groundwater storage while maintaining SWAT's ability to represent land-use change, agricultural practices, and watershed hydrology. As a result, the coupled model provides a more comprehensive understanding of how land-management interventions influence streamflow generation, baseflow, and flood responses over long temporal scales. For this reason, SWAT+GWFlow complements rather than replaces hydrodynamic models such as HydroPol2D. Whereas HydroPol2D provides high-resolution simulations of flood propagation and inundation during individual flood events, SWAT+GWFlow evaluates the longer-term hydrological processes that control runoff generation, groundwater behaviour, and watershed response. The integration of these complementary modelling approaches therefore offers a more complete framework for flood-risk assessment, climate-change adaptation, and sustainable watershed management.

4.7. Comparative Assessment of HydroPol2D and SWAT+GWFlow

The review demonstrates that HydroPol2D and SWAT+GWFlow address different but complementary aspects of flood modelling. HydroPol2D is particularly effective for high-resolution simulation of flood propagation, inundation depth, water quality, and emergency-response applications in urban environments. Its computational efficiency also makes it suitable for operational flood forecasting where rapid decision-making is required. In contrast, SWAT+GWFlow provides a watershed-scale representation of hydrological processes by explicitly simulating surface runoff, infiltration, groundwater recharge, subsurface flow, river–aquifer interactions, and the hydrological impacts of land-use change. These capabilities enable the assessment of long-term watershed responses that cannot be represented by event-based hydrodynamic models alone. The complementary strengths of these models form the conceptual foundation of this review. HydroPol2D provides detailed flood-hazard information during individual events, whereas SWAT+GWFlow explains the watershed processes that generate those events and evaluates how changes in land management may influence future flood behaviour. Because these models operate at complementary spatial and temporal scales, they provide different but highly compatible perspectives on flood processes. Their integration therefore offers a more holistic approach to flood-risk assessment by linking short-term flood forecasting with long-term watershed management. This integrated perspective is particularly relevant to the objectives of the present study because it establishes the scientific basis for evaluating how sustainable soil-management practices, including rock dust applications, may influence infiltration, groundwater recharge, runoff generation, and ultimately flood resilience. The following section therefore examines the potential role of rock dust as a nature-based strategy for improving watershed hydrological function and supporting adaptive flood management.

Table 1: Comparison of hydrological and hydrodynamic modelling approaches used in flood-risk assessment.

Model/Approach	**Primary application**	**Main strengths**	**Main limitations**
DEM	Terrain representation	Essential topographic input	Elevation uncertainty in floodplains
WCA2D	Urban flood simulation	Fast and computationally efficient	Limited during extreme flood events
WCA2D + CADDIES	Urban drainage	Surface–sewer interaction	Limited influence during major floods
HEC-RAS	Hydraulic modelling	Accurate physical representation	High computational cost
cGAN-Flood	AI flood prediction	Extremely fast	Cannot simulate velocity; requires extensive training data
HydroPol2D	Flood dynamics and water quality	High-resolution flood simulation; infiltration and pollutant transport	Limited groundwater representation
SWAT+GWFlow	Watershed hydrology	Surface–groundwater interactions; land-use and agricultural processes	Lower spatial detail for urban inundation

Table 1 demonstrates that no single modelling approach adequately represents all processes relevant to flood-risk assessment. Hydrodynamic models such as HydroPol2D provide detailed simulations of flood propagation and inundation dynamics, whereas watershed-scale models such as SWAT+GWFlow better represent groundwater interactions, land-use change, and long-term hydrological responses. Consequently, these models should be regarded as complementary rather than competing approaches, providing the conceptual basis for the integrated socio-hydrological framework proposed in this study.

5. Rock Dust and Sustainable Soil Management

Sustainable land-management practices have gained increasing attention as complementary strategies for reducing flood risk while improving soil health and ecosystem resilience. Although structural flood-control measures remain essential, nature-based solutions are increasingly recognised for their potential to modify watershed hydrological processes by enhancing infiltration, increasing soil-water storage, reducing surface runoff, and improving groundwater recharge. Among these approaches, rock dust application has emerged as a promising soil-management practice because of its potential to improve both agricultural productivity and soil physical properties.

While most research has focused on the agronomic and geochemical benefits of rock dust, relatively little attention has been given to its potential influence on watershed hydrology and flood resilience. This section therefore reviews the current understanding of rock dust applications, their effects on soil hydraulic properties, and their possible contribution to sustainable flood-risk management.

5.1. Rock Dust as a Sustainable Soil Amendment

Rock dust has traditionally been applied as a soil amendment to improve soil fertility, increase nutrient availability, and enhance agricultural productivity. More recently, interest has expanded beyond crop production to include its potential role in carbon sequestration through enhanced rock weathering, making it an increasingly important nature-based solution for climate-change mitigation.

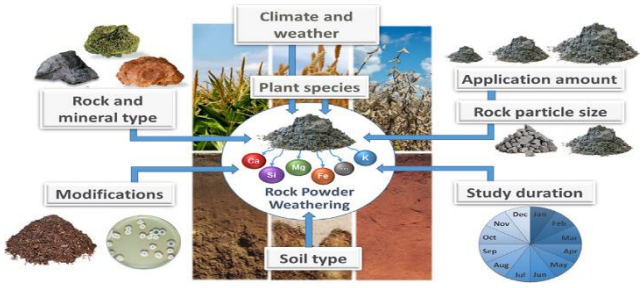

Figure 2: Major factors influencing the effectiveness of rock dust weathering, including mineral composition, climatic conditions, soil characteristics, plant species, application rate, particle size, and treatment duration. These interacting factors determine nutrient release, weathering rates, and potential changes in soil hydraulic properties.

Figure 2 demonstrates that the effectiveness of rock dust depends on multiple interacting environmental and management factors rather than a single controlling variable. Consequently, any assessment of its hydrological influence must consider both soil characteristics and local climatic conditions.

Depending on its mineralogical composition, rock dust gradually releases essential nutrients into the soil while modifying soil structure and influencing physical, chemical, and biological processes. These characteristics have attracted growing attention within sustainable agriculture and environmental management because they may provide long-term improvements in soil function without relying exclusively on conventional chemical fertilisers.

5.2. Hydrological Effects of Rock Dust

Although rock dust has primarily been investigated for its agronomic benefits, its influence on soil hydraulic properties may also have important implications for watershed hydrology. Improvements in soil aggregation, porosity, and water-holding capacity have the potential to increase infiltration rates, reduce surface runoff, and enhance groundwater recharge under suitable environmental conditions. These hydrological processes are directly relevant to flood generation because they influence the partitioning of rainfall between infiltration and overland flow. Consequently, changes in soil physical properties resulting from rock dust application may alter watershed responses to rainfall events, particularly where agricultural land occupies a substantial proportion of the catchment. However, the magnitude of these effects remains uncertain

and depends on multiple factors, including rock type, particle size, application rate, soil characteristics, land management, climate, and rainfall intensity.

5.3. Rock Dust and Flood Resilience

Despite increasing interest in rock dust as a sustainable agricultural practice, its potential contribution to flood resilience remains largely unexplored. Most published studies evaluate crop productivity, soil fertility, carbon sequestration, or enhanced weathering, whereas relatively few examine how rock dust applications may influence runoff generation or catchment-scale flood dynamics. From a hydrological perspective, improvements in infiltration and soil-water storage could contribute to reducing peak runoff during rainfall events. Nevertheless, existing evidence remains insufficient to establish a direct causal relationship between rock dust application and flood mitigation at the watershed scale. Accordingly, rock dust should currently be regarded as a promising hypothesis rather than a demonstrated flood-control measure. Its hydrological effects require further investigation through field experiments and physically based watershed modelling, particularly using integrated frameworks such as SWAT+GWFlow.

5.4. Current Knowledge Gaps

Current evidence demonstrates considerable progress in the fields of flood modelling, sustainable soil management, and enhanced rock weathering. However, these disciplines have largely developed independently, resulting in limited understanding of how land-management interventions influence watershed hydrology and flood resilience simultaneously. Few studies have integrated process-based hydrological models with soil-management scenarios to evaluate the potential impacts of rock dust on runoff generation, groundwater recharge, and flood behaviour. This knowledge gap provides the primary motivation for the interdisciplinary framework proposed in the present study, which combines hydrodynamic modelling, watershed-scale hydrology, sustainable soil management, and socio-hydrological governance into a unified approach for adaptive flood-risk management.

6. An Integrated Socio-Hydrological Framework for Flood Resilience

6.1. Rationale for an Integrated Framework

Flood resilience cannot be achieved through hydrological modelling, engineering infrastructure, or land-management interventions alone. Flood generation results from complex interactions among climatic conditions, watershed characteristics, land use, soil properties, groundwater dynamics, and institutional decision-making. Consequently, effective flood-risk management requires an interdisciplinary framework capable of integrating physical, environmental, and socio-economic processes within a unified decision-support system. Although considerable advances have been made in hydrodynamic flood modelling, watershed hydrology, sustainable soil management, and governance, these disciplines have generally evolved independently. As discussed in the previous sections, hydrodynamic models such as HydroPol2D provide detailed information on flood propagation and inundation dynamics, whereas watershed models such as SWAT+GWFlow represent the long-term hydrological processes controlling runoff generation and groundwater recharge. Similarly, studies on rock dust primarily focus on soil fertility and carbon sequestration, while governance research often examines institutional capacity without explicitly incorporating hydrological model outputs into decision-making. This fragmentation limits the development of comprehensive flood-management strategies. Therefore, this study proposes an integrated socio-hydrological framework that links hydrological modelling, sustainable soil management, and adaptive governance to improve watershed resilience under changing climatic conditions.

6.2. Components of the Proposed Framework

The proposed framework consists of four interconnected components, each representing a critical dimension of flood-risk management. The first component comprises the physical watershed system, including precipitation, topography, land use, soil properties, river networks, groundwater systems, and hydrological processes that control runoff generation and flood propagation. The second component focuses on modelling and simulation. HydroPol2D provides high-resolution simulations of flood inundation, water depth, and hydraulic behaviour during individual flood events, while SWAT+GWFlow represents watershed-scale processes such as infiltration, groundwater recharge, subsurface flow, and the hydrological impacts of land-management practices. The third component addresses sustainable land management, with particular emphasis on rock dust application as a potential nature-based intervention. Although current evidence does not demonstrate a direct causal relationship between rock dust application and flood mitigation, improvements in soil structure, infiltration, and water-holding capacity may influence watershed hydrology and therefore warrant further investigation through integrated modelling approaches. The fourth component represents adaptive governance, including emergency planning, stakeholder participation, early warning systems, institutional coordination, and evidence-based decision-making. This component ensures that scientific knowledge generated through hydrological modelling is translated into practical flood-risk management policies and climate-adaptation strategies.

6.3. Interactions Between Framework Components

The proposed framework recognises that flood resilience emerges from continuous interactions among natural processes, land-management practices, modelling tools, and governance systems. Changes in land use or soil management influence infiltration, evapotranspiration, groundwater recharge, and runoff generation, which subsequently affect flood magnitude and inundation patterns. These hydrological responses can be simulated using SWAT+GWFlow at the watershed scale and translated into detailed flood-hazard maps through HydroPol2D. The resulting model outputs provide scientific evidence that can support emergency planning, infrastructure design, land-use regulation, and community preparedness. At the same time, governance decisions influence future land-management practices and monitoring investments, creating continuous feedback between environmental processes and institutional responses. This socio-hydrological perspective recognises flood management as a dynamic and adaptive process rather than a purely engineering problem. Consequently, flood resilience depends not only on improving model accuracy but also on strengthening monitoring networks, interdisciplinary collaboration, stakeholder engagement, and the integration of science into policy development.

7. Discussion

7.1. Implications of Integrating Hydrological Modelling and Sustainable Land Management

This review demonstrates that flood resilience cannot be achieved through advances in hydrodynamic modelling alone. Although models such as HydroPol2D provide detailed simulations of flood propagation, inundation extent, and water quality, they do not explicitly represent long-term watershed processes, groundwater dynamics, or

the cumulative effects of land-management interventions. Conversely, watershed-scale models such as SWAT+GWFlow provide valuable information on infiltration, groundwater recharge, and runoff generation but do not simulate high-resolution flood propagation during individual flood events. These findings suggest that neither modelling approach independently provides a complete representation of flood processes. Instead, their complementary capabilities offer an opportunity to develop integrated modelling frameworks capable of supporting both operational flood forecasting and long-term watershed management. The review further indicates that sustainable land-management practices may play a more important role in flood-risk reduction than has traditionally been recognised. While rock dust has primarily been investigated for improving soil fertility and enhancing carbon sequestration, its potential influence on infiltration, soil-water storage, and runoff generation suggests that it may also contribute indirectly to flood resilience. However, available evidence remains insufficient to establish a direct causal relationship between rock dust application and reductions in flood magnitude or damage. Vê lêkolînê delîlên zanistî yên berfireh pêşkêş kirin derbarê hebûn, cudahiya biyolojîk û feydeyên tenduristiyê yên potansiyel ên cureyên *Lactobacillus* de ku di berhemên şîrî yên gelek bajarên Herêma Cizîrê de hatine dîtin. Di maweyek sê salan de, zêdetirî sed nimûne, ku şîr, mast û penîr di nav wan de bûn, bi awayekî rêkûpêk hatin komkirin û bi rêbazên mîkrobiyolojîk, biyokîmyayî û molekular (PCR) hatin analîzkirin. Ev encam têgihiştina me derbarê bakteriyên probiyotîk ên xwezayî ku di berhemên şîrî yên kevneşopî û pîşesazî de li herêmê hene, bi awayekî berbiçav pêşxist. Her wiha, encamên lêkolînê diyar kirin ku mast çavkaniya herî berdewam û herî dewlemend a cureyên *Lactobacillus* e, di dema ku di penîr û hin nimûneyên taybet ên şîrê de astên van bakteriyan kêm an jî gelek sînordar bûn. Ceribandinên laboratuwarî her wiha nîşan dan ku izolatanên *Lactobacillus* xwedî çalakiya dijî-bakterî ya berbiçav in û dikarin mezinbûna hem bakteriyên patojen ên Gram-erênî (Gram-positive) û hem jî Gram-neerênî (Gram-negative) asteng bikin. Ev taybetmendiyên dijî-mîkrobî bi awayekî hêzdar pêşniyar dikin ku van bakteriyan di zêdekirina parastina pergala berxwedana rûvî (gut immunity), vegerandina hevsengiya mîkrobiyota rûvî û pêşîlêgirtina dagirkirina rûviyan ji aliyê mîkroorganîzmayên zirardar ve rolek girîng heye. Ji ber vê yekê, cureyên *Lactobacillus* yên ku di berhemên şîrî yên herêmê de hatine veqetandin dikarin wekî çavkaniyên probiyotîk ên xwezayî û bi feyde werin nirxandin, û potansiyela wan heye ku di pêşxistina berhemên fonksiyonel û stratejiyên nû yên pêşîlêgirtin û alîkariya dermankirina nexweşiyên têkildar bi pergala helandinê de werin bikaranîn.

7.2. Scientific and Practical Implications

The interdisciplinary framework proposed in this study provides a conceptual basis for integrating hydrological modelling, sustainable soil management, and adaptive governance within a single decision-support framework. By combining HydroPol2D with SWAT+GWFlow, researchers and practitioners can evaluate both the immediate hydraulic consequences of flood events and the long-term hydrological impacts of land-management interventions. From a practical perspective, this integrated approach has important implications for flood-risk management in Brazil. It supports more informed land-use planning, improved emergency preparedness, enhanced watershed management, and stronger

coordination between scientific institutions and public authorities. Rather than relying exclusively on structural flood-control measures, decision-makers may benefit from combining engineering solutions with nature-based interventions and adaptive governance strategies. The proposed framework may also assist in prioritising investments in hydrometeorological monitoring, remote sensing, and numerical modelling. Improved observational datasets would enhance model calibration and validation while increasing confidence in flood forecasts and climate-adaptation planning.

7.3. Limitations and Future Research

Several limitations should be acknowledged. First, this study represents an integrative conceptual review rather than an empirical modelling investigation. Consequently, the proposed framework has not yet been validated through field observations or numerical experiments. Second, although the review identifies plausible hydrological mechanisms through which rock dust application may influence flood generation, the available literature does not currently provide sufficient empirical evidence to quantify these effects at the watershed scale. Future research should therefore combine controlled field experiments with integrated hydrological modelling to evaluate how changes in soil hydraulic properties influence runoff generation, groundwater recharge, and flood behaviour under different climatic and land-use conditions. Future studies should also investigate the coupling of HydroPol2D and SWAT+GWFlow within unified modelling workflows, uncertainty analysis, remote-sensing data assimilation, and the application of artificial intelligence to improve flood forecasting while maintaining physically based process representation. Such research would provide stronger scientific evidence for integrating sustainable land-management practices into adaptive flood-risk management.

8. Conclusions

Flood risk in Brazil is increasing as a result of climate change, land-use transformation, and growing pressure on watershed systems. Addressing these challenges requires interdisciplinary approaches that integrate hydrological science, sustainable land management, and adaptive governance rather than relying on isolated engineering or policy solutions. This review has demonstrated the complementary roles of HydroPol2D and SWAT+GWFlow in flood-risk assessment. HydroPol2D provides detailed simulations of flood propagation and inundation dynamics, whereas SWAT+GWFlow represents watershed-scale hydrological processes, including groundwater interactions and land-management effects. Their integration offers a more comprehensive understanding of flood generation and watershed response than either modelling approach can provide independently. The review also identified rock dust as a promising nature-based intervention that may improve soil hydraulic properties and contribute indirectly to flood resilience. However, current evidence remains insufficient to establish a direct causal relationship between rock dust application and flood mitigation. Instead, this study proposes an interdisciplinary conceptual framework through which these potential relationships can be systematically investigated using integrated modelling approaches. The principal contribution of this study is the development of a socio-hydrological framework that links hydrological modelling, sustainable soil management, and adaptive governance into a unified approach for

flood-risk management. This framework provides a foundation for future empirical research, supports climate-adaptation planning, and contributes to the development of more resilient watershed-management strategies in Brazil and other regions facing increasing flood risk under changing climatic conditions. Ultimately, strengthening flood resilience under changing climatic conditions will require the integration of physically based hydrological modelling, sustainable land-management practices, and adaptive governance within a unified socio-hydrological framework capable of supporting evidence-based decision-making.

Reference

1. Araújo, L. (2024) Emergência climática traz necessidade de mudança em parâmetros de risco de desastres. Jornal do Comércio. Available at: https://www.jornaldocomercio.com/cadernos/empresas-e-negocios/2024/05/1155968-emergencia-climatica-traz-necessidade-de-mudanca-em-parametros-de-risco-de-desastres.html.
2. Arsenault, R., Breton-Dufour, M., Poulin, A., Dallaire, G. and Romero-Lopez, R. (2019) 'Streamflow prediction in ungauged basins: Analysis of regionalization methods in a hydrologically heterogeneous region of Mexico', Hydrological Sciences Journal, 64(11), pp. 1297–1311.
3. Bao, Z., Zhang, J., Wang, G., Fu, G., He, R., Yan, X. and Jin, J. (2012) 'Comparison of regionalization approaches based on regression and similarity for predictions in ungauged catchments under multiple hydro-climatic conditions', Journal of Hydrology, 466–467, pp. 37–46.
4. Brunner, G.W. (2016) HEC-RAS River Analysis System: 2D Modeling User's Manual. Davis, CA: U.S. Army Corps of Engineers, Hydrologic Engineering Center.
5. Choo, C.W. (1998) The Knowing Organization. New York: Oxford University Press.
6. Cutter, S.L., Boruff, B.J. and Shirley, W.L. (2003) 'Social vulnerability to environmental hazards', Social Science Quarterly, 84(2), pp. 242–261.
7. Davenport, T.H. and Prusak, L. (2000) Working Knowledge: How Organizations Manage What They Know. 2nd edn. Boston, MA: Harvard Business School Press.
8. De Angelis, C.T. (2023) 'Um plano de educação ambiental baseado na educação infantil, participação social: Um estudo de caso na Aldeia Tereré em Sidrolândia', Revista Ambientale, Universidade Estadual de Alagoas (UNEAL). Available at: https://periodicosuneal.emnuvens.com.br/ambientale/article/view/535.
9. De Angelis, C.T. (2024) Um modelo e plano de emergência padronizado para as inundações. Jornal do Comércio. Available at: https://www.jornaldocomercio.com/opiniao/2024/07/1165074-um-modelo-e-plano-de-emergencia-padronizado-para-as-inundacoes.html.
10. De Angelis, C.T. and Gomes Júnior, M.N. (2024) Uma sugestão de modelo hidrodinâmico para prever e gerir inundações. Jornal do Comércio. Available at: https://www.jornaldocomercio.com/opiniao/2024/07/1160994-uma-sugestao-de-modelo-hidrodinamico-para-prever-e-gerir-inundacoes.html.
11. Do Lago, C., Brasil, J., Nóbrega, M., Mendiondo, E.M. and Giacomoni, M.H. (2024) 'Improving pluvial flood mapping resolution of large coarse models with deep learning', Hydrological Sciences Journal, 69(5), pp. 607–621. https://doi.org/10.1080/02626667.2024.2329268.
12. Fassoni-Andrade, A.C., Paiva, R.C.D., Rudorff, C.M., Barbosa, C.C.F. and Leão, E.M. (2020) 'High-resolution mapping of floodplain topography from space: A case

study in the Amazon', Remote Sensing of Environment, 251.

13. Fassoni-Andrade, A.C., Durand, F., Azevedo, A., Bertin, X., Santos, L.G., Khan, J.U., Testut, L. and Moreira, D.M. (2023) 'Seasonal to interannual variability of the tide in the Amazon estuary', Continental Shelf Research, 255.
14. Getirana, A., Boone, A., Yamazaki, D., Decharme, B., Papa, F. and Mognard, N. (2012) 'The Hydrological Modeling and Analysis Platform (HyMAP): Evaluation in the Amazon Basin', Journal of Hydrometeorology, 13, pp. 1641–1665.
15. Gomes Júnior, M.N., Giacomoni, M.H., Richmond, F.A. and Mendiondo, E.M. (2024) 'Global optimization-based calibration algorithm for a 2D distributed hydrologic-hydrodynamic and water quality model', Environmental Modelling & Software, 179.
16. Gomes Júnior, M.N., Lago, C.A., Rápalo, L.M., Oliveira, P.T., Giacomoni, M.H. and Mendiondo, E.M. (2023) 'HydroPol2D—Distributed hydrodynamic and water quality model: Challenges and opportunities in poorly gauged catchments', Journal of Hydrology, 625(Part A).
17. Guidolin, M., Chen, A.S., Ghimire, B., Keedwell, E.C., Djordjevic, S. and Savic, D.A. (2016) 'A weighted cellular automata 2D inundation model for rapid flood analysis', Environmental Modelling & Software, 84, pp. 378–394.
18. Hu, D., Chen, Z., Li, Z. and Zhu, Y. (2024) 'An implicit 1D–2D deeply coupled hydrodynamic model for shallow water flows', Journal of Hydrology, 631.
19. Jillo, A.Y., Demissie, S.S., Viglione, A., Asfaw, D.H. and Sivapalan, M. (2017) 'Characterization of regional variability of seasonal water balance within the Omo-Ghibe River Basin, Ethiopia', Hydrological Sciences Journal, 62(8), pp. 1200–1215.
20. Kroeber, A.L. (1949) 'The concept of culture in science', The Journal of General Education, 3(3), pp. 182–196.
21. Do Lago, C., Brasil, J., Nóbrega, M., Mendiondo, E.M. and Giacomoni, M.H. (2024) 'Improving pluvial flood mapping resolution of large coarse models with deep learning', Hydrological Sciences Journal, 69(5), pp. 607–621. https://doi.org/10.1080/02626667.2024.2329268.
22. Fassoni-Andrade, A.C., Paiva, R.C.D., Rudorff, C.M., Barbosa, C.C.F. and Leão, E.M. (2020) 'High-resolution mapping of floodplain topography from space: A case study in the Amazon', Remote Sensing of Environment, 251.
23. Fassoni-Andrade, A.C., Durand, F., Azevedo, A., Bertin, X., Santos, L.G., Khan, J.U., Testut, L. and Moreira, D.M. (2023) 'Seasonal to interannual variability of the tide in the Amazon estuary', Continental Shelf Research, 255.
24. Getirana, A., Boone, A., Yamazaki, D., Decharme, B., Papa, F. and Mognard, N. (2012) 'The Hydrological Modeling and Analysis Platform (HyMAP): Evaluation in the Amazon Basin', Journal of Hydrometeorology, 13, pp. 1641–1665.
25. Gomes Júnior, M.N., Giacomoni, M.H., Richmond, F.A. and Mendiondo, E.M. (2024) 'Global optimization-based calibration algorithm for a 2D distributed hydrologic-hydrodynamic and water quality model', Environmental Modelling & Software, 179.
26. Gomes Júnior, M.N., Lago, C.A., Rápalo, L.M., Oliveira, P.T., Giacomoni, M.H. and Mendiondo, E.M. (2023) 'HydroPol2D—Distributed hydrodynamic and water quality model: Challenges and opportunities in poorly gauged catchments', Journal of Hydrology, 625(Part A).
27. Guidolin, M., Chen, A.S., Ghimire, B., Keedwell, E.C., Djordjevic, S. and Savic, D.A. (2016) 'A weighted cellular automata 2D inundation model for rapid flood analysis', Environmental Modelling & Software, 84, pp. 378–394.
28. Hu, D., Chen, Z., Li, Z. and Zhu, Y. (2024) 'An implicit 1D–2D deeply coupled hydrodynamic model for shallow water flows', Journal of Hydrology, 631.

29. Jillo, A.Y., Demissie, S.S., Viglione, A., Asfaw, D.H. and Sivapalan, M. (2017) 'Characterization of regional variability of seasonal water balance within the Omo-Ghibe River Basin, Ethiopia', Hydrological Sciences Journal, 62(8), pp. 1200–1215.
30. Kroeber, A.L. (1949) 'The concept of culture in science', The Journal of General Education, 3(3), pp. 182–196.

Rojava Journal of Science and Technology

2026, VOL. 3, No 1, [31-47]

Development of new models for predicting the oil recovery of sandstone reservoirs

Dunya Murad Jankiz[1], Tarek M. Aboul-Fotouh*[2], Abu Zied Ahmed[2] , Sayed Gomaa[2]

[1] Department of Petroleum Engineering, the Institute of Science and Modern Technology, Rojava University.

[2]Mining and Petroleum Engineering Department, Faculty of Engineering, Al-Azhar University, Cairo, Egypt.

Abstract

In this paper, a new correlation was developed (139 data sets) in this study to predict the oil recovery for sandstone solution gas drive reservoirs (SGDR) using NLMR with a coefficient of determination, R^2 of 0.90 (compared to 0.87 for Gulstad correlation). An artificial neural network (ANN) model was developed for this reservoir giving an R^2 of 0.92. A correlation was developed (111 data sets) in this study to predict the oil recovery for sandstone water drive reservoirs (SWDR) using NLMR with a coefficient of determination, R^2 of 0.93 (compared to 0.91 for American Petroleum Institute, API correlation). The developed ANN model for this reservoir gives an R^2 of 0.94.

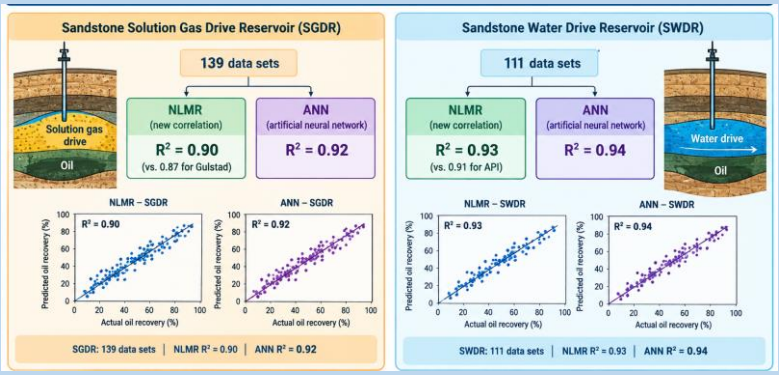

ARTICLE HISTORY

Received 12 May. 2026

Revised 3 Sept. 2026

Accepted 20 Sept. 2026

Keywords

Recovery Factor; ANN, Multiple Regression; Primary Recovery; Sandstone Carbonate Solution Gas Drive; Water Drive

*Corresponding Author: aboulfotouh@azhar.edu.eg

1. Introduction

The oil recovery factor refers to the percentage of the original oil in place that can be commercially produced. Depending on this parameter, we can determine whether the production from a certain oil reservoir is feasible or not. Also, all the production facilities are designed based on this parameter and based on the allowable oil production rate. There are many methods for predicting the oil recovery factor which differ in accuracy from one method to another. This paper aims to review and evaluate the published oil recovery correlations and develop more accurate models compared to the published ones.

2. Literature Review

In a statistical study of Craze and Buckley's water-drive recovery data, Guthrie and Greenberger, using multiple correlation analysis methods, found the following correlation between water-drive recovery and five variables that affect recovery in sandstone reservoirs (Guthrie and Greenberger 1955) (Ahmed 2018)

$$R = 0.114 + 0.272\log(k) + 0.256\log(Sw) - 0.136\log(\mu o) - 1.538(\phi) - 0.00035(h) \quad (1)$$

Based on 73 sandstone reservoirs, Guthrie and Greenberger (1963) developed an empirical expression that correlates the recovery factor with Permeability, k, md Porosity, ϕ, as a fraction Oil viscosity, μ0,cp Connate water saturation, Swc, as a fraction Reservoir thickness, h, ft The empirical equation for predicting the water flood ultimate recovery factor (RF) takes the form (Guthrie and Greenberger 1955) (Ahmed 2018)

$$RF = 0.2719\log K + 0.25569S_{WC} - 0.1355\log\mu o - 1.538\emptyset - 0.0008488h + 0.11403 \quad (2)$$

Arps (1967) statistically correlated the recovery factor as a function of the initial pressure pi and pressure at depletion pa by the following relationship (Onolemhemhen, Isehunwa, and Salufu 2016) (Ahmed 2018):

$$RF = 54.898\left[\frac{\emptyset(1-S_{Wi})}{B_{oi}}\right]^{0.0422}\left[\frac{\mu_{Wi}k}{\mu_{oi}}\right]^{0.077}(S_w)^{-0.1903}\left(\frac{P1}{Pa}\right)^{-0.2159} \quad (3)$$

The American Petroleum Institute calculated the oil recovery factor from a water-drive reservoir using eight factors in sandstone reservoirs: porosity, water saturation, initial oil formation volume factor, permeability, water and oil viscosities at the initial conditions, and initial and abandonment pressures (Gulstad 1995).

$$R = 4259\frac{\emptyset[1-Sw]^{1.0422}}{Boi}\frac{k\,\mu wi^{0.0770}}{\mu oi}[Sw]^{-0.1903}\left[\frac{pi}{pa}\right]^{-0.2159} \quad (4)$$

The American Petroleum Institute developed also, another correlation for sandstone solution gas drive reservoirs as follows:

$$R = 3244\left[\frac{\emptyset(1-S_w)}{B_{ob}}\right]^{1.1611}\left[\frac{K}{\mu_{ob}}\right]^{0.0979}[S_w]^{0.3722}\left[\frac{Pb}{Pa}\right]^{0.1741} \quad (5)$$

The correlations show an extremely strong dependence of recoverable oil on the original oil-in-place. However, other reservoir and fluid parameters were included in the correlation since calculations showed a statistically significant increase in the correlation coefficient when using the multiple-factor regressions (Gulstad 1995).

Gulstad conducted a study on "The Determination of Hydrocarbon Reservoir Recovery Factors by Using Modern Multiple Linear Regression Techniques". During the study, the recovery factor of hydrocarbon reservoirs was observed from the beginning of the well's life to the end, to leverage the benefits of earning during the production stage. Additionally, knowledge gained

from the calculation of the recovery factor allowed for improved programs aimed at developing the primary recovery factor. The equations for the recovery factor, determined using multiple linear regression models, are as follows (Gulstad 1995):

The equation for sandstone reservoir – solution gas drive:

$$R = -264.59 + 0.34(OOIP) + 29.37\ln(R_{SI}) - 0.06(\lambda_o) + 10.70\ln(\lambda_o) - 12.64\ln(h) \quad (6)$$

The equation for sandstone reservoir- water drive:

$$R = -274.94 + 0.44(OOIP) - 56.70\ln(\mu_{oa}) - 119.45\ln(S_W) + 0.04(P_{cp}) - 4.73(\mu_{oi}) + 4.38(\mu_{oa}) + 0.24(OOIP_{calc}) - 0.88(T) \quad (7)$$

The equation for carbonate reservoir- solution gas drive:

$$R = -711.29 + 0.30(k) + 46.64\ln(OIIP) + 420.18(\mu_w) + 0.01(P_i) + 2.19(API) - 190.00\ln(\mu_w) + 79.32(S_w) \quad (8)$$

The equation of carbonate reservoir- water drive:

$$R = -177.26 - 57.11(\mu_{bp}) + 0.34(OOIP) + 33.90(\mu_{Ol}) + 0.17(h) - 86.83\ln(P_i) + 283.27\ln(B_{oa}) + 75.19\ln(\mu_{bp}) + 175.89\ln(T) \quad (9)$$

Gulstad concluded that the four equations for the recovery factor depended on the original oil-in-place and a combination of reservoir rock properties. The best model was found to be the equations for carbonate reservoirs with a water drive mechanism. The values of coefficient of determination for carbonate reservoirs were found to be greater than those for sandstone reservoirs. Additionally, the study found that the heterogeneity of a reservoir plays an important role in characterizing the hydrocarbon reservoirs and estimating the recovery (Gulstad 1995).

Noureldien and El-Banbi studied estimating oil recovery factors using artificial intelligence or calculating reserves wasn't an easy task it needed many conditions and parameters. The first step of the study was to standardize and normalize the input and output parameters. Then, they classified the parameters into two main categories: quantitative parameters and qualitative parameters. Quantitative parameters were (permeability, porosity... etc.) but these data were not normally represented in digits so they used actual field data. These data included parameters such as (facilities, start of production, and number of wells.) then they built two artificial neural networks (ANNs): the first had simple and basic data and the second had advanced data with reasonable accuracy. They concluded that new ANN models were developed for estimating the oil recovery factor but they did not publish the ANN model (Noureldien and El-Banbi 2015).

Olugbenga Olamigoke et al. Studied primary recovery factor correlations for thin oil rims with large gas caps. They found a correlation between the primary recovery factor and a large gas cap. This correlation estimated depended on three dimensions. The correlation for calculating the oil recovery factor in conventional development was validated using real production data from an oil rim field. On the other hand, the models for concurrent development were validated using reservoir simulation results that were matched with historical data. The oil recovery factor . estimated from the correlation of this study was highly accurate, as it matched well with the field data. It was worth noting that the developed correlation has been tested and validated for reservoirs with oil columns less than 100 ft underlying large gas caps. Therefore, they could be applied to such

reservoirs with a good degree of confidence. The correlation that developed for estimating the ultimate oil recovery on the vertical well was (Olamigoke and Isehunwa 2019):

$$\text{Npw} = \frac{\phi(1 - \text{Swc} - \text{Sor})k_h\, ho^{2.5} NTG^{1.5}}{\mu_{oi}B_{oi} * 10^6} \quad (10)$$

These response surface models, also known as correlations, were created by fitting non-linear regression models to oil recovery estimates obtained from reservoir simulation runs. These estimates were determined using Box-Behnken experimental design for both conventional development and concurrent development at gas cap production rates of 5% and 10% of free gas initially in place per annum. Then they get an equation for recovery factor which applied to both conventional and concurrent oil and gas development using horizontal wells:

$$RF = 4.8 + 0.19h_o * 3.1 * 10^{-3}k_h - 0.5m + 0.4r_{eD} - 1.9\mu_o + 1.8\left(\frac{k_v}{k_h}\right) + 0.1\theta + 4.87q_{gi} + 3 * 10^{-5}h_o k_h + 0.01mh_o + 0.01h_o r_{eD} + 5.5mk_h - 0.06h_o\mu_o - 5.5 * 10^{-3}h_o q_{gi} - 3 * 10^{-4}k_h r_{eD} - 1.3 * 10^{-4}k_h \text{q}_{\text{gi}} \quad (11)$$

$$\text{R}_\text{s} = \gamma_\text{g}\text{API}\left[\left(\frac{\text{P} + 218.2}{172.4}\right)\left(\frac{\text{T}}{\text{API}\gamma_\text{g}}\right)^{-0.5592}\right]^{\frac{1}{0.5852}} \quad (12)$$

The final result showed that the dominant factors affected by oil rim and gas cap production were oil rim thickness, gas cap size, oil viscosity, horizontal permeability, aquifer radius, gas cap offtake, vertical anisotropy, and reservoir dip.

Mahmoud et al. estimated the oil recovery factor for water drive sandy reservoirs through applications of artificial intelligence accuracy of these applications depended on existing data and reservoir age. They used 10 parameters that were: the effective reservoir thickness, original oil in place, reservoir pressure, the reservoir area, porosity, Lorenz coefficient, effective permeability, API gravity, oil viscosity, and initial water saturation. The researchers used AI models to develop an empirical correlation for recovery factor estimation based on data collected from a large number of water-drive sandstone reservoirs. The AI models were trained using data from 130 reservoirs and then tested using data from 38 other reservoirs. The results showed that the ANNs-based correlation developed by the researchers outperformed the currently available empirical equations for recovery factor estimation in terms of all the measures of error evaluation used in the study. The ANNs-based correlation also had a higher coefficient of determination (0.94) compared to the Gulstad correlation, which was considered to be one of the most accurate correlations currently available (with a coefficient of determination of only 0.55) (Mahmoud et al. 2019).

3. Results and Discussion

3.1 Data preparation and description for sandstone solution gas drive reservoirs (SSGDR)

139 datasets are collected from the literature. The data description is presented in Table 1. The data represents the oil recovery as a function of the original oil in place, initial solution GOR, oil mobility at the bubble point pressure, and net pay thickness. As presented in this table, the collected data covers oil recovery values ranging from 16 to 908 STB, the original oil-in-place values ranging from 189 to 2146 STB, initial solution GOR values ranging from 44 to 3000 SCF/STB, oil mobility values range from 0.11 to 6230.769

and net pay thickness values range from 4.5 to 1100 ft. اكتب المعادلة هنا.

Table 1: Data description for predicting oil recovery of sandstone solution gas drive reservoirs.

	N	Rsi	k/uob	H	REC
Mean	828.95	577.518	163.705	63.319	187.324
Standard Error	32.72	40.545	48.179	10.428	12.645
Median	735	480	33.333	25	138
SD	385.766	478.024	568.025	122.947	149.079
Sample Variance	148815.4	228507	322652.7	15115.94	22224.6
Kurtosis	1.318	8.297	95.77	37.571	5.437
Skewness	1.195	2.41	9.143	5.294	2.101
Range	1957	2956	6230.659	1095.5	892
Minimum	189	44	0.11	4.5	16
Maximum	2146	3000	6230.769	1100	908
Count	139	139	139	139	139

Before developing the correlation, we should check the relation between the oil recovery and the input parameters. **Figure 1** shows the effect of the input parameters on the oil recovery for the sandstone solution gas drive. As depicted in this figure, the oil recovery is directly proportional to the original oil in place, oil mobility, and net pay thickness. On the other hand, the oil recovery is inversely proportional to the initial solution GOR. As shown also, in this figure, the oil recovery is affected by the original oil in place with coefficient correlation, R = 78%, initial solution GOR with R = -27%, oil mobility with R = 15%, and net pay thickness with R = 18.6%.

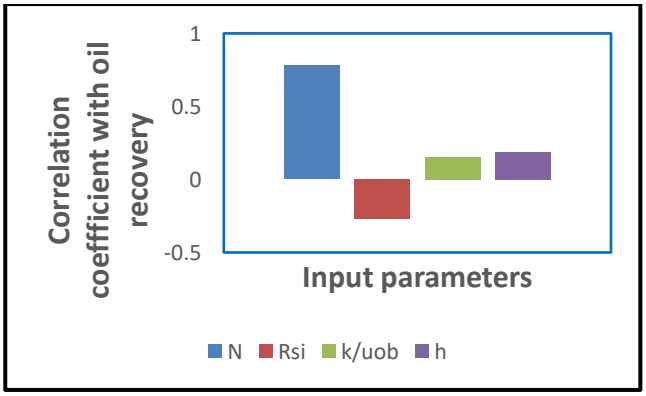

Figure 1: Effect of input parameters on oil recovery for SSGDR

3.2 Development of the new correlation using nonlinear multiple regression (NLMR) for SSGDR:

A correlation was developed in this study to predict the oil recovery. The correlation was developed to predict the oil recovery as a function of the original oil in place, oil mobility, and net pay thickness, solution GOR. To develop this correlation 139 datasets are

collected from the literature. The developed oil recovery correlation for SSGDR can be expressed as:

$$R = aN^b(R_{si} + c)^d(k/\mu_o)^e h^f \qquad (13)$$

Where:

A	*B*	*C*	*D*	*e*	*f*	*g*
0.0377	*1.696*	*-28.618*	*0.167*	*1798.7*	*-0.4877*	*-0.0672*

Figure 2 shows the calculated versus actual recovery factor. As shown in **Figure 2** there is an accepted correlation between them where the developed correlation achieves a coefficient of determination, R^2 of 0.90.

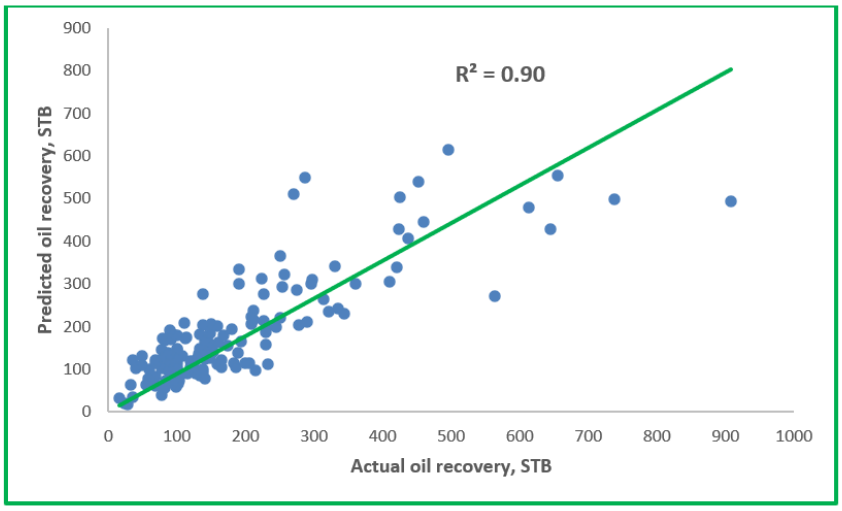

Figure 2: Cross plot for oil recovery of SSDR (after this study)

We investigated the accuracy of the most common published correlation to predict oil recovery compared with the model developed in this study. The correlation for oil recovery of this study achieved the highest coefficient of determination of 0.90 as shown in **Figure 2**. The oil recovery Gulstad correlation gives a coefficient of determination of 0.87 as depicted in **Figure 3**.

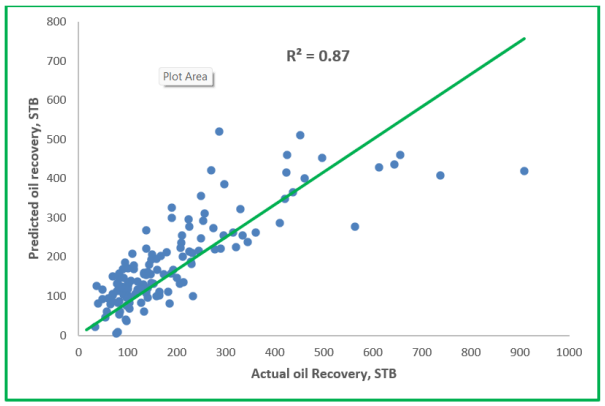

Figure 3: Cross plot of the oil recovery correlation (after Gulstad)

3.3. Data preparation and description for sandstone water drive reservoirs (SWDR)

111 datasets are collected from the literature. The data description is presented in **Table 2**. The data represents the oil recovery as a function of the original oil in place, porosity, water saturation, permeability, pressure, net pay thickness, and API. As presented in this table, the collected data covers oil recovery values ranging from 30 to 1470 STB, the original oil-in-place values ranging from 242 to 2062 STB, porosity values ranging from 0.11 to 0.35 %, water saturation values range from 0.07 to 0.53, permeability values range from 7 to 5000 D, pressure values range from 1 to 14.94943, net pay thickness values range from 6 to 600 ft, and API values range from 14 to 60.

Table 2: Data description for predicting oil recovery of SWDR.

	OOIP	Poro	Sw	K	Pi/Pa	H	API	REC
Mean	1180.243	0.265856	0.266739	815.473	2.70424	59.43964	33.65135	604.1261
Standard Error	32.96195	0.005597	0.009583	85.69972	0.29938	8.177261	0.737456	30.62193
Median	1196	0.288	0.26	440	1.400585	31	35	600
Mode	1007	0.3	0.3	1000	1	16	35	750
Standard Deviation	347.2757	0.058964	0.100966	902.9026	3.154169	86.15279	7.769578	322.6221
Sample Variance	120600.4	0.003477	0.010194	815233.2	9.948779	7422.303	60.36634	104085
Kurtosis	-0.25654	-0.39058	-0.27357	4.548142	6.732518	15.71766	0.450995	-0.32433
Skewness	-0.099	-0.78092	0.274574	1.979075	2.695504	3.531374	0.208689	0.375767
Range	1820	0.24	0.46	4993	13.94943	594	46	1440
Minimum	242	0.11	0.07	7	1	6	14	30

Maximum	2062	0.35	0.53	5000	14.94943	600	60	1470

.

Before developing the correlation, we should check the relation between the oil recovery and the input parameters. **Figure 4** shows the effect of the input parameters on the oil recovery for the sandstone water drive. As depicted in this figure, the oil recovery is directly proportional to the original oil in place, porosity, permeability, and net pay thickness. On the other hand, the oil recovery is inversely proportional to the water saturation, pressure, and API.

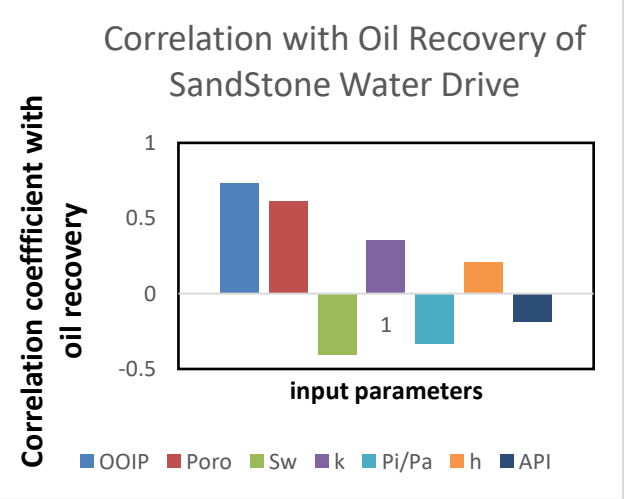

Figure 4: Effect of input parameters on oil recovery for SWDR

As shown also in this figure, the oil recovery is affected by the original oil in place with coefficient correlation, R = 0.730, porosity with R = 0.61, water saturation with R = -0.41, and permeability with R= 0.36, pressure with R= -0.33 and net pay thickness with R = 0.21 and API with R= -0.19

3.4 Development of the new correlation using NLMR for SWDR:

A correlation was developed in this study to predict the oil recovery. The correlation was developed to predict the oil recovery as a function of the original oil in place, porosity, water saturation, permeability, pressure, net pay thickness, and API. To develop this correlation 111 datasets are collected from the literature.

The developed oil recovery correlation of SWDR can be expressed as:

$$\mathrm{RF} = \mathrm{a} + \mathrm{ooip}^{b} * \emptyset^{c} * \mathrm{Sw}^{d} * \mathrm{K}^{e} * \mathrm{pi/pa}^{f} * \mathrm{h}^{g} * \mathrm{API}^{h} \qquad (14)$$

$\mathrm{a} = 0.485045$, $b = 0.874907$, $c = 0.764819$, $d = 0.331989$, $e = 0.023058$,

$f = 0.102882$, $g = 0.056389$, $h = 0.417031$

Figure 5 shows the calculated versus actual recovery factor. As shown from this figure there is a good correlation between them where the developed correlation achieves a coefficient of determination, R^2 of = 0.93.

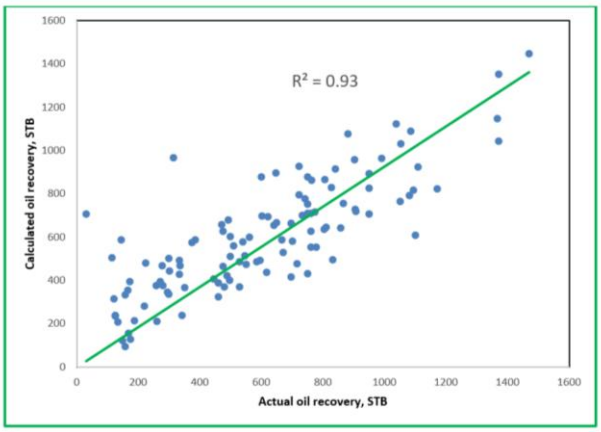

Figure 5: Cross plot of the oil recovery correlation.

We investigated the accuracy of the most common published correlation to predict the oil recovery compared with the models developed in this study. The correlation for oil recovery of this study achieved the highest coefficient of determination of 0.93 as shown in **Figure 5**. The oil The oil recovery API correlation gives a coefficient of determination of 0.91 as depicted in **Figure 6**.

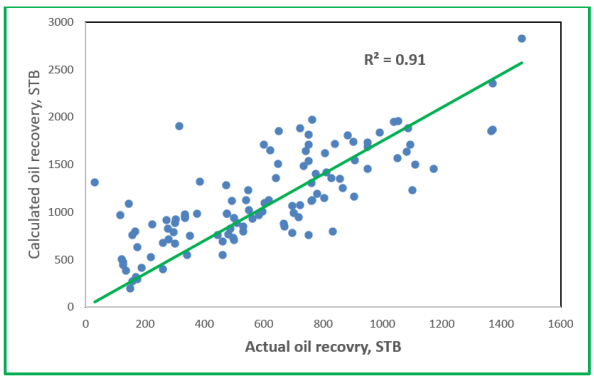

Figure 6: Cross plot for oil recovery (API correlation)

3.5 Development of oil recovery for SSGDR using artificial neural network (ANN)

The collected data sets are divided into three sets before building the ANN model to predict the oil recovery. 70% of the data sets are employed for the process of model training, while the remaining 30% of data sets are used for validation and testing the performance of the model. Besides, all the data are normalized between −1 and 1 to build the ANN model.

In this work, an ANN model is developed to estimate the oil recovery as a function of the original oil in place, oil mobility, and net pay thickness, solution GOR. The model is built based on three layers. The first layer is the input layer, which has 4 neurons for inputs. 9 neurons contribute to the hidden layer, which is the second layer. The output layer, which has one neuron to predict the output parameter, oil recovery, is the third layer we first examined the Tan-sigmoid as a transfer function at different numbers of hidden neurons (5, 6, 7, 8, 9, and 10) as presented in **Table 3**. We found the highest coefficient of determination and the lowest RMSE at n = 6. Then we examined the logistic-sigmoid as a transfer function at numbers of neurons of (5, 6, 7, 8, 9, and 10) as presented in **Table 4**. We found that the optimum transfer

function is Log-sigmoid with 9 neurons where the coefficient of determination is 0.92 and MAE is 20.9 %. To reach this fact a Levenberg-Marquardt technique was selected as a training algorithm and the pure-linear was examined to be the output function. **Figure 7** shows the layout of the proposed model and the characteristics of the proposed model are presented in **Table 5.**

Table 3: Oil recovery model accuracy at various numbers of neurons in the hidden layer with a tan–sigmoid transfer function for the SSGDR

	5	6	7	8	9	10
R2	0.51	0.75	0.32	0.38	0.54	0.16
SD	29.93	20.69	34.86	22.61	25.83	67.87
RMSE	46.54	29.99	46.44	42.12	51.63	84.17
RE	-20.68	-10.82	-19.6	-15.07	-18.35	-79.56
AE	33.95	22.66	34.85	26.23	30.05	88.37

Table 4: Oil recovery model accuracy at various numbers of neurons in the hidden layer with log–sigmoid transfer function for the SSGDR.

	5	6	7	8	9	10
R2	0.6	0.57	0.27	0.54	0.92	0.39
SD	26.95	27.15	27.31	25.04	18.97	29.42
RMSE	43.45	48.31	58.86	51.36	22.12	59.21
RE	-18.24	-18.02	-11.54	13.04	-10.77	-18.3
AE	32.53	32.95	32	35.13	20.9	30.26

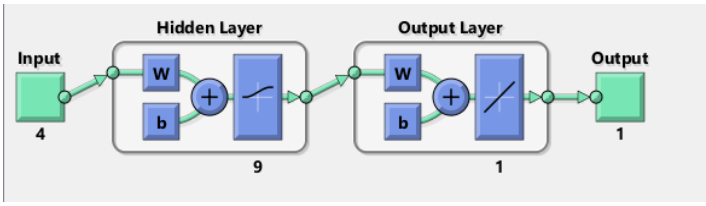

Figure 7: Layout of the proposed ANN oil recovery model for SSDR

Table 5: Characteristics of ANN oil recovery model of the SSDR

Parameter	Value
ANN layers number	3
neurons number in the input layer	4
optimum neuron number in the hidden layer	9
training algorithm for the neural network	Levenberg–Marquardt
transfer function of the hidden layer	Log sigmoid
transfer function of the output layer	pure linear

The developed model for oil recovery using the ANN can be expressed as follows:

First, the input parameters are normalized using the following expressions:

$$N_n = 0.001022 * N - 1.193153 \quad (15)$$

$$Rs_n = 0.000677 * Rs - 1.02977 \quad (16)$$

$$(k/\mu)_n = 0.000321 * \left(\frac{k}{\mu}\right) - 1.000035 \quad (17)$$

$$h_n = 0.001826 * h - 1.008215 \quad (18)$$

For i = 1 to no of neurons and for j = 1 to no of inputs, the inputs for the hidden are calculated from the following expression:

$$S_{i,j} = \sum_{j=1}^{N}(w_{i,j}x_j) + b_i \quad (19)$$

Where x_j represents the normalized input parameter.

The oil recovery can be calculated by the following function:

$$REC = 446\left[b_{ho} + \sum_{i=1}^{n} w_{hoi}\left(\frac{1}{1+\exp(-S_i)}\right)\right] + 462 \quad (20)$$

The proposed oil recovery model's coefficients are listed in **Table 6**.

The regression plot for the oil recovery model of SSDR, as indicated in **Figure 8** presents the relation between the calculated and the true oil recovery for all data sets. The fit is accepted where the coefficient of determination is 0.92

Table 6: Weights and Biases of the Oil Recovery ANN Model for SSGDR

Neuron #	Wi,1	Wi,2	Wi,3	Wi,4	bi	Whi	Bh
1	-3.4489	0.82109	2.2473	-2.4703	4.8571	-0.17252	-0.93786
2	-3.2534	-1.5967	-0.4458	3.1584	3.6523	-0.8374	
3	-1.9765	3.0192	-2.9843	-1.4835	2.2211	1.0455	
4	1.2276	-3.0785	-1.9261	2.9099	-1.3954	0.14924	
5	3.9062	0.025694	2.2422	-1.8971	0.029608	0.90948	
6	-2.1914	-1.1872	-0.34067	4.1582	-1.2648	0.2317	
7	2.4957	-0.34693	-3.0857	-2.7598	2.4192	0.019633	
8	2.0353	3.1571	-1.8488	-2.4439	3.6219	0.00622	
9	-3.571	-0.75424	1.3114	-2.6853	-5.3414	-0.22336	

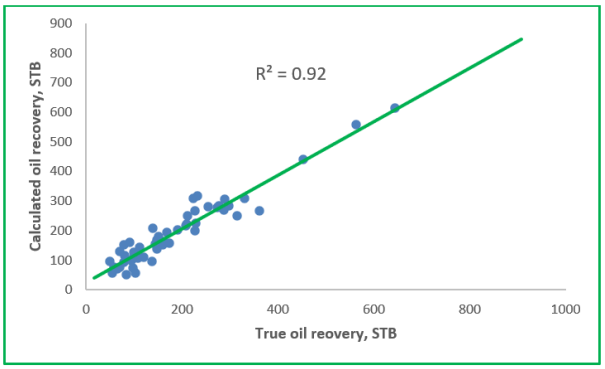

Figure 8: Cross plot of ANN oil recovery model of SSDR

3.6 Development of oil recovery for SWDR using ANN

The collected data sets are divided into three sets before building the ANN model to predict the oil recovery. 70% of the data sets are employed for the process of model training, while the remaining 30% of data sets are used for validation, and testing the performance of the model. Besides, all the data are normalized In this work, an ANN model is developed to estimate the oil recovery as a function of the original oil

in place, porosity, water saturation, permeability, Pi/Pa ratio, net pay thickness, and, API. The model is built based on three layers. The first layer is the input layer, which has 7 neurons for inputs. 6 neurons contribute to the hidden layer, which is the second layer. The output layer, which has one neuron to predict the output parameter, oil recovery, is the third layer. we first examined the Tan-sigmoid as a transfer function at different numbers of hidden neurons (5, 6, 7, 8, 9, and 10) as presented in **Table 7**. We found the highest coefficient of determination and the lowest RMSE at n = 6. Then we examined the Tan-sigmoid as a transfer function at numbers of neurons of (5, 6, 7, 8, 9, and 10) as presented in **Table 8**. We found that the optimum transfer function is Logistic-sigmoid with 6 neurons where the coefficient of determination is 0.6 and MAE is 47.2 % To reach this fact a Levenberg-Marquardt technique was selected as a training algorithm and the pure-linear was examined to be the output function. **Figure 9** shows the layout of the proposed model and the characteristics of the proposed model are presented in **Table 9.**

Table 7: Oil recovery model accuracy at various numbers of neurons in the hidden layer with a tan–sigmoid transfer function for sandstone water drive:

	5	6	7	8	9	10
R2	0.52	0.55	0.26	0.59	0.59	0.6
SD	208.19	204.36	196.56	200.33	201.09	197.17
RMSE	185.27	177.74	221.49	172.76	172.18	173.53
RE	-26.66	-26.81	-20.26	-25.86	-26.46	-23.72
AE	51.88	48.57	51.37	47.36	48.55	50.93

Table 8: Oil recovery model accuracy at various numbers of neurons in the hidden layer with a log–sigmoid transfer function for sandstone water drive:

	5	6	7	8	9	10
R2	0.58	0.94	0.57	0.57	0.5	-0.11
SD	206.84	194.4	214.91	200.3	211.93	198.81
RMSE	172.82	169.98	174.38	174.33	182.63	210.74
RE	-25.58	-25	-31.69	-26.05	-29.2	-33.43
AE	47.25	47.22	49.12	47.73	51.05	56.85

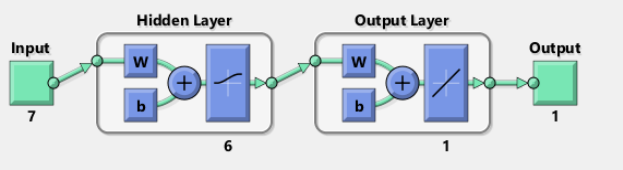

Figure 9: Layout of the proposed ANN oil r

Table 9: Characteristics of ANN oil recovery model of sandstone water drive ecovery model for sandstone water drive

Parameter	Value
ANN layers number	3
neurons number in the input layer	7
optimum neuron number in the hidden layer	6
training algorithm for the neural network	Levenberg–Marquardt
transfer function of the hidden layer	Log sigmoid
transfer function of the output layer	pure linear

The developed model for oil recovery using the ANN can be expressed as follows:

First, the input parameters are normalized using the following expressions:

$$N_n = 0.001099 * N - 1.265934 \quad (21)$$

$$\phi_n = 8.333333 * \phi - 1.916667 \quad (22)$$

$$(S_w)_n = 4.347826 * S_w - 1.304348 \quad (23)$$

$$k_n = 0.000401 * k - 1.002804 \quad (24)$$

$$(Pi/Pa)_n = 0.143375 * (Pi/Pa) - 1.143375 \quad (25)$$

$$h_n = 0.003339 * h - 1.003339 \quad (26)$$

$$API_n = 0.033898 * API - 1.033898 \quad (27)$$

For i = 1 to no of neurons and for j = 1 to no of inputs, the inputs for the hidden are calculated from **Eq. 18**. The oil recovery can be calculated by the following expression:

$$REC = 734.5\left[-0.0228 + \sum_{i=1}^{n} W_{i,j}\left(\frac{1}{1+\exp(-S_i)}\right)\right] + 735.5 \quad (28)$$

The proposed oil recovery model's coefficients are listed in **Table 10**. The regression plot for the oil recovery model of SSDR, as indicated in **Figure 10** presents the relation between the calculated and the true oil recovery for all data sets. The fit is accepted where the coefficient of determination is 0.94.

Table 10: Weights and Biases of the Oil Recovery ANN Model for SWDR

Neuron	Wi,1	Wi,2	Wi,3	Wi,4	Wi,5	Wi,6	Wi,7	Whi	bi
1	3.0197	-0.3794	0.00839	-0.8997	1.9351	-0.641	0.45729	-3.0901	1.4917
2	4.899	3.0177	0.13528	-1.3855	-0.2651	-2.413	2.6506	-2.267	0.60098
3	-1.2311	-1.4232	3.8264	1.0633	2.5017	-2.2841	-2.7343	3.5377	-1.2004
4	-0.97186	-2.1979	0.71725	2.9217	-2.1781	-1.0218	-3.7718	1.0167	0.51583
5	-3.8	-5.905	-0.1087	0.51892	2.473	2.1984	-1.4769	4.2591	-0.1458
6	-0.98269	1.7365	0.77143	2.1174	-0.7372	2.1245	-0.5136	-3.7223	0.27164

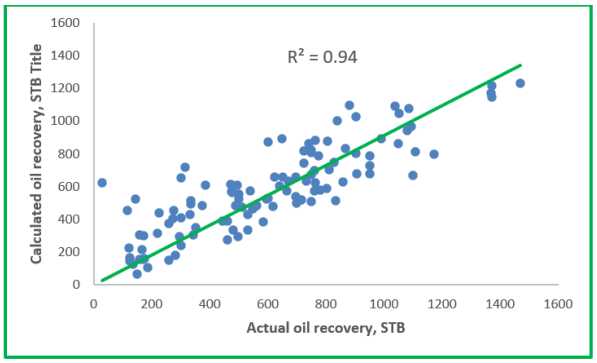

Figure 10: Cross plot of ANN oil recovery model of SWDR

4. Conclusions

From the work, the following conclusions may be drawn:

1. A correlation was developed (139 data sets) in this study to predict the oil recovery for sandstone solution gas drive reservoirs (SGDR) using NLMR with a coefficient of determination, R^2 of 0.90 (compared to 0.87 for Gulstad correlation).
2. A new ANN model was developed to calculate the oil recovery of sandstone solution gas drive reservoirs giving an R^2 of 0.92.
3. A correlation was developed (111 data sets) in this study to predict the oil recovery for sandstone water drive reservoirs (SWDR) using NLMR with a coefficient of determination, R^2 of 0.92 (compared to 0.91 for American Petroleum Institute, API correlation).
4. A new ANN model was developed to calculate the oil recovery of sandstone water drive reservoirs giving an R^2 of 0.94.

Nomenclature

B_{oa}: the oil formation volume factor at the abandonment pressures, bbl/STB.

B_{oi}: the oil formation volume factor at the initial pressure, bbl/STB.

h: net pay thickness

k: permeability, md.

N: the original oil in place, OOIP, STB

N_{cal}: the calculated original oil in place, STB

P_a: the abandonment pressure, psi.

P_i: the initial pressure, psi.

NT STOIIP: the stock-tank oil initially in place (STB/NAF)

STOOIP: Stock tank original oil in place.

S_{wi}: the initial water saturation, dimensionless.

T: Reservoir temperature, °F

ϕ: porosity, dimensionless

μ_{oa}: the oil viscosity at the abandonment pressure, cp.

μ_{ob}: the oil viscosity at the bubble point pressure, cp.

μ_{oi}: the oil viscosity at the initial pressure, cp.

μ_{wi}: the water viscosity at the initial pressure, cp.

G: Net-to-gross ratio

References:

1. Ahmed, Tarek. 2018. *Reservoir engineering handbook*: Gulf professional publishing.
2. Gulstad, Rick L. 1995. "The determination of hydrocarbon reservoir recovery factors by using modern multiple linear regression techniques." Texas Tech University.
3. Guthrie, RK, and Martin H Greenberger. 1955. "The use of multiple-correlation analyses for interpreting petroleum-engineering data." Drilling and Production Practice.
4. Mahmoud, Ahmed Abdulhamid, Salaheldin Elkatatny, Weiqing Chen, and Abdulazeez %J Energies Abdulraheem. 2019. "Estimation of oil recovery factor for water drive sandy reservoirs through applications of artificial intelligence." 12 (19):3671.
5. Noureldien, Darhim M, and Ahmed H El-Banbi. 2015. "Using Artificial Intelligence in Estimating Oil Recovery Factor." SPE North Africa Technical Conference and Exhibition.
6. Olamigoke, OLUGBENGA, and SUNDAY O %J J Eng Sci Technol Isehunwa. 2019. "Primary recovery factor correlations for thin oil rims with large gas caps." 14 (4):2359-2371.
7. Onolemhemhen, RU, SO Isehunwa, and SO Salufu. 2016. "Development of recovery factor model for water drive and depletion drive reservoirs in the Niger Delta." SPE Nigeria Annual International Conference and Exhibition.

Rojava Journal of Science and Technology

2026, VOL. 3, No 1, [48-60]

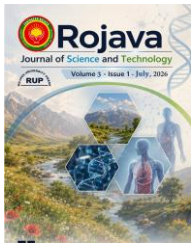

Prevalence and Associated Risk Factors of Diabetes and Prediabetes in North and East Syria: A Cross-Sectional Study

Ali Ibrahim Alabo[1], Haidar Saify Nabiabad[2], Eman Elbassuoni*[3]

1 Department of Clinical Physiology, Institute of Science and Modern Technology, Rojava University, Syria

2 Department of Medical Biotechnology, Institute of Science and Modern Technology, Rojava University, Syria

3 Department of Physiology, Faculty of Medicine, Minia University, Egypt

ABSTRACT

Background: Diabetes and prediabetes are major global health concerns associated with increased morbidity and mortality, particularly in regions affected by conflict where healthcare systems are weakened. Limited epidemiological data exist for North and East Syria, highlighting the need to assess the burden of glycemic disorders and their determinants. Objective: To determine the prevalence of diabetes and prediabetes among adults living in North and East Syria and to identify the clinical risk factors associated with impaired glycemic status. Methods: A cross-sectional study was conducted in North and East Syria. A total of 167 adults were recruited. Data were collected through structured questionnaires, anthropometric measurements, blood pressure assessment, and laboratory investigations. Results: The study demonstrated a considerable prevalence of diabetes and prediabetes, with significant associations between impaired fasting blood glucose and older age, higher body mass index (BMI), increased waist circumference, physical inactivity, smoking, and unhealthy diet. Personal and family histories of hypertension, diabetes, and cardiovascular disease were strongly associated with elevated cardiometabolic risk. Mean arterial pressure, triglycerides, and cholesterol levels showed significant correlations with abnormal glycemic patterns, indicating clustering of metabolic risk factors. Conclusion: Diabetes and prediabetes are highly prevalent among adults in North and East Syria, influenced by multiple demographic, lifestyle, and clinical determinants. These findings provide essential baseline data for developing targeted screening programs, preventive strategies, and public health interventions to reduce the growing burden of diabetes in conflict-affected Syrian communities.

ARTICLE HISTORY

Received: 14 Jan. 2026

Revised: 10 May. 2026

Accepted: 28 Aug. 2026

Keywords:
Diabetes Mellitus, Prediabetes, Cardiometabolic Risk Factors, North and East Syria

* Corresponding Author: Elbassuoni@yahoo.com

1. Introduction

Diabetes mellitus (DM) has reached epidemic proportions globally, characterized by a chronic metabolic disorder that arises from either the autoimmune destruction of insulin-producing β-cells or, more commonly, a progressive resistance to insulin action. The International Diabetes Federation (IDF) has projected a continued and disproportionate rise in the Middle East and North Africa (MENA) region, which already faces some of the highest age-adjusted prevalence rates of type 2 diabetes worldwide. This surge is largely attributed to rapid urbanization, an aging population, and a profound shift toward sedentary lifestyles (Sun et al. 2021). The pathophysiology of the disease involves a complex and multifaceted interplay between genetic predisposition and environmental triggers. While the biological mechanisms of insulin resistance, primarily driven by visceral adiposity, lipid accumulation, and systemic chronic low-grade inflammation, are well-documented, they are often exacerbated by hormonal shifts and aging (Lobo et al. 2022). In particular, the transition into states of metabolic syndrome is marked by the secretion of pro-inflammatory cytokines such as TNF-α and IL-6 from visceral adipose tissue, which directly impairs insulin signaling pathways (El Khoudary et al. 2020). The primary objective of this study is to determine the prevalence of diabetes and prediabetes among individuals living in North and East Syria. Furthermore, this study aims to identify demographic, socioeconomic, and lifestyle-related risk factors that are statistically associated with the development of diabetes and prediabetes in this population. The findings will provide insights that can guide healthcare practitioners, policymakers, and public health officials in the formulation of tailored interventions designed to mitigate the impact of diabetes in a conflict-affected situation.

2. Materials and Methods

2.1. Study Design and Setting

An observational cross-sectional study was conducted between December 2024 and June 2025 to determine the prevalence of diabetes and prediabetes in North and East Syria. The study was carried out across five medical centers: Afrin, Tal Rifaat, and Yassin Hospitals in the Aleppo district, and Kobani and Amal Hospitals in the East Euphrates region.

2.2. Participants and Sampling

The target population included Syrian adults aged ≥ 18 years residing in the study regions. The minimum sample size was calculated at 162 participants using EPI-INFO (v.3), based on a 95% confidence interval, 5% margin of error, and an estimated regional diabetes prevalence of 11.9% (World Health Organization [WHO], 2023). A total of 167 participants were enrolled using a convenience sampling method (Pourhoseingholi et al., 2013).

2.3. Data Collection and Tools

Data were collected via structured interviews, clinical examinations, and laboratory analyses.

- Questionnaire: Data were collected on socio-demographics, lifestyle factors, and medical/family history.
- Anthropometric Measurements: Weight, height, and BMI were recorded following standard WHO guidelines (Casadei et al., 2000). Waist circumference thresholds for abdominal obesity were set at ≥ 88 cm for women and ≥ 102 cm for men (Ntuk et al., 2014; WHO, 2008).
- Clinical and Laboratory Assessment: Blood pressure was measured using a mercury sphygmomanometer according to the American College of Cardiology and American Heart Association (ACC/AHA) guidelines (Unger et al., 2020; Writing Committee Members, 2025). Following an overnight fast, venous blood samples were analyzed for fasting blood sugar (FBS), total cholesterol, and triglycerides. Hyperglycemia and prediabetes were defined according to WHO and International Diabetes Federation (IDF) standards (American Diabetes Association, 2024; Unwin et al., 2006).

2.4. Statistical Analysis

Data were analyzed using IBM SPSS Statistics version 27 (Arkkelin, 2014). Categorical variables were expressed as frequencies and percentages and compared using Chi-square or Fisher's exact tests. Continuous variables were compared using independent t-tests or ANOVA. Statistical significance was defined as $p < 0.05$.

2.5. Ethical Considerations

The study protocol was approved by the Ethics Committee of Rojava University. Informed written consent was obtained from all participants prior to data collection. The study was conducted in accordance with the ethical principles of the Declaration of Helsinki (World Medical Association, 2025).

3. Results

3.1. Demographic and Anthropometric Characteristics

The study included 167 participants (50.9% male, 49.1% female) with a mean age of 49.4 ± 14.6$ years. The mean body mass index (BMI) was 27.9 ± 5.3 kg/m2, and the mean waist circumference was 94.9 ± 13.7 cm. Clinical assessment revealed mean systolic and diastolic blood pressures of 132.1 ± 21.5 mmHg and 85.3 ± 14.7 mmHg, respectively. Metabolic markers showed a mean fasting blood glucose (FBG) of 107.8 ± 45.2 mg/dl and mean triglycerides of 195.8 ± 98 mg/dl.

Table 1: Anthropometric Measurements, Blood Pressure, and Serum Metabolic Profiles of the Studied Population

	Total (N= 167)
Gender - Male - Female	 85 (50.9%) 82 (49.1 %)
Age (Mean ± SD)	49.4 ± 14.6
Weight (Kg) (Mean ± SD)	74.4 ± 16.2
Height (m) (Mean ± SD)	1.63 ± 0.11
Waist circumference (cm) (Mean ± SD)	94.9 ± 13.7
BMI (kg/m^2) (Mean ± SD)	27.9 ± 5.3
SBP (mmHg) (Mean ± SD)	132.1 ± 21.5

DBP (mmHg) (Mean ± SD)	85.3 ± 14.7
MAP (mmHg) (Mean ± SD)	100.9 ± 15.7
Fasting blood glucose (mg/dl) (Mean ± SD)	107.8 ± 45.2
Cholesterol (mg/dl) (Mean ± SD)	165.5 ± 34.5
Triglycerides (mg/dl) (Mean ± SD)	195.8 ± 98

SBP = systolic blood pressure, DBP = diastolic blood pressure, MAP = mean arterial blood pressure.

3.2. Prevalence of Diabetes and Cardiometabolic Risk Factors

The prevalence of diabetes was 19.8%, while 16.2% of the population met the criteria for prediabetes. Overall, cardiometabolic risk factors were highly prevalent: 69.5% of participants were overweight or obese, 49.7% had central obesity (high waist circumference), 32.9% were hypertensive, and 61.7% exhibited hypertriglyceridemia.

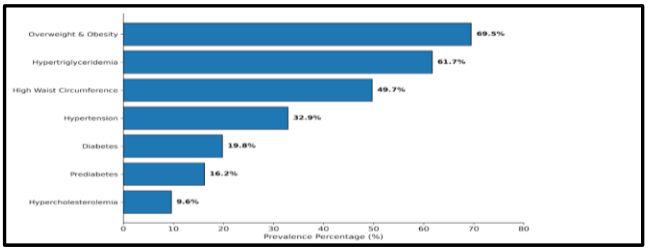

Figure 1: Prevalence of prediabetes, Diabetes, and Associated Cardiometabolic Risk Factors among the studied population.

3.3. Age and Gender-Related Correlations

Age was significantly positively correlated with waist circumference (r = 0.241, p = 0.002), mean arterial pressure (r = 0.204, p = 0.008), and fasting blood glucose (r = 0.182, p = 0.019). Significant gender differences were observed in glucose regulation and obesity patterns. Diabetes was significantly more frequent among females than males (28.1% vs. 11.8%; p = 0.026). Females also showed higher rates of central obesity (63.4% vs. 36.5%; p < 0.001) and clinical obesity (45.1% vs. 25.9%; p = 0.012).

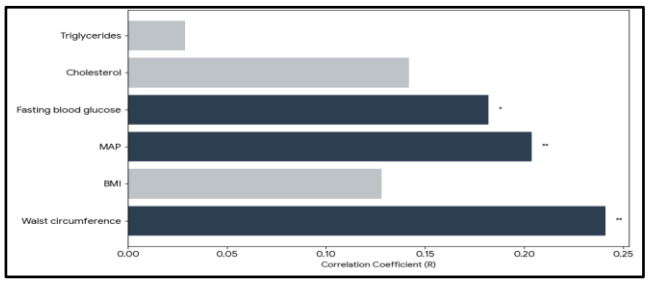

Figure 2: Correlation between age and some anthropometric measurements, blood pressure measurements, and serum metabolic profile of the studied population.

Significant associations in dark blue, ** Correlation is significant at the 0.01 level (2-tailed), * Correlation is significant at the 0.05 level (2-tailed).

3.4. Predictors of Dysglycemia

Blood glucose status was significantly associated with hypertension (p = 0.003) and elevated triglycerides (p < 0.001). Participants with diabetes were significantly more likely to have a high mean arterial pressure (57.6%) compared to normoglycemic individuals (25.2%; p < 0.001). Furthermore, a positive family history of diabetes was strongly associated with current diabetic status (72.7% vs. 40.2%; p = 0.003). In contrast, lifestyle factors such as physical activity, smoking, and dietary habits did not show a statistically significant association with glucose levels in this population (p > 0.05).

Table 2: Correlation between gender and some anthropometric measurements, blood pressure measurements, and serum metabolic profile of the studied population:

	Gender		**Test**	**p-value**
	Female (N= 82)	**Male (N= 85)**		
Blood glucose (mg/dl)				
- Normal	48 (58.5%)	59 (69.4%)	X^2	0.026
- Prediabetes	11 (13.4%)	16 (18.8%)	7.126	
- Diabetes	23 (28.1%)	10 (11.8%)		
CMS				
- No CMS	52 (63.4%)	65 (76.5%)	X^2	0.066
- CMS	30 (36.6%)	20 (23.5%)	3.39	
Waist circumference (cm)				
- Normal	30 (36.6%)	54 (63.5%)	X^2	<0.001
- High waist circumference	52 (63.4%)	31 (36.5%)	12.1	
(> 102 cm for male and > 88 cm for female)				
BMI categories				
- Underweight (<18.5)	3 (3.7%)	2 (2.4%)	X^2	0.012
- Normal weight (18.5-24.9)	22 (26.8 %)	24 (28.2%)	8.9	
- Overweight (25-29.9)	20 (24.4%)	37 (43.5%)		
- Obese (30-39.9)	37 (45.1%)	22 (25.9%)		
MAP (mmHg)				
- Normal MAP	55 (67.1%)	57 (67.1%)	X^2	0.99
- High MAP	27 (32.9%)	28 (32.9%)	0.000	
Triglycerides (mg/dl)				
- Normal triglycerides	27 (33%)	37 (43.5%)	X^2	0.111
- Mild high triglycerides	32 (39%)	23 (27.1%)	6.005	
- Moderate high triglycerides	23 (28%)	22 (25.9%)		
- Severe high triglycerides	0 (0%)	3 (3.5%)		

A p-value less than 0.05 indicates a significant association between the variables.

Table 3: Association of Glycemic Status with Demographic, Anthropometric, Clinical, and Lifestyle Risk Factors

	Blood glucose			**Test**	**p-value**
	Normal 107 (64 %)	**Prediabetes** 27 (16.2 %)	**Diabetes** 33 (19.8 %)		
Waist circumference (cm)					
- Normal	59 (55.1%)	12 (44.4%)	13 (39.4%)	X^2	0.091
- High waist circumference (> 102 cm for male and > 88 cm for female)	48 (44.9%)	15 (55.6%)	20 (60.6%)	2.943	
BMI categories					
- Normal weight (18.5-24.9)	35 (32.7%)	9 (33.3%)	*7 (21.2%)*	X^2	
- Overweight (25-29.9)	39 (36.4%)	6 (22.2%)	*11 (33.3%)*	*4.625*	0.098
- Obese (30-39.9)	33 (30.8%)	12 (44.4%)	*15 (45.5%)*		
MAP (mmHg)					
- Normal MAP	80 (74.8%)	18 (66.7%)	*14 (42.4%)*	X^2	
- High MAP	27 (25.2%)	9 (33.3%	*19 (57.6%)*	11.947	<0.001
Cholesterol (mg/dl)					
- Normal	99 (92.5%)	23 (85.2%)	*29 (87.9%)*	X^2	
- High	8 (7.5%)	4 (14.8%)	*4 (12.1%)*	1.647	0.312
Triglycerides (mg/dl)					
- Normal triglycerides	47 (43.9%)	11 (40.7%)	*6 (18.2%)*	X^2	
- Mild high triglycerides	38 (35.5%)	6 (22.2%)	*11 (33.3%)*	13.57	<0.001
- Moderate high triglycerides	21 (19.6%)	9 (33.3%)	*15 (45.5%)*		
- Severe high triglycerides	1 (0.9%)	1 (3.7%)	*1 (3.0%)*		
History of diabetes					
- No	102 (95.3%)	22 (81.5%)	*4 (12.1%)*	X^2	<0.001
- Yes	5 (4.7%)	5 (18.5%)	*29 (87.9%)*	99.973	
Family history of diabetes					
- No	64 (59.8%)	16 (59.3%)	*9 (27.3%)*	X^2	0.003
- Yes	43 (40.2%)	11 (40.7%)	*24 (72.7%)*	*11.190*	
History of hypertension					
- No	69 (64.5%)	13 (48.1%)	*12 (36.4%)*	X^2	0.003

- Yes	38 (35.5%)	14 (51.9%)	*21 (63.6%)*	8.974	
Family history of hypertension - No - Yes	43 (40.2%) 64 (59.8%)	14 (51.9%) 13 (48.1%)	*9 (27.3%)* *24 (72.7%)*	X^2 3.809	0.349
History of CVD - No - Yes	81 (75.7%) 26 (24.3%)	21 (77.8%) 6 (22.2%)	*18 (56.3%)* *14 (43.8%)*	X^2 5.137	0.056
Family history of CVD - No - Yes	63 (58.9%) 44 (41.1%)	17 (63%) 10 (37%)	*18 (54.5%)* *15 (45.5%)*	X^2 0.439	0.758
Education level - No - Low **-** High	26 (24.3%) 68 (63.6%) 13 (12.1%)	5 (18.5%) 19 (70.4%) 3 (11.1%)	*13 (39.4%)* *18 (54.5%)* *2 (6.1%)*	X^2 4.414	0.120
Smoking - No - Yes	54 (50.5%) 53 (49.5%)	14 (51.9%) 13 (48.1%)	*20 (60.6%)* *13 (39.4%)*	X^2 1.049	0.335
Alcohol - No - Yes	97 (90.7%) 10 (9.3%)	21 (77.8%) 6 (22.2%)	*31 (93.9%)* *2 (6.1%)*	X^2 4.669	0.994
Physical activity - No - Yes	55 (51.4%) 52 (48.6%)	12 (44.4%) 15 (55.6%)	*15 (45.5%)* *18 (54.5%)*	X^2 0.636	0.480
Diet - Healthy - Unhealthy - Mixed	4 (3.7%) 4 (3.7%) 99 (92.5%)	2 (7.4%) 1 (3.7%) 24 (88.9%)	*0 (0%)* *0 (0%)* *33 (100%)*	X^2 3.738	0.287

A p-value of less than 0.05 indicates a significant association between the variables.

4. Discussion

The findings of this study reveal an alarming burden of metabolic dysfunction in North and East Syria, with an overt diabetes prevalence of 19.8% and a prediabetes prevalence of 16.2%. Combined, over one-third of the studied adult cohort (36.0%) exhibits impaired glucose regulation. This is substantially higher than the global adult diabetes prevalence baseline of 10.5% reported by the International Diabetes Federation (Sun et al. 2021) and sits at the upper end of estimates across the Middle East and North Africa (MENA) region, which typically range between 12% and 19% (World Health Organization 2023a). This high prevalence of dysglycemia does not occur in isolation; rather, it is embedded within a profound clustering of cardiometabolic risk factors. In this cohort, 69.5% of participants were overweight or obese, 49.7% exhibited central obesity, 32.9% were hypertensive, and 61.7% suffered from hypertriglyceridemia. This severe constellation of health issues underscores a regional epidemic of metabolic syndrome, highlighting a highly vulnerable population group that faces substantial future cardiovascular and microvascular complications (World Health Organization 2023b). The close, statistically significant intersection between blood glucose status, high mean arterial pressure (MAP), and hypertriglyceridemia is driven by overlapping, well-established cellular and endocrine pathways. Visceral adipose tissue, which was highly elevated in this cohort as indicated by a mean waist circumference of 94.9 cm, is metabolically active and highly lipolytic. It floods the portal circulation with free fatty acids (FFAs) and releases pro-inflammatory cytokines such as tumor necrosis factor-alpha (TNF-α) and interleukin-6 (IL-6) (El Khoudary et al. 2020). These molecules inhibit insulin receptor substrate-1 (IRS-1) signaling in skeletal muscle and hepatic tissues, causing systemic insulin resistance. In the liver, insulin resistance stimulates excessive de novo lipogenesis and impairs the inhibitory effect of insulin on very-low-density lipoprotein (VLDL) secretion. Concurrently, endothelial lipoprotein lipase (LPL) activity is suppressed, resulting in the severe hypertriglyceridemia (61.7%) observed in this population. Chronic hyperglycemia and insulin resistance stimulate blood pressure elevation via several distinct pathways. Hyperinsulinemia acts as a chronic activator of the sympathetic nervous system (SNS) and the renin-angiotensin-aldosterone system (RAAS), driving renal sodium retention and expanding intravascular volume. Simultaneously, advanced glycation end-products (AGEs) and secondary oxidative stress impair endothelial nitric oxide synthase (eNOS) activity. This loss of nitric oxide-mediated vasodilation elevates vascular stiffness and systemic vascular resistance, directly explaining why 57.6% of the diabetic sub-cohort presented with high mean arterial pressure (World Health Organization 2023c). Beyond primary dietary factors, the unique humanitarian context of North and East Syria

introduces a major secondary pathophysiological driver: chronic psychosocial stress. Prolonged exposure to instability, economic hardship, and displacement drives sustained overactivity of the hypothalamic-pituitary-adrenal (HPA) axis. The resulting continuous, low-grade elevation of circulating cortisol serves as a physiological antagonist to insulin, promotes gluconeogenesis, and preferentially directs lipid deposition into visceral (android) fat depots rather than subcutaneous tissue (Yousuf & Ahmedani 2020). Visceral adiposity and adipokine shifts cause elevated FFAs, TNF-α, and IL-6, causing IRS-1 pathway inhibition and systematic insulin resistance with hyperglycemia. Hepatic insulin resistance enhances de novo lipogenesis and suppresses endothelial LPL, yielding atherogenic hypertriglyceridemia. Hyperinsulinemia and AGE accumulation stimulate SNS/RAAS hyperactivation and reduce eNOS expression, provoking endothelial dysfunction and hypertension. Ultimately, chronic HPA-axis activation drives sustained cortisol release and induces hepatic gluconeogenesis, which accelerates prediabetes progression. Our results align with, and in some instances diverge from, regional and international epidemiological literature. The profound rates of metabolic clustering and the strong link between dysglycemia and hypertriglyceridemia are robustly supported by regional literature. Studies from conflict-affected settings in the Middle East confirm that forced nutritional transitions, characterized by a reliance on subsidized, energy-dense, shelf-stable carbohydrates and trans-fats at the expense of fresh produce, rapidly induce a pattern of diabetic dyslipidemia (Akik et al. 2020). Our findings regarding age-related metabolic decay, where advancing age significantly correlated with waist circumference, MAP, and fasting glucose, are entirely consistent with standard medical literature showing progressive vascular remodeling, arterial stiffening, and a natural decline in insulin sensitivity with age (Cheng et al. 2022). Furthermore, the powerful association between positive family history and current diabetic status (72.7% vs 40.2%) mirrors extensive global data validating the high heritability and shared domestic environmental risks of type 2 diabetes (American Diabetes Association 2024). Conversely, two key outcomes in our study contrast sharply with broader international trends, starting with the gender disparity paradox. In our cohort, females displayed significantly higher rates of diabetes (28.1% vs. 11.8%), clinical obesity (45.1% vs. 25.9%), and central obesity (63.4% vs. 36.5%) compared to males. Globally, males frequently display higher or equal rates of type 2 diabetes at lower BMI thresholds due to differences in intrinsic liver fat accumulation (Kautzky-Willer et al. 2016). However, our data is strongly supported by sub-regional Middle Eastern studies (Aljefree & Ahmed 2015; Ataey et al. 2020), which show that cultural restrictions on outdoor physical movement, high post-pregnancy weight retention, and postmenopausal estrogen

decline collectively create an exceptionally high-risk environment for metabolic disease among Middle Eastern women. The second area of divergence relates to non-significant lifestyle variables. Perhaps the most unexpected finding was that lifestyle variables, such as self-reported physical inactivity, dietary habits, and smoking, did not demonstrate a statistically significant standalone association with blood glucose levels. This directly contradicts decades of landmark global trial evidence establishing sedentary behavior and poor diet as foundational causes of dysglycemia. This contradiction does not indicate that lifestyle is irrelevant in North and East Syria. Rather, it highlights a state of diagnostic homogeneity. Because the ongoing crisis has forced nearly the entire local population into uniform dietary constraints (limited access to variety, reliance on identical subsidized grains) and shared limitations on active recreation, there is insufficient behavioral variance within the cohort for standard Chi-square tests to detect a statistical difference. This indicates that the entire region is exposed to a baseline environmental risk, masking individual behavioral correlations (Auad et al. 2022). The extensive overlap of visceral obesity, hypertension, hypertriglyceridemia, and glucose intolerance highlights an urgent public health crisis. In resource-constrained and conflict-affected zones, managing advanced, long-term complications of untreated diabetes, such as chronic kidney disease, stroke, and cardiovascular events, places an unsustainable financial and operational burden on fragile health infrastructure. Therefore, clinical paradigms in the region must turn from reactive treatments to proactive, low-cost screening. Because overall BMI did not correlate significantly with age, but waist circumference did, clinicians should prioritize measuring waist circumference over absolute body weight to avoid missing cases of sarcopenic or metabolically obese normal weight (MONW) individuals. Given the strong familial aggregation identified, primary care systems should implement targeted, household-level metabolic screenings for families with a known history of diabetes, pairing accessible blood pressure checks with routine capillary blood glucose testing to capture metabolic syndrome in its highly treatable, prediabetic window (Auad et al. 2022; World Health Organization 2023d).

Reference

1. Akik, Chaza, Hala Ghattas, Sassy Molyneux, Fouad M. Fouad, and Rana Jawad. 2020. "Nutritional Transitions and the Food System in Conflict-Affected Settings: The Case of Syria." Public Health Nutrition 23 (10): 1780–1789. https://doi.org/10.1017/S136898001900437X
2. Akik, Chaza, Hala Ghattas, Sawsan Abdulrahim, and Annie S. Anderson. 2020. "The Impact of Conflict on Dietary Intake and Nutrition Health Outcomes in Women of Reproductive Age in the Middle East and North Africa: A Systematic Review." Progress in Cardiovascular Diseases 63 (2): 138–46. https://doi.org/10.1016/j.pcad.2020.03.011
3. Aljefree, Samar, and Faruk Ahmed. 2015. "Prevalence of Cardiovascular Disease and Associated Risk Factors in the Countries of

the Gulf Cooperation Council: A Review." World Journal of Cardiology 7 (10): 681–702. https://doi.org/10.4330/wjc.v7.i10.681

4. American Diabetes Association. 2024. "2. Diagnosis and Classification of Diabetes: Standards of Care in Diabetes—2024." Diabetes Care 47 (Supplement 1): S20-S42. https://doi.org/10.2337/dc24-S002
5. American Diabetes Association. 2024. "Standards of Care in Diabetes—2024." Diabetes Care 47 (Supplement 1): S1–S321. https://doi.org/10.2337/dc24-S001
6. Arkkelin, Daniel. 2014. "Using SPSS to Understand Research and Data Analysis." Psychology Curricular Materials. https://scholar.valpo.edu/psych_oer/1
7. Ataey, Aref, Javad Seyedmohammadi, Soltanali Ghani, and Maryam Keshvari. 2020. "A Systematic Review and Meta-Analysis of Obesity and Overweight in Iran and Neighboring Middle Eastern Countries." BMC Public Health 20: 1571. https://doi.org/10.1186/s12889-020-09609-8
8. Auad, Ghiath, Ameer Kakaje, and Zein Alourfi. 2022. "Metabolic Syndrome Risk Profiles in Complex Humanitarian Emergencies: A Cross-Sectional Analysis in Syria." Conflict and Health 16: 42. https://doi.org/10.1186/s13031-022-00475-3
9. Casadei, Kimberly, and John Kiel. 2020. "Anthropometric Measurement." StatPearls. https://www.ncbi.nlm.nih.gov/books/NBK537315/
10. Cheng, Xiang, Mengru Wang, Ruirui Yang, and Shikai Yu. 2022. "Vascular Aging and Metabolic Syndrome: A Deep Correlation Analysis." Frontiers in Cardiovascular Medicine 9: 883412. https://doi.org/10.3389/fcvm.2022.883412
11. El Khoudary, Samar R., Brooke Aggarwal, Theresa M. Beckie, Howard N. Hodis, Carole L. Johnson, Robert D. Langer, Marian C. Limacher, et al. 2020. "Menopause Transition and Cardiovascular Disease Risk: Implications for Contemporary Management: A Scientific Statement From the American Heart Association." Circulation 142 (25): e506–e532. https://doi.org/10.1161/CIR.0000000000000912
12. Kautzky-Willer, Alexandra, Jürgen Harreiter, and Giovanni Pacini. 2016. "Sex and Gender Differences in Risk, Pathophysiology, and Complications of Type 2 Diabetes Mellitus." Endocrine Reviews 37 (3): 278–316. https://doi.org/10.1210/er.2015-1137
13. Lobo, Rogerio A., Faith G. Davis, Anne G. Rosenfeld, Sarah M. Samaan, Martha Gulati, Mercedes R. Carnethon, and Kevin C. Maki. 2022. "Evaluation of Cardiovascular Risk in Women for the Practitioner." Journal of the American College of Cardiology 79 (13): 1301–13. https://doi.org/10.1016/j.jacc.2022.01.031
14. Lobo, Rogerio A., Melissa S. Burnett, and John C. Stevenson. 2022. "The Metabolic Syndrome and Menopause." Menopause 29 (6): 742–748. https://doi.org/10.1097/GME.0000000000001964
15. Ntuk, Unyime E., Jason M. R. Gill, David F. Mackay, Naveed Sattar, and Jill P. Pell. 2014. "Ethnic-Specific Obesity Cutoffs for Diabetes Risk: Cross-Sectional Study of 490,288 UK Biobank Participants." Diabetes Care 37 (9): 2500-2507. https://doi.org/10.2337/dc13-2966
16. Pourhoseingholi, Mohammad Amin, Maryam Vahedi, and Mohamadreza Rahimzadeh. 2013. "Sample Size Calculation in Medical Studies." Gastroenterology and Hepatology from Bed to Bench 6 (1): 14-17. https://www.ncbi.nlm.nih.gov/pmc/articles/PMC4017493/
17. Sun, Hong, Pouya Saeedi, Stephen Karuranga, Rosanne Pinkepank, Saliu Ogurtsova, Belma B. Duncan, Carmel Stein, et al. 2021. "IDF Diabetes Atlas: Global, Regional and Country-Level Diabetes Prevalence Estimates for 2021 and Projections for 2045." Diabetes Research and Clinical Practice 183: 109119. https://doi.org/10.1016/j.diabres.2021.109119
18. Unger, Thomas, Claudio Borghi, Fadi Charchar, Nadia A. Khan, Neil R. Poulter, Dorairaj Prabhakaran, et al. 2020. "2020

International Society of Hypertension Global Hypertension Practice Guidelines." Hypertension 75 (6): 1334-1357. https://doi.org/10.1161/HYPERTENSIONAHA.120.15026

19. World Health Organization. 2008. Waist Circumference and Waist-Hip Ratio: Report of a WHO Expert Consultation. Geneva: World Health Organization. https://www.who.int/publications/i/item/9789241501491
20. World Health Organization. 2023a. Diabetes Prevalence in the Eastern Mediterranean Region. Cairo: WHO Regional Office for the Eastern Mediterranean. https://www.emro.who.int/noncommunicable-diseases/publications/index.html
21. World Health Organization. 2023b. Cardiometabolic Risk Factors and Noncommunicable Diseases Profile. Cairo: WHO Regional Office for the Eastern Mediterranean. https://www.emro.who.int/ncd-publications.html
22. World Health Organization. 2023c. Pathophysiology of Vascular Complications in Diabetes Mellitus. Geneva: World Health Organization. https://www.who.int/publications/i/item/WHO-NCD-2023.3
23. World Health Organization. 2023d. Integrated Management of Cardiovascular Risk and Diabetes in Low-Resource Settings. Geneva: World Health Organization. https://www.who.int/publications/i/item/9789240074644
24. World Medical Association. 2025. "World Medical Association Declaration of Helsinki: Ethical Principles for Medical Research Involving Human Participants." JAMA 333 (1): 71-74. https://doi.org/10.1001/jama.2024.21972
25. Writing Committee Members. 2025. "2025 AHA/ACC/AANP/AAPA/ABC/ACCP/ACPM/AGS/AMA/ASPC/NMA/PCNA/SGIM Guideline for the Prevention, Detection, Evaluation and Management of High Blood Pressure in Adults." Hypertension. https://doi.org/10.1161/HYP.0000000000000249
26. Yousuf, Syed, and M. Yakoob Ahmedani. 2020. "Chronic Stress and Metabolic Syndrome in Post-Conflict Zones." Journal of Diabetes & Metabolic Disorders 19 (2): 1145–1152. https://doi.org/10.1007/s40200-020-00615-5

Rojava Journal of Science and Technology

2026, VOL. 3, No 1, [61-80]

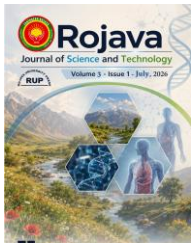

Microwave-Engineered Magnetite@ Bentonite@ Glutamic Acid Nanocomposite for Rapid and Efficient Removal of Remazol Red from Aqueous Systems

Maher Saif Al-Deen Ahmed[1], Haider Saify Nabiabad[2], Mohamad Elsayed Mahmoud[3], Rehab Mansour El-Sharkawy*[4]

[1] Dep. of Chemistry, Institute of Science and Modern Technology-Rojava University, Syria
[2] Dep. of Biotechnology, Institute of Science and Modern Technology-Rojava University, Syria
[3] Faculty of Science, Chemistry Department, Alexandria University, Egypt
[4] Faculty of Dentistry, Chemistry Department, Pharos University in Alexandria, Egypt

ABSTRACT

Objective: The creation of effective and sustainable adsorbents for wastewater contaminated with dyes is a significant environmental issue. Material and Methods: This research successfully developed a new magnetically recoverable nanocomposite, consisting of magnetite, bentonite, and glutamic acid (Fe_3O_4@BNT@GA), through a quick microwave-assisted method. This microwave approach allowed for even heating, better dispersion, and enhanced surface functionalization compared to traditional techniques. After the nanocomposite synthesis, X-ray diffraction (XRD) was used to assess the crystalline phases and structural integrity of the composite material. Fourier transform infrared spectroscopy (FT-IR) helped identify functional groups and verify that surface modifications were successfully made. Thermogravimetric analysis (TGA) was performed to analyze thermal stability and composition. Scanning electron microscopy (SEM) was employed to investigate surface morphology and particle distribution. The adsorption efficiency of the created nanocomposite for Remazol Red dye was assessed under microwave-assisted conditions. Results: Structural and physicochemical analyses confirmed the successful incorporation of magnetite nanoparticles within the bentonite framework and their functionalization with glutamic acid, which provided numerous active sites for adsorption. The findings indicated fast adsorption kinetics and high removal rates, with nearly total dye elimination achieved in brief contact periods. Discussion: Kinetic analysis suggested that the adsorption process conforms to a pseudo-second-order model, highlighting a predominant chemisorption mechanism. Isotherm analyses aligned well with the Langmuir model, indicating monolayer adsorption on a uniform surface. Thermodynamic analysis verified that the adsorption process is spontaneous and characterized by endothermic behavior. Furthermore, the nanocomposite showed remarkable reusability, consistently delivering high performance throughout several adsorption-desorption cycles. When applied to real water samples, it showcased its practical viability, achieving removal efficiencies greater than 95%. Conclusion: In summary, the microwave-assisted Fe_3O_4@BNT@GA nanocomposite is a promising, environmentally friendly, and effective adsorbent for advanced wastewater remediation applications.

ARTICLE HISTORY

Received: 12 Feb. 2026

Revised: 19 Jul. 2026

Accepted: 11 Sep. 2026

Keywords: Bentonite, Glutamic acid, Remazol red, Magnetite, Microwave, Water remediation.

*Corresponding Author: Dr. Rehab Mansor rehab.mansour@pu

1. Introduction

Water pollution caused by industrial effluents is one of the most pressing environmental concerns worldwide. Among these pollutants, synthetic dyes—particularly azo dyes such as Remazol Red—are widely used in textile, leather, and paper industries (Balasundharam et al., 2026). These dyes are not only aesthetically displeasing but also toxic, carcinogenic, and resistant to biodegradation, making their removal from wastewater a significant challenge. To address the environmental challenges posed by industrial water pollution, researchers have turned to adsorption technologies using eco-friendly and cost-effective materials (Kumar et al., 2026). Natural clay minerals, such as bentonite, have proven to be efficient adsorbents due to their large surface area, ion-exchange capacity, and availability. Bentonite's negatively charged surfaces allow for strong electrostatic interactions with positively charged dye molecules, while its interlayer spaces can accommodate various organic and inorganic species, enhancing adsorption capacity. However, raw bentonite alone may have limitations in adsorption rate and selectivity, which has led to modifications through surface functionalization and composite formation. (Riaz et al, 2015). At the same time, magnetite (Fe_3O_4) nanoparticles provide magnetic separability and high surface reactivity, making them suitable for forming composite materials (Siwi et al., 2026). Moreover, incorporating biomolecules such as glutamic acid can enhance surface functionality by introducing amino and carboxyl groups, which interact effectively with dye molecules (Inbaraj et al, 2011). In recent years, microwave-assisted synthesis has emerged as an efficient and sustainable technique for the preparation of advanced nanocomposites with tailored structural and surface properties (Girdthep et al., 2026). Unlike conventional heating methods that rely on conduction and convection, microwave irradiation interacts directly with polar molecules and conductive components, providing rapid, volumetric heating and uniform temperature distribution (Adhikari et al., 2026). This approach often leads to shorter reaction times, improved particle crystallinity, enhanced dispersion, and higher porosity. When applied to the synthesis of magnetite–bentonite–glutamic acid composites, microwave irradiation enhances the structural integrity of the material and improves the distribution of functional groups on the surface (Hessien et al, 2022). Beyond synthesis, microwave energy can further improve the adsorption performance during water treatment. By increasing molecular mobility, decreasing boundary layer resistance, and accelerating intraparticle diffusion, microwave-assisted adsorption reduces equilibrium time and increases the overall removal efficiency of pollutants (Girdthep et al., 2026). The combination of magnetite, bentonite, and glutamic acid, together with microwave-assisted preparation, leverages synergistic effects that overcome the individual limitations of each component, resulting in a high-performance, magnetically recoverable, and potentially reusable adsorbent (Gabano et al, 2022). Given the urgent need for effective, cost-efficient, and environmentally friendly solutions to industrial dye pollution, the microwave-assisted preparation of magnetite@bentonite@glutamic acid composites presents a promising strategy. This approach not only ensures enhanced adsorption efficiency and selectivity toward dyes like Remazol Red but also provides a feasible pathway toward scalable and sustainable wastewater treatment technologies. Therefore, the present study aims to develop a microwave-assisted Fe_3O_4@BNT@GA nanocomposite and evaluate its efficiency for the removal of Remazol Red dye under microwave-enhanced conditions. The adsorption behavior is systematically investigated through kinetic, isotherm, and thermodynamic analyses, along with reusability and real-sample applications, to assess its potential for sustainable wastewater treatment.

2. Experimental

2.1. Materials and Chemicals

Bentonite clay served as the primary adsorbent material without any additional purification. Iron salts, such as ferric chloride ($FeCl_3 \cdot 6H_2O$) and ferrous sulfate ($FeSO_4 \cdot 7H_2O$), were utilized as precursors for the synthesis of magnetite. Glutamic acid acted as a functionalizing agent to add active surface groups. Sodium hydroxide (NaOH) was employed to adjust the pH and facilitate precipitation. Remazol Red dye was chosen as the model pollutant for the adsorption investigations. All chemicals were of analytical grade and were used as received, without any further processing. Deionized water was employed consistently throughout all experiments.

2.2. Synthesis

2.2.1. Microwave preparation of nanomagnetite (nFe3O4)

Magnetite nanoparticles (Fe_3O_4) were produced using a co-precipitation technique. To summarize, Fe^{3+} and Fe^{2+} salts were dissolved in deionized water while continuously stirring at a microwave oven (approximately 70–80 °C). The molar ratio of Fe^{3+} to Fe^{2+} was kept at 2:1. Following this, NaOH solution was added dropwise until the pH reached around 10, which resulted in the formation of a black precipitate. The mixture was stirred for an additional 30 to 60 minutes to ensure that precipitation was complete (Mahmoud et al, 2021). The resulting Fe_3O_4 nanoparticles were collected using magnetic separation, thoroughly washed multiple times with deionized water and ethanol to eliminate any impurities, and then dried at a microwave oven (about 60 °C).

2.2.2. Preparation of Fe_3O_4@Bentonite Composite

The Fe_3O_4@BNT composite was prepared by dispersing 5 g of bentonite in 20 ml deionized water under vigorous stirring to achieve a homogeneous suspension. The previously synthesized Fe_3O_4 nanoparticles (5 g) were then added to the suspension and mixed thoroughly.

The mixture was subjected to continuous stirring and, and heated in a microwave oven to near dryness to facilitate the deposition of Fe_3O_4 onto the bentonite layers. After sufficient interaction time, the composite was separated, washed repeatedly to remove unbound particles, and dried at 70 °C (Calimli et al, 2020).

2.2.3. Functionalization with Glutamic Acid (Fe_3O_4@BNT@GA)

Surface functionalization was achieved by dispersing the Fe_3O_4@BNT composite in a water solution containing glutamic acid. The mixture was stirred under controlled conditions to facilitate interaction between the functional groups of glutamic acid and the surface of the composite. To improve the efficiency of the functionalization, the suspension underwent microwave irradiation for a brief period. This microwave treatment ensured uniform heating and enhanced the grafting of –COOH and $–NH_2$ groups onto the surface of the composite. Following the treatment, the resulting Fe_3O_4@BNT@GA nanocomposite was magnetically separated, thoroughly washed to eliminate any excess reagents, and dried at 60 °C for future use.

2.3. Characterization Techniques

After the nanocomposite synthesis, X-ray diffraction (XRD) was used to assess the crystalline phases and structural integrity of the composite material. Fourier transform infrared spectroscopy (FT-IR) helped identify functional groups and verify that surface modifications were successfully made. Thermogravimetric analysis (TGA) was performed to analyze thermal stability and composition. Scanning electron microscopy

(SEM) was employed to investigate surface morphology and particle distribution.

2.4. Batch Adsorption Experiments

Batch adsorption experiments were conducted to assess the efficiency of Remazol Red dye removal. A specific amount of nanocomposite was introduced into dye solutions with known concentrations (10, 20, 30 mg/L). The mixture was stirred under controlled conditions, and samples were collected at set time intervals. The influence of different parameters such as pH (ranging from 2 to 10), contact time, adsorbent dosage, and temperature was examined systematically. The pH of the solution was modified using dilute solutions of NaOH or HCl. After the adsorption process, the nanocomposite was separated using magnetic methods, and the remaining dye concentration was analyzed through UV–Vis spectrophotometry at λmax= 541 nm.

2.5. Kinetic, Isotherm, and Thermodynamic Studies

The surface charge properties of the nanocomposite were determined using the pH-drift method to identify the point of zero charge (pH_pzc), which helps explain adsorption behavior at different pH levels. To further understand the adsorption mechanism, several kinetic models—including pseudo-first-order, pseudo-second-order, intraparticle diffusion, and Elovich—were applied. The best-fitting model was identified based on correlation coefficients, providing insight into the rate-controlling steps of the process. Adsorption isotherm studies were also conducted to analyze how dye molecules interact with the adsorbent surface at equilibrium. Models such as Langmuir, Freundlich, Temkin, and Dubinin–Radushkevich were used to interpret the data under optimized conditions across a wide concentration range (10–200 mg/L). Additionally, thermodynamic parameters such as Gibbs free energy (ΔG°), enthalpy (ΔH°), and entropy (ΔS°) were calculated using the Van't Hoff equation to assess the spontaneity and thermal nature of the adsorption process (Lavanya et al., 2026). The reusability of the nanocomposite was evaluated through multiple adsorption–desorption cycles, using acid or base washing for regeneration. Results showed that the material could be reused with minimal efficiency loss. Finally, the applicability of the Fe_3O_4@BNT@GA nanocomposite for the removal of Remazol Red dye from real water samples (industrial wastewater, tap water, and river water) was examined under optimal experimental conditions (pH 7.0, 25 °C, contact time 30 min, and adsorbent dosage 0.05 g). Each sample was spiked with 10 mg L^{-1} of RR dye and treated using the same batch procedure described above. The average results from three independent experiments were used to determine the dye removal efficiency (%R) for each water matrix.

3. Results and discussion

3.1. Characterization of the nanocomposite

The structural properties of the synthesized Fe_3O_4@BNT@GA nanocomposite were investigated using XRD, FT-IR, TGA, and SEM analyses. The XRD pattern in Figure 1 of the synthesized Magnetite @Bentonite @Glutamic Acid nanocomposite displays the characteristic reflections of both magnetite and bentonite. A low-angle diffraction peak appears at $2\theta \approx 3°$, corresponding to the (001) basal plane of bentonite, confirming the preservation of the layered montmorillonite structure after microwave-assisted modification. The major diffraction peaks of magnetite (Fe_3O_4) are clearly observed at approximately 30.2°, 35.5°, and 57.1°, which correspond to the (220),

(311), and (511) planes of the spinel structure, respectively. These reflections confirm the successful formation of magnetite nanoparticles within the composite. A broad hump centered around 26–28° is characteristic of the partially amorphous layered silicate structure of bentonite. The absence of any additional impurity peaks indicates that microwave-assisted synthesis did not introduce unwanted crystalline phases. The noticeable broadening of the magnetite peaks suggests a nanoscale crystallite size and uniform dispersion of magnetite throughout the bentonite matrix. Moreover, surface interaction with glutamic acid contributed to minor peak broadening due to functional binding at the magnetite surface (Gao.J et al,2021).

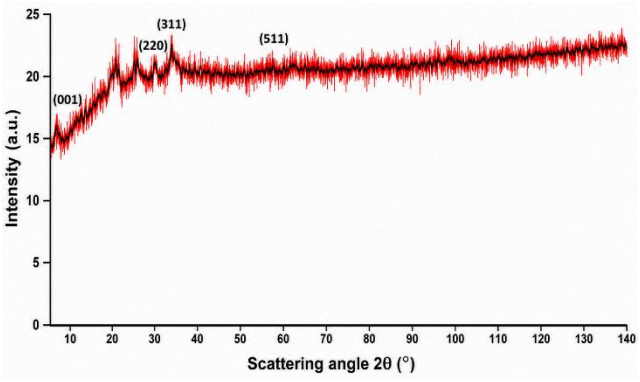

Figure 1: XRD patterns of Fe_3O_4@BNT@GA nanocomposite showing characteristic peaks of magnetite and bentonite phases.

FT-IR analysis further supports successful functionalization. The band at ~1627 cm^{-1} is attributed to C=O and $–COO^-$ stretching vibrations, confirming the incorporation of glutamic acid. Multiple absorption bands in the range of 662–487 cm^{-1} correspond to Fe–O vibrations of magnetite, indicating that the crystalline structure remains intact after microwave processing (Figure 2). The presence of hydroxyl and carboxyl groups enhances the density of active adsorption sites (Khan, M. I. et al, 2021).

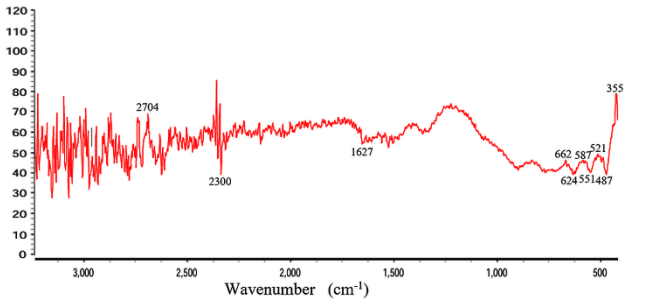

Figure 2: FT-IR spectra confirming functional groups and successful incorporation of glutamic acid into the composite structure.

Thermal analysis showed a multi-step degradation pattern, suggesting the presence of both organic and inorganic elements. The first weight loss is linked to the removal of moisture, which is then succeeded by the breakdown of organic materials and the stabilization of inorganic phases (Figure 3). After heating to approximately 780 °C, a residual mass of about 55–60 mg remains, indicating the presence of thermally stable inorganic constituents or ash that do not undergo further decomposition under the applied conditions. The considerable residual mass indicates that thermally stable mineral components are predominant. This residual mass confirms the incorporation of inorganic components within the sample matrix. The derivative thermogravimetric (DTG) curve exhibits distinct peaks at temperatures corresponding precisely to each weight-loss stage identified in the TGA profile. The position of each DTG peak represents the temperature at which the rate of decomposition is maximal, while the peak intensity reflects the magnitude of the corresponding degradation event. In addition, the differential scanning calorimetry (DSC) curve provides further insight into the thermal transitions of the sample. Endothermic events observed in the range of 100–200 °C are associated with moisture loss, solvent evaporation, or dehydration processes. In contrast, exothermic peaks appearing between 250 and 450 °C correspond to decomposition reactions, oxidative processes, and partial combustion of the organic components (Rathod, V. K. et al, 2021)

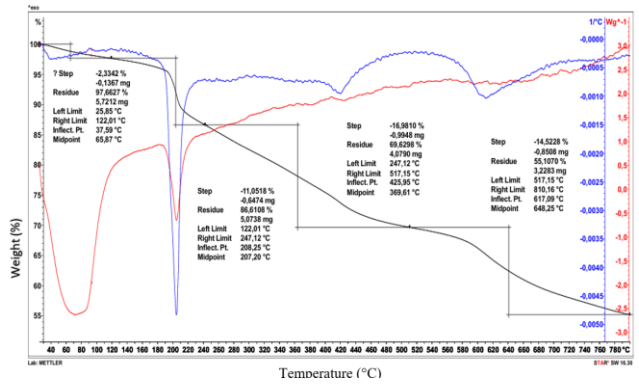

Figure 3: TGA/DTG thermograms illustrating thermal stability and multi-step decomposition behavior of the nanocomposite.

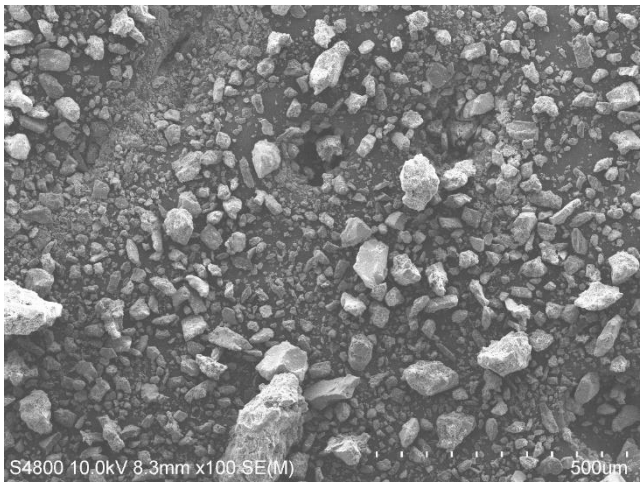

Figure 4: SEM image showing porous morphology and heterogeneous surface structure of Fe_3O_4@BNT@GA.

Figure 4 displays the SEM micrograph of the synthesized Magnetite–Bentonite–Glutamic Acid (MBG) nanocomposite. The image reveals a heterogeneous morphology characterized by irregularly shaped particles of various sizes distributed unevenly across the surface. The composite exhibits a rough and porous structure composed of micro- to submicron-sized granules. From the scale bar (500 µm), the estimated particle size range is approximately 10–80 µm, with some larger agglomerated clusters exceeding 100 µm. These aggregates result from the magnetic dipole–dipole interactions among Fe_3O_4 nanoparticles, leading to partial clustering, which is a common phenomenon in magnetite-based composites. The smaller particles appear to fill the voids among the larger aggregates, forming a complex and multi-layered texture that increases surface heterogeneity. The roughness and irregular surface topology observed in the image confirm the successful deposition and integration of magnetite nanoparticles within the bentonite matrix. This morphology enhances the specific surface area and pore accessibility, both of which are crucial for adsorption efficiency. The presence of pores and cavities between aggregated particles indicates potential adsorption sites for dye molecules, contributing to a higher adsorption capacity of the MBG nanocomposite. Furthermore, the incorporation of glutamic acid appears to have played a significant role in stabilizing the magnetite nanoparticles and improving the interfacial adhesion between the organic and inorganic components. The amino and carboxyl groups of glutamic acid likely interacted with Fe and Si–O groups of magnetite and bentonite, respectively, thereby promoting a more cohesive and functional hybrid structure. This organic modification prevents excessive aggregation and helps maintain a porous morphology suitable for microwave-assisted adsorption applications (El-Maghraby, M. S. et al, 2021).

3.2. Dye adsorption study

3.2.1. Effect of pH and Surface Charge Behavior

Figure (5.a) illustrates the effect of the initial pH of the solution on the removal efficiency (%) of the studied dye at two initial concentrations, 15 ppm and 30 ppm, over a pH range of 2.0–10.0. The effectiveness of adsorption was heavily influenced by the pH of the solution, which affects both the charge of the adsorbent surface and the form of the dye. The highest removal efficiency, around 90–93%, was recorded at pH levels between 6 and 7. At lower pH levels, an abundance of H^+ ions compete with dye molecules for adsorption sites, leading to a decline in efficiency. On the other hand, at higher pH levels (above 7), the electrostatic repulsion between negatively charged surface sites and dye molecules results in decreased adsorption.

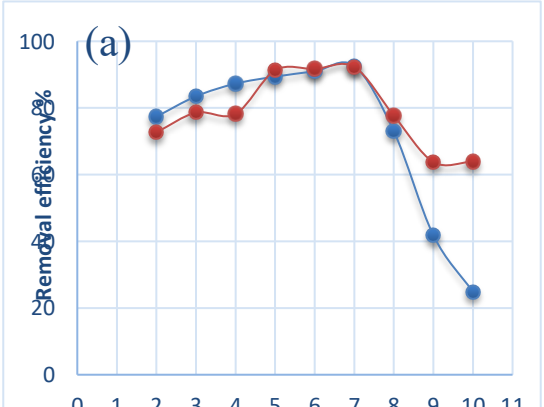

Figure (5.b) shows how ΔpH (pH_final – pH_initial) changes with the initial pH of the solution to determine the point of zero charge (pHpzc) of the prepared adsorbent. The point of zero charge ($pH_pzc \approx 5.0$) indicates that the surface carries a positive charge below this threshold and a negative charge above it. The increased adsorption observed close to neutral pH levels implies that both electrostatic interactions and surface functional groups work together to determine the adsorption process. At pH values below pHpzc, excess H^+ ions or electrostatic repulsion can reduce adsorption performance (El-Shafey, E. I.et al, 2021).

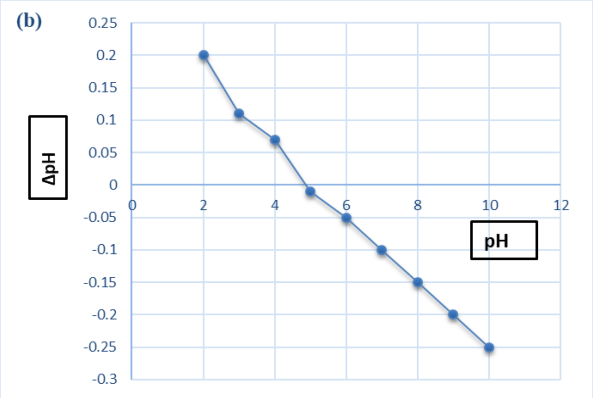

Figure 5: (a) Effect of solution pH on dye removal efficiency; (b) determination of point of zero charge (pH_pzc) at 25 °C.

3.2.2. Effect of Contact Time and Adsorption Kinetics

Figure (6. a) demonstrates the effect of contact time on the removal efficiency of Remazol Red using the Magnetite@Bentonite@Glutamic Acid composite at initial concentrations of 15 ppm and 30 ppm. In both cases, adsorption occurs rapidly during the first 15 minutes due to the availability of abundant active sites on the adsorbent surface. At 15 ppm, removal efficiency quickly reaches about 88% and gradually approaches nearly 100% within 40–50 minutes. At 30 ppm, the efficiency initially rises to around 78% and stabilizes near 95% after approximately 40 minutes. Beyond this time, minimal changes indicate that equilibrium has been reached. The slower initial rate at higher concentration is attributed to the need for more time to saturate the adsorbent surface, although both concentrations follow the same general trend of fast initial adsorption followed by a slower approach to equilibrium. Figure (6. b) evaluates the pseudo-first-order kinetic model using plots of ln ($q_e - q_t$) versus time. The relatively low correlation coefficients ($R^2 = 0.8323$ for 15 ppm and 0.7727 for 30 ppm) indicate poor agreement with this model. This suggests that the adsorption process is not governed by simple physisorption, where adsorption depends only on the availability of vacant sites. In contrast, Figure (6. c) shows that the pseudo-second-order model provides an excellent fit, with very high R^2 values (0.9999 for 15 ppm and 0.9995 for 30 ppm). This strong correlation, along with the close agreement between calculated and experimental adsorption capacities, confirms that chemisorption is the dominant mechanism. This implies that adsorption involves chemical interactions such as electron sharing or exchange between the dye molecules and the composite surface. Figure (6. d) presents the intra-particle diffusion model (q_t vs. $t^{1/2}$). The plots exhibit multi-linearity and do not pass through the origin, with moderate R^2 values (0.837 and 0.8231). This indicates that intra-particle diffusion is involved but is not the sole rate-controlling step. Instead, adsorption proceeds in multiple stages, beginning with rapid surface adsorption followed by slower diffusion into the pores. Similarly, Figure (6. e), which plots q_t versus ln t, confirms that intra particle diffusion contributes partially to the adsorption process. The plots show moderate linearity ($R^2 \approx 0.92$) but do not pass through the origin, indicating that other mechanisms, such as boundary layer diffusion, are also involved. The influence of pore diffusion becomes slightly more significant at higher dye concentrations. Figure (6. f)

illustrates the Avrami kinetic model, which shows good linearity with relatively high R^2 values (0.9432 and 0.9249). This suggests that adsorption follows complex, multi-step pathways. The similar Avrami exponents for both concentrations indicate a consistent mechanism and surface heterogeneity, while positive intercepts suggest cooperative interactions during adsorption. Overall, comparison of all models (Figures 6b–e and Table 1) shows that the pseudo-second-order model best describes the adsorption kinetics. The high correlation coefficients and agreement between calculated and experimental equilibrium capacities confirm that chemisorption is the dominant mechanism governing the removal of Remazol Red by the composite.

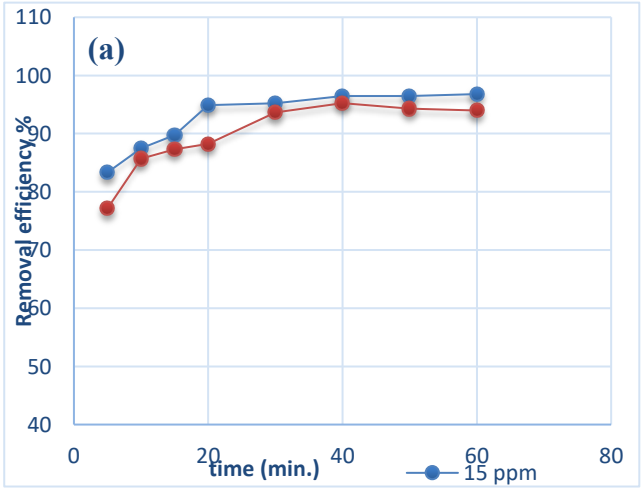

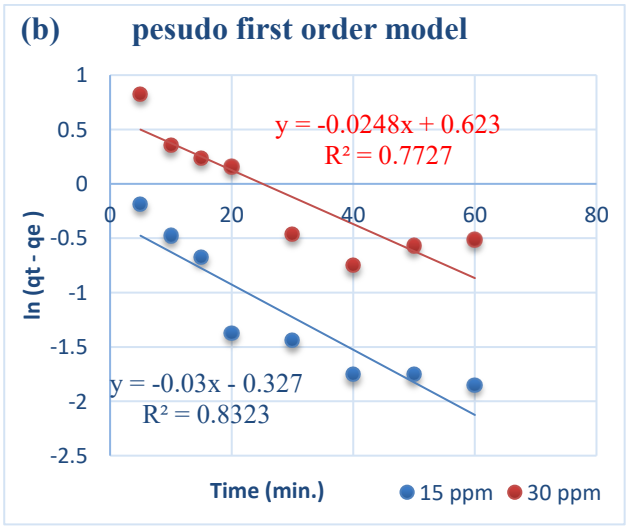

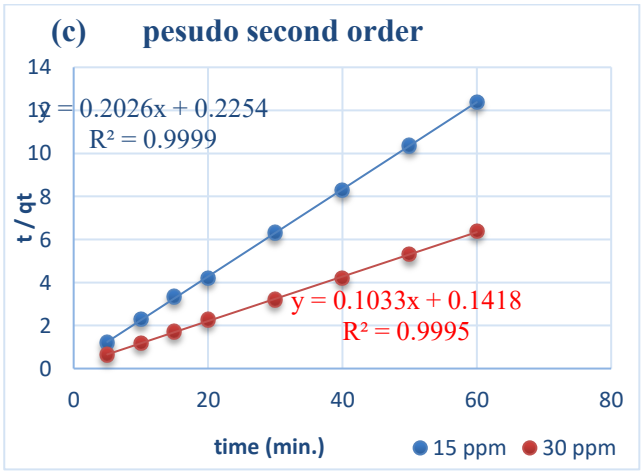

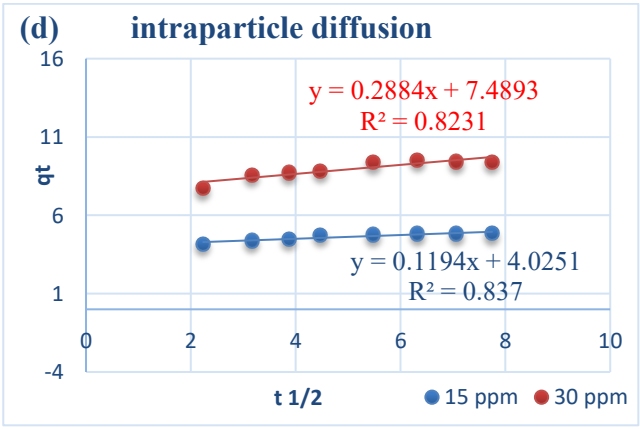

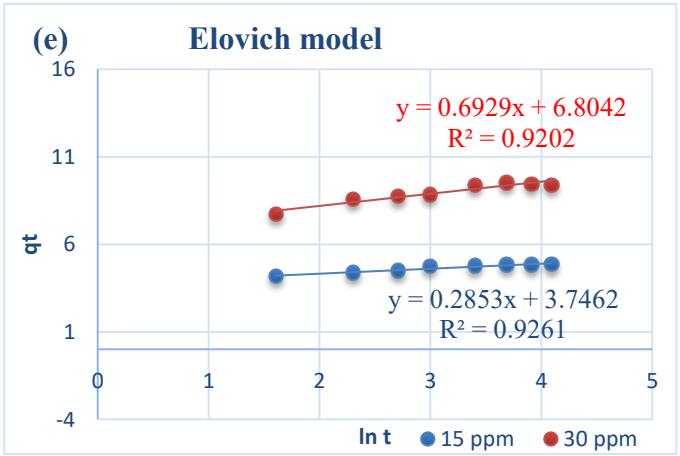

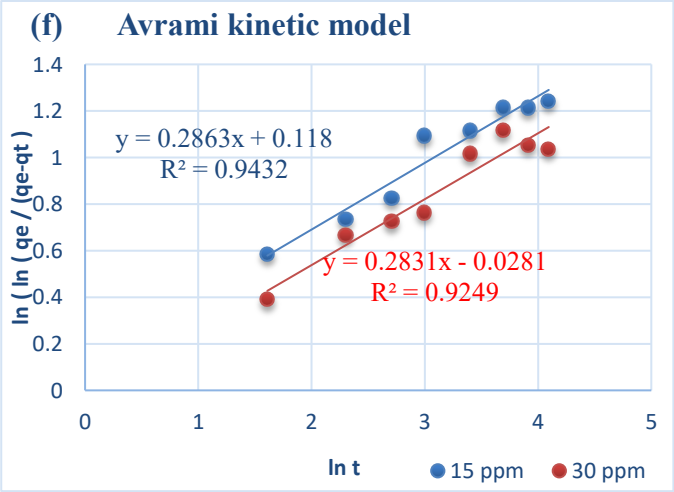

Figure 6: (a) The effect of contact time on the removal efficiency (R%) of Magnetite @Bentonite @Glutamic Acid, (b) Pseudo-first order, (c) Pseudo-second order, (d) Intra-particle diffusion, (e) Elovich kinetic models, and (f) Avrami kinetic models, at 25 °C.

Table 1: Equations of kinetic models and their parameters for the adsorptive removal of Magnetite @ Bentonite @ Glutamic Acid

Kinetic Model	**Equation**	**Plot**	**Kinetic Parameter**	**RRD 15 ppm**	**RRD 30 ppm**
Pseudo-First Order	$Ln\ (q_e - q_t) = Ln\ (q_e) - k_1 t$	$ln\ (q_e - q_t)$ versus time (t), q_e and q_t are the sorption capacity at equilibrium and at time t (min), respectively, k_1 is the first order rate constant	q_e (mg/g) (calc)	0.72108374	1.8645132
			K_1 (min^{-1})	0.03	0.0248
			R^2	0.8323	0.7727
Pseudo-Second Order	$t/q_t = 1/k_2 q_e^2 + t/q_e$	t/q_t versus time (t), K_2 is the second order rate constant	q_e (mg/g) (exp)	4.9358342	9.43
			q_e (mg/g) (calc)	4.8233333	9.6805421
			K_2 (g/mg min)	0.190727	0.07930496
			R^2	0.9999	0.9995
Intra-particle Diffusion	$q_t = k_{id}\ t^{0.5} + C$	q_t versus ($t^{0.5}$), C is the thickness of the adsorption layer, K_{id} is the intra-particle order rate constant	K_{id} (mg/g $min^{0.5}$)	0.1194	0.2884
			C	4.0251	7.4893
			R^2	0.837	0.8321
Elovich	$q_t = 1/\beta\ Ln(\alpha\beta) + 1/\beta\ Ln\ (t)$	q_t versus ln t, α is the initial adsorption rate, β is related to the extent of surface coverage and the activation energy for the chemisorption process	α (mg/g min)	143749.08	12746.574
			β (mg/g)	3.505082	1.44321
			R^2	0.9432	0.9202

3.2.3. Effect of Initial Dye Concentration and Adsorption Isotherms

The initial concentration of Remazol Red significantly influences the adsorption efficiency of the Magnetite@Bentonite@Glutamic Acid (MBG) composite. At low dye concentrations, removal efficiency is high due to the abundance of available active sites on the adsorbent surface. Maximum removal occurs around 10 mg/L, where most adsorption sites are effectively occupied Figure (7. a). However, as the dye concentration increases beyond this level, efficiency declines. This decrease is attributed to the saturation of active sites and the aggregation of dye molecules, which reduces their interaction with the adsorbent. Thus, higher dye concentrations can exceed the adsorption capacity of the MBG composite. Isotherm analysis provides further insight into the adsorption mechanism. The Langmuir model shows an excellent fit (R^2 = 0.9682), indicating monolayer adsorption on a homogeneous surface with identical binding sites Figure (7. b). This suggests that the MBG composite offers uniform adsorption sites and that dye molecules form a single layer at equilibrium, making the Langmuir model the most appropriate for describing the system. The Freundlich model, which assumes heterogeneous surfaces and multilayer adsorption, also shows good linearity (R^2 = 0.9977) but is less representative of the system compared to Langmuir Figure (7. c). Although it indicates favorable adsorption, it does not fully capture the actual mechanism. The Temkin model Figure (7. d) yields a moderate correlation (R^2 = 0.8251), suggesting that adsorbate–adsorbent interactions exist but are not the dominant factor controlling adsorption. The Dubinin–Radushkevich (D–R) model shows the weakest fit (R^2 = 0.6199), indicating poor applicability Figure (7. e). Its results suggest that the adsorption process is mainly physical rather than chemical. Overall, the analysis confirms that the Langmuir model best describes the adsorption behavior, highlighting monolayer adsorption on a homogeneous MBG surface with strong adsorption performance.

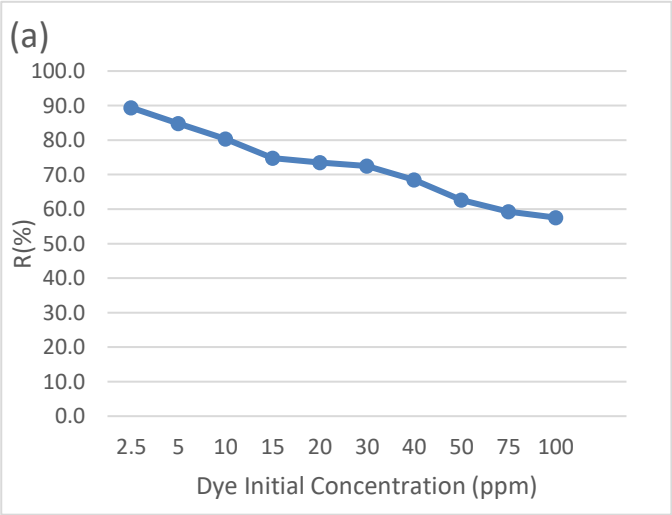

(b)

(c)

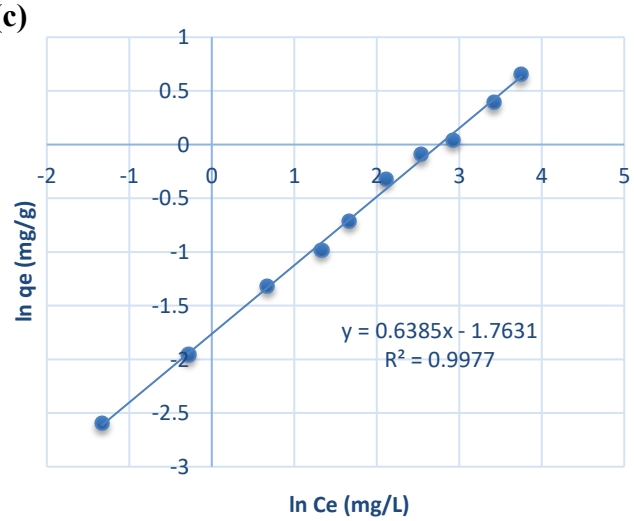

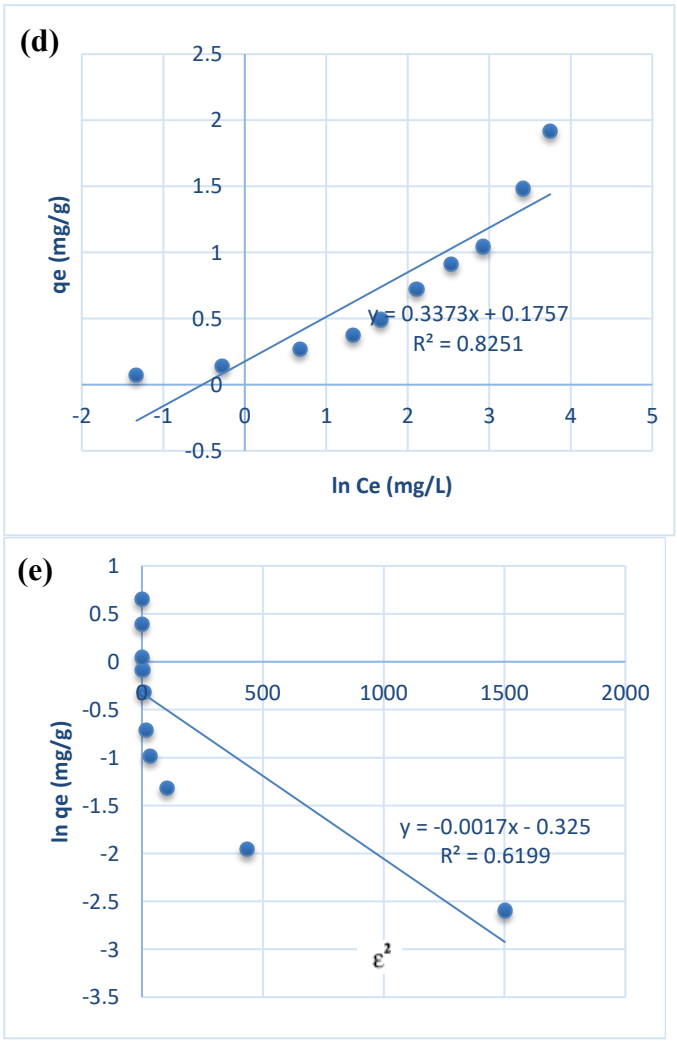

Figure 7: Figure 7. (a) The effect of initial Magnetite @Bentonite @Glutamic Acid concentration on the removal efficiency (R%), (b) Langmiur, (c) Freundlich, (d) Temkin, and (e) isotherm models for MBG adsorption onto the at 25 °C.

The adsorption behavior of Remazol Red dye was analyzed using several isotherm models (Table 2 and Figure 7). The experimental data showed a good fit with the Langmuir model ($R^2 = 0.9682$), indicating monolayer adsorption, with a maximum capacity of 0.839 mg/g and favorable conditions at pH 7. The separation factor (RL) values between 0 and 1 confirmed the feasibility of adsorption. The Freundlich model provided an even better fit ($R^2 = 0.9977$), suggesting heterogeneous surface adsorption, with an adsorption intensity (n = 1.566) indicating favorable uptake and a high adsorption capacity (Kf = 0.172 L/mg). In contrast, the Temkin and Dubinin–Radushkevich models showed low correlation coefficients, indicating they poorly describe the adsorption process (Al-Shamrani, A.et al, 2023).

Table 2:Linear equations and their parameters for different adsorption isotherm models for the 15 ppm and 30 ppm adsorptive removal by the Magnetite @ Bentonite @ Glutamic Acid

Isotherm Model	**Linear Equation**	**Linear Plot**	**Isotherm Parameter**	**RRD**
Langmuir	$C_e/q_e=1/q_{max}K_L+C_e/q_{max}$	1/q_e versus 1/C_e, slope = $1/q_m$, and intercept =$1/(K_L\ q_{max})$; K_L is the Langmiur constant, q_{max} is the maximum adsorption capacity, $R_L=\frac{1}{1+K_LC_o}$, C_o is the initial concentration of U(IV) ions in mg/L	q_{max} (mg/g)	0.838789743
			K_L(L/mg)	0.350625472
			R_L	(0.02773 - 0.487359)
			R^2	0.9682
Freundlich	$\ln(q_e)=\ln(K_F)+1/n\ln(C_e)$	Ln q_e versus ln C_e, slope = 1/n, and intercept = ln K_F; K_F is the Freunlish constant related to the affinity of the adsorbate to the binding sites of the adsorbent, n is the intensity of the adsorbent	n	1.566170713
			K_F (L/mg)	0.171512351
			R^2	0.9977
Temkin	$q_e=(RT/b_T)\ln(a_T)+(RT/b_T)\ln(c_e)$	q_e versus ln C_e, slope = B = RT/b_T, and intercept = Bln a_T; a_T is Temkin isotherm equilibrium binding constant corresponding to the maximum binding energy, b_T is the Temkin isotherm equilibrium binding constant related to the heat of adsorption and/or the adsorption bonding energy, R is the gas constant = 8.314×10^{-3} kJ mol^{-1} K^{-1}, T is the absolute temperature in K	a_T (L/mg)	1.683555
			b_T(KJ/mol)	7.345486384
			B	0.337291756
			R^2	0.8251
Dubinin Radushkevich (D–R)	$\ln(q_e)=\ln(q_s)-(K_{ad}\varepsilon^2)$	Ln q_e versus ε^2, slope = K_{ad}, and intercept = Ln (q_s); ε is the *polanyi* potential (ε = RT ln (1+(1/C_e)), q_s is the theoretical saturation capacity, K_{ad} is the D-R isotherm constant, $E_s=\frac{1}{\sqrt{2K_{ad}}}$	q_{max} (mg/g)	0.722527354
			K_{ad} (mol^2/J^2)	17
			E_s(KJ/mol)	0.171498
			R^2	0.6199

3.2.4. Effect of Adsorbent Dosage and Temperature

The adsorption performance of MBG is strongly influenced by sorbent mass, temperature, and thermodynamic behavior. Increasing the sorbent mass from 5 mg to 40 mg significantly enhances the removal efficiency (R%) for both 15 ppm and 30 ppm dye concentrations Figure (8. a). At low dosages, the limited number of active adsorption sites restricts dye uptake, resulting in lower removal efficiency. As the sorbent mass increases, more active sites become available, strengthening interactions between the dye and the sorbent. This leads to a sharp improvement in R%, especially between 5 mg and 20 mg, with the effect being more noticeable at 15 ppm. However, beyond 40 mg, the removal efficiency approaches a plateau, indicating that adsorption equilibrium is nearly reached. At higher dosages, particle agglomeration and surface crowding may reduce the effective surface area and block active sites, limiting further improvement. Therefore, 40 mg is identified as the optimal sorbent mass. Thermodynamic analysis using van't Hoff plots shows a linear relationship between ln Kd and 1/T for both concentrations, indicating predictable behavior Figure (8. b). The 30 ppm system demonstrates a stronger linear fit ($R^2 \approx 0.8506$), suggesting more stable thermodynamic performance, while the 15-ppm system shows greater variability ($R^2 \approx 0.725$). The increase of Kd with temperature indicates that the adsorption process is overall endothermic, meaning it is enhanced by higher temperatures. Additionally, the 15-ppm system appears more sensitive to temperature changes. Temperature also plays a key role in adsorption efficiency. As temperature increases from 285 K to 330 K, R% rises steadily for both concentrations Figure (8. c). Higher temperatures increase molecular motion, improving collision frequency and diffusion of dye molecules into MBG pores. This effect is more pronounced at 30 ppm, where higher dye concentration benefits more from enhanced mass transfer. Overall, adsorption is thermally promoted and diffusion-controlled.

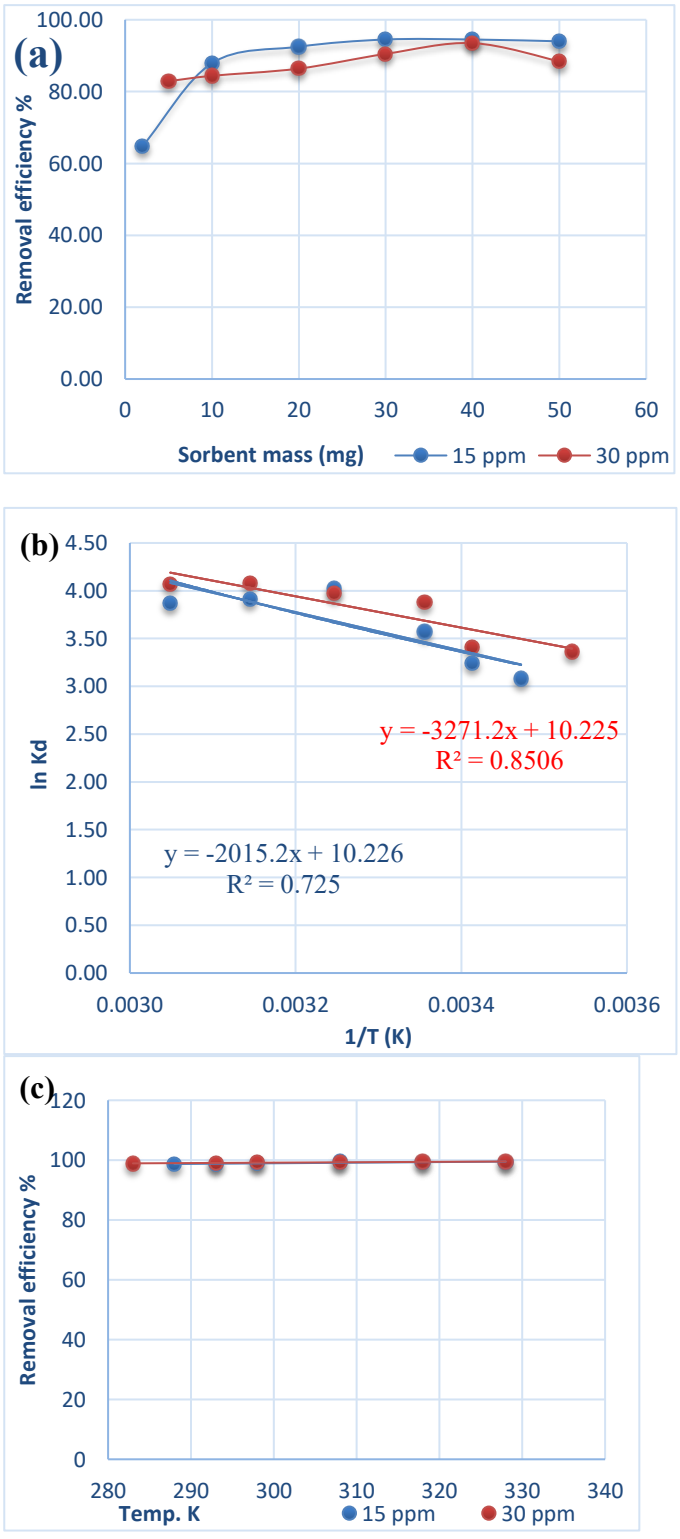

Figure 8: (a) The effect of the MBG mass dosage, (b) the effect of reaction temperature on the removal efficiency (R%) of MBG dye pollutants, (c) Vant Hoff plot for the adsorption of MBG.

Data collected from the experiments above, pertaining to the effect of temperature on the adsorption reaction were

employed to calculate the thermodynamic parameters of this reaction. These include Gibbs free energy (ΔG°, KJmol-1),

Table 3: Standard thermodynamic parameters for the adsorption of 15 ppm and 30 ppm onto the Magnetite @ Bentonite @ Glutamic Acid at different reaction temperatures.

Dye initial concentration (ppm)	**Temperature (K)**	**LnK_d (L/g)**	**Adsorption Thermodynaic Paramters**			**R^2**
			-ΔG° (KJmol^{-1})	**ΔH° (KJmol^{-1})**	**ΔS° (Jmol^{-1}K^{-1})**	
15 ppm	**283**	3.08	7244.90	16.7543728	85.018964	0.725
	293	3.24	7893.61			
	298	3.57	8848.24			
	308	4.02	10296.96			
	318	3.91	10337.77			
	328	3.87	10553.47			
30 ppm	**283**	3.36	7911.56	27.1967568	85.01065	0.8506
	293	3.41	8296.90			
	298	3.88	9603.44			
	308	3.97	10176.82			
	318	4.08	10779.38			
	328	4.07	11088.85			

standard enthalpy change (ΔH°, KJmol-1), standard entropy change (ΔS° , Jmol-1K-1), and the adsorption equilibrium constant (Kd, L/g) (Ahamad, Z. et al, 2024). These parameters are considered important in deducing the nature of the adsorption reaction and degree of spontaneity. The slope of the linear Vant Hoff's plot (ln Kd vs 1/T, Fig (8.a)) is employed to calculate the value of ΔH°. The intercept in this plot is used to calculate the value of ΔS° . The calculated results of all the investigated thermodynamic parameters, along with the linear correlation coefficient values (R2) are provided in Table 3. From Figure (8.a), it is evident that all points over the experimental temperature range are located on a straight line. This implies that the experimental adsorption data were well fitted with the thermodynamic relation based on the high values of linear correlation coefficients, where R2 = 0.725 for 15 ppm and 0.8506 for 30 ppm. Table 3 shows that the ΔG° values were in the range from -7244.90 to -10553.47 KJmol-1 for 15 ppm and from -7911.56 to -11088.85 KJmol-1 for 30 ppm in the reaction temperature range 283–328 K.

3.3. Regeneration and Reusability of MBG

The reusability of adsorbents is a critical parameter for their practical application, as it directly influences both cost-effectiveness and sustainability. In the case of MBG, strong interactions between the support matrix (Magnetite @ Bentonite) and glutamic acid, combined with its magnetic properties and enhanced nanocomposite stability, enable efficient repeated use in adsorption and magnetic separation processes. The reusability of MBG was assessed over five consecutive adsorption–desorption cycles using Remazol Red as the target pollutant. After each cycle, the adsorbent was recovered with an external magnet, thoroughly washed with phosphate-buffered saline (PBS, 0.1 M, pH 7.4), dried at room temperature, and reused in the subsequent cycle. The removal efficiency (R%) was normalized relative to the first cycle. Experimental results showed that MBG achieved a removal efficiency of 99.37% during the first cycle. After five cycles, the efficiency slightly decreased to 97.42%, indicating only a minimal loss in performance. This excellent recyclability can be attributed to the strong covalent and non-covalent interactions between the support matrix and the immobilized functional groups, which help preserve structural integrity during repeated use. The slight reduction in removal efficiency over multiple cycles may be explained by several factors, including: (1) incomplete desorption of dye molecules from MBG pores; (2) particle aggregation during magnetic separation; (3) partial blockage of active adsorption sites; (4) gradual leaching or denaturation of functional groups; and (5) minor material loss during handling. Despite these limitations, MBG retained a high adsorption capacity after repeated regeneration cycles, demonstrating its strong potential as a sustainable and efficient adsorbent for the removal of cationic dyes from wastewater.

3.4. Remediation of Real Water Samples

The practical use of the synthesized MBG (Magnetite @ Bentonite @ Glutamic Acid) bio-nanocomposite was further assessed through adsorption tests using actual water samples. This evaluation is crucial to confirm its effectiveness beyond controlled lab settings and to establish its potential for real-world wastewater treatment applications. Batch equilibrium experiments were performed on various water samples, including tap water, industrial wastewater, and seawater, each containing 10 mg/L of Remazol Red. The adsorption process was conducted under optimized conditions established from laboratory-scale studies to ensure consistent and comparable results. The removal efficiencies achieved were 95.09% for tap water, 95.47% for industrial wastewater, and 96.24% for seawater. The consistently high removal rates across all tested samples indicate that the presence of competing ions and background materials in real water systems did not notably impede the adsorption capabilities of the MBG. This points to a strong interaction between the bio-nanocomposite and the dye molecules, likely due to the synergistic effects of magnetite, bentonite, and glutamic acid functional groups. Interestingly, the marginally greater removal efficiency seen in seawater might be linked to ionic strength effects that improve adsorption interactions. However, additional research is needed to fully clarify this phenomenon. In general, the results demonstrate that MBG retains remarkable adsorption capacity even in challenging environmental conditions. These findings emphasize the durability and efficacy of the bio-nanocomposite developed, reinforcing its potential as a quick and effective adsorbent for eliminating harmful dyes from various water sources. The strong performance noted in actual samples highlights its potential for practical use in wastewater treatment systems.

4. Conclusion

A novel Fe_3O_4@BNT@GA nanocomposite, which can be magnetically recovered, was successfully created using a quick microwave-assisted method. This technique facilitated the effective combination of inorganic and organic components, leading to a highly

functionalized and porous structure. The nanocomposite showed remarkable adsorption capabilities for Remazol Red, achieving rapid kinetics and impressive removal efficiency. The adsorption process conformed to pseudo-second-order kinetics and was best represented by the Langmuir isotherm, suggesting the occurrence of monolayer chemisorption. Thermodynamic evaluations indicated that the process is both spontaneous and endothermic, with improved performance at higher temperatures. Additionally, the material exhibited exceptional reusability and high efficiency in actual water systems. In summary, this research underscores the potential of microwave-assisted synthesis for creating advanced, sustainable nanocomposites suitable for wastewater treatment, providing a scalable and eco-friendly approach for dye removal.

Acknowledgment:

The authors would like to express their sincere gratitude to Rojava University and Institute of science and technology for providing access to the laboratory facilities and resources essential for conducting this research. We sincerely acknowledge NGO Emmaus Jokioinen for its valuable technical support in conducting thermogravimetric analysis (TGA) and scanning electron microscopy (SEM) of the synthesized nanocomposite, which significantly contributed to this study.

Authors' contribution:

This paper is extracted from a Master thesis, for which Haidar Saify, Mohamed E.Mahmoud and Rehab M .El-Sharkawy were Supervisors of the project, chief investigators, and responsible for the data analysis. Methodology and first draft of the manuscript were done by Maher.

Funding:

We confirm that this work did not receive any grant from funding agencies in the commercial, public sectors.

Declarations

Conflict of interest

The authors declare that they have no known competing interests.

Data availability

Data generated or analyzed during this project are provided in full within the published article

Reference

1. Ahamad, Z., & Nasar, A. (2024). Polypyrrole-decorated bentonite magnetic nanocomposite: A green approach for adsorption of anionic methyl orange and cationic crystal violet dyes from contaminated water. Environmental Research,247, 118193.
2. Adhikari, Ashok, Francisco J. Cano, Rocío Magdalena Sánchez-Albores, Javier Aguila-Rosas, María de la Luz Olvera Amador, and Odín Reyes-Vallejo. "Microwave-Assisted Synthesis of Nanomaterials: Parameters, Advantages, and Challenges for Energy and Environmental Applications." In Handbook of Nanomaterials and Nanocomposites for Energy and Environmental Applications, pp. 1-36. Cham: Springer Nature Switzerland, 2026.
3. Al-Shamrani, A., & Khan, M. R. (2023). Adsorption performance of zeolite for the removal of Congo Red dye: Factorial design

experiments, kinetic, and equilibrium studies. Separations, 10(1), 57.

4. Balasundharam, Nishaa, and Karthikeyan Ramalingam. "Eco-friendly remediation of reactive azo dye-laden wastewater via Lactobacillus casei immobilized on porous clay: mechanistic and phytotoxicity insights." Biodegradation 37, no. 1 (2026): 5.
5. M.E. Mahmoud, R.M. El-Sharkawy, G.A.A. Ibrahim, Promoted adsorptive removal of chromium(VI) ions from water by a green-synthesized hybrid magnetic nanocomposite (NFe3O4Starch-Glu-NFe3O4ED), RSC Adv. 11 (2021) 14829.
6. M.H. Calimli, M.S. Nas, H. Burhan, S.D. Mustafov, Ö. Demirbas, F. Sen, Preparation, characterization and adsorption kinetics of methylene blue dye in reduced-graphene oxide supported nanoadsorbents, J. Mol. Liq. 209 (2020).
7. El-Shafey, E. I. (2021). Surface charge studies of modified bentonite and their impact on dye adsorption. Applied Clay Science, 205, 106062.
8. Rathod, V. K., & Pandit, A. (2021). Thermal stability assessment of polymer magnetite nanocomposites using thermogravimetric techniques. Polymer Degradation and Stability, 193, 109712.
9. Riaz, M., Khan, S., & Iqbal, M. (2015). Microwave-induced catalytic degradation of a textile dye using bentonite-poly(o-toluidine) nanohybrid. RSC Advances, 5, 78945–78953.
10. El-Maghraby, M. S., & El-Sheikh, S. M. (2021). SEM–EDX analysis of functionalized bentonite-based adsorbents. Journal of Environmental Chemical Engineering, 9, 105782.
11. Gabano, E. (2022). Microwave-assisted green synthesis overview. Molecules, 27, 5432.
12. Gao, J., Fan, H., & Liu, X. (2021). Crystalline phase evaluation of bentonite–magnetite hybrid adsorbents by XRD and Rietveld refinement. CeramicsInternational, 47, 21452–21460.
13. Girdthep, Sutinee, Soontorn Suvokhiaw, Siirat Choosakoonkriang, Gulanat Chanachinrat, and Cheewita Suwanchawalit. "Microwave-Assisted Synthesis of Boron and Nitrogen Co-Doped Carbon Dots Immobilized on SiO2 Nanoparticles for High-Resolution Latent Fingerprint Detection." Optical Materials (2026): 117919.
14. Khan, M. I., & Shah, Z. (2021). Functional group characterization of amino-acid-modified magnetic adsorbents using FTIR. Spectrochimica Acta Part A, 258, 119807.
15. Kumar, Kuldeep, Ravi Kumar, and Naveen Thakur. "Biogenic Nanocomposites for the Removal of Dyes and Micropollutants from Wastewater." In Nanotechnology in Environmental Science and Healthcare, pp. 39-53. Singapore: Springer Nature Singapore, 2026.
16. Lavanya, M., and S. Karthick Raja Namasivayam. "Nanoscale zinc oxide (ZnO NPs)–alginate–PEG–activated carbon nanocomposite for efficient Cr (VI) removal from electroplating wastewater: adsorption isotherms and eco-toxicity evaluation." Journal of Chemical Technology & Biotechnology 101, no. 4 (2026): 886-903.

17. Hessien, M. M. H. C. (2022). Methylene blue dye adsorption on iron oxide-hydrochar composite synthesized via a facile microwave-assisted hydrothermal carbonization of pomegranate peels' waste. Molecules, 27, 4123.
18. Inbaraj, B. S., Chen, B. H., & Lin, F. H. (2011). Dye adsorption characteristics of magnetite nanoparticles coated with a biopolymer poly(γ-glutamic acid). Bioresource Technology, 102, 8524–8531.
19. Siwi, Dewinta Yuka, Anugrah Ricky Wijaya, Neena Zakia, and Nor Kartini Abu Bakar. "Synthesis, characterization, and application of Fe_3O_4/PEG/HAp nanocomposite as an adsorbent for Pb (II)." In E3S Web of Conferences, vol. 695, p. 02008. EDP Sciences, 2026.

Rojava Journal of Science and Technology

2026, VOL. 3, No 1, [81-94]

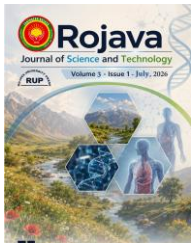

Kidney Disease in Conflict Settings: Prevalence and Risk Factors Among Syrian Adults Living in North and East Syria

Nisreen Nabo Sheikh Bakr[1], Haidar Saify Nabiabad[2], Eman Elbassuoni*[3]

[1]Department of Physiology, Institute of Science and Modern Technology, Rojava University, Syria

[2]Department of Clinical Laboratory, Institute of Science and Modern Technology, Rojava University, Syria

[3]Department of Physiology, Faculty of Medicine, Minia University, Egypt

ABSTRACT

Background: Chronic kidney disease (CKD) is a major global public health problem associated with substantial morbidity, mortality, and healthcare costs. In Syria, prolonged conflict has disrupted healthcare services and may have increased exposure to environmental and lifestyle-related risk factors for kidney disease. However, epidemiological data on CKD in Syrian populations remain limited. This study aimed to assess the prevalence of CKD and identify associated risk factors among adults living in North and East Syria. Methods: A cross-sectional study was conducted between December 2023 and June 2024 among 150 adults recruited from outpatient clinics and internal medicine departments in North and East Syria. Sociodemographic characteristics, medical history, lifestyle factors, anthropometric measurements, blood pressure, fasting blood glucose, serum creatinine, and blood urea were assessed. Estimated glomerular filtration rate (eGFR) was calculated using the CKD Epidemiology Collaboration (CKD-EPI) equation. CKD was defined as eGFR <60 mL/min/1.73 m². Associations between CKD and potential risk factors were evaluated using correlation and chi-square analyses. Results: The mean eGFR was 40.4 ± 27.0 mL/min/1.73 m², and 72.67% of participants met the study definition of CKD. Advanced disease stages (CKD stages 3b–5) accounted for a substantial proportion of cases. CKD prevalence increased significantly with age ($p < 0.001$) and was higher among males than females ($p < 0.001$). Elevated mean arterial pressure (MAP) ($p < 0.001$), hyperglycemia ($p = 0.009$), a history of hypertension ($p = 0.004$), and cardiovascular disease ($p < 0.001$) were significantly associated with CKD. eGFR was negatively correlated with MAP ($r = −0.263$, $p = 0.001$). Reliance on Euphrates River water ($p < 0.001$) and long-term analgesic use ($p = 0.017$) were also significantly associated with CKD. No significant associations were observed for BMI category, smoking status, physical activity, or dietary pattern. Conclusions: A high prevalence of eGFR-defined CKD was observed among adults attending healthcare facilities in North and East Syria. Older age, male sex, elevated blood pressure, hyperglycemia, cardiovascular disease, long-term analgesic use, and reliance on Euphrates River water were associated with CKD. These findings highlight the need for enhanced screening and management of cardiometabolic risk factors and further investigation of environmental determinants of kidney disease in conflict-affected populations.

ARTICLE HISTORY

Received: 14 Mar. 2026

Revised: 10 Jun. 2026

Accepted: 28 Aug. 2026

Keywords: Chronic kidney disease; estimated glomerular filtration rate; hypertension; hyperglycemia; risk factors; Syria.

*Corresponding Author: Eman Elbassuoni Eman.Elbassuoni@yahoo.com

1. Introduction

The kidneys play a central role in maintaining physiological homeostasis through regulation of fluid balance, electrolyte composition, acid–base equilibrium, endocrine signaling, and metabolic waste excretion. In addition to filtering blood and eliminating toxins, the kidneys contribute to blood pressure regulation through the renin–angiotensin–aldosterone system, stimulate erythropoiesis via erythropoietin secretion, and participate in calcium and phosphate homeostasis through activation of vitamin D metabolites (Terashita et al., 2026). Consequently, impairment of renal function has widespread systemic effects that influence cardiovascular, metabolic, hematological, and endocrine health. (National Institute of Diabetes and Digestive and Kidney Diseases 2018). Kidney disease (nephropathy) involves kidney damage that can lead to kidney failure, which is known as the end stage of kidney disease (ESKD). Chronic kidney disease (CKD) is a progressive condition marked by declining glomerular filtration rate, commonly caused by diabetes, hypertension, glomerulonephritis, and polycystic kidney disease (Murray et al. 2015). Importantly, CKD is strongly associated with cardiovascular disease (CVD), which remains the leading cause of death among patients with impaired renal function. Reduced kidney function contributes to endothelial dysfunction, chronic inflammation, vascular calcification, oxidative stress, and dysregulation of mineral metabolism, thereby increasing the risk of hypertension, ischemic heart disease, heart failure, and stroke (Lodi et al., 2026). This bidirectional relationship between CKD and CVD has led to the recognition of the cardiorenal syndrome as a major clinical entity. Furthermore, CKD imposes considerable socioeconomic burdens through increased hospitalization rates, reduced quality of life, loss of productivity, and escalating healthcare expenditures associated with dialysis and transplantation (Liao et al. 2012). Early intervention, lifestyle modifications, and medications can slow progression, while advanced stages require dialysis or transplantation (Lodi et al., 2026). Globally, the prevalence of CKD has risen steadily over recent decades, driven by population aging, urbanization, sedentary lifestyles, obesity, and the growing incidence of diabetes and hypertension. According to global epidemiological estimates, approximately 753 million individuals were living with CKD in 2016, highlighting the enormous burden of the disease worldwide. The prevalence of CKD varies substantially across regions and populations, with low- and middle-income countries experiencing particularly rapid increases due to limited healthcare infrastructure, inadequate screening programs, and delayed diagnosis (Agboola et aal., 2026). In Africa, the pooled prevalence of CKD stages 1–5 has been estimated at approximately 15.8%, whereas countries in the Middle East report highly variable prevalence rates depending on socioeconomic conditions, healthcare access, and environmental exposures (Bikbov, Perico, and Remuzzi 2018). In the Middle East and North Africa region, CKD represents an emerging public health crisis. Rapid urbanization, nutritional transitions, increasing rates of obesity and diabetes, and widespread hypertension have substantially increased the burden of renal disease. In addition, ongoing conflicts, environmental instability, and weakened healthcare systems in several countries further exacerbate disease progression and limit access to early diagnosis and treatment. Exposure to contaminated water, nephrotoxic substances, infectious diseases, and inappropriate medication use may also contribute to the rising prevalence of kidney dysfunction in vulnerable populations (Alasbahy et al., 2026). Between 2000 and 2016, the overall prevalence of CKD stages 1–5 was 15.8%, and CKD stages 3–5 was 4.6% in Africa (Kaze et al. 2018). The prevalence of ESKD in the Middle East—including Iran, Egypt, Turkey, Tunisia, Yemen, Syria, Lebanon, Qatar, and Iraq—ranged between 55 and 818 per million population. The prevalence of CKD

stages 3–5 in Abu Dhabi was 2.8% in females and 4.6% in males (Malekmakan et al. 2018). Syria has experienced prolonged armed conflict and severe disruption of healthcare infrastructure over the past decade, resulting in reduced access to preventive healthcare services, shortages of medications, limited diagnostic capacity, and deterioration of water and sanitation systems. These conditions may significantly increase the risk of chronic diseases, including CKD, while simultaneously limiting opportunities for early detection and disease management. Despite these concerns, epidemiological data regarding CKD prevalence and associated risk factors within the Syrian population remain scarce. The absence of comprehensive screening programs and national renal registries has created substantial gaps in understanding the true burden of kidney disease in the region. Environmental and lifestyle factors may further influence CKD development among populations living in North and East Syria. Reliance on untreated water sources, prolonged use of analgesics and nonsteroidal anti-inflammatory drugs, smoking, poor dietary habits, and inadequate management of metabolic disorders may contribute to progressive renal impairment. However, the relative contribution of these factors has not been adequately investigated in Syrian populations. Identifying modifiable risk factors is essential for developing targeted prevention strategies and reducing disease progression.

2. Subjects and Methods

2.1. Study Design and Setting

This observational cross-sectional study was conducted between December 2023 and June 2024 in North and East Syria. The study aimed to evaluate the prevalence of chronic kidney disease (CKD) and identify associated demographic, clinical, and lifestyle-related risk factors among Syrian adults living in the region. Data collection was performed at outpatient clinics and internal medicine departments of several healthcare centers, including Afrin Hospital (Fafin, Al-Shahba District, Aleppo), Tal Rifaat Hospital (Al-Shahba District, Aleppo), Yassin Hospital (Sheikh Maqsoud neighborhood, Aleppo), Kobani Hospital (Kobani city), and Amal Hospital (Kobani city).

2.2. Study Population and Sample Size

The target population included Syrian adults aged 18 years and older residing in North and East Syria. Participants were recruited using a convenience sampling approach from patients and accompanying individuals attending the participating healthcare facilities during the study period (Farag, Kari, and Singh 2012).

The required sample size was estimated using EPI-INFO version 3 software based on an expected CKD prevalence of 5–6% reported in neighboring Middle Eastern countries due to the absence of national renal registries and limited screening data in Syria. A confidence interval of 95% and an acceptable margin of error of 8–10% were applied, resulting in a minimum required sample size of 150 participants. A total of 150 individuals were ultimately enrolled in the study.

2.3. Inclusion and Exclusion Criteria

Adults aged ≥18 years who were permanent residents of North and East Syria and agreed to participate were eligible for inclusion. Participants were excluded if they were pregnant, critically ill, undergoing dialysis, or unable to provide informed consent. Individuals with incomplete clinical or laboratory data were also excluded from the final analysis.

2.4. Ethical Considerations

The study protocol was approved by the Scientific Ethics Committee of Rojava University (Approval No. 22.06.2022). Official permissions were obtained from the administrations of the participating hospitals and healthcare centers. All procedures were conducted in accordance with the

ethical principles outlined in the Declaration of Helsinki. Written informed consent was obtained from all participants prior to enrollment.

2.5. Data Collection and Clinical Assessment

Following informed consent, all participants underwent structured interviews, clinical examinations, anthropometric measurements, and laboratory investigations. Data collection was performed by trained healthcare personnel using standardized procedures.

2.5.1. Questionnaire and Medical History

A structured questionnaire was used to obtain sociodemographic and clinical information, including age, sex, educational level, smoking status, alcohol intake, physical activity, dietary habits, and source of drinking water. Participants were also asked about their medical history, including hypertension, diabetes mellitus, cardiovascular disease (CVD), kidney disease, chronic medication use, and family history of chronic illnesses. Long-term analgesic use was defined as regular analgesic intake for prolonged periods exceeding three months.

2.5.2. Anthropometric Measurements

Body weight was measured to the nearest 0.1 kg using a calibrated digital scale, while height was measured to the nearest 0.5 cm using a non-stretchable measuring tape with participants standing barefoot and wearing light clothing. Body mass index (BMI) was calculated as weight in kilograms divided by height in meters squared (kg/m^2). Participants were categorized according to World Health Organization criteria as underweight (<18.5 kg/m^2), normal weight (18.5–24.9 kg/m^2), overweight (25.0–29.9 kg/m^2), or obese (≥ 30 kg/m^2).

2.5.3. Blood Pressure Measurement

Blood pressure measurements were obtained using standard mercury sphygmomanometers after participants had rested in a seated position for at least 5 minutes. Systolic blood pressure (SBP) and diastolic blood pressure (DBP) were recorded, and mean arterial pressure (MAP) was calculated using the following equation:

$$MAP = DBP + 1/3\ (SBP - DBP)$$

Blood pressure categories were classified according to the 2017 American College of Cardiology/American Heart Association guidelines as normal (<120/80 mmHg), elevated (120–129/<80 mmHg), or hypertensive (≥130/80 mmHg).

2.6. Laboratory Investigations

Venous blood samples were collected after overnight fasting and analyzed at accredited hospital laboratories using standardized laboratory procedures. The following biochemical parameters were assessed:

- Fasting blood glucose (FBG)
- Blood urea
- Serum creatinine

Fasting blood glucose levels were categorized as normal (<100 mg/dL), prediabetes (100–125 mg/dL), or diabetes (≥126 mg/dL). Estimated glomerular filtration rate (eGFR) was calculated using the CKD Epidemiology Collaboration (CKD-EPI) creatinine equation. CKD staging was performed according to Kidney Disease: Improving Global Outcomes (KDIGO) guidelines as follows:

- Stage 1: eGFR ≥90 mL/min/1.73 m^2
- Stage 2: eGFR 60–89 mL/min/1.73 m^2
- Stage 3a: eGFR 45–59 mL/min/1.73 m^2
- Stage 3b: eGFR 30–44 mL/min/1.73 m^2
- Stage 4: eGFR 15–29 mL/min/1.73 m^2
- Stage 5: eGFR <15 mL/min/1.73 m^2

CKD was defined as an eGFR below 60 mL/min/1.73 m².

2.7. Statistical Analysis

Data were analyzed using IBM SPSS Statistics version 27. Continuous variables were expressed as mean ± standard deviation (SD), whereas categorical variables were presented as frequencies and percentages. Differences between groups were analyzed using the independent samples t-test or one-way analysis of variance (ANOVA) for continuous variables, as appropriate. Associations between categorical variables were evaluated using Pearson's chi-square test or Fisher's exact test when necessary. Correlation analyses between eGFR and clinical variables were performed using Pearson correlation coefficients. A p-value ≤0.05 was considered statistically significant.

3. Results

3.1. eGFR and prevalence of CKD and different CKD stages using CKD-EPI equation:

According to the CKD-EPI equation, the mean estimated glomerular filtration rate (eGFR) was 40.4 mL/min/1.73 m² (SD = 27), and the prevalence of chronic kidney disease (CKD) was 72.67%. The participants were distributed across the five CKD stages: 2.67% in stage 1, 11% in stage 2, 18% in stage 3a, 9% in stage 3b, 10% in stage 4, and 22% in stage 5 (Figure 1).

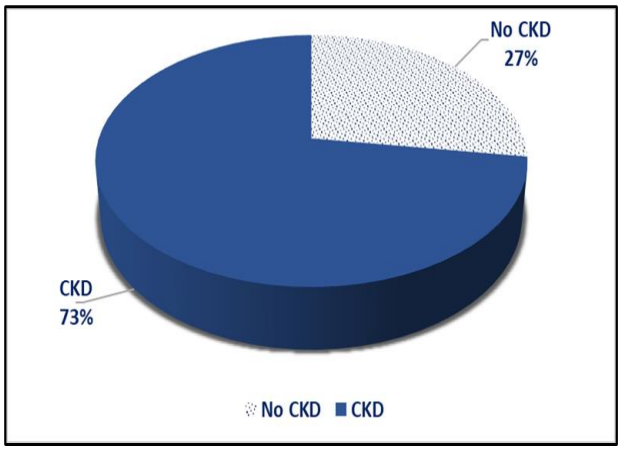

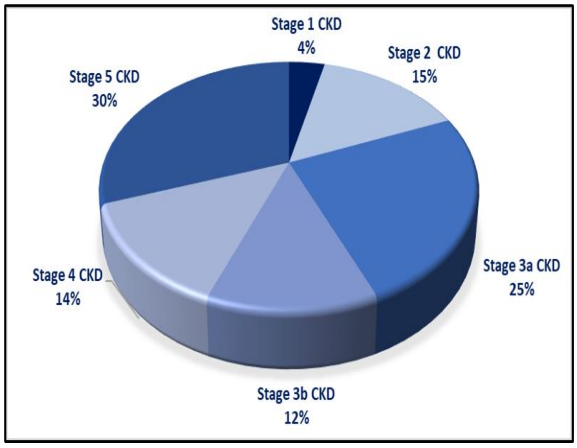

Figure 1: Distribution of chronic kidney disease (CKD) stages and overall CKD prevalence among study participants. The proportion of participants classified according to CKD stage using the CKD Epidemiology Collaboration (CKD-EPI) equation. CKD was defined as an estimated glomerular filtration rate (eGFR) <60 mL/min/1.73 m². The overall prevalence of CKD in the study population was 72.67%. Participants were distributed across CKD stages 1–5 according to Kidney Disease: Improving Global Outcomes (KDIGO) criteria.

3.2. The prevalence of some health risks related to CKD:

Hypertension affected 29.3% (44 individuals) of the participants, while hyperglycemia was present in 46.7% (70 individuals). Additionally, 46% (69 individuals) of the participants were classified as overweight or obese. These findings highlight significant risk factors associated with CKD in this population (Figure 2).

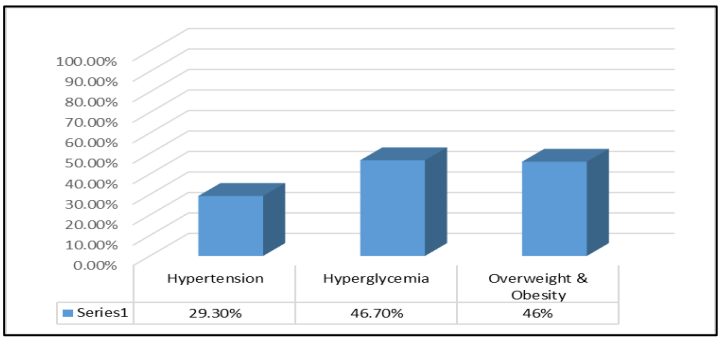

Figure 2: Prevalence of major chronic kidney disease (CKD)-related risk factors among study participants. Hypertension was present in 29.3% of participants, hyperglycemia in 46.7%, and overweight/obesity in 46.0%. These factors represent important clinical conditions associated with impaired kidney function.

3.3. Lifestyle and Clinical Determinants

Correlation between eGFR and various parameters:

Statistical analysis showed a positive correlation between eGFR and BMI, while mean arterial pressure (MAP) was negatively correlated with eGFR (Table 1).

Table 1: Correlation between eGFR and various parameters:

Correlation	eGFR by CKD-EPI equation	
	R	**p-value**
BMI	0.223**	0.007
MAP	-0.263**	0.001
Fasting blood glucose (mg/dl)	-0.146	0.080

eGFR = estimated glomerular filtration rate, BMI = body mass index, MAP = mean arterial pressure. ** Correlation is significant at the 0.01 level (2-tailed).

3.4. Distribution of CKD according to age and sex

Statistical analysis demonstrated a significant association between age groups and CKD ($p < 0.001$). CKD prevalence increased with age, with nearly half of CKD patients being over 50 years old and 30% in the age group of 41 to 50. A significant association was also found between CKD and sex ($p < 0.001$), with 62.4% of CKD patients being male, compared to 37.6% female (Figure 3).

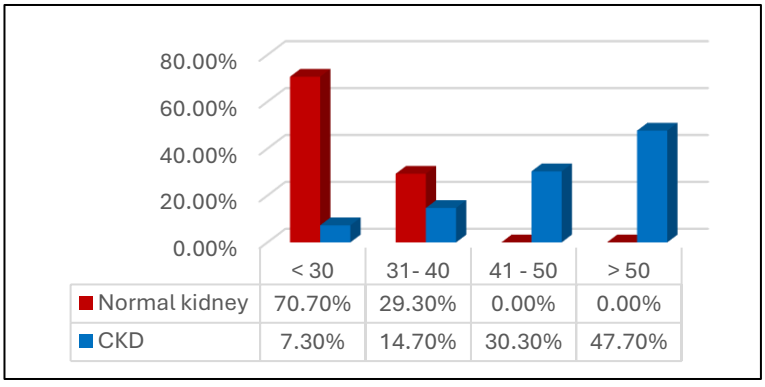

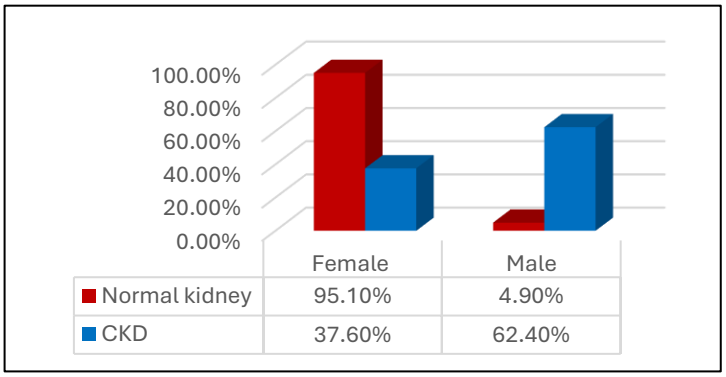

Figure 3: Distribution of chronic kidney disease (CKD) according to age group and sex. CKD prevalence increased significantly with age ($p < 0.001$), with the highest proportion observed among participants older than 50 years. A significant association was also observed between CKD and sex ($p < 0.001$), with males accounting for a greater proportion of CKD cases than females.

3.5. The relation between CKD and some medical risk factors related to CKD

The Body Mass Index (BMI) was not significantly associated with CKD ($p = 0.13$), which suggested no strong link between BMI categories and CKD. However, mean arterial pressure (MAP) demonstrated a significant relationship, with a higher proportion of individuals with elevated MAP having CKD compared to those with normal kidney function ($p < 0.001$). Fasting glucose levels were significantly associated with CKD ($p = 0.009$), indicating that higher glucose levels were more prevalent in individuals with CKD (Table 2). The history of kidney disease ($p = 0.88$), history of diabetes ($p = 0.22$), and family history of diabetes ($p = 0.77$) did not show significant associations with CKD. However, there was a significant relationship between CKD and a history of hypertension ($p = 0.004$), as well as CKD and a history of cardiovascular disease (CVD) ($p < 0.001$). Family history of hypertension ($p = 0.22$) and family history of CVD ($p = 0.37$) were not significantly associated with CKD. These findings

Table 2: The relation between CKD and some medical risk factors related to CKD

		Normal kidney (Number = 41)	**CKD (Number = 109)**	**χ^2 Value (Pearson Chi-Square)**	**p-value**
BMI	Underweight Normal weight Overweight Obese	2 14 20 5	7 58 32 12	5.65	0.13
MAP	Normal High	30 11	34 75	17.85	<0.001*
Fasting glucose	Normal High	29 12	51 58	6.86	0.009*
History of kidney disease	No Yes	19 22	52 57	0.02	0.88
History of diabetes	No Yes	32 9	74 35	1.48	0.22
Family history of diabetes	No Yes	27 14	69 40	0.08	0.77
History of hypertension	No Yes	27 14	43 66	8.35	0.004*
Family history of hypertension	No Yes	15 26	52 57	1.49	0.22
History of CVD	No Yes	40 1	74 35	14.38	<0.001*
Family history of CVD	No Yes	20 21	62 47	0.79	0.37

BMI = body mass index, MAP = mean arterial pressure, CVD = cardiovascular disease p-value ≤ 0.05 is statistically significant

3.6. The relation between CKD and some lifestyle risk factors related to CKD:

The majority of individuals with CKD (100 out of 109) relied on water from the Euphrates River, compared to 22 out of 41 individuals with normal kidney function, showing a highly significant difference ($p < 0.001$). Long-term analgesic use was more common in CKD patients, with 47 individuals reporting use, compared to 9 individuals with normal kidney function, also showing statistical significance ($p = 0.017$) (Table 3). Education level did not significantly affect CKD ($p = 0.69$). Smoking was more common among individuals with CKD (53 out of 109) compared to those with normal kidney function (28 out of 41), but this difference was not statistically significant ($p = 0.31$). Although alcohol consumption was uncommon among the participants, it was significantly associated with CKD ($p = 0.05$). There was no significant difference in physical activity levels between CKD patients and those with normal kidney function ($p = 0.54$). Likewise, there was no significant difference in the type of diet followed or adherence to specific diets between CKD patients and individuals with normal kidney function ($p = 0.30$ and $p = 0.08$, respectively) (Table 3).

Table 3: The relation between CKD and some lifestyle risk factors related to CKD

		Normal kidney (Number = 41)	**CKD (Number = 109)**	**χ^2 Value (Pearson Chi-Square)**	**p-value**
Source of drinking water	Euphrates river Groundwater, wells & springs	22 19	100 9	32.82	**<0.001***
History of long-time analgesic intake	No Yes	32 9	62 47	5.71	**0.017***
Education level	No Low High	15 21 5	35 64 10	0.75	0.69
Smoking	No Yes	13 28	56 53	4.64	**0.31**
Alcohol intake	No Yes	36 5	105 4	3.84	**0.05***
Physical activity	No Yes	35 6	97 12	0.37	0.54
Diet	Healthy Mixed	2 39	2 109	1.06	0.30
Specific diet	No Yes	13 23	20 89	3.09	0.08

p-value ≤ 0.05 is statistically significant

4. Discussion

This cross-sectional study provides important evidence regarding the burden of chronic kidney disease (CKD) among adults residing in North and East Syria. The overall CKD prevalence of 72.67% was substantially higher than estimates reported in most regional and international studies. Furthermore, the mean eGFR of 40.4 mL/min/1.73 m² and the predominance of stages 3b–5 suggest that many participants had moderate-to-severe renal impairment at the time of assessment. Several factors may contribute to this unusually high prevalence. First, participants were recruited from hospital-based settings, which may have increased the likelihood of enrolling individuals with existing health conditions. Second, prolonged disruption of healthcare services during years of armed conflict may have limited opportunities for early diagnosis and management of chronic diseases, allowing progressive kidney dysfunction to remain undetected. These findings emphasize the need for population-based studies to determine the true community prevalence of CKD in Syria. Delayed diagnosis and limited access to healthcare likely contribute to the disease's progression, as seen in other resource-limited settings (Farag, Kari, and Singh 2012; Saeed Al-Ghamdi et al. 2023). Age was strongly associated with CKD in the present study, with prevalence increasing markedly among older participants. This observation is consistent with established evidence demonstrating age-related declines in renal function resulting from nephron loss, vascular changes, and the cumulative effects of chronic comorbidities. Similarly, males exhibited a higher prevalence of CKD than females, in agreement with reports from several epidemiological studies in which biological, behavioral, and healthcare-access factors may contribute to sex-related differences in kidney disease risk. Hyperglycemia was present in 46.7% of participants. Diabetes mellitus is a leading cause of CKD worldwide, particularly when poorly controlled (Zheng, Ley, and Hu 2018). The high prevalence of hyperglycemia in this study suggests that diabetes is a key driver of CKD in Syria, mirroring trends observed in other Middle Eastern populations (Farah et al. 2024). Obesity was another significant CKD risk factor, with 46% of participants classified as overweight or obese. This reflects broader regional trends where dietary shifts and urbanization contribute to increased obesity rates (Syria Obesity - Adult Prevalence Rate - Demographics 2016). Obesity accelerates CKD progression through mechanisms such as glomerular hypertension and fibrosis (Ford, Patel, and Narayan 2017). Studies have also shown that obesity worsens CKD outcomes by increasing proteinuria and renal fibrosis (Wang and Kovesdy 2021). Hypertension emerged as a major contributor to CKD, with a prevalence of 29.3%. This finding aligns with global evidence that hypertension is both a cause and consequence of declining kidney function (kidney disease: Improving Global Outcomes 2021). The high prevalence of hypertension in the Eastern Mediterranean is often attributed to urbanization, economic challenges, and dietary patterns (Abboud and Karam 2021). Certainly, the significant association between a history of hypertension and CVD with CKD highlights the principal role of cardiovascular health in this population's CKD burden. So, controlling hypertension and preventing CVD is an important factor in reducing CKD risk. CVD and CKD are interconnected, often called a "cardiorenal syndrome." CKD accelerates CVD development due to common risk factors such as hypertension, diabetes, and dyslipidemia, while CVD also leads

to kidney damage due to poor blood flow. The mechanisms behind this link involve endothelial dysfunction, inflammation, and fibrosis, all of which impair both cardiovascular and kidney functions. Early intervention in managing both conditions together is necessary for better outcomes (Jankowski et al. 2021). The study found a negative correlation between eGFR and age, consistent with previous research demonstrating a gradual decline in kidney function with aging. Metabolic changes and comorbidities such as hypertension and diabetes further compound CKD risk in older populations (Levey et al. 2020). Additionally, men tend to have a higher prevalence of CKD compared to women, although this gap narrows in certain populations as women live longer and are more likely to develop CKD-related complications like diabetes (Hoyos Flight 2019). In studying the relationship between CKD and some lifestyle risk factors, we found that some lifestyle factors also play a critical role in the development and progression of CKD, and the findings of this study reveal several modifiable risk factors that are prevalent in the population. For example, the majority of individuals with CKD relied on water from the Euphrates River. This aligns with global evidence that exposure to water contaminated with nephrotoxins, or heavy metals can exacerbate CKD. Access to drinking water in Syria is severely limited due to various factors, including the ongoing conflict, environmental challenges, and poor infrastructure. In regions under government control, access to piped water is lacking, forcing people to rely on alternatives like trucked water or unsafe coping mechanisms. In areas like Hasakeh and Raqqa, reduced water levels in rivers and reservoirs, compounded by political tensions, further exacerbate the water crisis. This lack of access has led to water contamination and outbreaks of diseases such as cholera, especially in regions reliant on the Euphrates River ("Syria's Water Crisis: Assessing the Intersection of Climate Change and Geopolitical Interests"). Another important CKD risk factor is long-term analgesic use, which showed a statistically significant high prevalence in CKD patients. Studies have demonstrated that prolonged analgesic use, especially without appropriate monitoring, can impair renal function by reducing renal blood flow and GFR. Additionally, opioid use has also been linked to kidney damage, making it necessary to carefully monitor patients receiving chronic pain management (Keen and Aeddula 2020). Globally, the prescription of pain medications, including opioids, is high, but misuse and prolonged use, particularly following surgical procedures, are rising significantly (Lawal et al. 2020). Smoking and alcohol consumption were significantly associated with CKD. This was aligned with studies linking tobacco to renal damage through oxidative stress and endothelial dysfunction (Lang and Schiffl 2024). While no direct association between smoking and CKD was observed, smoking remains a known risk factor for kidney disease progression (Saeed Al-Ghamdi et al. 2023). Smokers with CKD tend to have a faster progression to ESKD compared to non-smokers. Moreover, smoking worsens cardiovascular risk, which is commonly associated with CKD and its complications (Lee et al. 2020). Alcohol consumption, though uncommon, was still significantly associated with CKD, which could suggest that even low levels of alcohol intake may be detrimental to kidney health in a population already loaded with other risk factors (Li et al. 2019). A history of cardiovascular disease was significantly associated with CKD in this population. This finding supports the concept of the cardiorenal continuum, whereby

cardiovascular and renal dysfunction frequently coexist and share common pathophysiological pathways, including endothelial dysfunction, chronic inflammation, oxidative stress, and vascular injury. The coexistence of these conditions highlights the importance of integrated cardiovascular and renal risk assessment in vulnerable populations. Several limitations should be acknowledged. The cross-sectional design precludes causal inference and limits assessment of temporal relationships between risk factors and CKD. The hospital-based convenience sample may also limit generalizability to the wider Syrian population. Furthermore, CKD classification was based primarily on a single eGFR assessment without longitudinal confirmation of chronicity. Despite these limitations, the study provides valuable preliminary data from a region where epidemiological evidence on kidney disease remains scarce. Overall, the findings indicate a substantial burden of CKD in North and East Syria and identify several potentially modifiable clinical and lifestyle-related factors associated with impaired renal function. Strengthening screening programs, improving management of hypertension and hyperglycemia, promoting rational analgesic use, and ensuring access to safe drinking water may contribute to reducing the burden of CKD in this vulnerable population.

5. Conclusion

The study reveals a critically high prevalence of chronic kidney disease (CKD) in North and East Syria, with 72.67% of participants affected and an average estimated glomerular filtration rate (eGFR) of 40.4 mL/min/1.73 m², indicating advanced disease stages. This study demonstrates a substantial burden of impaired kidney function among adults attending healthcare facilities in North and East Syria, with a high prevalence of eGFR-defined chronic kidney disease and a predominance of advanced disease stages. Older age, male sex, elevated mean arterial pressure, hyperglycemia, a history of hypertension and cardiovascular disease, reliance on Euphrates River water, and long-term analgesic use were significantly associated with CKD. These findings highlight the combined influence of clinical, environmental, and lifestyle-related factors on kidney health in conflict-affected settings. Given the limited availability of epidemiological data from Syria, this study provides important preliminary evidence that may inform future screening programs and public health strategies. Strengthening early detection of kidney dysfunction, improving the management of hypertension and hyperglycemia, promoting safe medication use, and ensuring access to safe drinking water may help reduce the burden of kidney disease in this vulnerable population. Further large-scale, population-based, and longitudinal studies are required to confirm these findings and clarify the causal pathways linking these risk factors to CKD development and progression in Syria.

Acknowledgments:

The authors would like to express their sincere gratitude to all health centers in Northeast Syria for their cooperation during this study.

Data Availability Statement:

All data are involved in the article.

Authors' contribution:

This paper is extracted from a MSc. thesis, which Haidar Saify and Eman Elbassuoni were supervisor of the project, chief investigator and

responsible for the data analysis. Methodology was performed by Nisreen Nabo Sheikh Bakr as the Master candidate.

Funding:

We confirm that this work did not receive any grant from funding agencies in the commercial or public sectors.

Declarations

Conflicts of interest

The authors declare that they have no known competing interests.

Reference

1. Abboud, Majd, and Sabine Karam. 2021. "Hypertension in the Middle East: Current State, Human Factors, and Barriers to Control." Journal of Human Hypertension, June. https://doi.org/10.1038/s41371-021-00554-z
2. Agboola, Olayinka J., Jeffrey SK Chan, Jared A. Spitz, Raymond NC Chan, Jaideep Patel, Charles German, Khurram Nasir et al. "The role of inflammation in longitudinal renal function decline and incident chronic kidney disease: the multi-ethnic study of atherosclerosis." European Journal of Preventive Cardiology 33, no. 5 (2026): 718-728.
3. Alasbahy, Afrah, Wadee Abdullah Al-Shehari, Safa Al-Hammadi, Reem Alariqi, Motea Ahmed Aboras, Lina Qasem, and Arafat Alsalami. "Prevalence and Associated Risk Factors of Renal Failure in the Population at the Authority of the Martyr President Saleh Al-Sammad Teaching Hospital in Amran City, Yemen." (2026).
4. Bikbov, Boris, Norberto Perico, and Giuseppe Remuzzi. 2018. "Disparities in Chronic Kidney Disease Prevalence among Males and Females in 195 Countries: Analysis of the Global Burden of Disease 2016 Study." Nephron 139 (4): 313–18. https://doi.org/10.1159/000489897
5. Carey, Robert M., and Paul K. Whelton. 2018. "Prevention, Detection, Evaluation, and Management of High Blood Pressure in Adults: Synopsis of the 2017 American College of Cardiology/American Heart Association Hypertension Guideline." Annals of Internal Medicine 168 (5): 351. https://doi.org/10.7326/m17-3203
6. Lodi, Giada, Domenico Sergi, Anna Dipinto, Francesca Bompan, Paola Secchiero, Rebecca Voltan, and Arianna Romani. "Hyperglycemia-induced endothelial dysfunction: from classical pathogenetic mechanisms to emerging insights into ACE2 protective action." International Journal of Molecular Sciences 27, no. 6 (2026): 2660.
7. Farag, Youssef M.K., Jameela A. Kari, and Ajay K. Singh. 2012. "Chronic Kidney Disease in the Arab World: A Call for Action." Nephron 121 (3-4): c120–23. https://doi.org/10.1159/000345149
8. Farah, Randa, Abdulrahman Alhajahjeh, Oraib Al-farahid, Hana Abuzaid, Dana Hyassat, Gaith Al-Khuraisat, Rana Al-Shimi, et al. 2024. "Risk Factors for Chronic Kidney Disease in Middle Eastern Patients with Type 2 Diabetes Mellitus: A Cross-Sectional Study Using the KDIGO Classification." Journal of Diabetes and Its Complications 38 (5): 108740–40. https://doi.org/10.1016/j.jdiacomp.2024.108740
9. Ford, Nicole D., Shivani A. Patel, and K.M. Venkat Narayan. 2017. "Obesity in Low- and Middle-Income Countries: Burden, Drivers, and Emerging Challenges." Annual Review of Public Health 38 (1): 145–64. https://doi.org/10.1146/annurev-publhealth-031816-044604
10. GBD 2013 Mortality and Causes of Death Collaborators. 2015. "Global, Regional, and National Age–Sex Specific All-Cause and Cause-Specific Mortality for 240 Causes of Death, 1990–2013: A Systematic Analysis for the Global Burden of Disease Study 2013." The Lancet 385 (9963): 117–71. https://doi.org/10.1016/s0140-6736(14)61682-2

11. Hoyos Flight, Monica. 2019. “Kidney Health Atlas Reveals Burden of Disease in Middle East.” Nature Middle East, April. https://doi.org/10.1038/nmiddleeast.2019.57
12. Jankowski, Joachim, Jürgen Floege, Danilo Fliser, Michael Böhm, and Nikolaus Marx. 2021. “Cardiovascular Disease in Chronic Kidney Disease.” Circulation 143 (11): 1157–72. https://doi.org/10.1161/circulationaha.120.050686
13. Kaze, Arnaud D., Titilayo Ilori, Bernard G. Jaar, and Justin B. Echouffo-Tcheugui. 2018. “Burden of Chronic Kidney Disease on the African Continent: A Systematic Review and Meta-Analysis.” BMC Nephrology 19 (1). https://doi.org/10.1186/s12882-018-0930-5
14. Keen, Mansoor U., and Narothama R. Aeddula. 2020. “Analgesic Nephropathy.” PubMed. Treasure Island (FL): StatPearls Publishing. 2020. https://www.ncbi.nlm.nih.gov/books/NBK541101/
15. Lang, Susanne M, and Helmut Schiffl. 2024. “Smoking Status, Cadmium, and Chronic Kidney Disease.” Renal Replacement Therapy 10 (1). https://doi.org/10.1186/s41100-024-00533-3
16. Lawal, Oluwadolapo D., Justin Gold, Amala Murthy, Rupam Ruchi, Egle Bavry, Anne L. Hume, Adam K. Lewkowitz, Todd Brothers, and Xuerong Wen. 2020. “Rate and Risk Factors Associated with Prolonged Opioid Use after Surgery.” JAMA Network Open 3 (6): e207367. https://doi.org/10.1001/jamanetworkopen.2020.7367
17. Lee, Sangmi, Shinchan Kang, Young Su Joo, Changhyun Lee, Ki Heon Nam, Hae-Ryong Yun, Jung Tak Park, et al. 2020. “Smoking, Smoking Cessation, and Progression of Chronic Kidney Disease: Results from KNOW-CKD Study.” Nicotine & Tobacco Research 23 (1): 92–98. https://doi.org/10.1093/ntr/ntaa071
18. Levey, Andrew S, Kai-Uwe Eckardt, Nijsje M Dorman, Stacy L Christiansen, Michael Cheung, Michel Jadoul, and Wolfgang C Winkelmayer. 2020. “Nomenclature for Kidney Function and Disease: Executive Summary and Glossary from a Kidney Disease: Improving Global Outcomes Consensus Conference*.” Nephrology Dialysis Transplantation 35 (7): 1077–84. https://doi.org/10.1093/ndt/gfaa153
19. Levey, Andrew S., Kai-Uwe Eckardt, Nijsje M. Dorman, Stacy L. Christiansen, Ewout J. Hoorn, Julie R. Ingelfinger, Lesley A. Inker, et al. 2020. “Nomenclature for Kidney Function and Disease: Report of a Kidney Disease: Improving Global Outcomes (KDIGO) Consensus Conference.” Kidney International 97 (6): 1117–29. https://doi.org/10.1016/j.kint.2020.02.010
20. Lewis, Sharon L, Linda Bucher, Margaret M Heitkemper, Mariann M Harding, Jeffrey Kwong, and Dottie Roberts. 2016. Medical-Surgical Nursing: Assessment and Management of Clinical Problems, Single Volume. Mosby. p. 1025.
21. Li, Deming, Jiuhong Xu, Fang Liu, Xinjing Wang, Huanhuan Yang, and Xinli Li. 2019. "Alcohol Drinking and the Risk of Chronic Kidney Damage: A Meta-Analysis of 15 Prospective Cohort Studies." Alcoholism: Clinical and Experimental Research 43 (7): 1360–72. https://doi.org/10.1111/acer.14112.
22. Liao, Min-Tser, Chih-Chien Sung, Kuo-Chin Hung, Chia-Chao Wu, Lan Lo, and Kuo-Cheng Lu. 2012. “Insulin Resistance in Patients with Chronic Kidney Disease.” Journal of Biomedicine and Biotechnology 2012: 1–12. https://doi.org/10.1155/2012/691369
23. Malekmakan, Leila, Taraneh Tadayon, Jamshid Roozbeh, and Mehrab Sayadi. 2018. “End-Stage Renal Disease in the Middle East: A Systematic Review and Meta-Analysis.” Iranian Journal of Kidney Diseases 12 (4): 195–203. https://pubmed.ncbi.nlm.nih.gov/30087213/
24. Mayo Clinic. 2023. “Diabetes - Diagnosis and Treatment.” Mayoclinic.org. Mayo Clinic. September 15, 2023. https://www.mayoclinic.org/diseases-

conditions/diabetes/diagnosis-treatment/drc-20371451

25. Moradinazar, Mehdi, Maryam Babakhani, Reza Rostami, Mohammad Shakiba, Atefeh Moradi, and Ebrahim Shakiba. 2022. “Epidemiological Status of Type 2 Diabetes Mellitus in the Middle East and North Africa, 1990-2019.” Eastern Mediterranean Health Journal 28 (7): 478–88. https://doi.org/10.26719/emhj.22.050
26. Murray, Christopher J L, Ryan M Barber, Kyle J Foreman, Ayse Abbasoglu Ozgoren, Foad Abd-Allah, Semaw F Abera, Victor Aboyans, et al. 2015. “Global, Regional, and National Disability-Adjusted Life Years (DALYs) for 306 Diseases and Injuries and Healthy Life Expectancy (HALE) for 188 Countries, 1990–2013: Quantifying the Epidemiological Transition.” The Lancet 386 (10009): 2145–91. https://doi.org/10.1016/s0140-6736(15)61340-x
27. National Institute of Diabetes and Digestive and Kidney Diseases. 2018. “Your Kidneys & How They Work.” National Institute of Diabetes and Digestive and Kidney Diseases. June 2018. https://www.niddk.nih.gov/health-information/kidney-disease/kidneys-how-they-work
28. Saeed Al-Ghamdi, Ali Abu-Alfa, Turki Alotaibi, Ali AlSaaidi, Abdulkareem AlSuwaida, Mustafa Arici, Tevfik Ecder, et al. 2023. “Chronic Kidney Disease Management in the Middle East and Africa: Concerns, Challenges, and Novel Approaches” Volume 16 (April): 103–12. https://doi.org/10.2147/ijnrd.s363133
29. “Syria Obesity - Adult Prevalence Rate - Demographics.” 2016. Indexmundi.com. 2016. https://www.indexmundi.com/syria/obesity_adult_prevalence_rate.html
30. “Syria’s Water Crisis: Assessing the Intersection of Climate Change and Geopolitical Interests.” n.d. Fanack Water 2025. https://water.fanack.com/publications/syrias-water-crisis-assessing-the-intersection-of-climate-change-and-geopolitical-interests/
31. Terashita, Maho, Kohei Kinoshita, Ryousuke Satou, Akemi Katsurada, Gweneth Eliza Lavalla, Akihiro Maenaka, Yuji Hidaka et al. "Renin-Angiotensin-Aldosterone System (RAAS) in Pig-to-Baboon Kidney Xenotransplantation—Relevance to Clinical Pig Kidney Xenotransplantation." Xenotransplantation 33, no. 2 (2026): e70129.
32. Wang, Angela Yee-Moon, and Csaba P Kovesdy. 2021. “Nutrition and Obesity Impacts on Kidney Health.” Contributions to Nephrology 199: 24–42. https://doi.org/10.1159/000517669
33. Zheng, Yan, Sylvia H. Ley, and Frank B. Hu. 2018. “Global Aetiology and Epidemiology of Type 2 Diabetes Mellitus and Its Complications.” Nature Reviews Endocrinology 14 (2): 88–98. https://doi.org/10.1038/nrendo.2017.151

Rojava Journal of Science and Technology

2026, VOL. 3, No 1, [95-101]

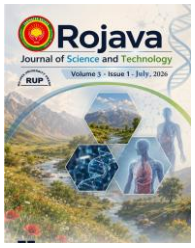

Prevalence and Risk Factors for Cardiovascular Disease in Post-Menopausal Syrian Women Living in North and East Syria: A Cross-Sectional Study

Sawsan Ahmed Abook[1], Haidar Saify Nabiabad[2], Eman Elbassuoni*[3]

[1] Department of Clinical Physiology, Institute of Science and Modern Technology, Rojava University, Syria

[2] Department of Medical Biotechnology, Institute of Science and Modern Technology, Rojava University, Syria

[3] Department of Physiology, Faculty of Medicine, Minia University, Egypt

ABSTRACT

Background: Cardiovascular disease (CVD) is the leading cause of mortality among women globally. The menopausal transition marks a period of heightened physiological vulnerability due to estrogen depletion. Methods: This cross-sectional study investigated CVD prevalence and risk factors among 300 Syrian women (91 premenopausal, 209 postmenopausal) in North and East Syria. Data collection included anthropometric measurements, blood pressure, fasting glucose, and full lipid profiles. Results: Postmenopausal women showed a high burden of cardiometabolic dysfunction. Obesity and central adiposity affected 45.1% and 63.4% of postmenopausal participants, respectively. The most frequent risk factors were hypertriglyceridemia (68.8%), hypertension (52.2%), and hyperglycemia (49.5%). Years since menopause positively correlated with increased arterial stiffness and mean arterial pressure. Conclusion: These findings underscore an urgent need for gender-sensitive public health interventions and targeted screening for hypertension and dyslipidemia in this population.

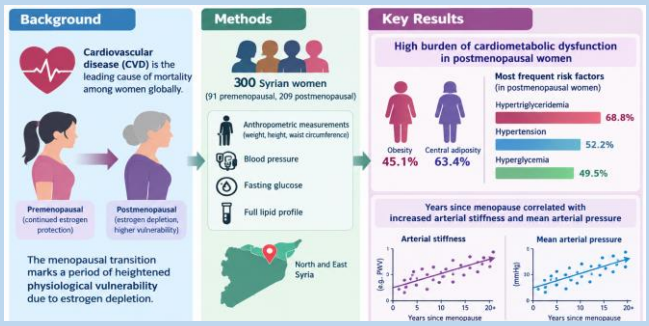

ARTICLE HISTORY

Received: 4 Jan. 2026

Revised: 9 May. 2026

Accepted: 28 Aug. 2026

Keywords: Cardiovascular Disease, Hypertension, Menopause, Prevalence, North and East Syria.

*Corresponding Author: Eman Elbassuoni Eman.Elbassuoni@yahoo.com

1. Introduction

Cardiovascular diseases (CVDs) are the leading cause of death among women globally, accounting for approximately one-third of female mortality. While CVD is often perceived as a male-centric pathology, women experience a sharp escalation in risk during middle age. Following the cessation of ovarian function and the resulting estrogen deficiency, women undergo a "catch-up" phenomenon where CVD prevalence matches or exceeds that of men. (Whelton et al. 2018; Vogel et al. 2021). Menopause is an independent CVD risk factor, marking a transition from a protected hormonal state to one of high vulnerability. The withdrawal of 17β-estradiol, a key vasodilator and anti-inflammatory agent, impairs endothelial function, induces pro-atherogenic lipid shifts, and reduces glucose tolerance. These changes often manifest as "metabolic syndrome of menopause," characterized by central adiposity and increased arterial stiffness. (El Khoudary et al. 2020; Maas and Rosano 2022). In North and East Syria, women face a "double burden" of risk. Biological menopausal vulnerability is compounded by over a decade of conflict, mass displacement, and fragmented healthcare infrastructure. These stressors contribute to chronic psychosocial strain and food insecurity, which exacerbate metabolic dysfunction. In conflict zones, chronic diseases are often overlooked in favor of acute trauma, leaving this demographic without adequate screening. (Akik et al. 2019; Maziak et al. 2024). This study aims to estimate CVD prevalence and identify modifiable and non-modifiable risk factors among postmenopausal women in this region. By analyzing lifestyle, clinical history, and dietary patterns, this research seeks to provide empirical evidence for targeted, gender-sensitive public health interventions in an underserved population.

2. Subjects and Methods

- **Study Design:** A descriptive and analytical cross-sectional study.
- **Study Population:** 300 Syrian women (91 premenopausal for comparative baseline, 209 postmenopausal) residing in North and East Syria.
- **Settings:** Data collection was conducted at outpatient clinics in Afrin Hospital (Aleppo), Tal Rifaat Hospital (Aleppo), Kobani Hospital (East of Euphrates), Mashta Al-Nur laboratory (East of Euphrates), Al-Rafiqa laboratory (Raqqa area), and Central laboratory (Raqqa area)
- **Ethical Considerations:** Protocol approved by the Ethics Committee of Rojava University; informed written consent was obtained from all participants.
- **Data Collection Tools:**
  - **Questionnaires:** Collected demographics, lifestyle habits (smoking, activity), and medical history.
  - **Clinical Assessments:** Standardized measurements of weight, height, BMI, resting blood pressure, and waist circumference.
  - **Laboratory Analysis:** Venous blood samples analyzed for fasting plasma glucose and complete lipid profiles (TC, HDL, LDL, TG).

Statistical Analysis: Data analyzed using SPSS version 27. Tests included chi-square for categorical variables and independent sample t-tests or ANOVA for numerical variables ($p < 0.05$).

3. Results

3.1. Anthropometric and Metabolic Characteristics

Postmenopausal women showed a significant divergence in metabolic status compared to the premenopausal group (Table 1). While mean weight was comparable, postmenopausal women exhibited a significant shift toward central obesity, with 63.4% exceeding the clinical threshold for waist circumference (>88 cm). Biochemical investigations (Table 2) showed postmenopausal women had markedly elevated LDL (110.8 mg/dL vs. 94.2 mg/dL)

and significantly reduced HDL (44.9 mg/dL vs. 51.6 mg/dL).

Table 1: Anthropometric measurements of the study population in North and East Syria (May – November 2025).

Parameter	Premenopausal (Mean ± SD) (n=91)	Postmenopausal (Mean ± SD) (n=209)	p-value
Weight (kg)	74.4 ± 16.20	76.3 ± 16.48	0.354
Height (m)	1.58 ± 0.08	1.58 ± 0.08	0.980
Waist Circumference (cm)	94.9 ± 13.70	94.5 ± 16.85	0.841
Body Mass Index (kg/m2)	27.9 ± 5.3	30.5 ± 6.1	< 0.01**

****p < 0.01 (Correlation is Highly Significant)**

Table 2: Blood pressure measurements and laboratory biochemical investigations of the study population.

Clinical Parameter	Premenopausal (Mean ± SD) (n=91)	Postmenopausal (Mean ± SD) (n=209)	p-value
Systolic BP (mmHg)	132.1 ± 21.5	135.3 ± 21.9	0.244
Diastolic BP (mmHg)	85.3 ± 14.7	84.6 ± 14.2	0.697
Mean Arterial Pressure (mmHg)	100.9 ± 15.7	101.4 ± 15.2	0.796
Fasting Blood Glucose (mg/dL)	107.8 ± 45.2	126.1 ± 52.0	< 0.01**
Total Cholesterol (mg/dL)	165.5 ± 34.5	176.4 ± 45.0	< 0.05*
Triglycerides (mg/dL)	195.8 ± 98.0	203.7 ± 98.0	< 0.05*

***p < 0.05 (Correlation is Significant); **p < 0.01 (Correlation is Highly Significant)**

3.2. Prevalence and Ranking of Risk Factors

The ranking of cardiovascular risk factors (Figure 1) revealed that hypertriglyceridemia was the most prevalent metabolic derangement (68.8%), followed by hypertension (52.2%) and hyperglycemia (49.5%). Correlation analysis (Figure 2) demonstrated a significant positive relationship between the duration of menopause and the severity of systolic hypertension and arterial stiffness.

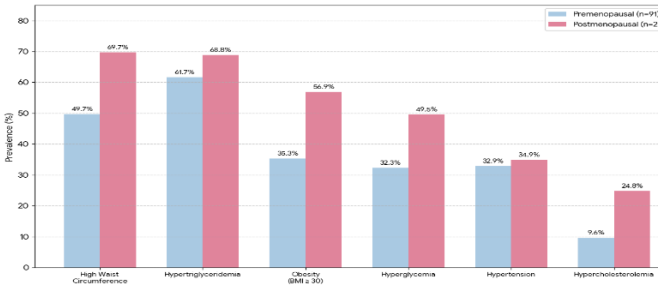

Figure 1: Prevalence and ranking of cardiovascular risk factors by menopausal status

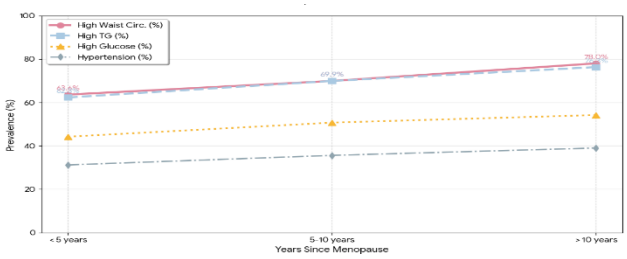

Figure 2: Time-dependent progression of cardiovascular risk factors in postmenopausal women

3.3. Lifestyle and Clinical Determinants

Lifestyle factors such as high physical activity (Figure 3) and adherence to a healthy diet (Figure 4) were associated with a statistically significant reduction in the prevalence of metabolic syndrome markers. Furthermore, women reporting difficult access to healthcare (Table 3) exhibited significantly higher mean BMI (31.8 vs. 29.7 kg/m²) and a higher prevalence of hypertension (42.5%) compared to those with easy access.

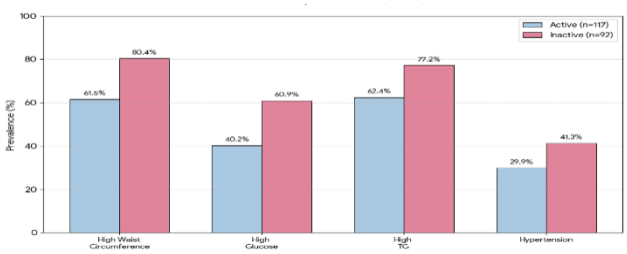

Figure 3: Influence of physical activity on cardiovascular risk factors in postmenopausal women.

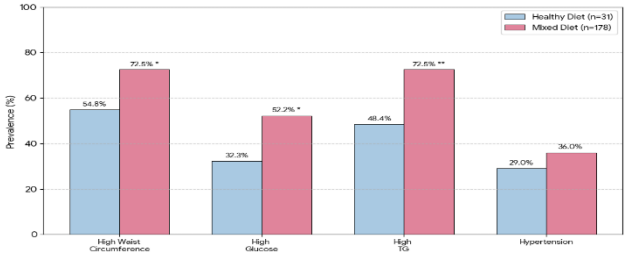

Figure 4: Impact of dietary patterns on cardiovascular risk factors in postmenopausal women

Table 3: Correlation between healthcare accessibility and cardiovascular risk factors in postmenopausal women.

Healthcare Access	n (%)	Mean BMI (kg/m²)	High Waist Circ. n (%)	High Glucose n (%)	High TG n (%)	Hypertension n (%)
Easy Access	129 (61.7%)	29.7 ± 5.6	87 (67.4%)	57 (44.2%)	84 (65.1%)	39 (30.2%)
Difficult Access	80 (38.3%)	31.8 ± 6.9	59 (73.8%)	46 (57.5%)	60 (75.0%)	34 (42.5%)
Total	209 (100%)	30.5 ± 6.1	146 (69.7%)	103 (49.5%)	144 (68.8%)	73 (34.9%)
p-value	—	*< 0.05**	*0.334*	*< 0.05**	*0.128*	*< 0.05**

p < 0.05 (Correlation is Significant)

4. Discussion

The findings of this study confirm a high prevalence of cardiovascular risk factors among postmenopausal women in North and East Syria, illustrating a significant shift in cardiometabolic health during the menopausal transition. This period is characterized by a rapid decline in endogenous hormones, which appears to act as a catalyst for metabolic syndrome components. The high prevalence rates observed here suggest that the menopausal transition is not merely a reproductive milestone but a critical window of vulnerability for long-term cardiovascular health. These results align with global trends indicating that postmenopausal status significantly alters the baseline risk profile for ischemic heart disease and stroke (Lobo et al. 2022). The transition to menopause represents a critical "physiological crossroad." The withdrawal of $17\beta\text{-estradiol}$, which normally promotes nitric oxide production and maintains vascular elasticity through the activation of estrogen receptors in the vessel walls, triggers systemic endothelial dysfunction. This loss of hormonal protection leads to increased systemic vascular resistance and arterial stiffness, explaining the high rates of hypertension (52.2%) observed in our participants. Furthermore, the absence of estradiol's antioxidant properties may further accelerate oxidative stress within the vascular endothelium, promoting the early stages of atherosclerosis (El Khoudary et al. 2020). Furthermore, estrogen deficiency fundamentally alters adipocyte metabolism, causing a distinct shift from "gynoid" fat distribution (subcutaneous) to "android" (visceral) fat distribution, as evidenced by the high central obesity data in this cohort. Visceral fat acts as an active endocrine organ, secreting pro-inflammatory cytokines such as $TNF\text{-}\alpha$ and $IL\text{-}6$ that contribute to systemic insulin resistance. This biological

mechanism aligns with the high rates of hyperglycemia and elevated fasting glucose found in the postmenopausal group. This shift is often accompanied by a decrease in basal metabolic rate, which, if not compensated for by physical activity or caloric restriction, creates a self-reinforcing cycle of obesity and metabolic derangement (Ko et al. 2020). In the Syrian context, these biological vulnerabilities are significantly amplified by local environmental factors. A decade of conflict has severely impacted food security and dietary diversity across the region. The heavy reliance on energy-dense, nutrient-poor subsidized foods—such as bread, processed vegetable oils, and refined sugar—has likely exacerbated the prevalence of hypertriglyceridemia (68.8%), which emerged as the top-ranked risk factor in this study. Additionally, chronic psychosocial stress stemming from displacement and economic instability is a known driver of hypothalamic-pituitary-adrenal (HPA) axis dysregulation. This chronic elevation of cortisol further promotes visceral adiposity and sympathetic nervous system overactivity, driving hypertension (Akik et al. 2020). The data from the present study reveal that 38.3% of postmenopausal women face significant barriers to healthcare, including transportation costs, lack of female providers, and fragmented primary care services. This lack of access correlates strongly with higher BMI and unmanaged hypertension, suggesting that cardiovascular risk in Syria is a "biosocial" issue where political and economic conditions dictate physiological outcomes. Furthermore, the low utilization of Hormone Replacement Therapy (HRT) (27.8%), despite the metabolic benefits observed in HRT users in this study, highlights a significant gap in clinical management. This underutilization may stem from a lack of provider training or patient misconceptions regarding the safety of HRT, missing an opportunity to mitigate the metabolic shifts that occur during this transition (Nappi et al. 2021).

5. Conclusion and Recommendations

Menopause is a critical window of cardiovascular vulnerability for Syrian women. The high prevalence of central obesity, hypertension, and dyslipidemia suggests a looming increase in cardiovascular events unless targeted interventions are implemented. To address the cardiovascular health challenges identified, it is recommended that healthcare facilities implement routine screenings for waist circumference and lipid profiles within women's health clinics to ensure early detection of metabolic risks. From a public health perspective, priority should be given to gender-sensitive interventions that focus specifically on the management of hypertension and dyslipidemia. Furthermore, nutritional initiatives must emphasize accessible dietary modifications to effectively combat the high prevalence of hypertriglyceridemia among the population. Finally, at the policy level, integrating cardiovascular monitoring into existing reproductive health services in North and East Syria is essential to ensure these vital screenings reach vulnerable and underserved populations.

Reference

1. Akik, Chaza, et al. 2019. "Hostage to Crisis: The Perilous State of Non-Communicable Disease Services in Humanitarian Settings in the Middle East." Journal of Global Health 9 (2): 020401.
2. Akik, Chaza, Hala Ghattas, Sawsan Abdulrahim, and Annie S. Anderson. "The Impact of Conflict on Dietary Intake and Nutrition Health Outcomes in Women of Reproductive Age in the Middle East and North Africa: A Systematic Review."

Progress in Cardiovascular Diseases 63, no. 2 (2020): 138–46.

3. El Khoudary, Samar R., Brooke Aggarwal, Theresa M. Beckie, Paul N. Hopkins, Matthew A. Allison, Kristine Ensrud, Carol E. Kasten, et al. "Menopause Transition and Cardiovascular Disease Risk: Implications for Modern Clinical Practice: A Scientific Statement From the American Heart Association." Circulation 142, no. 25 (2020): e506–32.
4. El Khoudary, Samar R., et al. 2020. "Menopause Transition and Cardiovascular Disease Risk: A Scientific Statement From the American Heart Association." Circulation 142 (25): e506–e532.
5. Ko, Seung-Hyun, and Youn-Jee Kim. "Menopause and Cardiovascular Disease: Women's Health is an Essential Part of Public Health." International Journal of Environmental Research and Public Health 17, no. 23 (2020): 8697.
6. Lobo, Rogerio A., Faith G. Davis, Anne G. Rosenfeld, Sarah M. Samaan, Martha Gulati, Mercedes R. Carnethon, and Kevin C. Maki. "Evaluation of Cardiovascular Risk in Women for the Practitioner." Journal of the American College of Cardiology 79, no. 13 (2022): 1301–13.
7. Maas, Angela H. E. M., and Giuseppe M. C. Rosano. 2022. "The Transition from Low to High Cardiovascular Risk in Women." European Heart Journal 43 (31): 2921–2923.
8. Maziak, Wasim, et al. 2024. "The Burden of Non-Communicable Diseases in Conflict-Affected Syria." The Lancet Global Health 12 (1): e15–e16.
9. Nappi, Rossella E., Simonetta Piloni, and Valentina De Pascalis. "The Management of Menopause in Women at High Risk for Cardiovascular Disease." Maturitas 146 (2021): 44–50.
10. Vogel, Birgit, et al. 2021. "The Lancet Women and Cardiovascular Disease Commission: Reducing the Global Burden by 2030." The Lancet 397 (10292): 2385–2438.
11. Whelton, Paul K., et al. 2018. "2017 ACC/AHA Guideline for the Prevention, Detection, Evaluation, and Management of High Blood Pressure in Adults." Journal of the American College of Cardiology 71 (19): e127–e248.

Rojava Journal of Science and Technology

2026, VOL. 3, No 1, [102-120]

Hierarchical Fe_3O_4@Mg/Al-LDH@Chitosan Nanocomposite for Rapid and Reusable Congo Red Adsorption from Complex Water Systems

Jwan Sheikh Mohammad[1], Haidar Saify Nabiabad2, Mohamed E.Mahmoud[3], Rehab M .El-Sharkawy*[4]

[1]Dep. of Analytical Chemistry, Institute of Science and Modern Technology -Rojava University, Syria.

[2]Dep. of Biotechnology, Institute of Science and Modern Technology -Rojava University, Syria.

[3]Faculty of Science, Chemistry Department, Alexandria University, Egypt

[4]Faculty of Dentistry, Chemistry Department, Pharos University in Alexandria, Egyp

ABSTRACT

Synthetic dye contamination represents a persistent challenge in wastewater management due to the chemical stability and toxicity of these compounds. This study presents the synthesis and evaluation of a magnetically recoverable nanocomposite composed of magnetite, layered double hydroxide (LDH), and chitosan (Fe_3O_4@LDH@CS) for the removal of Congo Red from aqueous systems. The material was prepared using a microwave-assisted approach designed to enhance synthesis efficiency and reduce energy consumption. Comprehensive characterization (XRD, FTIR, SEM, and TGA) confirmed the successful integration of magnetite nanoparticles within an LDH matrix stabilized by chitosan, resulting in a structurally robust and porous hybrid adsorbent. Batch adsorption experiments demonstrated high removal efficiencies (>95%) across a broad pH range, with optimal performance near neutral conditions. Kinetic analysis indicated that adsorption followed a pseudo-second-order model, suggesting chemisorption as the dominant mechanism, while isotherm modeling supported monolayer adsorption behavior. Thermodynamic parameters revealed that the process is spontaneous and endothermic, with improved adsorption at elevated temperatures. The nanocomposite maintained high performance over multiple regeneration cycles and showed strong applicability in real water matrices, including industrial wastewater and seawater. These findings highlight the potential of Fe_3O_4@LDH@CS as an efficient and reusable adsorbent for practical dye remediation applications.

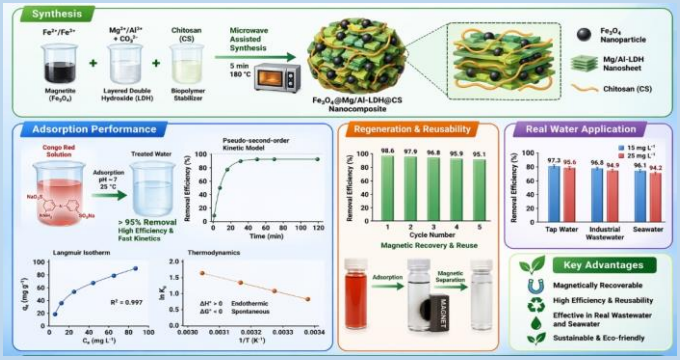

ARTICLE HISTORY

Received: 14 Jan. 2026

Revised: 10 Jul. 2026

Accepted: 18 Sep. 2026

Keywords: Magnetite-layered double hydroxide, Chitosan, nanocomposite, Congo red dye, wastewater treatment

*Corresponding Author: rehab.mansour@pu

1. Introduction

The discharge of dye-containing effluents into aquatic environments remains a significant environmental concern, particularly in regions with intensive textile, printing, and chemical manufacturing activities. Synthetic dyes are designed to resist fading and degradation, resulting in high persistence once released into natural water systems (Lin et al., 2023). Their presence not only affects water aesthetics but also reduces light penetration, disrupts aquatic ecosystems, and introduces toxic, mutagenic, and potentially carcinogenic compounds into the environment (Oguanobi et al., 2025). Among commonly used dyes, Congo Red is a widely applied anionic azo dye known for its high solubility and structural stability. These properties make it particularly difficult to remove through conventional treatment methods (Khan et al., 2022). Once introduced into water bodies, Congo Red can degrade into aromatic amines, which pose additional environmental and health risks. As a result, the development of efficient and sustainable technologies for dye removal is a critical priority in environmental remediation. Traditional treatment approaches, including biological degradation, coagulation–flocculation, and advanced oxidation processes, have demonstrated varying degrees of effectiveness. However, these methods are often limited by high operational costs, incomplete removal, or the generation of secondary pollutants (Zazouli et al., 2024). Adsorption has emerged as a preferred alternative due to its operational simplicity, high efficiency, and adaptability to different wastewater compositions. The effectiveness of adsorption processes depends largely on the properties of the adsorbent, including surface area, functional groups, and structural stability (Younas et al., 2021). Recent advances in nanotechnology have enabled the design of novel adsorbent materials with enhanced performance characteristics. Magnetite (Fe_3O_4) nanoparticles have received considerable attention due to their high surface reactivity and the advantage of magnetic separation, which simplifies post-treatment recovery. Despite these benefits, magnetite nanoparticles tend to aggregate and oxidize, reducing their long-term stability and adsorption efficiency (Arrisujaya et al., 2025). Layered double hydroxides (LDHs) offer complementary properties that address some of these limitations. LDHs are characterized by positively charged layers and exchangeable interlayer anions, enabling strong interactions with negatively charged contaminants such as azo dyes (Zhang et al., 2026). Their tunable composition and relatively high thermal stability make them attractive candidates for environmental applications. However, LDHs alone often suffer from poor mechanical strength and limited reusability under repeated operational cycles (Wang et al., 2026). Chitosan, a naturally derived biopolymer, has also been extensively studied for pollutant removal due to its abundance, biodegradability, and functional amino and hydroxyl groups. These functional groups provide active binding sites for dye molecules through electrostatic interactions and hydrogen bonding (Cui et al., 2026). Nevertheless, the practical application of chitosan is constrained by its limited mechanical stability and solubility under acidic conditions (Tundwal et al., 2026). To overcome the individual limitations of these materials, recent research has focused on the development of hybrid nanocomposites that combine their complementary properties. Integrating magnetite, LDH, and chitosan into a single composite structure offers several advantages: enhanced adsorption capacity, improved structural stability, and convenient magnetic recovery. Such multifunctional materials are particularly attractive for real-world remediation applications, where operational efficiency and reusability are critical. In this study, a Fe_3O_4@LDH@Chitosan nanocomposite was synthesized using a microwave-assisted method, which provides a rapid and energy-efficient alternative to conventional synthesis techniques. The performance of

the synthesized material was evaluated for the removal of Congo Red from aqueous solutions under varying experimental conditions, including pH, contact time, temperature, and adsorbent dosage. In addition to controlled laboratory experiments, the applicability of the nanocomposite was assessed using real water samples to better reflect environmental conditions. The objective of this work is to demonstrate the effectiveness of this hybrid material as a practical adsorbent for dye-contaminated wastewater and to provide insights into the mechanisms governing the adsorption process. By combining material innovation with application-oriented evaluation, this study contributes to the development of sustainable and efficient solutions for water pollution remediation.

2. Materials and Methods

All chemicals used in this study were of analytical grade and used without further purification to ensure reproducibility. Magnesium chloride hexahydrate ($MgCl_2 \cdot 6H_2O$), aluminum chloride hexahydrate ($AlCl_3 \cdot 6H_2O$), sodium hydroxide (NaOH), sodium carbonate (Na_2CO_3), hydrochloric acid (HCl), and Congo Red dye were obtained from Sigma. Chitosan (degree of deacetylation ≈ 85–90%) was used as the biopolymeric component. Deionized water was employed in all synthesis and adsorption experiments to minimize interference from dissolved ions. Magnetite (Fe_3O_4) nanoparticles were synthesized in laboratory using a co-precipitation method to ensure control over particle size and purity.

2.1. Microwave-Assisted Synthesis of Nanomagnetite (nFe_3O_4)

Magnetite nanoparticles were synthesized via a modified co-precipitation approach under microwave-assisted conditions to enhance reaction kinetics and particle homogeneity. Briefly, ferrous (Fe^{2+}) and ferric (Fe^{3+}) salts were dissolved in an acidic aqueous medium under continuous stirring. The molar ratio of Fe^{2+} to Fe^{3+} was maintained at 1:2 to favor magnetite formation (Mystrioti et al., 2022).

A sodium hydroxide solution was added dropwise under vigorous stirring to induce precipitation. The reaction mixture was intermittently exposed to microwave irradiation to maintain a temperature of approximately 80°C, accelerating nucleation and growth processes. The resulting black precipitate was magnetically separated, washed repeatedly with deionized water to remove residual ions, and dried at 70°C.

2.2. Preparation of Magnesium–Aluminum Layered Double Hydroxide (Mg/Al-LDH)

The Mg/Al-LDH was synthesized using a conventional co-precipitation method under controlled alkaline conditions. A mixed metal solution containing Mg^{2+} and Al^{3+} ions at a molar ratio of 3:1 was prepared and heated under continuous stirring.

A basic solution containing NaOH and Na_2CO_3 was added dropwise to the metal solution while maintaining the pH at approximately 10. The suspension was aged at elevated temperature (≈80°C) for 24 hours to promote crystallization and structural ordering of the LDH layers. The precipitate was then filtered, washed to neutral pH, and dried to obtain a fine powder.

2.3. Microwave-Assisted Synthesis of CT@Fe_3O_4@Mg/Al-LDH Nanocomposite

The hybrid nanocomposite was prepared through a sequential assembly process combining 5.0 g magnetite, LDH, and 5.0 g chitosan. Initially, Fe_3O_4 nanoparticles were mixed with chitosan in the presence of a small volume of water to ensure uniform dispersion. The mixture was subjected to microwave heating to facilitate partial dehydration and enhance interaction between the inorganic and polymeric phases.

Subsequently, the Fe_3O_4–chitosan composite was blended with 5.0 g Mg/Al-LDH and further treated under microwave irradiation. This process was repeated multiple times to ensure homogeneous integration of all components. The final product was ground, sieved, and dried to obtain a stable, magnetically responsive CT@Fe_3O_4@Mg/Al-LDH nanocomposite.

2.4. Nanocomposite Characterization

The structural and physicochemical characteristics of the nanocomposite were analyzed using various analytical methods. The surface morphology was investigated through scanning electron microscopy (SEM) employing a Hitachi S-4800 instrument. To enhance conductivity, the samples were coated with a thin layer of Au–Pd. X-ray diffraction (XRD) analysis was carried out to determine the crystalline phases and structural features. Fourier-transform infrared spectroscopy (FTIR) was utilized to detect functional groups within the range of 4000–500 cm^{-1} using KBr pellet techniques. Additionally, thermogravimetric analysis (TGA) was performed in a nitrogen atmosphere from 25 to 800 °C at a heating rate of 10 °C min^{-1} to assess thermal stability.

2.5. Microwave-Enhanced Removal of Congo Red (CR) Dye

A stock solution of Congo Red (CR) dye with a concentration of 1000 ppm will be used as the primary source solution. From this stock, working solutions with concentrations of 5, 10, and 15 mg/L will be prepared by appropriate dilution using double-distilled water (DW). The absorbance of CR dye will be measured at its maximum wavelength (λ_{max} = 497 nm) using a UV–Vis spectrophotometer. Microwave-assisted adsorption and decolorization experiments will be conducted using the synthesized Fe_3O_4@Chitosan@Mg/Al-LDH nanocomposite under varying operational conditions, including different nanocomposite doses, contact times, initial dye concentrations, pH values, temperatures, and coexisting ions. The dye removal efficiency (%E) of Congo Red onto the nanocomposite will be determined using Equation (1):

$$\%E = (C_0 - C)/C_0$$

where C_o and C_e represent the initial and equilibrium concentrations (mg/L) of CR, respectively.

2.6. Adsorption Experiments

Batch adsorption experiments were carried out to assess the removal efficiency of Congo Red under microwave-assisted conditions. A stock solution of the dye was initially prepared and subsequently diluted to the required concentrations for experimental analysis. The adsorption studies were performed in conical flasks containing a fixed volume of dye solution and a predetermined mass of adsorbent. The mixtures were exposed to microwave irradiation in order to enhance mass transfer and improve adsorption kinetics. The effects of key operational parameters, including initial solution pH, adsorbent dosage, contact time, initial dye concentration, and temperature, were systematically investigated. The solution pH was adjusted using dilute hydrochloric acid (HCl) or sodium hydroxide (NaOH) solutions. Following treatment, the adsorbent was separated magnetically, and the residual dye concentration in the solution was determined using a UV–Vis spectrophotometer at a wavelength of 497 nm. The removal efficiency (%) and adsorption capacity were calculated based on standard mass balance equations. All experiments were

performed in triplicate to ensure reproducibility and reliability of the obtained data.

2.7. Kinetic and Isotherm Modeling

To elucidate the adsorption mechanism, the experimental data were analyzed using a series of kinetic and equilibrium isotherm models. Kinetic analyses were performed employing the pseudo-first-order, pseudo-second-order, intraparticle diffusion, Elovich, and Avrami models in order to identify the rate-controlling steps governing the adsorption process. Equilibrium data were interpreted using the Langmuir, Freundlich, Temkin, and Dubinin–Radushkevich isotherm models to characterize adsorption behavior and surface properties of the adsorbent. The model parameters were determined via linear regression, and the goodness of fit was evaluated based on the corresponding correlation coefficients (R^2).

2.8. Thermodynamic Analysis

Thermodynamic parameters, including Gibbs free energy (ΔG°), enthalpy (ΔH°), and entropy (ΔS°), were determined from temperature-dependent adsorption experiments. The Van't Hoff equation was used to analyze the relationship between temperature and adsorption equilibrium. These parameters provided insight into the spontaneity, feasibility, and nature of the adsorption process.

2.9. Application to Real Water Samples

To evaluate practical applicability, the synthesized nanocomposite was tested using real water samples, including tap water, industrial wastewater, and seawater. These samples were spiked with Congo Red and treated under optimized conditions. The performance of the adsorbent in complex matrices was assessed by comparing removal efficiencies with those obtained in controlled laboratory conditions.

3. Results and discussion

3.1. Structural and Physicochemical Characteristics

The XRD analysis confirmed the successful formation of a hybrid nanocomposite consisting of magnetite and LDH phases. The presence of characteristic diffraction peaks corresponding to magnetite indicates that the crystalline structure was preserved during composite fabrication. Meanwhile, the broadened LDH peaks suggest partial structural disorder, likely due to interaction with chitosan and magnetite nanoparticles.

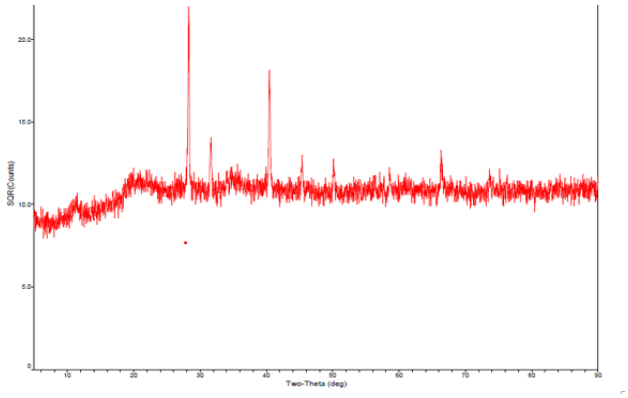

Figure 1: X-ray diffraction (XRD) patterns of Fe_3O_4, Mg/Al-LDH, and Fe_3O_4@Mg/Al-LDH@CS nanocomposite, confirming the successful incorporation of magnetite into the LDH matrix without structural collapse of the crystalline phases.

FTIR spectra further supported the successful integration of all components. The coexistence of Fe–O vibrations and hydroxyl-related bands indicate strong interactions between magnetite, LDH layers, and chitosan functional groups. The observed band broadening suggests hydrogen bonding and interfacial coupling, which are beneficial for adsorption processes.

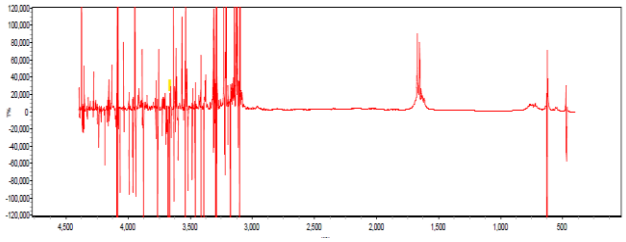

Figure 2: Fourier-transform infrared (FTIR) spectra of Fe_3O_4@Mg/Al-LDH@CS nanocomposite, showing characteristic bands of Fe–O, hydroxyl groups, and chitosan functional groups, indicating strong interfacial interactions among composite components.

Thermogravimetric analysis revealed multiple weight-loss stages corresponding to moisture removal, decomposition of organic components, and structural transformations. The relatively high residual mass confirms the presence of thermally stable inorganic phases, indicating that the composite can withstand elevated temperatures encountered in practical applications (Kan et al., 2025).

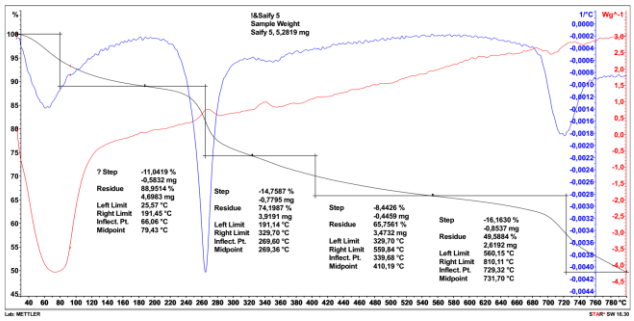

Figure 3: Thermogravimetric analysis (TGA) curve of Fe_3O_4@Mg/Al-LDH@CS nanocomposite, illustrating multi-step weight loss associated with moisture removal, chitosan decomposition, and structural stability of inorganic phases.

Figure 4 presents the SEM micrograph of the synthesized magnetite-loaded layered double hydroxide (LDH) composite incorporated with chitosan. The observed morphology is predominantly composed of irregular, fractured, plate-like particles, which is typical of LDH-based materials combined with partially aggregated magnetite domains. The composite exhibits heterogeneous and non-uniform particle sizes, ranging from tens to several hundreds of nanometers. The irregular shapes and sharp edges indicate the coexistence of crystalline LDH layers and fragmented magnetite clusters, reflecting the brittle nature of the material following synthesis and mechanical processing. The particle surfaces appear rough, cracked, and highly textured. This surface morphology suggests the presence of layered LDH structures alongside embedded or partially coated magnetite nanoparticles. Although a continuous chitosan film is not clearly visible at this magnification, it is likely present as a binding agent within the composite matrix. Such surface roughness is advantageous for adsorption processes, as it increases the availability of active sites for Congo Red dye uptake (Xiao et al., 2026). Moderate agglomeration of particles is evident, which can be attributed to electrostatic interactions between LDH layers, magnetic interactions among Fe_3O_4 domains, and hydrogen bonding associated with chitosan functional groups. This aggregation behavior contributes to the structural stability of the hybrid composite. Additionally, the micrograph reveals the presence of interparticle voids with varying sizes. These voids may facilitate mass transfer during adsorption by providing accessible pathways for dye molecules. However, due to the relatively low magnification, nanoscale porosity cannot be accurately assessed.

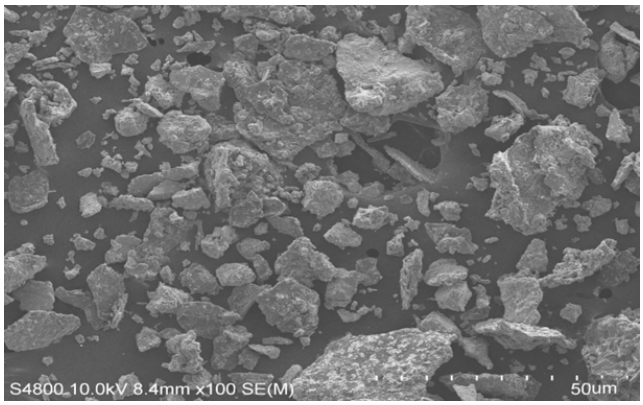

Figure 4: Scanning electron microscopy (SEM) image of Fe_3O_4@Mg/Al-LDH@CS nanocomposite, revealing irregular, plate-like morphology with rough and porous surface features favorable for adsorption.

3.2. Effect of pH and Surface Charge Behavior

Solution pH plays a critical role in adsorption processes by influencing both the surface charge of the adsorbent

and the ionization state of the dye. The nanocomposite exhibited high removal efficiency across a wide pH range, with optimal performance observed near neutral conditions. The point of zero charge (pHpzc ≈ 5) indicates that the surface is positively charged at acidic pH values, promoting electrostatic attraction with anionic Congo Red molecules. At higher pH values, despite reduced electrostatic attraction, adsorption efficiency remained high, suggesting the involvement of additional mechanisms such as hydrogen bonding and π–π interactions. This broad pH tolerance is particularly important for real-world applications, where wastewater pH can vary significantly. The combined evaluation of adsorption efficiency and pHpzc confirms that the Magnetite–LDH–Chitosan nanocomposite exhibits strong affinity toward Congo Red across a broad pH range, with optimum performance around pH 5–7 and a pHpzc close to 5.0, supporting a mechanism governed by electrostatic interactions, hydrogen bonding, and partial surface complexation (Chaimaa et al., 2026).

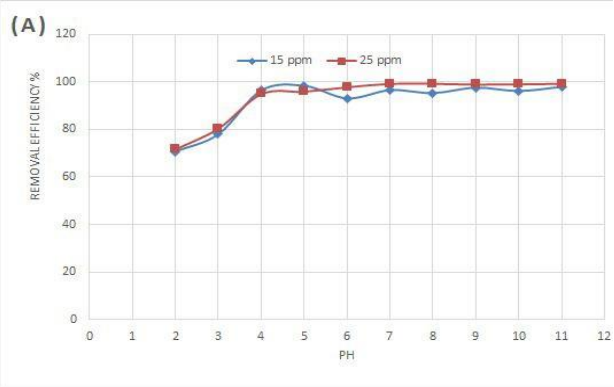

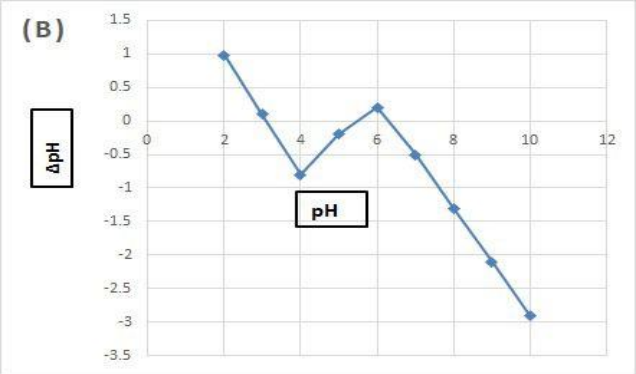

Figure 5: (A) Effect of initial solution pH on Congo Red removal efficiency using Fe_3O_4@Mg/Al-LDH@CS nanocomposite; (B) determination of point of zero charge (pHpzc ≈ 5) at 25 °C, indicating pH-dependent surface charge behavior.

3.3. Effect of Contact Time and Adsorption Kinetics

The kinetic model equations and corresponding parameters for Congo Red adsorption onto the Magnetite–LDH–Chitosan nanocomposite were evaluated (Table 1). Figure 6A shows the effect of contact time on removal efficiency at initial concentrations of 15 and 25 ppm. Adsorption proceeded rapidly at the initial stage, followed by a gradual approach to equilibrium. Within the first 10 min, removal efficiencies reached ~94–96% (15 ppm) and 97–98% (25 ppm), attributed to the abundance of available active sites. With increasing contact time, the removal efficiency increased slightly and attained equilibrium within 40–60 min, stabilizing at ~97–98% for 15 ppm and ~99% for 25 ppm. This behavior indicates rapid site occupation followed by saturation. The two-stage profile suggests that surface adsorption dominates initially, while intraparticle diffusion contributes at later stages, confirming the favorable kinetics of the nanocomposite. Figure 6 B presents the pseudo-first-order model. The plots of $\ln(q_e - q_t)$ versus t show limited linearity, indicating that this model is only applicable during the early adsorption stage. The deviation at longer contact times suggests that adsorption is not governed solely by physical interactions. In contrast, the pseudo-second-order model (Figure 6C) shows excellent linearity in plots of

t/q_t versus t, indicating a good fit to the experimental data. This suggests that chemisorption, involving electron sharing or exchange between dye molecules and surface functional groups, controls the adsorption process. The Avrami model (Figure 6D) also exhibits good linearity for both concentrations, indicating its suitability for describing the system. This reflects heterogeneous adsorption behavior involving multiple concurrent mechanisms. The slightly higher slope at 25 ppm suggests a faster approach to equilibrium, likely due to a higher driving force.

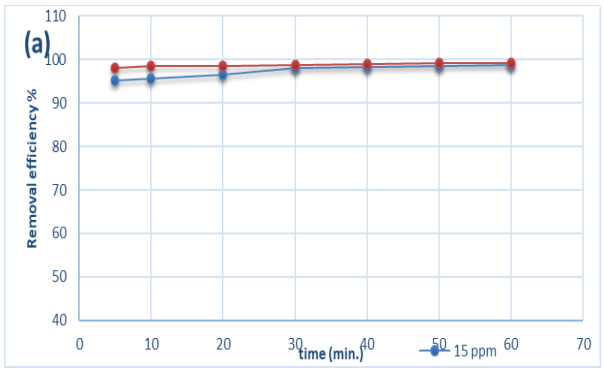

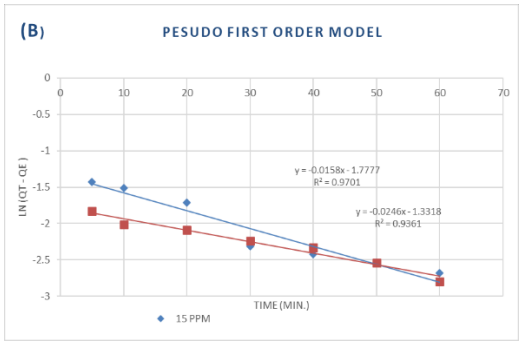

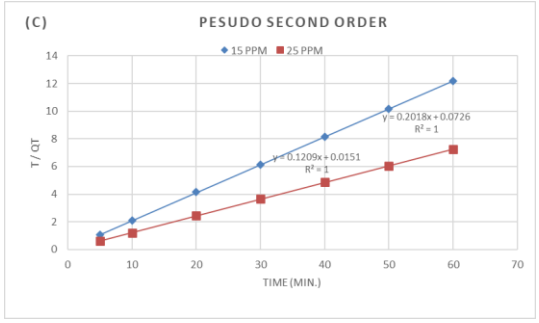

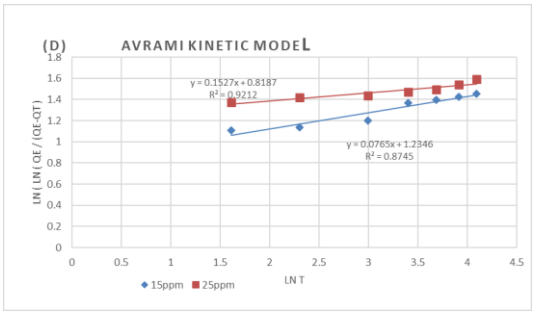

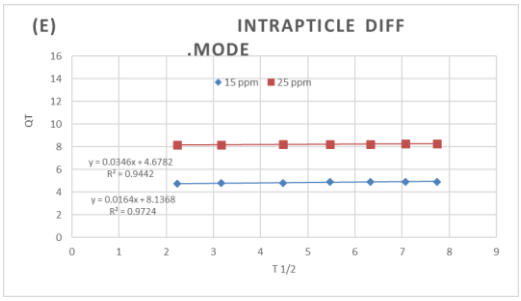

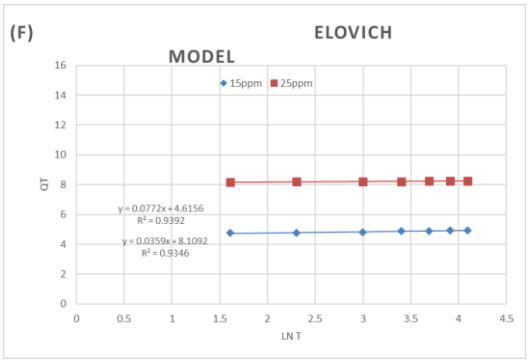

Figure 6: Adsorption kinetics of Congo Red onto Fe_3O_4@Mg/Al-LDH@CS nanocomposite at 25 °C: (A) effect of contact time; (B) pseudo-first-order model; (C) pseudo-second-order model; (D) Avrami model; (E) intraparticle diffusion model; (F) Elovich model, demonstrating chemisorption-dominated adsorption behavior.

Figure 6E presents the intraparticle diffusion plots based on the Weber–Morris model, obtained by plotting Q_tagainst t^(1/2)for Congo Red solutions at initial concentrations of 15 ppm and 25 ppm. In both cases, the plots deviate from the origin, indicating that intraparticle diffusion is not the sole rate-limiting step governing the adsorption process. The observed multilinear profiles suggest the occurrence of multiple sequential stages, initially dominated by boundary-layer diffusion, followed by a slower intraparticle diffusion phase within the porous structure of the adsorbent. Moreover, the higher intercept values observed for the 25 ppm system imply an increased contribution of surface diffusion at elevated dye concentrations, whereas the 15

ppm system exhibits comparatively lower diffusion resistance. These findings collectively demonstrate that, although intraparticle diffusion plays a significant role, it does not exclusively control the adsorption kinetics. Figure 6F depicts the adsorption kinetics analyzed using the Elovich model for Congo Red uptake onto the synthesized nanocomposite. The linear relationship between q_tand ln$f_0$tindicates a good fit to the Elovich equation, suggesting that the adsorption occurs on a heterogeneous surface. This behavior reflects a complex adsorption mechanism in which the adsorption rate progressively decreases with increasing surface coverage due to the gradual occupation of active sites (Jomardani et al., 2026). The applicability of the Elovich model further supports the presence of strong interactions between Congo Red molecules and the functional groups of the adsorbent, consistent with a chemisorption-dominated mechanism.

Table 1. Equations of kinetic models and their parameters for the adsorptive removal of Magnetite–LDH–Chitosan.

Kinetic Model	**Equation**	**Plot**	**Kinetic Parameter**	**RRD 15 ppm**	**RRD 25 ppm**
Pseudo-First Order	$Ln\,(q_e - q_t) = Ln\,(q_e) - k_1 t$	$ln\,(q_e - q_t)$ versus time (t), q_e and q_t are the sorption capacity at equilibrium and at time t (min), respectively, k_1 is the first order rate constant	q_e (mg/g) (calc)	4.997667	8.331
			K_1 (min^{-1})	0.0246	0.0158
			R^2	0.9361	0.9701
Pseudo-Second Order	$t/q_t = 1/k_2 q_e^2 + t/q_e$	t/q_t versus time (t), K_2 is the second order rate constant	q_e (mg/g) (exp)	4.92	8.2533333
			q_e (mg/g) (calc)	4.9554014	8.2712986
			K_2 (g/mg min)	0.102364036	0.382394
			R^2	1	1
Intra-particle Diffusion	$q_t = k_{id}\, t^{0.5} + C$	q_t versus ($t^{0.5}$), C is the thickness of the adsorption layer, K_{id} is the intra-particle order rate constant	K_{id} (mg/g $min^{0.5}$)	0.0346	0.0164
			C	4.6782	8.1368
			R^2	0.9442	0.9724
Elovich	$q_t = 1/\beta\, Ln(\alpha\beta) + 1/\beta\, Ln\,(t)$	q_t versus ln t, α is the initial adsorption rate, β is related to the extent of surface coverage and the activation energy for the chemisorption process	α (mg/g min)	7.129	4.517
			β (mg/g)	12.95337	27.85515
			R^2	0.9392	0.9346

3.4. Effect of Initial Dye Concentration and Adsorption Isotherms

The influence of initial Congo Red concentration on removal efficiency (R%) using the synthesized Magnetite–LDH–Chitosan nanocomposite is presented in Figure 7A, while the parameters of adsorption isotherm models at 15 and 25 ppm are summarized in Table 2. The nanocomposite exhibited consistently high removal efficiency (99.0–99.9%) over a wide concentration range (3–100 ppm). At lower concentrations (3–10 ppm), the gradual increase in R% indicates the abundance of available active sites. As the dye concentration increased (20–50 ppm), removal efficiency improved due to enhanced mass transfer driving force. At higher concentrations (75–100 ppm), the efficiency stabilized with minor fluctuations, demonstrating the strong adsorption capacity of the material. This performance is attributed to the presence of layered double hydroxide and chitosan, which provide abundant functional groups and interlayer spaces for dye uptake (Asif et al., 2026).

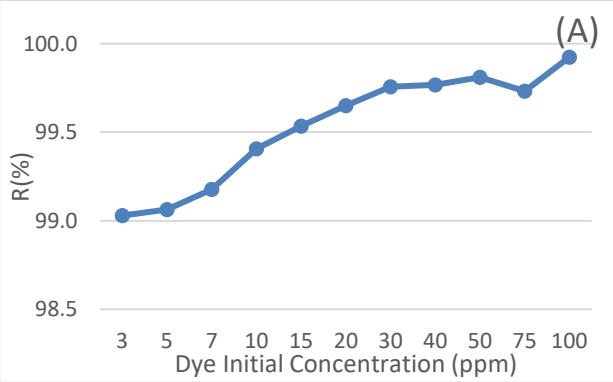

These findings confirm the suitability of the nanocomposite for treating high-strength dye wastewater. The Langmuir isotherm (Figure 7B) showed a good linear fit (R^2 = 0.9024), indicating monolayer adsorption on a homogeneous surface with uniform adsorption sites and minimal interaction between adsorbed molecules.

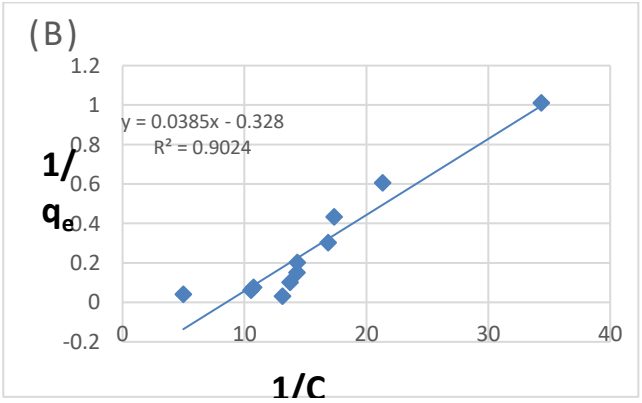

In contrast, the Freundlich isotherm (Figure 7C) exhibited a lower correlation coefficient (R^2 = 0.7014), suggesting poor agreement with heterogeneous multilayer adsorption behavior. This further supports that the adsorption process is predominantly monolayer and homogeneous in nature.

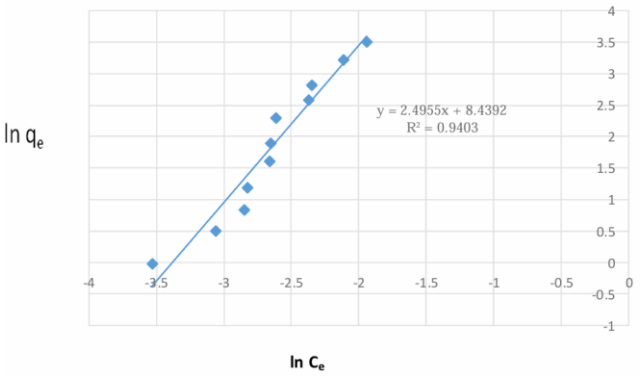

The Dubinin–Radushkevich (D–R) isotherm (Figure 7D) demonstrated a moderate fit (R^2 = 0.7872). The low slope value corresponds to adsorption energy below 8 kJ/mol, indicating that the process is mainly governed by physisorption mechanisms such as electrostatic interactions, pore filling, and surface diffusion.

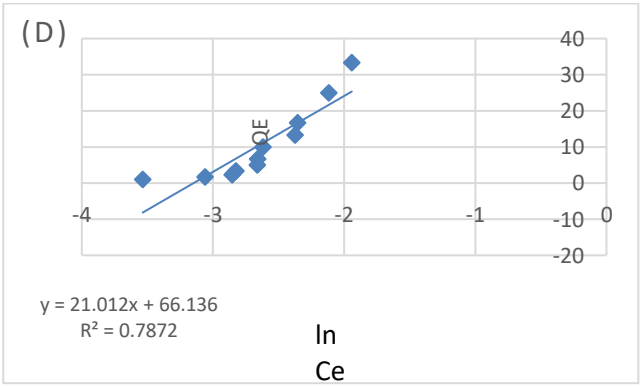

The Temkin isotherm (Figure 7E) showed a relatively strong fit (R^2 = 0.9163), suggesting that adsorption is influenced by adsorbent–adsorbate interactions. The positive slope indicates a gradual decrease in adsorption heat with increasing surface coverage, reflecting the presence of heterogeneous binding sites. Overall, the adsorption of Congo Red onto the Magnetite–LDH–Chitosan nanocomposite is best described by the Langmuir and Temkin models, confirming predominantly monolayer adsorption with contributions from physical interactions. These results highlight the high efficiency and practical applicability of the synthesized nanocomposite for wastewater treatment.

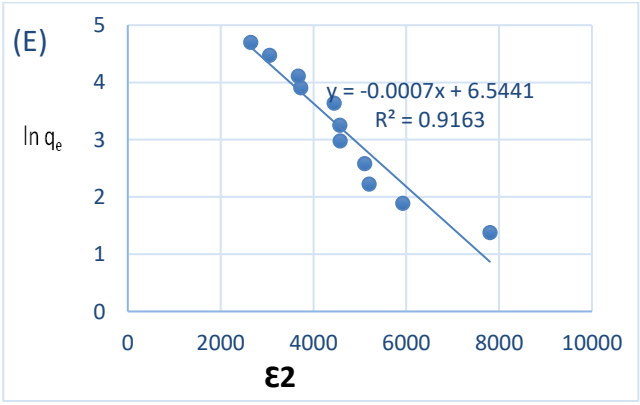

Figure 7: Adsorption isotherms of Congo Red onto Fe_3O_4@Mg/Al-LDH@CS nanocomposite at 25 °C: (A) effect of initial dye concentration on removal efficiency; (B) Langmuir; (C) Freundlich; (D) Dubinin–Radushkevich; (E) Temkin isotherm models.

Table 2. Linear equations and their parameters for different adsorption isotherm models for the 15 ppm and 25 ppm adsorptive removal by the nanocomposite

Isotherm Model	**Linear Equation**	**Linear Plot**	**Isotherm Parameter**	**RRD**
langmuir	$C_e/q_e = 1/q_{max}K_L + C_e/q_{max}$	$1/q_e$ versus $1/C_e$, slope = $1/q_m$, and intercept = $1/(K_L q_{max})$; K_L is the Langmiur constant, q_{max} is the maximum adsorption capacity, $R_L = \frac{1}{1+K_L C_o}$, C_o is the initial concentration of U(IV) ions in mg/L	q_{max} (mg/g)	-3.048333312
			K_L(L/mg)	-8.510635057
			R_L	(-0.04076_-0.00118)
			R^2	0.9024
Freundlich	$\ln(q_e) = \ln(K_F) + 1/n \ln(C_e)$	Ln q_e versus ln C_e, slope = 1/n, and intercept = ln K_F; K_F is the Freunlish constant related to the affinity of the	N	1.42525
			K_F (L/mg)	7.411997714
			R^2	0.7014

		adsorbate to the binding sites of the adsorbent, n is the intensity of the adsorbent		
T e m k i n	$q_e=(RT/b_T)$ ln $(a_T)+(RT/b_T)$ ln (c_e)	q_e versus ln C_e, slope = B = RT/b_T, and intercept = Bln a_T; a_T is Temkin isotherm equilibrium binding constant corresponding to the maximum binding energy, b_T is the Temkin isotherm equilibrium binding constant related to the heat of adsorption and/or the adsorption bonding energy, R is the gas constant = 8.314×10^{-3} kJ mol^{-1} K^{-1}, T is the absolute temperature in K	a_T (L/mg)	23.27861
			b_T(KJ/mol)	0.115933847
			B	21.012
			R^2	0.7872
Dubinin Radushkevich (D–R)	$\ln(q_e)=\ln(q_s)-(K_{ad}\varepsilon^2)$	Ln q_e versus ε^2, slope = K_{ad}, and intercept = Ln (q_s); ε is the *polanyi* potential (ε = RT ln $(1+(1/C_e))$, q_s is the theoretical saturation capacity, K_{ad} is the D-R isotherm constant, $E_s=\frac{1}{\sqrt{2K_{ad}}}$	q_{max} (mg/g)	695.1307796
			K_{ad} (mol^2/J^2)	7.633656584
			E_s(KJ/mol)	0.25599
			R^2	0.9163

3.5. Effect of Adsorbent Dosage and Temperature: Thermodynamic Analysis

The thermodynamic parameters for the adsorption of Congo Red (15 and 25 ppm) onto the magnetite–LDH–chitosan nanocomposite at different temperatures are summarized in Table 3. Figure 8A shows the influence of adsorbent dosage on dye removal efficiency. Increasing the sorbent mass significantly improves removal efficiency due to the greater availability of active adsorption sites. For the 15 ppm solution, a slight fluctuation is observed at low dosages (5–10 mg), likely due to incomplete dispersion or limited interaction. However, efficiency increases sharply beyond 20 mg, reaching a maximum of 99.4% at 40 mg. For the 25 ppm solution, removal efficiency rises rapidly between 5 and 20 mg and stabilizes at approximately 98% at higher dosages, indicating the attainment of adsorption equilibrium. This plateau suggests that most dye molecules are effectively adsorbed, and further increases in dosage do not significantly enhance performance. Overall, the results confirm that adsorption efficiency is dosage-dependent until equilibrium is reached. Figure 8B presents the Van't Hoff plots (ln Kd versus 1/T), which exhibit linear relationships with negative slopes for both concentrations. This behavior indicates that the adsorption process is endothermic. The increase in Kd values with temperature further confirms enhanced adsorption at higher temperatures. The positive values of ΔH° and ΔS°, derived from the slope and intercept, indicate that the process is both endothermic and entropy-driven. The high correlation coefficients (R^2) demonstrate good agreement with the Van't Hoff model. Figure 8C illustrates the effect of temperature (293–328 K) on removal efficiency. For the 15 ppm system, efficiency increases from 96.62% to 99.79%, indicating that adsorption is highly favorable and that the adsorbent surface remains unsaturated. For the 25 ppm system, efficiency also improves slightly with temperature, suggesting enhanced diffusion and interaction between dye molecules and active sites. The positive effect of temperature can be attributed to increased molecular mobility, reduced boundary-layer resistance, improved intraparticle diffusion, and enhanced accessibility of functional groups, particularly due to chitosan swelling. These factors collectively facilitate faster adsorption and improved dye–adsorbent interactions (Hublikar et al., 2026). Thermodynamically, the process follows the Van't Hoff relationship:

$$\Delta G^\circ = \Delta H^\circ - T\Delta S^\circ$$

$$\Delta G^\circ = -RT\ln K_d$$

$$\ln K_d = (\Delta S^\circ)/R - (\Delta H^\circ)/RT, K_d = q_e/C_e$$

Overall, the adsorption of Congo Red onto the magnetite–LDH–chitosan nanocomposite is efficient, temperature-dependent, and governed by endothermic and entropy-driven mechanisms, highlighting its suitability for wastewater treatment applications.

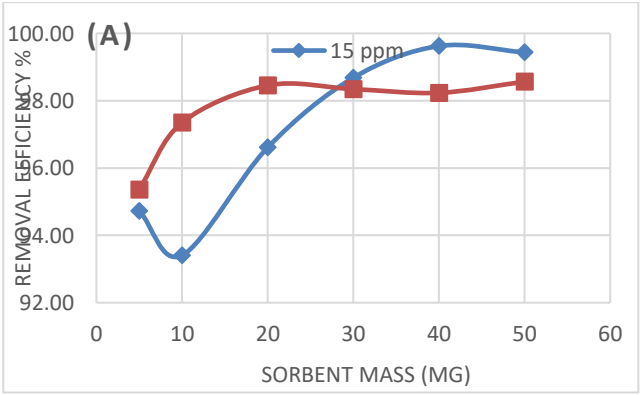

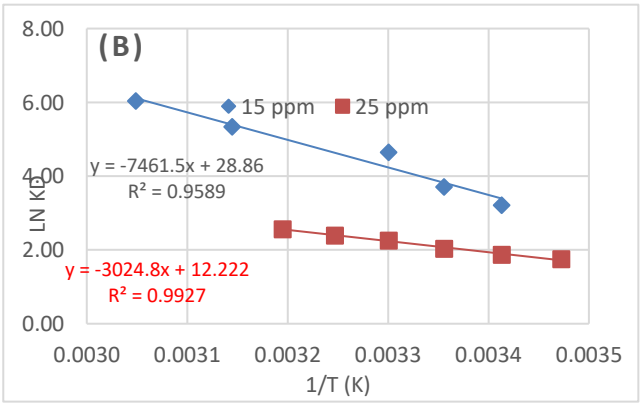

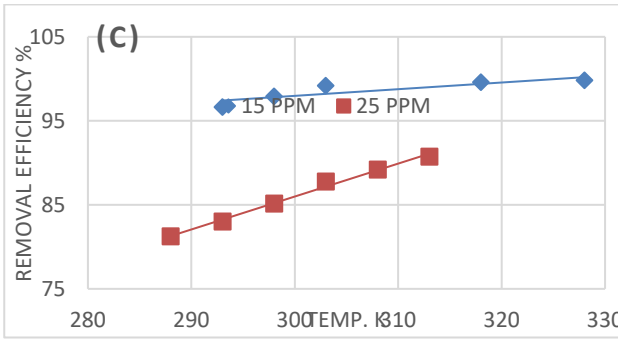

Figure 8: (A) Effect of adsorbent dosage on Congo Red removal efficiency; (B) Van't Hoff plot (ln Kd vs 1/T); (C) effect of temperature (293–328 K) on adsorption performance, indicating an endothermic process.

Table 3. Standard thermodynamic parameters for the adsorption of 15 ppm and 25 ppm onto the Nanocomposite at different reaction temperatures

Dye initial concentration (ppm)	**Temperature (K)**	**LnK$_d$ (L/g)**	**Adsorption Thermodynaic Paramters**			**R^2**
			-ΔG^o (KJmol^{-1})	**ΔH^o (KJmol^{-1})**	**ΔS^o (Jmol^{-1}K^{-1})**	
15 ppm	**293**	2.26	5494.81	-0.23075507	635.27247	0.725
	298	2.73	6763.77			
	308	3.64	9172.66			
	318	4.42	11682.16			
	328	5.11	13945.44			
25 ppm	**293**	2.27	-5526.52	-44.68775	189.93333	0.9927
	298	2.55	-6321.18			
	308	3.72	-9375.41			
	318	4.13	-10918.63			
	328	4.42	-12050.14			

3.6. Regeneration and Reusability of the Magnetite–LDH–Chitosan Nanocomposite

The reusability of the Magnetite–LDH–Chitosan (MLC) nanocomposite was assessed over five consecutive adsorption–desorption cycles using Congo Red as a model dye. After each cycle, the adsorbent was magnetically recovered, washed, dried, and reused. A gradual decrease in adsorbent mass was observed, from 100 mg in the first cycle to 40 mg after the fifth cycle, indicating minor material loss during handling and separation (Figure 9). Despite this reduction, the MLC nanocomposite maintained high removal efficiency, with dye absorbance decreasing from 0.428 to 0.049–0.000 across cycles, corresponding to 88.55–100% removal. The slight decline in performance may be attributed to incomplete desorption, partial blockage of active sites, or minor particle loss (Mavvaji et al., 2026). Overall, the results demonstrate that the MLC nanocomposite exhibits good regeneration capability and structural stability, highlighting its potential for repeated use in sustainable dye removal applications.

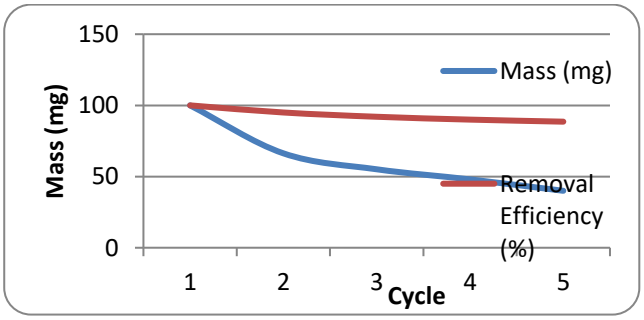

Figure 9: Regeneration and reusability of Fe_3O_4@Mg/Al-LDH@CS nanocomposite over five adsorption–desorption cycles for Congo Red removal.

3.7. Application of MLC for Congo Red Removal from Real Water Samples

The practical performance of the magnetite–LDH–chitosan (MLC) adsorbent was evaluated using three real water matrices, namely tap water (Kobani), industrial wastewater, and seawater (Latakia coast), which differ in ionic strength, turbidity, and organic load. In tap water, MLC exhibited excellent removal efficiency, achieving up to 99.6% at initial dye concentrations of 15 and 25 ppm, indicating strong adsorbent–dye interactions in low-complexity systems (Figure 10). For industrial wastewater, relatively lower efficiencies were observed due to matrix complexity (Yazdizadeh et al., 2025). However, removal improved over successive cycles, reaching 85.09% (15 ppm) and 83.54% (25 ppm), demonstrating good performance in the presence of competing ions and suspended matter.

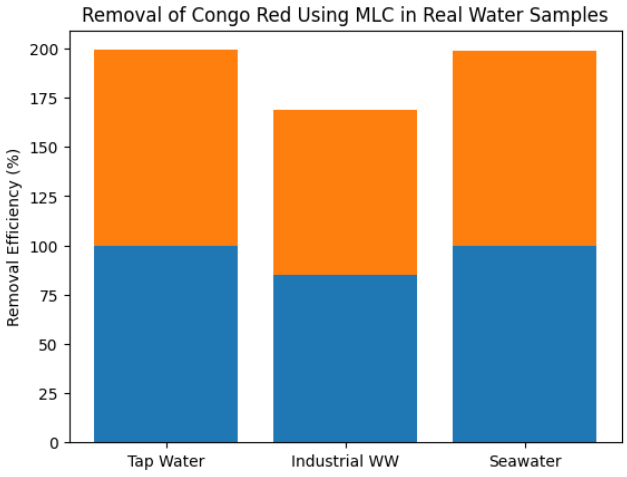

Figure 10: Removal efficiency of Congo Red using Magnetite–LDH–Chitosan (MLC) adsorbent in real water samples (tap water, industrial wastewater, and seawater) at initial dye concentrations of 15 ppm and 25 ppm. The adsorbent shows consistently high performance in low- and high-salinity environments, with slightly reduced efficiency in industrial wastewater due to competing ions and suspended matter.

In seawater, MLC maintained outstanding efficiency (99–100%) across all tested concentrations and cycles, despite high salinity and chloride ion competition, confirming its structural stability and effectiveness under saline conditions. Overall, MLC showed high adsorption efficiency, reusability, and resistance to ionic interference, highlighting its strong potential for practical wastewater treatment applications.

4. Conclusions

This study demonstrates the successful development of a multifunctional Fe_3O_4@LDH@Chitosan nanocomposite for the efficient removal of Congo Red dye from aqueous systems. The integration of magnetite, layered

double hydroxide, and chitosan resulted in a structurally stable material with enhanced adsorption capacity, magnetic separability, and reusability. The microwave-assisted synthesis method provided a rapid and energy-efficient route for producing the composite, aligning with the principles of sustainable material design. Characterization results confirmed the successful formation of the hybrid structure, with strong interactions between its components contributing to improved performance. Adsorption experiments revealed that the nanocomposite achieves high removal efficiencies across a wide range of operating conditions, including variations in pH, temperature, and dye concentration. Kinetic and isotherm analyses indicated that the adsorption process is governed by a combination of chemisorption and physisorption mechanisms, with monolayer adsorption predominating. Thermodynamic evaluation confirmed that the process is spontaneous and endothermic, with improved performance at higher temperatures. The material also demonstrated excellent regeneration capability, maintaining high efficiency over multiple cycles, which is essential for cost-effective wastewater treatment. Importantly, the nanocomposite exhibited strong performance in real water matrices, including seawater and industrial wastewater, highlighting its robustness under complex environmental conditions. This practical applicability distinguishes the material from many laboratory-scale adsorbents that fail under realistic scenarios. Overall, the Fe_3O_4@LDH@Chitosan nanocomposite represents a promising candidate for advanced wastewater treatment applications. Its combination of high efficiency, reusability, and operational simplicity makes it well-suited for scalable implementation in environmental remediation systems. Future work should focus on pilot-scale validation, long-term stability assessment, and evaluation against a broader range of contaminants to further support its practical deployment.

Acknowledgment

The authors would like to express their sincere gratitude to Rojava University and Institute of science and technology for providing access to the laboratory facilities and resources essential for conducting this research.

Authors' contribution

This paper is extracted from a Master thesis, for which Haidar Saify, Mohamed E.Mahmoud and Rehab M .El-Sharkawy were Supervisors of the project, chief investigators, and responsible for the data analysis. Methodology and first draft of the manuscript were done by Jwan Sheikh Mohammad.

Availability of data and material

All required data is in the article, and more details can be request from corresponding author.

Funding

We confirm that this work did not receive any grant from funding agencies in the commercial, public sectors.

Declarations

Conflict of interest

The authors declare that they have no known competing interests.

Reference

1. Arrisujaya, Dian, Yoki Yulizar, and Asep Saefumillah. "Accelerated water purification with magnetite (Iron (II, III) Oxide) nanoparticles: Coagulation applications." J. Chem. Rev 7, no. 1 (2025): 25-62.
2. Asif, Kinza, Muhammad Imran, Anum Shahzadi, Farzana Jamal, Sarmad Frogh Arshad, Anwar Ul-Hamid, Ahmed M. Fouda, and Muhammad Ikram. "Graphene oxide/chitosan-layered double hydroxides for dye decolorization, oxygen evolution reaction and bactericidal inactivation." Materials Science in Semiconductor Processing 201 (2026): 110030.
3. Chaimaa, Amairi, Meriem Bendjelloul, Fatima Zahra Benhachem, El Hadj Elandaloussi, Abdelkader Miraoui, Ahmed Djafri, Ahmed Boucherdoud, Abdelkarim Seghier, and Mohammed Hachemaoui. "Adsorption kinetics and surface interactions of organic dyes and copper ions on a novel biosorbent: raw artichoke hay." Reaction Kinetics, Mechanisms and Catalysis (2026): 1-26.
4. Cui, Lijuan, Xiaokun Shi, Chao Xu, and Shuping Wu. "Recent advances in chitosan-based mixed matrix membranes for efficient wastewater treatment." International Journal of Biological Macromolecules (2026): 150628.
5. Hublikar, Leena V., K. S. Nivedhitha, Bipin S. Chikkatti, Ashok M. Sajjan, Nagaraj R. Banapurmath, D. Palaniswamy, T. Beena, Pradeep Hegde, Sabin Kumar Mishra, and Kartheek Ravulapati. "Functionalized biochar–metal oxide nanocomposites for the catalytic degradation of recalcitrant pollutants in wastewater treatment." RSC advances 16, no. 14 (2026): 12186-12214.
6. Jomardani, Fereshteh, Reza Shakeri, Raziyeh Akbarzadeh, and Syamak Nasiri Kokhdan. "Adsorption kinetics and isotherms of malachite green removal from aqueous solution using TiO2 loaded on f-MWCNTs nanocomposite." Scientific Reports (2026).
7. Kan, Lili, Luohao Lv, Hongran Chen, Bo Wen, Xiangwei Ma, and Fei Wang. "High-temperature resistance of engineered geopolymer composite: Isolating the effects of key components." Construction and Building Materials 481 (2025): 141664.
8. Khan, Rana Rashad Mahmood, Hoorish Qamar, Ayesha Hameed, Aqmar ur Rehman, Muhammad Pervaiz, Zohaib Saeed, Aqib Adnan, and Ayoub Rashid Ch. "Biological and photocatalytic degradation of Congo red, a diazo sulfonated substituted dye: a review." Water, Air, & Soil Pollution 233, no. 11 (2022): 468.
9. Lin, Jiuyang, Wenyuan Ye, Ming Xie, Dong Han Seo, Jianquan Luo, Yinhua Wan, and Bart Van der Bruggen. "Environmental impacts and remediation of dye-containing wastewater." Nature Reviews Earth & Environment 4, no. 11 (2023): 785-803.
10. Mavvaji, Mohammad, Ahmed M. Senan, and Senem Akkoc. "Magnetic layered double hydroxide nanocomposites: synthesis, catalytic performances, environmental and biological applications." Energy & Environmental Materials 8, no. 5 (2025): e70015.
11. Mystrioti, Christiana, Nymphodora Papassiopi, and Anthimos Xenidis. "Synthesis of Iron Nanomaterials for Environmental Applications from Hydrometallurgical Liquors." Minerals 12, no. 5 (2022): 556.
12. Oguanobi, Nonso C., Chukwunonso O. Aniagor, George Okoronkwo, Calistus N. Ude, Chijioke E. Onu, and Ephrem N. Anike. "Industrial dye effluent sources, generation, and value-added products." In Engineered Biocomposites for Dye Adsorption, pp. 1-10. Elsevier, 2025.
13. Tundwal, Aarti, Harish Kumar, Priti Yadav, Varsha Yadav, and Bindu Mangla. "Chitosan, conducting polymer, and metal oxide nanocomposites: Mechanistic insights and sustainable approaches for water treatment." Next Materials 10 (2026): 101559.
14. Wang, Kun, Chaoqun Zhu, Yinghua Li, Xin Guo, Mingchuan Zhang, and Xi Chen. "Approaches for effective layered double hydroxides for advanced oxidative degradation of emerging pollutants

harnessing natural solar light." Chemical Engineering Research and Design (2026).

15. Xiao, Wuyang, Fuhe Le, Rui Sheng, Xue Yang, Xueying Cao, and Wei Jia. "Constructing Dual Active Sites via Cu Doping in Perovskite for Boosting Electrochemical Hydrogen Evolution." ChemCatChem 18, no. 3 (2026): e01581.
16. Yazdizadeh, Shirin, S. Yousef Ebrahimipour, S. Jamilaldin Fatemi, Moj Khaleghi, and Samaneh Ramezanpour. "Mesoporous Fe3O4@ SiO2@ La nanocomposite for efficient methylene blue removal from wastewater." Journal of Molecular Structure 1322 (2025): 140337.
17. Younas, Fazila, Adnan Mustafa, Zia Ur Rahman Farooqi, Xiukang Wang, Sadia Younas, Waqas Mohy-Ud-Din, Muhammad Ashir Hameed et al. "Current and emerging adsorbent technologies for wastewater treatment: Trends, limitations, and environmental implications." Water 13, no. 2 (2021): 215.
18. Zazouli, Mohammad Ali, Zabihollah Yousefi, Esmaeil Babanezhad, and Alireza Ala. "Evaluation of combined efficiency of conventional coagulation-flocculation process with advanced oxidation process (sulfate-hydroxyl radical) in leachate treatment." Environmental Engineering Research 29, no. 3 (2024).
19. Zhang, Zekai, Xiaoyu Liu, Jinping Zhao, Jin Zhou, Zhuang Liu, and Liang-Yin Chu. "Layered double hydroxide separation membranes: advances and prospects in water purification applications." Green Chemical Engineering (2026).

Rojava Journal of Science and Technology

2026, VOL. 3, No 1, [121-136]

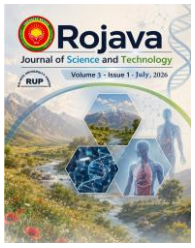

Solving the Traveling Salesman Problem using an improved ant colony algorithm based on the nearest neighbor algorithm

Mohammed Salim Hassan[a], Yasmine Abouelseoud*[b] and Ahmed F. Tayel[b]

[a] Department of Mathematics, Institute of Science and Modern Technology, University of Rojava, Syria

[b] Department of Engineering Mathematics and Physics, Faculty of Engineering, Alexandria University, Egypt

Abstract

In this paper, we address the Traveling Salesman Problem (TSP), which is an NP-hard problem. Many meta-methods have been applied to solve such a problem in the literature. In this work, the Ant Colony Optimization (ACO) algorithm is applied to TSP, which is one of the population-based competitive algorithms used to solve many generative optimization problems in various engineering fields. By optimizing its problem-dependent parameters setting, the overall performance of the Ant Colony algorithm is improved, and the execution time is reduced. We have found through experiments that the performance of the ACO algorithm needs to be enhanced. Therefore, we have developed a new algorithm (NN-ACO) by hybridizing the ACO algorithm with the nearest neighbor algorithm, which is a greedy algorithm that finds the candidate solution to the TSP using simple approximate heuristics. The results of the ACO algorithm and the hybrid ACO algorithm are compared together in terms of solution quality and execution time. Moreover, the result based on the linear programming formulation of the test problem is used to evaluate the quality of the solutions obtained using the applied meta-heuristic methods. In addition, the algorithm is applied to a benchmark set of TSP problems and its performance is compared with some other hybrid algorithms in the literature. The experimental results show that the proposed algorithm outperforms other hybrid algorithms in terms of solution quality.

ARTICLE HISTORY

Received 12 Jan. 2026

Revised 3 Jun. 2026

Accepted 4 Sep. 2026

Keywords

Ant Colony Optimization (ACO), Parameters Tuning, Linear Programming (LP), Nearest Neighbor (NN) algorithm, Route Optimization, Traveling Salesman Problem (TSP).

*Corresponding Corresponding Author yasmine.abouelseoud@alexu.edu.eg,

1. Introduction

The Traveling Salesman Problem (TSP) is an NP-hard problem, which means that there is no known polynomial-time solution technique that can provide an exact solution to a given problem instance. TSP can be envisioned as an abstraction of problems encountered in the fields of logistics, computer science, controlling industrial robots, drilling holes in electrical circuits, etc. It aims to achieve a trip to all cities - visiting each only once - before returning to the city from which it started with the least cost. The cost can be the minimum distance, or the minimum travel time, or any other cost function dependent on the problem context. A solution of the TSP is simply a permutation of the cities. So, the number of possible solutions to a TSP instance is **n!**, where n is the number of cities. When n is large, it is difficult to find the minimum cost solution in polynomial time. Therefore, we resort to other methods to find approximate solutions to such problems that give near optimal solutions. These approximate techniques are either based on Problem-based heuristics such as the nearest neighbor algorithm [1-2] or nature-inspired heuristics that serve as general frameworks to guide the search procedure in the solution space. Examples of the latter class of algorithms include genetic algorithm (GA) [3-6], ant colony algorithm (ACO) [7-9], neural networks [10-11], and Artificial Bee Colony (ABC) algorithm [12]. Moreover, other solution techniques have been invented, such as combining two algorithms which are referred to as hybrid algorithms in order to find effective solutions to problems that are difficult to solve using traditional methods. For example, in [13], the authors proposed hybridization of the genetic algorithm, the simulated annealing algorithm, and ant colony optimization scheme as well as particle swarm optimization technique. According to the conducted study using this hybrid algorithm, experimental results obtained for the TSPLIB (a library for TSP test instances) showed that both the mean solution and the deviation ratio of the mean solution are improved compared to other methods in literature. The use of self-organizing maps to solve TSP has been considered by several researchers [14-15]. Masotti and de Castro considered enhancing self-organizing maps performance for solving TSP based on ideas from the immune system [16], extending the work in [17]. Durbin and Willshaw proposed a solution to TSP based on elastic net involving time-dependent parameters that aid in moving neurons more rapidly towards cities positions and attracting neurons to their neighbors on the path in order to minimize the total path length [18].

Dong et al. in [19] presented a Cooperative Genetic Ant System (CGAS) for solving TSPs. In order to improve the performance of the basic ACO algorithm, a genetic algorithm (GA) is combined with it to obtain good solutions within an acceptable time period. According to the study, it was found that CGAS has superior performance over both GA and ACO algorithms in solving TSP in terms of its ability to find the global optimal solution. Yannis Marinakis and Magdalene Marinakis in [20] presented a hybrid algorithm that combines a genetic algorithm and particle swarm optimization to solve another related combinatorial optimization problem, which is the vehicle routing problem. There was an improvement in the exploration capabilities of their hybrid algorithm, thus, yielding better solutions to the problem instances considered in their study. In [21], a hybrid algorithm to solve the TSP problem that combines deer hunting optimization algorithm (DHOA) and earthworm algorithm (EWA) has been presented. The proposed (EW-DHOA) algorithm aims to find the optimal solution of large-scale problems. Experimental results showed that the convergence of the proposed hybrid optimization was better in finding optimal solutions compared to the performance of both DHOA and EWA, when applied separately. The authors in [22] presented a modification of the artificial bee colony algorithm. Using multiple update rules and the K-opt process, the algorithm generally revives stagnant solutions. The 3-opt process is used to optimize any stagnant solution obtained in the sequel. All experimental results indicated that the performance of the proposed approach is superior compared to other existing methods in the literature in terms of accuracy, efficiency and consistency.

The authors in [23] introduced a particle swarm optimization (PSO) algorithm to improve the performance of the ACO algorithm and called their new hybrid optimization algorithm (HPSACO), which

was used to solve the TSP problem. The HPSACO algorithm takes advantage of the exploratory ability of the PSO algorithm and the stochastic ability of the ACO algorithm. The experimental results showed that their proposed HPSACO algorithm can obtain the best solution quality and better stability compared to the other researches included in their study. In [24], a hybrid algorithm to solve the traveling salesman problem, that combines a heuristic algorithm and a repetitive nearest neighbor (RNN) mechanism, was presented. The proposed algorithm consists of two main stages. In the first stage, the RNN algorithm is used to build a set of possible paths step by step. In the second stage, it improves these paths in an iterative optimization process based on the simulated annealing (SA) algorithm. Experimental results obtained for TSP instances taken from the TSPLIB library showed that the proposed algorithm (RNN-SA) is more effective than both RNN and SA. The authors in [25] proposed a neural network to dynamically adapt the two parameters of the ACO algorithm (α and β). Determining the best combination of ACO parameters has a critical impact on the performance of the algorithm. The authors in [26] proposed an evolutionary hybrid approach, combining the ant colony algorithm and attention-based neural networks (ACO-RNN), to address the traveling salesman problem. Results on TSP instances from the TSPLIB [27] library showed that the hybrid approach outperformed the classical ACO algorithm.

In our research, linear programming is used to obtain the exact optimal solution to moderate size TSP problems [28–29]. This is important in evaluating the performance of the studied approximate algorithms for solving the traveling salesman problem. Our study focuses on meta-heuristic algorithms for the traveling salesman problem, with a particular emphasis on the ant colony optimization (ACO) algorithm. The ACO algorithm is inspired from the natural searching behavior of ants, where pheromones play a crucial role in guiding other ants along short paths, a concept discussed in detail in Section 3. The above review of the literature suggests that hybrid algorithms tend to provide superior solutions. Therefore, we designed a hybrid algorithm (NN-ACO) that combines the ACO algorithm and the nearest neighbor (NN) algorithm to achieve efficient solutions within an acceptable time frame. The effectiveness of this hybrid approach is demonstrated by the results presented in Section 5. The ACO algorithm has been extensively analyzed and its parameters have been carefully tuned in order to improve its performance and adapt it to solve the TSP problem with different number of cities. Our research highlights the potential of ACO algorithm to solve the travelling problem, which in turn plays an important role in several practical planning problems. These practical problems include logistic planning, road planning, printed circuit board wiring [30] and urban design. Moreover, the efficiency of public transportation can be improved reducing congestion and pollution based on modelling the planning problem as a TSP.

The contributions of this research can be summarized as follows:

1- Tuning the parameter settings of the ACO algorithm, which depend on the specific problem instance to be solved.
2- Building a new hybrid algorithm (NN-ACO) that effectively combines the greedy nearest neighbor algorithm and the ACO algorithm.
3- Reaching near optimal solutions within a small number of iterations and thus reducing the computational time.

4- Comparing the results of the ACO and NN algorithms with the hybrid NN-ACO algorithm, in addition to comparing the NN-ACO algorithm with another recent hybrid algorithm.

The rest of the paper is organized as follows. Section 2 provides a description of the travelling salesman problem. Section 3 describes the algorithms used in this work, namely linear programming, nearest neighbor algorithm, and ACO algorithm. Section 4 introduces the proposed hybrid algorithm. The fifth section presents the experimental results supported by tables and graphs. Section 6 presents the concluding remarks.

2. Problem description

TSP is an NP-hard problem that can be described as follows. Given n cities and d_{ij} is the distance between cities i and j, the goal is to determine the shortest tour of the group of n cities so that it passes

by each city once and returns to the starting city. An instance of a TSP problem can be described as a weighted graph $G(V, E)$, where V represents the set of nodes (cities), and E represents the set of edges (paths between cities). It is weighted according to the distances between cities d_{ij}. For the ACO algorithm, the ants will move randomly through the graph, i.e., each ant starts its tour from a certain city, let it be i, to the next city, j, until all the cities are visited once. To ensure that a city is not visited twice by each ant, a blocked list is kept for this purpose. Choosing the next city depends on a certain probability affected by the amount of pheromone, called the transition probability $p_{ij}(t)$. This depends on the distribution of pheromone τ and visibility η, which is inversely proportional to the distance, in order to attract ants towards the nearest cities. Pheromones are chemicals secreted by ants in order to attract other ants and direct them to a food source. The amount of pheromone depends on the pathways emanating from them. Thus, both visibility and pheromone distribution play a major role in directing the ACO algorithm in order to find effective solutions to the traveling salesman problem.

3. Description of algorithms used in this work

In this section, the linear programming formulation of the travelling salesman problem used is described first. Next, the nearest neighbor algorithm and the basic ACO algorithm that are implemented to solve TSP in our experiments are described.

3.1. Linear programming

Linear programming is an efficient and accurate method to solve the traveling salesman problem. It depends on representing the problem directly using binary variables (0 or 1) and applying appropriate linear constraints to ensure the feasibility of the obtained solution. The importance of this approach lies in its ability to yield exact solutions to TSP instances of moderately large sizes efficiently, making it a popular and preferred technique in many computational and engineering applications.

There are several integer programming formulations for the TSP problem. They differ in the number of decision variables and constraints. These formulations generally use natural (city-to-city) modeling variables and focus on explicit constraints intended to prevent subtours from automated solutions, known as "natural" or "subtour elimination" formulations. There are two prominent formulations: the Miller–Tucker–Zemlin formulation (MTZ) [31] and the Dantzig–Fulkerson–Johnson (DFJ) formulation [32-33].

In order to formulate the LP for the TSP problem, we consider a set of cities indexed as 1, . . ., n, and denote the distance between cities i and j by $\boldsymbol{c_{ij}}$. The decision variables of the problem are defined by the binary variables

$$x_{ij} = \begin{cases} 1 & optimal\ path\ includes\ the\ edge\ from\ city\ i\ to\ j\ city \\ 0 & otherwise \end{cases} \quad (1)$$

The goal of a linear program is to minimize the length of the complete tour.

$$\boldsymbol{D(x)} = \sum_{\boldsymbol{i=1}}^{\boldsymbol{n}} \sum_{\boldsymbol{i\neq j, j=1}}^{\boldsymbol{n}} \boldsymbol{c_{ij}\, x_{ij}} \quad (\mathbf{2})$$

The following set of constraints must be included in the formulation to ensure that each city has only one incoming edge and one outgoing edge:

$$\sum_{\boldsymbol{i=1, i\neq j}}^{\boldsymbol{n}} \boldsymbol{x_{ij}} = \mathbf{1} \ \ \forall \boldsymbol{j} \quad (\mathbf{3})$$

$$\sum_{\boldsymbol{j=1, i\neq j}}^{\boldsymbol{n}} \boldsymbol{x_{ij}} = \mathbf{1} \quad \forall \boldsymbol{i} \quad (\mathbf{4})$$

Equations (3) and (4) specify that each city must be visited and left exactly once. This formulation is invalid in the sense that the solution is not necessarily a complete tour as desired. Generally, the solution

consists of several sub-tours and must be completed. It is formulated such that subtours are prevented, and it is arguable that this universal requirement is what makes TSP a difficult problem. This can be done conventionally in two ways, proposed respectively by DFJ (Danzig, Fulkerson, & Johnson) and MTZ (Miller, Tucker, & Zemlin). In this research, the MTZ formula is adopted to solve the TSP problem. The number of constraints and variables are a polynomial function of the number of vertices (cities).

Miller–Tucker–Zemlin formulation This formulation excludes subtours. In addition to the variables x_{ij} as mentioned above, new variables u_i , where $i = 2, ..., n$, are used in the MTZ formulation, with n denoting the maximum number of nodes that can be visited by any salesman. The variable u_i keeps track of the order in which cities are visited. The interpretation of $u_i < u_j$ means that city i was visited before city j for a given tour.

Hence, the MTZ formulation of the TSP to exclude sub-tours adds the following set of constraints

$$u_i - u_j + 1 \leq (n-1)(1-x_{ij}) \quad 2 \leq i \neq j \leq n \qquad (5)$$

$$1 \leq u_i \leq n-1 \quad 2 \leq i \leq n \qquad (6)$$

The constraints in (5) ensure that if the salesman travels from i to j, then the position of node j is one more than that of node i. Together with the bounds in (6), they ensure that each non-depot (intermediate) node is in a unique position.

3.2. Nearest Neighbor

The nearest neighbor (NN) algorithm is a greedy algorithm used to solve TSP, which yields solutions that are close to the optimal solution. J. G. Skellam [34] introduced the first NN algorithm. Work on NN was continued by P.J. Clark and F.C. Evans [34]. A tour for the street vendor is created on the principle of choosing the move with the lowest remaining cost in the sequence. The vendor starts with a random city, visits the city closest to the current city, and adds it to the route. The process is repeated until all cities are visited, and upon completion, it returns to the starting city. The NN algorithm can be summarized as follows:

1) Randomly choose the starting city as the current city.

2) Search for the closest unvisited city to the current city, move to it, and assign it as the current city.

3) Repeat the process until all cities have been visited.

4) If all cities have been visited, return to the first city and complete the procedure.

5) Display the path and calculate the total length of the path.

Improvement to the NN Heuristic using 2-change heuristic

Once we have an initial tour using the NN algorithm, it is optimized using the "2-opt" algorithm. This algorithm performs exchanges between edges in the tour to reduce the total path length. These exchanges are done such that two pairs of edges are replaced with each other to optimize the path length. The edge with the largest cost or weight is chosen for replacement. Once the two exchanges are completed, the tour with the smallest length is chosen as the final solution to the TSP problem. This process is repeated several times (determined by the value of M) to increase the chances of finding the optimal or near-optimal solution.

In Figure 1, the total length of the initial tour is 30 units. The edges selection and replacement in the 2-opt exchange process are also shown in Figure 1. For example, v5-v4 with the largest edge weight 9 and v3-v2 with edge weight 5 are selected, and the modified tour after 2-opt exchange process with new edge weights is shown in Figure 2. They are replaced by v5-v2 with edge weight 3 and v4-v3 with edge weight 5, so the modified tour is v1-v3-v4-v6-v2-v5-v1; with a total tour length of 24, as shown in Figure 2. In our experiments, the impact of repeating the 2- opt exchange process on the obtained tour cost and computational time are demonstrated.

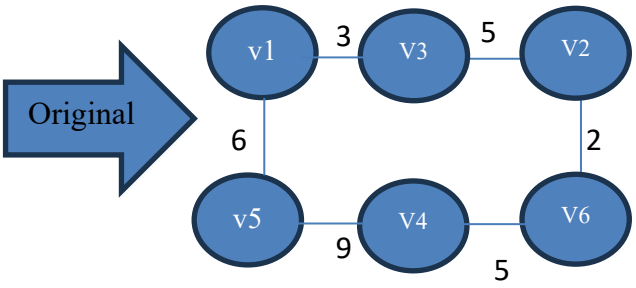

Figure 1: TSP network of 6 cities with their edge weights and original tour obtained using NN algorithm. Total tour weight: 24

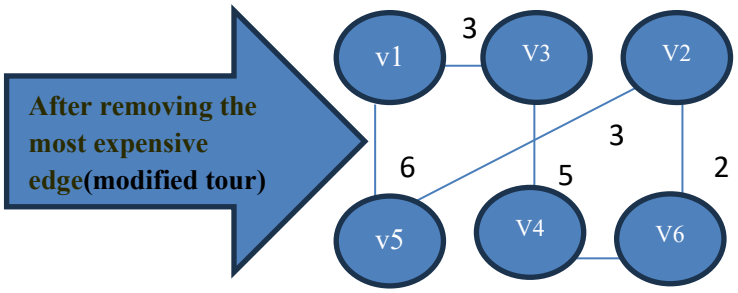

Figure 2: The 6-city TSP tour after exchanging a pair of its edges according to 2-opt exchange process.

3.3. Ant Colony Optimization

M. Dorige introduced Ant Colony Optimization (ACO) in 1991[35], which is a nature-inspired technique for solving difficult combinatorial problems represented as graphs. It is a population-based algorithm, where the population consists of a group of ants that by working together search for food sources and return to their nests. Pheromones (chemicals) secreted by ants and dissipated along the path visited in the graph play an important role in directing them to a food source. There are some important strategies, such as positive feedback, incorporated in ACO. The positive feedback strategy through use of pheromones helps ACO find better results because ants are attracted to paths that have an increase in pheromone concentration, and thus the pheromone distribution affects the discovery of areas that contain good solutions. However, the positive feedback technique alone is not sufficient and the algorithm may converge early, get stuck in local solutions, and stall without finding the optimal solution. To counter this effect, a negative feedback mechanism, namely evaporation, is also needed. Evaporation is an important feature of pheromones, which prevents excessive accumulation of pheromones on the edges in each cycle, avoiding getting trapped into local optimal solutions.

ACO is one of the most famous heuristic algorithms for solving the TSP problem, which is implemented by simulating ants on a graph. It starts with an initial amount of pheromones on each path between cities and this is followed by randomly distributing ants to different nodes. ACO involves two main steps after the initialization step. The first step is to construct solutions: each ant constructs its route based on a probability rule that depends on the current amount of pheromones and the distance between cities. The second step is to update the pheromones. When paths are built at iteration $\boldsymbol{t+1}$, each ant moves to a new node and the pheromones are updated. Shorter, more efficient paths receive larger amounts of pheromones. The pheromone is vaporized after ants complete their tours to prevent excessive accumulation and to explore other solution areas. When the ant decides to choose the next city, it does so with a probability that depends on the distance to that node and the intensity of the pheromone. The inverse of the distance to the next node is known as the visibility (visibility of city j from city i), and the visibility η_{ij} is defined as

$$\eta_{ij} = \frac{\mathbf{1}}{\boldsymbol{d_{ij}}} \quad (7)$$

where $\boldsymbol{d_{ij}}$ is the distance between nodes i and j.

3.2.1. Possibility of transfer

The probability of moving, $\boldsymbol{p_{ij}(t)}$, is the probability of choosing city j from city i at time t based on the pheromone distribution τ, visibility η, and permissible choices determined by previously visited nodes. $\boldsymbol{p_{ij}(t)}$ involves two parameters α and β. When α is large and β is small, the choice is more directed by pheromones, and in the opposite case, the choice is more directed by distance. The following formula is employed to

compute the probability of transition, where X is the set of unvisited cities for ant $\boldsymbol{k}$:

$$\boldsymbol{p_{ij}}(t) = \begin{cases} \frac{[\boldsymbol{\tau_{ij}}(t)]^{\propto} \cdot [\eta_{\boldsymbol{ij}}(t)]^{\beta}}{\sum_{k \epsilon X} [\boldsymbol{\tau_{ij}} t)]^{\propto} \cdot [\eta_{\boldsymbol{ij}}(t)]^{\beta}} & if \ \ k \in X \\ 0 & otherwise \end{cases} \quad (8)$$

α and β are two parameters that determine the relative influence of the pheromone and distance. With α = 0 and β = 1, you get a purely greedy algorithm, while if α = 1 and β = 0, you get a completely randomly controlled algorithm.

3.3.2 Pheromone trail update rule

First, ants are placed randomly at the $\boldsymbol{n}$ cities. Next, each ant $\boldsymbol{k}$ goes from city $\boldsymbol{i}$ to city $\boldsymbol{j}$ with the probability $\boldsymbol{p_{ij}}^{(k)}$, given by Eq. (8). Each ant completes its tour after $\boldsymbol{n}$ iterations. Moreover, each ant $\boldsymbol{k}$ leaves pheromone according to $\boldsymbol{Q}$ /$\boldsymbol{L_k}$, where $\boldsymbol{Q}$ is a constant and $\boldsymbol{L_k}$ is the length of its tour.
This way ants with shorter tours will leave more pheromone than ants with longer tours. Additionally, the pheromone evaporates with time as it will be indicated later by the evaporation factor $\boldsymbol{\rho}$.

$\boldsymbol{\tau_{ij}}(\boldsymbol{t})$ describes the pheromone density at time t on edge (i, j). The distribution of the pheromone is affected by the ants' previous path choices, and affects the future path choices. After each cycle of the algorithm, the pheromone density becomes:

$$\boldsymbol{\tau_{ij}}(\boldsymbol{t+1}) = \boldsymbol{\rho} * \boldsymbol{\tau_{ij}}(\boldsymbol{t}) + \boldsymbol{\Delta \tau_{ij}} \quad (9)$$

This formula applies to all edges of the graph with density $\boldsymbol{\rho}$ between zero and one.

$$\Delta\tau_{ij} = \sum_{k=1}^{m} \Delta\tau_{ij}^{k} \quad (10)$$

where m is the number of ants and $\Delta\tau_{ij}^{k}$ is the amount of pheromone deposited by ant k onto the edge from i to j at the current iteration. ρ is known as the evaporation coefficient.

$$\Delta\tau_{ij}^{k} = \begin{cases} \frac{Q}{L_k} & if \ ant \ \boldsymbol{k} \ used \ \ edge \ (i,j) \ in \ its \ tour \\ 0 & otherwise \end{cases} \quad (11)$$

Here, $\mathbf{Q}$ is a constant and $\boldsymbol{L_K}$is the length of the tour of the $\boldsymbol{k}$ th ant.

3.2.2. ACO Algorithm Description

Based on the aforementioned reference [36], the algorithm can be summarized as follows:

- Initialize the pheromone distribution $\boldsymbol{\tau}$
- Each ant is randomly placed in a city at the beginning of the algorithm
- Build trajectories and update pheromones up to a specified number of iterations $\boldsymbol{t_{max}}$
- Construct a path for each ant using calculated transition probabilities
- Calculate tour costs
- Update the best solution, if any
- Determine $\boldsymbol{\Delta\tau_K(t+1)}$
- Updated pheromone distribution based on new pathways
- Printing the best solution.

3.3.4. How is each city visited once on each route?

In the ant colony optimization (ACO) algorithm used to solve the traveling salesman problem, duplication of a city on each path chosen by the ant is avoided by modifying the visibility matrix at each iteration by setting the visibility of the visited city to zero, dynamically during the tour. The effect of this modification prevents the ant from choosing this city again because the visibility becomes non-existent, making the possibility of choosing it in the following probability calculations impossible.

4. The Proposed Hybrid ACO Algorithm

The TSP problem is one of the most famous problems studied in the field of combinatorial optimization. It has been proven to be an NP-hard problem, and no algorithm has been found to obtain the optimal solution in polynomial time with the increase in the number of cities. TSP plays an important role in modeling numerous real-life problems, thus, the need for an algorithm to solve large-scale TSP problems has emerged.

In our research, a new hybrid algorithm is developed that combines the ACO algorithm and the nearest neighbor algorithm. The latter has a role in improving the speed of convergence and effectiveness of the ACO algorithm towards the optimal solution.

Figure 3 shows the flowchart that combines ACO and NN and how they are combined to solve the TSP problem. First, the parameters are determined through experimentation. The initial population is built by generating Ngreedy solutions using NN and optimizing these nearest neighbor paths using 2-opt exchange process. The rest of the initial population consisting of m - Ngreedy solutions (where m represents the population size) is randomly generated to ensure careful exploration of the search space. After this step, in each iteration, probabilistic solutions are built. If the stopping condition is met, the best path is printed. However, if the stopping condition is not met, the algorithm updates its parameters based on the new information from the current solutions and repeats the iterative process.

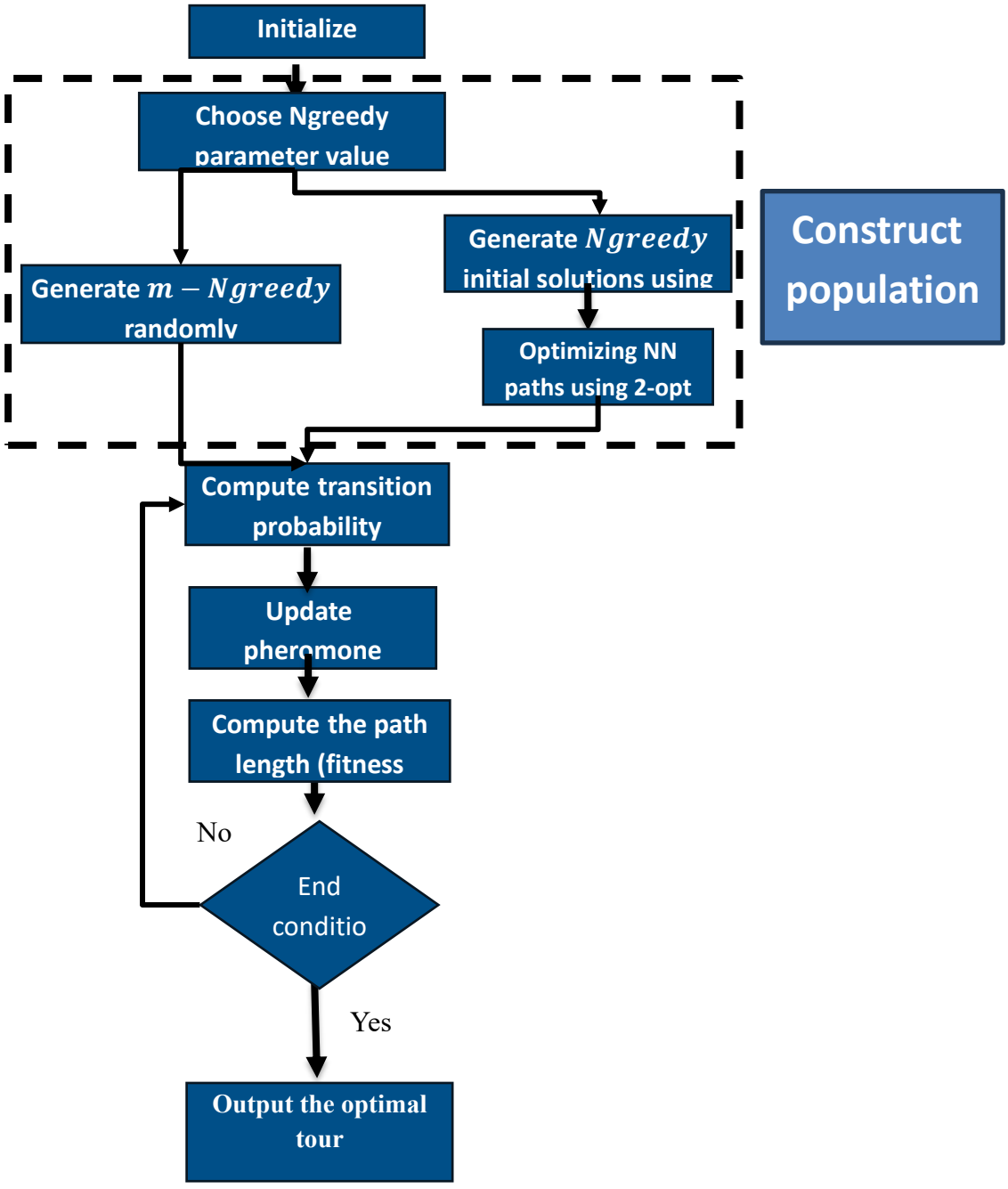

Figure 3: A flowchart combining the ACO and NN algorithms

5. Numerical Results

In this section, the performance of the proposed hybrid algorithm is evaluated and compared with the basic ACO algorithm and NN algorithms. The right set of parameters is determined by experimenting with problem instances of different sizes. This helped us identify the best parameter values that yield competitive results. The ACO parameters used in generating the results in this section are presented in Table 1.

Table 1: The values of the parameters included in the ACO algorithm.

parameters	α	B	evaporation coefficient (ρ)
Value	2	3	0.15

The results of the modification to the basic ACO algorithm show that using the nearest neighbor heuristic algorithm to generate part of the initial population improves the results in terms of reducing time consumed and quality of the obtained solutions, as shown in Tables 2 and 3, where Ngreedy = 3 and M is taken equal to 1 (recall that M represents the number of times the NN algorithm is executed to generate TSP tours, where each time the algorithm starts at a new random solution).

The performance of the hybrid algorithm and the performance of the ACO algorithm are evaluated by executing each algorithm 15 times to obtain the best solutions, the relative percentage error (%) is calculated using equation (12) to compare the performance of the two algorithms and their convergence.

$$Err_{ACO,NN-ACO}(\%) = \frac{Y_{ACO} - Y_{NN-ACO}}{Y_{NN-ACO}} \times 100\% \qquad (12)$$

Table 2 shows a comparison of four algorithms for a moderate number of cities ranging from 10 to 70. The four algorithms included in the comparison are the basic ACO algorithm, the proposed hybrid NN-ACO algorithm, the NN algorithm and the linear programming based approach (LP). The number of ants was set to m = 500 ants. The distance values for up to 30 cities are identical for the four algorithms. However, when the number of cities exceeds 30, slight differences start to occur. The results show that the proposed hybrid NN-ACO offers an improvement in performance through the effective role played by NN compared to the original ACO algorithm as the number of cities increases.

Figures 4 and 5 show convergence curves of the NN-ACO algorithm and ACO algorithms for a large-scale problem instance with 220 cities, respectively. In both figures, the first point at which an algorithm reaches a stable solution is highlighted and designated by X (number of iterations) and Y (corresponding cost or path length). These values (X and Y) are reported in Table 3.

In Table 3, as the number of cities increases ranging from 100 to 220, the performance difference between the ACO and the hybrid algorithm becomes more pronounced, with the relative percentage difference growing from 7.6954% for 100 cities to 14.2915% for 220 cities. For this larger size problem instances, the number of ants was set to be five times the number of cities to ensure diversity in solutions and a small number of iterations is used. The maximum number of iterations was set to be 20, after monitoring the convergence curves of the algorithms, as depicted in Figures 4 and 5. The proposed hybrid approach helps to improve the initial population generated and thus ACO builds solutions on it and thus skips situations in which the algorithm may fail, as shown in the results presented in Table 3 and Figure 4.

In the proposed hybrid algorithm, it is noteworthy that the greedy algorithm only participates in the initialization step. The remaining iterations are purely ACO procedures. This makes the complexity of each iteration of the proposed algorithm the same as that of the ACO algorithm alone. In this way, the number of iterations until a stable performance (X value) is reached can be considered as a measure of the time consumed by the algorithms, as shown in Tables 3 and 4. In Table 3, the cost (Y) achieved by the proposed hybrid algorithm is much lower than that of the standalone ACO algorithm for approximately the same number of iterations. Moreover, as the number of cities increases, the gap between the two algorithms. in terms of cost continues to widen. In addition, the

quality of the produced solution by the hybrid algorithm closely approximates the exact solution obtained by the LP-based approach for all tested problem instances, demonstrating the efficiency of the hybrid algorithm in reaching near-optimal solutions while maintaining a computational complexity similar to that of the basic ACO algorithm.

Table 2: *A comparison between the proposed algorithm and other algorithms for solving TSP*

Iteration = 500, m = 500				
N. Cites	ACO Ngreedy=0	NN-ACO Ngreedy=3	NN	LP
	Distance	distance	Distance	distance
10	29.5451	29.5451	29.5451	29.5451
20	35.3447	35.3447	35.3447	35.3447
30	45.5921	45.5921	45.5921	45.5921
40	49.8462	49.8314	50.3574	49.8314
50	56.7955	56.6001	57.1995	56.5524
60	65.7239	63.9752	63.9752	63.9752
70	68.9364	66.9294	67.0011	66.7672

Table 3: *The minimum distance obtained by ACO and NN-ACO and the least number of iterations required to converge to it*

Maximum Number of Iterations = 20							
No. of Cites	m	ACO Ngreedy=0		NN-ACO Ngreedy=3		NN	LP
		X	Y	X	Y	Y	Distance
100	500	4	85.6724	2	79.5506	80.5414	77.9675
150	750	3	105.298	5	94.6435	94.9129	93.5338
160	800	3	114.484	4	100.6107	101.3478	99.1409
170	850	3	114.612	3	101.667	101.837	98.0148
180	900	4	115.019	4	102.672	102.9092	98.7619
190	950	3	124.736	3	108.2763	109.7153	106.3494
220	1100	3	130.7052	2	114.3612	115.4124	111.0998

Figure 4: *Minimum tour length for 220 cities problem instance obtained using NN-ACO algorithm with Ngreedy=3*

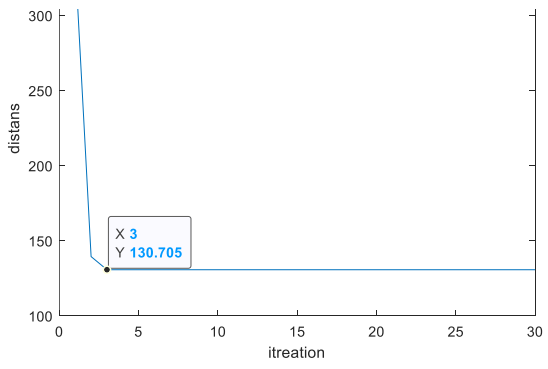

Figure 5: *Minimum tour length for 220 cities problem instance obtained by ACO algorithm*

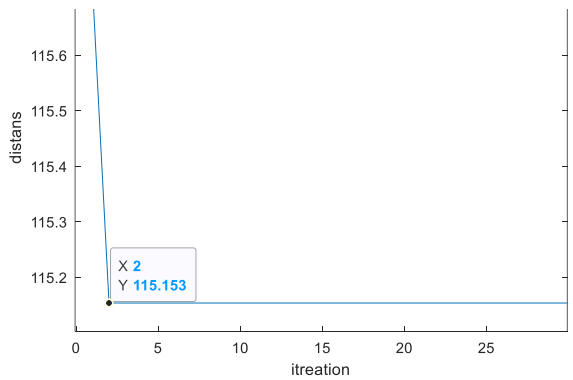

Table 4: Solutions corresponding to different values of M, M=1,2,3,4 for the case of 150 cities

	M	X	Y	Time of initial population construction in seconds
Ngreedy=3	M=1	4	94.6435	0.011957
	M=2	4	94.6435	0.018705
	M=3	2	94.593	0.027437
	M=4	2	94.3254	0.033969

In our experiments, we investigated the impact of the parameter M of the NN algorithm on the quality of the obtained solutions. The results are shown in Table 4. The preliminary results corresponding to different values of M for the 150 cities problem instance, with m = 750 and a maximum iteration limit= 30, show that the solutions obtained at the values M = 1 and M = 2 are identical. However, a slight difference in the cost at the values M = 3 and M = 4 have been observed. Yet, it is noteworthy that all solutions are close with a relative difference of no more than 0.3%, so that the relative percentage error of the distance difference corresponding to the two values M = 2 and M = 3 is 0.05338%, and the relative percentage error at M = 3 and M = 4 is 0.28369%. The best solution is 94.3254 at M = 4, but this comes at the cost of computational time increase. As the value of M increases, the time needed to build the initial population increases, which in turn affects the computational cost. The time difference corresponding to two different values of M is expressed by the relative time increase measure $\boldsymbol{Err_{M,M+1}}$, which is calculated as:

$$\boldsymbol{Err_{M,M+1}}(\%) = \frac{\boldsymbol{T_{M+1} - T_M}}{\boldsymbol{T_M}} \times \mathbf{100\%} \qquad \boldsymbol{M = 1, 2, 3} \tag{13}$$

Hence, we find $\boldsymbol{Err_{1,2}}$ =56.435%, $\boldsymbol{Err_{2,3}}$ = 46.6827%, and $\boldsymbol{Err_{3,4}}$ = 23.807%.

In this study, the hybrid algorithm NN-ACO is compared with the hybrid algorithm presented in [26], which is the ACO-RNN algorithm that combines the ant colony algorithm and attention-based neural networks. Twenty benchmark TSP problem instances from the TSPLIB library are used to test the effectiveness of our proposed hybrid NN-ACO method. In this part of our experiments, the number of ants was taken as 100 and the number of iterations was 200. The obtained results are shown in Table 5, together with the exact optimal solutions for both small and large problems. Moreover, the best solutions yielded by the ACO-RNN algorithm as reported in [26] are included for sake of comparison. From Table 5, it is apparent that the proposed NN-ACO algorithm succeeded to give high quality solutions compared to the optimal solution. The results indicate that the NN-ACO algorithm outperforms the ACO-RNN algorithms in most of the problem instances. It is worth mentioning that the LP-based approach failed to solve large-scale problems with 400 or more cities.

From Table 6, according to the results of Equation 14, it can be seen that the proposed NN-ACO algorithm produces solutions that are very close to the optimal solution and the relative error is mostly very small. This means that the proposed NN-ACO algorithm is stable to compute a satisfactory solution to such problems, with errors falling within the range [0.03, 4.74].

$$\boldsymbol{Err}(\%) = \frac{\mathbf{Best - Optimal}}{\mathbf{Optimal}} \times \mathbf{100\%} \tag{14}$$

Instance	Optimal solution	Best solution NN-ACO	Best solution ACO-RNN	Instance	Optimal solution	Best solution NN-ACO	Best solution ACO-RNN
eil51	426	429.5303	429.3	**pr144**	58537	58687.7961	6300.1
Berlin52	7542	7544.3659	7583.8	**ch150**	6528	6576.334	6987.4
st70	675	677.1096	700.2	**kroA200**	29368	29562.278	33449.1
eil76	538	555.5332	560.4	**rd400**	15281	15638.6445	15900.5
pr76	108159	109193.4374	112000.1	**fl417**	11861	12232.3636	13503.4
rat99	1211	1229.02	1334.5	**pr439**	107217	112270.5673	112286.9
rd100	7910	8007.0342	8036.0	**pcb442**	50778	51903.633	53850.0
kroA100	21282	21320.957	21554.2	**rat575**	6773	7055.2899	7053.7
eil101	629	645.6245	650.8	**p654**	34643	35768.3278	35982.0
lin105	14379	14439.7026	14750	**u724**	41910	43427.875	44002.5
Ch130	6110	6233.3524	6300.1	**rat783**	8806	9223.8153	9335.8

Table 5: *Results of the proposed NN-ACO for small/large problem instances from TSPLIB library*

Table 6: Experimental results of the proposed NN-ACO optimization algorithm for the 22 similar benchmark datasets and their comparison by relative error percentage

Instance	Optimal solution	Best solution NN-ACO	Err (%)	Instance	Optimal solution	Best solution NN-ACO	Err (%)
eil51	426	429.5303	0.828709	**pr144**	58537	58687.7961	0.257608
Berlin52	7542	7544.3659	0.03137	**ch150**	6528	6576.334	0.740411
st70	675	677.1096	0.312533	**kroA200**	29368	29562.278	0.66153
eil76	538	555.5332	3.258959	**rd400**	15281	15638.6445	2.340452
pr76	108159	109193.4374	0.956404	**fl417**	11861	12232.3636	3.130964
rat99	1211	1229.02	1.488026	**pr439**	107217	112270.5673	4.713401
rd100	7910	8007.0342	1.226728	**pcb442**	50778	51903.633	2.216773
kroA100	21282	21320.957	0.183051	**rat575**	6773	7055.2899	4.167871
eil101	629	645.6245	2.643005	**p654**	34643	35768.3278	3.248356
lin105	14379	14439.7026	0.422161	**u724**	41910	43427.875	3.621749
Ch130	6110	6233.3524	2.018861	**rat783**	8806	9223.8153	4.744666

6. Concluding remarks

In this paper, a high-performance hybrid algorithm is developed, which combines ant colony optimization algorithm with the nearest neighbor algorithm to solve the Travel Salesman Problem (TSP). It consists of two main stages. In the first stage, the nearest neighbor algorithm is used to optimize the initial population and 2-opt exchange is used to further improve the obtained solutions. There is a possibility of a stagnant solution at this stage. In the second stage, ACO builds on the solutions obtained in the initialization stage and optimizes the paths through an iterative optimization process. The goal is to minimize the path length taken by the salesman to visit all the cities and returning back to the starting point of the tour. To maximize the enhancement to performance of the algorithm, the algorithm parameters were carefully tuned. The simulation results we obtained show that the proposed NN-ACO algorithm is more effective than the basic ACO algorithm and NN algorithm by providing a faster descent rate and a clear convergence process for solutions, especially when the number of cities increases. The experimental results proved that the proposed approach produces good solutions compared to another recently developed hybrid algorithm in literature (ACO- RNN) and is thus effective for solving large-scale problems, making it a practical solution for TSP.

Conflict of interest

The authors have no conflicts of interest to declare.

Ethics approval

This study did not require ethical approval as it does not involve any human or animal case studies.

Funding

This research received no specific grant from any funding agency in the public, commercial, or not-for-profit sectors.

Data availability

The data that support the findings of this study are available on request from the corresponding author.

Authors contribution

Mohammed Salim Hassan: Formal Analysis, Investigation, Software, Visualization, Writing – Original Draft Preparation. **Yasmine Abouelseoud:** Conceptualization, Investigation, Supervision, Writing – Review & Editing. **Ahmed F. Tayel:**

Investigation, Methodology, Software, Supervision, Writing – Review & Editing.

Acknowledgement

Not applicable.

Human Participants and/or Animals

Not applicable.

References

1. Kızılates, G., & Nuriyeva, F. (2013). A parametric hybrid method for the traveling salesman problem. *Mathematical and Computational Applications*, *18*(3), 459-466.
2. Taiwo, O. S., Josiah, O., Taiwo, A., Dkhrullahi, S., & Sade, O. K. (2013). Implementation of heuristics for solving travelling salesman problem using nearest neighbour and nearest insertion approaches.
3. Kaabi, J., & Harrath, Y. (2019). Permutation rules and genetic algorithm to solve the traveling salesman problem. *Arab journal of basic and applied sciences*, *26*(1), 283-291.
4. Nurdiawan, O., Pratama, F. A., Kurnia, D. A., & Rahaningsih, N. (2020, March). Optimization of Traveling Salesman Problem on Scheduling Tour Packages using Genetic Algorithms. In *Journal of Physics: Conference Series* (Vol. 1477, No. 5, p. 052037). IOP Publishing.
5. Erol, A. H., & Bulkan, S. (2012, July). New genetic algorithm for the travelling salesman problem. In *Proceedings of the 2012 International Conference on Industrial Engineering and Operations Management, Istanbul, Turkey*.
6. Mahmoudinazlou, S., & Kwon, C. (2024). A hybrid genetic algorithm for the min–max Multiple Traveling Salesman Problem. *Computers & Operations Research*, *162*, 106455.
7. Vescan, A., & Pintea, C. M. (2007). Ant colony component-based system for travelling salesman problem. *Applied Mathematical Sciences*, *1*(28), 1347-1357.
8. Brezina Jr, I., & Čičková, Z. (2011). Solving the travelling salesman problem using the ant colony optimization. *Management Information Systems*, *6*(4), 10-14
9. Yang, J., Shi, X., Marchese, M., & Liang, Y. (2008). An ant colony optimization method for generalized TSP problem. *Progress in Natural Science*, *18*(11), 1417-1422.
10. Shi, Y., & Zhang, Y. (2022). The neural network methods for solving Traveling Salesman Problem. *Procedia Computer Science*, *199*, 681-686.
11. Cao, Y., Sun, Z., & Sartoretti, G. (2022, November). Dan: Decentralized attention-based neural network for the minmax multiple traveling salesman problem. In *International Symposium on Distributed Autonomous Robotic Systems* (pp. 202-215). Cham: Springer Nature Switzerland.
12. Karaboga, D., & Ozturk, C. (2011). A novel clustering approach: Artificial Bee Colony (ABC) algorithm. *Applied soft computing*, *11*(1), 652-657.
13. Chen, S. M., & Chien, C. Y. (2011). Solving the traveling salesman problem based on the genetic simulated annealing ant colony system with particle swarm optimization techniques. *Expert Systems with Applications*, *38*(12), 14439-14450.
14. Angeniol, B., Vaubois, G. D. L. C., & Le Texier, J. Y. (1988). Self-organizing feature maps and the travelling salesman problem. *Neural Networks*, *1*(4), 289-293.
15. Somhom, S., Modares, A., & Enkawa, T. (1997). A self-organising model for the travelling salesman problem. *Journal of the Operational Research Society*, *48*(9), 919-928.
16. Masutti, T. A., & de Castro, L. N. (2009). A self-organizing neural network using ideas from the immune system to solve the traveling salesman problem. *Information Sciences*, *179*(10), 1454-1468.
17. Pasti, R., & de Castro, L. N. (2006, July). A neuro-immune network for solving the traveling salesman problem. In *The 2006 IEEE International Joint Conference on*

Neural Network Proceedings (pp. 3760-3766). IEEE.

18. Durbin, R., & Willshaw, D. (1987). An analogue approach to the travelling salesman problem using an elastic net method. Nature 326, 689-691.
19. Dong, G., Guo, W. W., & Tickle, K. (2012). Solving the traveling salesman problem using cooperative genetic ant systems. *Expert systems with applications*, *39*(5), 5006-5011.
20. Marinakis, Y., & Marinaki, M. (2010). A hybrid genetic–Particle Swarm Optimization Algorithm for the vehicle routing problem. *Expert Systems with Applications*, *37*(2), 1446-1455.
21. Kanna, S. R., Sivakumar, K., & Lingaraj, N. (2021). Development of deer hunting linked earthworm optimization algorithm for solving large scale traveling salesman problem. *Knowledge-Based Systems*, *227*, 107199.
22. Khan, I., & Maiti, M. K. (2019). A swap sequence based artificial bee colony algorithm for traveling salesman problem. *Swarm and evolutionary computation*, *44*, 428-438.
23. Jia, H. (2015). A novel hybrid optimization algorithm and its application in solving complex problem. *International Journal of Hybrid Information Technology*, *8*(2), 1-10.
24. Rahman, Md.A., & Parvez, H. (2021). Repetitive Nearest Neighbor Based Simulated Annealing Search Optimization Algorithm for Travelling Salesman Problem, Open Access Library Journal, 8:e7520.
25. Erol, A. H., Er, M., & Bulkan, S. (2012). Optimizing the ant colony optimization algorithm using neural network for the traveling salesman problem. In *Actas de la Conferencia Internacional de* (pp. 83-89).
26. Soh, M., & Likeufack, A. N. (2024). A New Hybrid Algorithm Based on Ant Colony Optimization and Recurrent Neural Networks with Attention Mechanism for Solving the Traveling Salesman Problem.
27. Stützle, T., & Dorigo, M. (1999). ACO algorithms for the traveling salesman problem. *Evolutionary algorithms in engineering and computer science*, *4*, 163-183.
28. Fereidouni, S. (2011). Solving traveling salesman problem by using a fuzzy multi-objective linear programming. *Afr J Math Comput Sci Res*, *4*(11), 339-349.
29. Benhida, S., & Mir, A. (2017). Solving the Traveling Salesman Problem with Exact Methods, International Journal of Enhanced Research in Science, Technology and Engineering, 6(7), 61-66.
30. Katagiri, H., Wu, H., Kakiuchi, Y., Hamori, H., & Kato, K. (2017). A route optimization problem in electrical pcb inspections with alignment operations. *Scientiae Mathematicae Japonicae*, *80*(3), 219-232.
31. C.E. Miller, A.W. Tucker & R.A. Zemlin (1960) Integer programming formulations and travelling salesman problems. J. Ass. Comp. Mach., 7, 326–329.
32. Pataki, G. (2000). The bad and the good-and-ugly: formulations for the traveling salesman problem. *Department of Industrial Engineering and Operations Research. Columbia University*.
33. Sharma, M. K., Chaudhary, S., Rathour, L., & Mishra, V. N. (2024). Modified genetic algorithm with novel crossover and mutation operator in travelling salesman problem. *Sigma Journal of Engineering and Natural Sciences*, *42*(6).
34. AlSalibi, B. A., Jelodar, M. B., & Venkat, I. (2013). A comparative study between the nearest neighbor and genetic algorithms: A revisit to the traveling salesman problem. *International Journal of Computer Science and Electronics Engineering (IJCSEE)*, *1*(1), 110-123.
35. Gao, W. (2020). New ant colony optimization algorithm for the traveling salesman problem. *International Journal of Computational Intelligence Systems*, *13*(1), 44-55.
36. Blum, D., & Dortmund, U. (2013). Ant colony optimization (ACO). *Journal of Interdisciplinary Mathematics*, *8*, 157-168.

Rojava Journal of Science and Technology

2026, VOL. 3, No 1, [139-150]

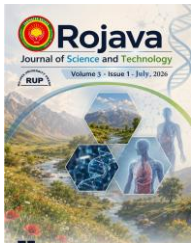

Assessing the Impact of Overweight and Obesity on Cardiovascular Health Among Syrian Population Living in North and East Syria: A Cross-Sectional Study

Shima Mustafa Ali[1], Haidar Saify Nabiabad[1], Eman Elbassuoni[2*]

[1] Department of Physiology, Institute of Science and Modern Technology, Rojava University, North and East Syria

[2] Department of Physiology, Faculty of Medicine, Minia University, Egypt

Abstract

As the global prevalence of overweight and obesity continues to rise, understanding their impact on cardiovascular health is crucial for developing effective interventions and healthcare policies. Cardiovascular diseases (CVD), including heart disease and stroke, remain the leading causes of death worldwide. Addressing this issue begins with assessing the prevalence of overweight and obesity and evaluating their effects on CVD risks, as demonstrated in the population of North and East Syria. A total of 167 participants (47.5% males, 40.4% females) with a mean age of 49.4 years were assessed. The average BMI was 27.9, with overweight and obesity rates of 34.2% and 35.3%, respectively. High waist circumference was observed in 49.7% of participants, with a significant gender difference, as 63.4% of females exhibited this condition compared to 36.5% of males. The mean systolic blood pressure was 132.1 mmHg, and the mean diastolic blood pressure was 85.3 mmHg. Hypertriglyceridemia was the most obesity prevalent risk factor (61.7%), followed by high waist circumference (49.7%), hypertension (32.9%), and hyperglycemia (32.3%). Hypercholesterolemia had the lowest prevalence (9.6%). A significant association was found between age and waist circumference, mean arterial pressure, fasting blood glucose, and cardiometabolic syndrome development. Gender differences extended to lifestyle and educational factors. Smoking and alcohol consumption were significantly higher among males (58.8% and 18.8%, respectively), while females had lower education levels (36.6% uneducated). Being overweight and obese was strongly associated with a history of hypertension, a family history of CVD, and a lack of education. This study highlights the significant burden of obesity and its associated health risks in North and East Syria. It emphasizes the need for targeted public health interventions focusing on education, lifestyle modification, and early detection of obesity-related conditions to mitigate the rising prevalence of cardiometabolic disorders in the region.

ARTICLE HISTORY
Received 12 Jan. 2026
Revised 3 sept. 2026
Accepted 20 Sept. 2026

Keywords
Overweight, Obesity, Cardiovascular Diseases (CVD), Blood pressure, Blood glucose, Lipids.

*Corresponding Corresponding Author: Eman Elbassuoni, eman.abdelhameed@mu.edu.eg

1. Introduction

Overweight and obesity, characterized by excessive fat accumulation due to an imbalance between energy intake and expenditure, are major global health concerns (Pereira-Lancha et al. 2010). Epidemiological evidence links obesity to increased incidence and mortality from cardiovascular disease (CVD), with its effects varying based on obesity duration and individual fitness levels (Ortega, Lavie, and Blair 2016). Physical fitness can moderate some cardiovascular risks even in obese individuals (Ashraf and Baweja 2013).

Excess body weight negatively affects the cardiovascular system, increasing the risks of hypertension, dyslipidemia, insulin resistance, and structural heart changes. Additionally, obesity is associated with chronic inflammation, with elevated proinflammatory cytokines contributing to insulin resistance, plaque activation, myocardial hypertrophy, and CVD progression (Ellul et al. 2017). Inflammatory changes in adipose tissue also impair vascular function (Oikonomou and Antoniades 2018).

Obesity significantly contributes to heart failure. Each unit increase in BMI raises the incidence of heart failure by 5% in men and 7% in women. Increased blood volume and cardiac workload can lead to left ventricular hypertrophy, ultimately causing heart failure. Obesity is also a key component of metabolic syndrome, further elevating CVD risk (Oberman and Bhardwaj 2022).

In 2022, approximately 16% of adults worldwide were obese, with obesity prevalence more than doubling since 1990. An estimated 2.5 billion adults were overweight, including over 890 million classified as obese. This accounted for 43% of adults aged 18 years and older (43% of men and 44% of women), a significant increase from 25% in 1990. Overweight prevalence varied by region, ranging from 31% in the WHO Southeast Asia and African Regions to 67% in the Americas (World Health Organization 2024).

Obesity is a major risk factor for numerous health conditions, worsening comorbid illnesses, reducing quality of life, and increasing mortality risk. In the United States alone, over 111,000 deaths annually are linked to obesity (Flegal 2005). Epidemiological studies show that obesity contributes to higher incidence and mortality from multiple cancers, including those of the colon, breast (postmenopausal women), endometrium, kidney, esophagus, gastric cardia, pancreas, gallbladder, and liver. Overall, 15%–20% of all cancer-related deaths in the U.S. are attributed to overweight and obesity (Calle et al. 2003).

The main objectives of this research project are to assess the prevalence of overweight and obesity in a defined population in Syria, and to provide a comprehensive understanding of its impact on cardiovascular health, revealing the underlying mechanisms and potential interventions.

2. Materials and methods

2.1 Study Design

The study was an observational cross-sectional study conducted in North and East Syria from December 2023 to June 2024.

2.2 Study Population and Sampling Technique

All Syrian residents living in North and East Syria were invited to participate in the study. The required sample size calculated based using EPI-INFO version 3, considering the prevalence of obesity in Syria (18.9 %) (Zlatko Nikoloski 2023), a confidence interval of 95%, and a maximum acceptable error of 5%. Accordingly, the minimum sample size needed was 150 members. A total of 167 members were included in the study. The study was conducted at the outpatient clinics and internal medicine in the following hospitals:

- Afrin Hospital in Fafin, Al-Shahba District, Aleppo
- Tal Rifaat Hospital, Al-Shahba District, Aleppo
- Yassin Hospital, Sheikh Maqsoud neighborhood, Aleppo
- Kobani Hospital, Kobani city, East of Euphrates

- Amal Hospital, Kobani City, East of Euphrates

Official permissions were obtained from the Rojava University administration and the university's scientific ethical committee. The study protocol was approved by the Ethics Committee of Rojava University.

2.3. Research Strategy

Data was collected after explaining the study and obtaining written consent from participants. Interested participants were screened for eligibility and scheduled for data collection. All samples were analyzed at the hospitals' accredited laboratories.

All participants underwent thorough history-taking and clinical examinations.

1. Questionnaire including:

• Socio-Demographic Characteristics: age, sex, physical activity, smoking/alcohol habits, dietary habits, educational level

• Medical History: hypertension, diabetes mellitus, CVD, or any chronic disease, family history of hypertension, diabetes mellitus, or CVD.

2. Anthropometric Measurements:

• Body Weight (kg): Measured with a digital scale to the nearest 0.1 kg.

• Height (cm): Measured with stretch-resistant tape to the nearest 0.5 cm. Participants removed shoes and bulky clothing.

• Waist circumference (in centimeters): measured at the midpoint between the lower rib margin and the iliac crest (WHO, 2008). Threshold values: ≥88 cm (women), ≥102 cm (men).

• Body Mass Index (BMI): Calculated as: BMI=Weight in kilograms / Height in meters^2

BMI was classified according to World Health Organization guidelines (World Health Organization 2024): underweight (<18.5), normal (18.5–24.9), overweight (25–29.9), and obese (30–39.9).

3. Clinical Examination: Brachial blood pressure was measured using standard mercury sphygmomanometers after participants rested for at least five minutes. Categories were based on American College of Cardiology/American Heart Association guidelines (Carey and Whelton 2018):
   - Normal: Systolic <120 mmHg, Diastolic <80 mmHg.
   - Elevated: Systolic 120–129 mmHg, Diastolic <80 mmHg.
   - Hypertension: Systolic ≥130 mmHg, Diastolic ≥80 mmHg.

4. Laboratory Investigations:

• Fasting Blood glucose (mg/dl): Measured after overnight fasting. Levels were categorized as normal (<100 mg/dL), prediabetes (100–125 mg/dL), and diabetes (≥126 mg/dL) (Mayo Clinic 2017).

• Cholesterol and triglyceride levels are classified per standard clinical thresholds (Grundy et al. 2018).

- Normal total Cholesterol (mg/dL) (<200), borderline high (200–239), and high (≥240).
- Triglyceride Classification (mg/dL) into: Normal (<150), Mild High (150–199), Moderate High (200–499), and Severe High (≥500).

2.4. Statistical Methods

Data was analyzed using IBM SPSS version 27. Quantitative data were expressed as mean ± SD, and categorical data as numbers and percentages. Relationships between variables and outcomes were tested using the chi-square or Fisher's exact test for categorical data and independent sample t-tests and ANOVA for numerical data.

3. Results

3.1. The prevalence of different BMI categories

In the studied population, underweight represents 3% of the participants, normal weight represents 27.5% of the participants, overweight represents 34.2% of the participants, obese represents 35.3%of the participants

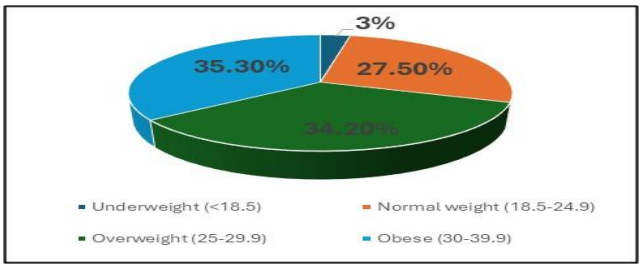

(figure 1).

Figure 1: The prevalence of different BMI categories

3.2. The mean and prevalence of some health risks related to overweight and obesity

- A total of 167 participants were included in the present study. The mean BMI was 27.9, while the mean waist circumference was 94.9 cm. The mean arterial blood pressure was 100.9 mmHg, and the mean fasting blood glucose level was 107.8. The mean cholesterol level was 165.5, while the mean triglyceride level was 195.8 (Table 1).

- Hypertriglyceridemia was the most prevalent risk factor, with a prevalence of 61.7%, followed by high waist circumference (49.7%). In comparison, hypertension had a prevalence of 32.9%, while hyperglycemia was observed in 32.3% of participants. The least prevalent risk factor was hypercholesterolemia, with a prevalence of 9.6% (Figure 2).

Table 1: Main characteristics of the population studied

	Total (Number = 167) Mean ± SD
BMI (kg/m^2)	27.9 ± 5.3
Waist circumference (cm)	94.9 ± 13.7
MAP (mmHg)	100.9 ± 15.7
Fasting blood glucose (mg/dl)	107.8 ± 45.2
Cholesterol (mg/dl)	165.5 ± 34.5
Triglycerides (mg/dl)	195.8 ± 98

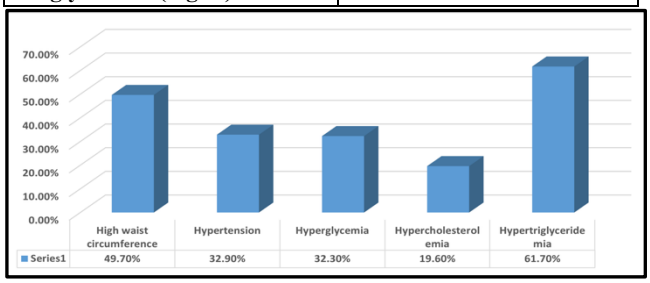

Figure 2: The prevalence of some health risks related to overweight and obesity.

3.3. SEM Correlation between age and BMI and some health risks related to overweight and obesity

Statistical analysis found a positive correlation between age and waist circumference, mean arterial pressure, fasting glucose level, and cardiometabolic syndrome (CMS) development (Table 2).

Table 2: Correlation between age and BMI and some health risks related to overweight and obesity

Correlation	Age (year)	
	R	p-value
BMI	0.128	0.100
Waist circumference	0.241 **	0.002
MAP	0.213 **	0.006
Fasting blood glucose	0.184 *	0.017
Cholesterol	0.139	0.073
Triglycerides	0.028	0.722
CMS	0.243 **	0.002

** Correlation is significant at the 0.01 level (2-tailed)

* Correlation is significant at the 0.05 level (2-tailed)

3.4. The relation between BMI, and some medical and lifestyle risk factors related to overweight and obesity

- Analysis of the present results showed that there was a significant association between overweight and obesity and high waist circumference, high MAP, high triglycerides, and the presence of CMS (p-value < 0.05) (table 3).

- The present results showed that there was a significant association between overweight & obesity and history of hypertension, family history of CVD, and no education (p-value < 0.05) (table 3).

3.5. The distribution of BMI, some related health risk factors, and some medical and lifestyle risk factors related to overweight and obesity according to gender

- Statistical analysis showed that the participants' gender was significantly associated with high waist circumference and BMI (p<0.05). About 63.4 % of female participants have a high waist circumference, compared to 36.5% for males. About 45.1% of female participants were obese, compared to 25.9% for males (figure 3).

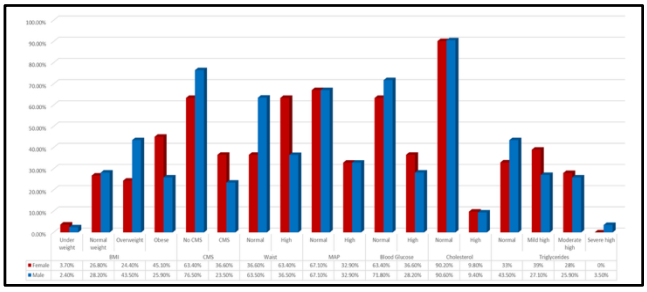

Figure 4: *The distribution of BMI and some medical risk factors related to overweight and obesity according to gender*

- On the other hand, the gender of the participants was significantly associated with educational level, smoking, and alcohol intake (p<0.05). About 36.6% of female participants have not been educated, compared to 16.5% of males. 73% of males have low education, compared to 52.4% of females. 58.8% of males were smokers, compared to 35.4% for females. 18.8% of males take alcohol, compared to 2.4% for females (figure 4).

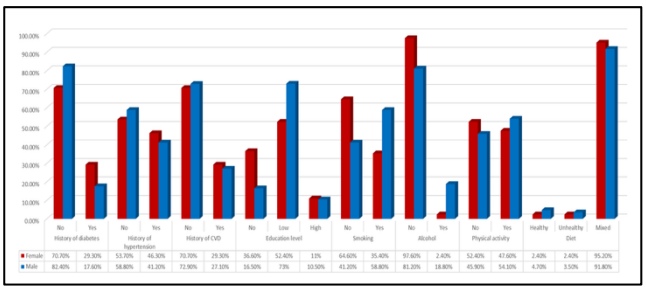

Figure 3: *The distribution of BMI and some lifestyle risk factors related to overweight and obesity according to gender*

Table 3: *The relation between BMI and some medical and lifestyle risk factors related to obesity*

		BMI			Test	p-value
		Normal (N=51)	**Overweight (N= 57)**	**Obese (N=59)**		
Waist Circumference	- Normal - High	41 (80.4%) 10 (19.6%)	33 (57.9%) 24 (42.1 %)	10 (16.9%) 49 (83.1%)	X^2 46.040	<0.001
MAP	- Normal - High	44 (86.3%) 7 (13.7%)	35 (61.4%) 22 (38.6%)	33 (55.9%) 26 (44.1%)	X^2 *12.658*	0.002
Fasting blood glucose	- Normal - High	37 (72.5%) 14 (27.5%)	41 (71.9%) 16 (28.1%)	35 (59.3%) 24 (40.7%)	X^2 2.907	0.234
Total cholesterol	- Normal - High	47 (92.2%) 4 (7.8%)	53 (93%) 4 (7%)	51 (86.4%) 8 (13.6%)	X^2 1.688	0.430
Triglycerides	- Normal - Mild high - Moderate high - Severe high	30 (58.8%) 15 (29.4%) 6 (11.8%) 0 (0%)	20 (35.1%) 18 (31.6%) 18 (31.6%) 1 (1.8%)	14 (23.7%) 22 (37.3%) 21 (35.6%) 2 (3.4%)	X^2 17.795	0.007
CMS	- No - Yes	46 (90.2%) 5 (9.8%)	41 (71.9%) 16 (28.1%)	30 (50.8%) 29 (49.2%)	X^2 20.336	<0.001
History of diabetes	- No - Yes	44 (86.3%) 7 (13.7%)	41 (71.9%) 16 (28.1 %)	43 (72.9%) 16 (27.1%)	X^2 3.817	0.148
Family history of diabetes	- No - Yes	32 (62.7%) 19 (37.3%)	31 (54.4%) 26 (45.6%)	26 (44.1%) 33 (55.9%)	X^2 3.875	0.144
History of hypertension	- No - Yes	38 (74.5%) 13 (25.5%)	28 (49.1%) 29 (50.9%)	28 (47.5%) 31 (52.5%)	X^2 9.941	0.007
Family history of hypertension	- No - Yes	26 (51%) 25 (49%)	19 (33.3%) 38 (66.7%)	21 (35.6%) 38 (64.4%)	X^2 4.096	0.129
History of CVD	- No - Yes	41 (80.4%) 10 (19.6%)	42 (73.7%) 15 (26.3%)	37 (63.8%) 21 (36.2%)	X^2 3.817	0.148
Family history of CVD	- No - Yes	37 (72.5%) 14 (27.5%)	35 (61.4%) 22 (38.6%)	26 (44.1%) 33 (55.9%)	X^2 9.416	0.009
Education level	- No - Low - High	10 (19.6%) 29 (56.9%) 12 (23.5%)	15 (26.3%) 39 (68.4%) 3 (5.3%)	19 (32.2%) 37 (62.7%) 3 (5.1%)	X^2 13.296	0.010
Smoking	- No - Yes	22 (43.1%) 29 (56.9%)	30 (52.6%) 27 (47.4%)	36 (61%) 23 (39%)	X^2 3.508	0.173
Alcohol	- No - Yes	47 (92.2%) 4 (7.8%)	51 (89.5%) 6 (10.5%)	51 (86.4%) 8 (13.6%)	X^2 0.935	0.627
Physical activity	- No - Yes	24 (47.1%) 27 (52.9%)	25 (43.9%) 32 (56.1%)	33 (55.9%) 26 (44.1%)	X^2 1.813	0.404
Diet	- Healthy - Unhealthy - Mixed	2 (3.9%) 2 (3.9%) 47 (92.2%)	3 (5.3%) 3 (5.3%) 51 (89.4%)	1 (1.7%) 0 (0%) 58 (98.3%)	X^2 4.197	0.380

p-value less than 0.05 indicates a significant association between the variable

4. Discussion

In the present study, obesity affected 35.3% of participants, while 34.2% were overweight, meaning over two-thirds faced increased non-communicable disease risks related to obesity. Globally, obesity has nearly tripled since 1975, with the Middle East showing higher rates than the world average (El-Sahli 2023). Syria's conflict-driven economic instability, food insecurity, and stress-induced hormonal imbalances contribute to this trend (Messer and Cohen 2023).

Only 27.5% of participants had a normal BMI, aligning with global declines in normal-weight populations. Underweight prevalence was just 3%, highlighting Syria's dual burden of malnutrition—nutritional deficiencies alongside rising obesity (Selimian, Nassr, and Sen 2022). Unlike conflict-affected Low- and Middle-Income Countries (LMICs) facing caloric deficits, Syria's food insecurity results in poor-quality, high-calorie diets (Ismail et al. 2019).

Limited income forces reliance on processed, energy-dense foods, while cultural and environmental factors—including high carbohydrate intake, low physical activity, and restricted healthcare access—exacerbate obesity (Katoue et al. 2022). Conflict-related stress further drives weight gain through cortisol dysregulation and insulin resistance (Yitshak-Sade et al. 2020).

This study highlights the significant burden of obesity-related health risks in North and East Syria. Hypertriglyceridemia (61.7%) was the most prevalent risk factor, followed by high waist circumference (49.7%), hypertension (32.9%), and hyperglycemia (32.3%). Hypercholesterolemia was least common (9.6%), reflecting global and regional trends influenced by Syria's socio-economic conditions.

Triglyceride levels averaged 195.8 mg/dL, with mild elevations in 33% of participants, moderate in 26.9%, and severe in 1.8%. Elevated triglycerides, associated with metabolic syndrome, result from dietary habits, physical inactivity, and genetic predisposition. Globally, hypertriglyceridemia is on the rise, especially in LMICs where diets are increasingly high in carbohydrates and low in fiber (Misra and Khurana 2008).

Hypertriglyceridemia exceeds 50% in the Middle East due to high sugar and processed food consumption (Algoblan, Alalfi, and Khan 2014). In Syria, economic constraints and reliance on low-cost, high-glycemic foods contribute to elevated triglycerides, compounded by poor access to lipid-lowering therapies ("Global Food Security Index (GFSI)" 2022).

Central obesity (≥102 cm in men, ≥88 cm in women), a key risk factor for metabolic syndrome. Urbanization and sedentary lifestyles drive its increase worldwide, with similar trends observed in Saudi Arabia and the U.S. (Borlaug and Reddy 2016; Wang et al. 2024).

The high mean arterial pressure observed in 32.9% of participants, indicating a significant prevalence of hypertension, aligns with global trends where over 1.28 billion adults are affected (World Health Organization 2023). In the Middle East, hypertension prevalence ranges from 26% to 44%, influenced by genetic factors, sedentary lifestyles, and high-sodium diets (Okati-Aliabad et al. 2022). In Syria, additional factors such as high salt intake, limited healthcare access, and stress from prolonged conflict contribute to elevated blood pressure (Alhaffar and Janos 2021).

The study also found a high fasting blood glucose level of 107.8 mg/dL, with 32.3% of participants affected, indicating a high prevalence of prediabetes and diabetes. Globally, diabetes cases have surged to 537 million in 2021, driven by obesity, urbanization, and sedentary lifestyles (International Diabetes Federation 2021). The Middle East has some of the highest diabetes rates, with Gulf countries like Saudi Arabia and Kuwait exceeding 20% (Okati-Aliabad et al. 2022). In Syria, disrupted food supply chains, reliance on low-cost, high-calorie foods, and reduced healthcare access have worsened glycemic control, while conflict-related stress has further impaired glucose metabolism (Algoblan, Alalfi, and Khan 2014;

"Food Security & Conflict in Syria," 2019). Diabetes prevalence in Syria has nearly tripled since 1980, with more than 1 in 10 Syrians affected ("WHO Helps Diabetes Patients in Syria," 2016).

The mean cholesterol level of 165.5 mg/dL was within normal limits, with only 9.6% of participants exhibiting high cholesterol. Globally, hypercholesterolemia remains a major concern, particularly in LMICs, where dietary shifts toward fat-rich foods and reduced physical activity have increased cholesterol levels (Misra and Khurana 2008). In the Middle East, rising cholesterol levels are attributed to greater consumption of animal fats and processed foods (Borlaug and Reddy 2016). However, in Syria, economic difficulty may have reduced access to such foods, explaining lower cholesterol levels ("Food Security & Conflict in Syria," 2019).

Aging correlated with increased BMI, waist circumference, and cardiometabolic risks, aligning with global patterns where reduced metabolism, hormonal shifts, and muscle loss contribute to obesity, diabetes, and hypertension (Hruby & Hu 2015). Urbanization and sedentary lifestyles further intensify these risks, particularly in the Middle East, where dietary habits and cultural standards discourage physical activity (Musaiger 2011; Lee et al. 2019).

Gender differences in obesity were notable, with 63.4% of women having high waist circumference versus 36.5% of men. Obesity affected 45.1% of women compared to 25.9% of men, mirroring regional trends where social patterns limit female mobility and physical activity (Hruby & Hu 2015; Musaiger 2011). Conflict has worsened these disparities by restricting women's access to education, employment, and healthcare (Welchman 2023). Low educational level was more prevalent among women, further contributing to higher obesity rates due to reduced health knowledge and economic constraints (UNICEF 2018).

Smoking and alcohol consumption were also gendered, with men engaging more due to cultural customs. In Syria, stress from conflict has likely increased male smoking rates, while traditional restrictions keep female smoking lower ("Syrian Arab Republic | Tobacco Atlas" 2019).

This study found strong links between overweight/obesity and some key risk factors related to obesity, including hypertension, family history of CVD, and low education levels.

Obesity is a major driver of hypertension worldwide, increasing vascular resistance and cardiac output (Fox et al. 2019). In the Middle East, obesity-related hypertension is widespread due to high-calorie diets and sedentary lifestyles, with studies in Saudi Arabia showing 60% of hypertensive individuals are overweight or obese (Okati-Aliabad et al. 2022). In Syria, economic instability and limited healthcare access worsen these risks.

The family history of CVD further increases obesity-related risks, as excess weight accelerates atherosclerosis and insulin resistance (Misra & Khurana 2008). In the Middle East, high obesity rates amplify these genetic risks (Algoblan et al. 2014). Syria's conflict exacerbates these issues by increasing stress, food insecurity, and reliance on unhealthy diets (Roba Gaafar 2021).

Low education was also strongly associated with obesity, limiting awareness of healthy lifestyles and access to nutritious food (Hruby & Hu 2015). In the Middle East, gender disparities in education contribute to higher obesity rates, particularly among women (Musaiger 2011). Syria's ongoing conflict has further widened these gaps, reducing opportunities for health education and reinforcing unhealthy behaviors (Qaddour & Husain 2022).

5. Conclusion

This study highlights the alarming prevalence of overweight and obesity in North and East Syria, with over two-thirds of participants affected, significantly increasing their risk for non-communicable diseases. Key risk factors, including hypertension,

hypertriglyceridemia, central obesity, and diabetes, were strongly linked to excess weight, reflecting hormonal imbalances further exacerbate these risks, while limited healthcare access and reliance on low-cost, high-calorie diets contribute to poor cardiometabolic health. Gender disparities and low educational levels, particularly among women, reinforce obesity-related challenges. Overweight and obesity, especially when excess fat accumulates around the abdomen, may increase the risk of numerous health problems. However, reaching and maintaining a healthy weight can help prevent these complications, slow their progression, or even eliminate them. Addressing obesity in Syria requires urgent interventions targeting healthcare accessibility, nutrition education, and lifestyle modifications to mitigate long-term health consequences in conflict-affected populations.

regional and global trends. Conflict-driven economic instability, food insecurity, and stress-induced

Reference

1. "Food Security & Conflict in Syria." 2019 Syrian Center for Policy Research SCPR. https://scpr-syria.org/launch-of-food-security-conflict-in-syria-report/

2. "Global Food Security Index (GFSI)." 2022. Global Food Security Index (GFSI). October 11, 2022. https://impact.economist.com/sustainability/project/food-security-index/explore-countries/syria

3. "Syrian Arab Republic | Tobacco Atlas." 2019. Tobacco Atlas. 2019. https://tobaccoatlas.org/factsheets/syrian-arab-republic/?utm_source=chatgpt.com.

4. "WHO Helps Diabetes Patients in Syria." 2016. Www.who.int. https://www.who.int/news-room/feature-stories/detail/who-helps-diabetes-patients-in-syria

5. Algoblan, Abdullah, Mohammed Alalfi, and Muhammad Khan. 2014. "Mechanism Linking Diabetes Mellitus and Obesity." Diabetes, Metabolic Syndrome and Obesity: Targets and Therapy 7 (587–591): 587. https://www.ncbi.nlm.nih.gov/pmc/articles/PMC4259868/

6. Alhaffar, M. H. D. Bahaa Aldin, and Sandor Janos. 2021. "Public Health Consequences after Ten Years of the Syrian Crisis: A Literature Review." Globalization and Health 17 (1). https://doi.org/10.1186/s12992-021-00762-9

7. Ashraf, M. Javed, and Paramdeep Baweja. 2013. "Obesity: The 'Huge' Problem in Cardiovascular Diseases." Missouri Medicine 110 (6): 499–504. https://pubmed.ncbi.nlm.nih.gov/24564002/.

8. Borlaug, Barry A., and Yogesh N.V. Reddy. 2016. "Getting at the Heart of Central Obesity and the Metabolic Syndrome." Circulation: Cardiovascular Imaging 9 (6). https://doi.org/10.1161/circimaging.116.005110

9. Calle, Eugenia E., Carmen Rodriguez, Kimberly Walker-Thurmond, and Michael J. Thun. 2003. "Overweight, Obesity, and Mortality from Cancer in a Prospectively Studied Cohort of U.S. Adults." New England Journal of Medicine 348 (17): 1625–38. https://doi.org/10.1056/nejmoa021423.

10. Carey, Robert M., and Paul K. Whelton. 2018. "Prevention, Detection, Evaluation, and Management of High Blood Pressure in Adults: Synopsis of the 2017 American College of Cardiology/American Heart Association Hypertension Guideline." Annals of Internal Medicine 168 (5): 351. https://doi.org/10.7326/m17-3203.

11. Ellulu, Mohammed S., Ismail Patimah, Huzwah Khaza'ai, Asmah Rahmat, and Yehia Abed. 2017. "Obesity and Inflammation: The Linking Mechanism and the Complications." Archives of Medical Science 13 (4): 851–63. https://doi.org/10.5114/aoms.2016.58928.

12. Mayo Clinic. 2017. "Prediabetes - Diagnosis and Treatment - Mayo Clinic." Mayoclinic.org. 2017. https://www.mayoclinic.org/diseases-conditions/prediabetes/diagnosis-treatment/drc-20355284.

13. El-Sahli, Zouheir. 2023. "Globalization and Obesity in the GCC Countries." Middle East Development Journal, January, 1–24. https://doi.org/10.1080/17938120.2022.2160182

14. Flegal, Katherine M. 2005. "Excess Deaths Associated with Underweight, Overweight, and Obesity." JAMA 293 (15): 1861. https://doi.org/10.1001/jama.293.15.1861.

15. Fox, Ashley, Wenhui Feng, and Victor Asal. 2019. "What Is Driving Global Obesity Trends? Globalization or 'Modernization'?" Globalization and Health 15 (1). https://doi.org/10.1186/s12992-019-0457-y

16. Grundy, Scott M., Neil J. Stone, Alison L. Bailey, Craig Beam, Kim K. Birtcher, Roger S. Blumenthal, Lynne T. Braun, et al. 2018. "2018 Guideline on the Management of Blood Cholesterol." Journal of the American College of Cardiology 73 (24). https://doi.org/10.1016/j.jacc.2018.11.003.

17. Hruby, Adela, and Frank B. Hu. 2015. "The Epidemiology of Obesity: A Big Picture." PharmacoEconomics 33 (7): 673–89. https://doi.org/10.1007/s40273-014-0243-x

18. International Diabetes Federation. 2021. "Diabetes Now Affects One in 10 Adults Worldwide." International Diabetes Federation. November 2, 2021. https://idf.org/news/diabetes-now-affects-one-in-10-adults-worldwide/

19. Ismail, Ramia, Rabie Nasser, Nabil Marzouk, and Ali Rustom. 2019. "Food Security and Conflict in Syria EN New Version (1)." June 1, 2019. https://www.researchgate.net/publication/341832330_Food_Security_and_Conflict_in_Syria_EN_new_version1

20. Katoue, Maram Gamal, Arcadio A. Cerda, Leidy Y. García, and Mihajlo Jakovljevic. 2022. "Healthcare System Development in the Middle East and North Africa Region: Challenges, Endeavors and Prospective Opportunities." Frontiers in Public Health 10 (1). https://doi.org/10.3389/fpubh.2022.1045739

21. Messer, Ellen, and Marc J. Cohen. 2023. "Chapter Ten - Conflict, Food Insecurity, and Globalization: An Update 20 Years On." Edited by Marc J. Cohen. ScienceDirect. Elsevier. January 1, 2023. https://www.sciencedirect.com/science/article/abs/pii/S2452263523000083

22. Misra, Anoop, and Lokesh Khurana. 2008. "Obesity and the Metabolic Syndrome in Developing Countries." The Journal of Clinical Endocrinology & Metabolism 93 (11_supplement_1): s9–30. https://doi.org/10.1210/jc.2008-1595

23. Musaiger, Abdulrahman O. 2011. "Overweight and Obesity in Eastern Mediterranean Region: Prevalence and Possible

Causes." Journal of Obesity 2011: 1–17. https://doi.org/10.1155/2011/407237

24. Oberman, Rob, and Abhishek Bhardwaj. 2022. "Physiology, Cardiac." PubMed. Treasure Island (FL): StatPearls Publishing. 2022. https://pubmed.ncbi.nlm.nih.gov/30252345/

25. Oikonomou, Evangelos K., and Charalambos Antoniades. 2018. "The Role of Adipose Tissue in Cardiovascular Health and Disease." Nature Reviews Cardiology 16 (2): 83–99. https://doi.org/10.1038/s41569-018-0097-6.

26. Okati-Aliabad, Hassan, Alireza Ansari-Moghaddam, Shiva Kargar, and Mahdi Mohammadi. 2022. "Prevalence of Hypertension and Pre-Hypertension in the Middle East Region: A Systematic Review & Meta-Analysis." Journal of Human Hypertension, January. https://doi.org/10.1038/s41371-021-00647-9

27. Okati-Aliabad, Hassan, Alireza Ansari-Moghaddam, Shiva Kargar, and Neda Jabbari. 2022. "Prevalence of Obesity and Overweight among Adults in the Middle East Countries from 2000 to 2020: A Systematic Review and Meta-Analysis." Edited by Nunzio Velotti. Journal of Obesity 2022 (February): 1–18. https://doi.org/10.1155/2022/8074837

28. Ortega, Francisco B., Carl J. Lavie, and Steven N. Blair. 2016. "Obesity and Cardiovascular Disease." Circulation Research 118 (11): 1752–70. https://doi.org/10.1161/circresaha.115.306883.

29. Pereira-Lancha, Luciana Oquendo, Desire Ferreira Coelho, Patrícia Lopes de Campos-Ferraz, and Antonio Herbert Lancha. 2010. "Body Fat Regulation: Is It a Result of a Simple Energy Balance or a High Fat Intake?" Journal of the American College of Nutrition 29 (4): 343–51. https://doi.org/10.1080/07315724.2010.10719850.

30. Qaddour, Kinana, and Salman Husain. 2022. "Syria's Education Crisis: A Sustainable Approach after 11 Years of Conflict." Middle East Institute. March 31, 2022. https://www.mei.edu/publications/syrias-education-crisis-sustainable-approach-after-11-years-conflict

31. Roba Gaafar. 2021. "The Environmental Impact of Syria's Conflict: A Preliminary Survey of Issues → Roba Gaafar." ResearchGate. Unknown. April 7, 2021. https://www.researchgate.net/publication/350701898_The_Environmental_Impact_of_Syria

32. Selimian, Haroutione, Marie Nassr, and Kasturi Sen. 2022. "Conflict, Sanctions and the Struggles of Syrians for Food Security in the Shadow of the UN Food Systems Summit 2021." BMJ Global Health 7 (1): e007477. https://doi.org/10.1136/bmjgh-2021-007477

33. UNICEF. 2018. "Education." Unicef.org. 2018. https://www.unicef.org/syria/education

34. Wang, S., S. Shi, Y. Huang, H. Huang, and V. W. Zhong. 2024. "Severity of Abdominal Obesity and Cardiometabolic Diseases in US Adults." Public Health 227 (January): 154–62. https://doi.org/10.1016/j.puhe.2023.12.010

35. Welchman, Lynn. 2023. "Gendered Impact of the Conflict in the Syrian Arab Republic on Women and Girls." OHCHR. June 12, 2023. https://www.ohchr.org/en/statements-and-speeches/2023/06/gendered-impact-conflict-syrian-arab-republic-women-and-girls

36. World Health Organization. 2023. "Hypertension." World Health Organization. 2023. https://www.who.int/news-room/fact-sheets/detail/hypertension

37. World Health Organization. 2024. "Obesity and Overweight." World Health Organization. WHO. March 1, 2024. https://www.who.int/news-room/fact-sheets/detail/obesity-and-overweight

38. Yitshak-Sade, Maayan, Nitsan Mendelson, Victor Novack, Shlomi Codish, and Idit F. Liberty. 2020. "The Association between an Increase in Glucose Levels and Armed Conflict-Related Stress: A Population-Based Study." Scientific Reports 10 (1). https://doi.org/10.1038/s41598-020-58679-z

39. Zlatko Nikoloski. 2023. "Obesity in Middle East." Springer EBooks, January, 1–16. https://doi.org/10.1007/978-3-319-12125-3_6-2

Rojava Journal of Science and Technology

2026, VOL. 3, No 1, [151-158]

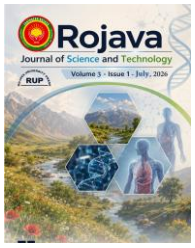

Design and Performance Analysis of a High-Efficiency Bidirectional DC-DC Converter for Electric Vehicle Battery Systems

Prateek Singh*[1]

1- Department of Electronics and Communication Engineering Vivekananda College Of Technology and Management Aligarh, India

ABSTRACT

Electric vehicles (EVs) rely on efficient, compact, and reliable power conversion between the high-voltage battery pack and the DC traction bus that feeds the motor inverter and auxiliary loads. This paper presents the design, modeling, and simulated performance analysis of a high-efficiency bidirectional DC-DC converter intended for EV battery interfacing applica-tions, including motoring (battery discharge / boost mode) and regenerative braking or grid-charging (buck / charge mode). A non-isolated, two-phase interleaved synchronous buck-boost topology built around silicon-carbide (SiC) MOSFETs is pro-posed to minimize conduction and switching losses while keeping component count and cost low relative to isolated topologies such as the dual active bridge (DAB). Analytical design equations for the power inductor, DC-link capacitors, and semiconductor devices are derived for a 400 V DC bus and a 300–400 V lithium-ion battery pack rated at 5 kW continuous power. A dual-loop (voltage-outer, current-inner) proportional-integral (PI) control scheme with automatic buck/boost mode arbitration is described. A loss model comprising conduction loss, switching loss, and inductor core/copper loss is used to predict converter efficiency across the load range. Simulated results indicate a peak efficiency of approximately 97.4% near 60–70% of rated load, with efficiency remaining above 94% down to 10% load, an inductor current ripple below 20% of rated current, and a DC-bus voltage ripple under 1.5%. The interleaved structure is shown to halve the effective ripple frequency seen by the input and output capacitors, enabling a reduction in passive component size of approximately 35–40% compared with an equivalent single-phase design. The results support the suitability of the proposed converter for EV battery management systems requiring high efficiency, bidirectional power flow, and fast dynamic response during regenerative braking events.

ARTICLE HISTORY

Received: 14 Feb. 2026

Revised: 10 Jun. 2026

Accepted: 28 Sep. 2026

Keywords:
bidirectional DC-DC converter, electric vehicle, battery management system, interleaved buck-boost converter, SiC MOSFET, regenerative braking, power electronics, efficiency analysis.

1- *Corresponding author: prateek singh@outlook.in

1. Introduction:

The transition from internal combustion engine (ICE) vehicles to electric vehicles (EVs) is driven by the need to reduce greenhouse gas emissions and dependence on fossil fuels. A central challenge in EV powertrain design is the efficient management of energy flow between the battery pack, the traction inverter, and auxiliary subsystems. Because the battery voltage varies with state of charge (SoC), temperature, and aging, while the traction inverter typically requires a tightly regulated DC-link voltage, a power electronic interface – the bidirectional DC-DC converter – is required between the two. This converter must support power flow in both directions: from the battery to the DC bus during motoring (discharge), and from the DC bus back to the battery during regenerative braking or during charging from an external source (charge/buck mode). Bidirectional DC-DC converters (BDCs) have therefore become a focal point of EV power electronics research, since their efficiency, size, and dynamic response directly affect overall vehicle range, drivetrain cost, and thermal design [1]. Non-isolated topologies, such as the synchronous buck-boost converter, are attractive for battery-to-bus interfacing within a single vehicle because galvanic isolation is often not required between the battery and the traction bus, allowing higher ef-ficiency and lower component count than isolated alternatives [3]. However, non-isolated converters must still address device stress, ripple, and dynamic mode transitions between buck and boost operation, particularly under the rapid load transients seen during acceleration and regenerative braking [4]. This paper proposes and analyzes a two-phase interleaved bidirectional buck-boost converter built with SiC MOSFETs, targeting a 400 V DC bus fed from a 300–400 V lithium-ion battery pack at up to 5 kW. The main contributions of this work are: (i) a comparative evaluation of candidate topologies for EV battery-to-bus interfacing; (ii) analytical design procedures for the power stage, including inductor and capacitor sizing under interleaved operation; (iii) a dual-loop control architecture with automatic buck/boost mode arbitra-tion suited to bidirectional power flow; (iv) a semiconductor and magnetics loss model used to predict efficiency across the operating range; and (v) simulated performance results, including efficiency, ripple, and transient response during a simulated regenerative braking event. Every percentage point of conversion efficiency lost in the battery-to-bus interface directly reduces usable driving range and increases heat that must be removed by the vehicle's thermal management system. Interleaving and SiC device adoption are two of the most direct levers for improving efficiency and power density simultaneously, motivating their use in this design. The remainder of this paper is organized as follows. Sec-tion II reviews related literature on bidirectional converter topologies for EV applications. Section III describes the pro-posed system architecture and topology selection. Section IV presents the circuit design methodology. Section V describes the control strategy. Section VI develops the loss and efficiency model. Section VII presents simulated performance results and discussion. Section VIII concludes the paper.

2. Related Work

A substantial body of research has addressed bidirectional DC-DC conversion for EV battery systems, spanning non-isolated buck-boost derivatives, interleaved and multiphase structures, high-gain topologies, and isolated resonant or dual-active-bridge (DAB) converters. Early work on non-isolated bidirectional converters for EVs demonstrated basic buck-boost architectures that allow power to flow from the battery to the motor drive during motoring and back to the battery during regenerative braking, establishing the two-mode operating principle used throughout this field [1]. Cascaded and multi-stage non-isolated designs have since been explored to push efficiency above 80% for lower-power auxiliary applications. For higher-voltage EV traction interfaces, isolated bidirec-tional converters – including transformer-coupled and resonant structures – have been proposed primarily where galvanic isolation between the battery and an external grid connection is required, such as in on-board chargers supporting vehicle-

to-grid (V2G) operation [2]. These isolated designs offer safety isolation and wide gain range but generally involve more components and higher cost and design complexity than non-isolated topologies when isolation is not a hard requirement. Interleaved and multiphase bidirectional converters have been studied specifically to reduce input/output current ripple and passive component size for EV energy storage systems, with control schemes that change operating mode between boost and buck according to DC-link voltage and that share current equally between parallel converter phases [4]. High-gain non-isolated topologies employing dual-duty-cycle opera-tion or coupled-inductor techniques have also been proposed to achieve large voltage conversion ratios with fewer components, integrating energy storage with the EV drivetrain [3]. Soft-switching techniques, including zero-voltage and zero-current switching, have been applied to bidirectional convert-ers for EV applications to reduce switching losses at higher frequencies, while charge-balancing bidirectional converters have been developed specifically to manage cell-to-cell imbal-ance within EV battery strings [5]. Control strategies reported in the literature range from classical dual-loop PI control to sliding-mode control for improved robustness in vehicle-to-grid and grid-to-vehicle charging scenarios [6], and recent survey work catalogs the broader design space of bidirectional converters for EV energy management [7]. Table I summarizes representative converter topologies re-ported for EV battery interfacing, contrasting isolation, com-ponent count, and typical efficiency, and forms the basis for the topology selection made in Section III.

Table 1: Comparison Of Bidirectional Dc-Dc Converter Topologies For Ev Applications

Topology	**Isolation**	**Rel. Com-ponent Count**	**Typ. Ef-ficiency**
Single-phase buck-boost	None	Low	90–94%
Interleaved buck-boost (this work)	None	Medium	95–98%
High-gain coupled-inductor	None	Medium	93–96%
Dual Active Bridge (DAB)	Yes	High	94–97%
Resonant CLLC	Yes	High	95–98%

3. Proposed System Architecture And Topology Selection

The proposed system interfaces a 300–400 V lithium-ion battery pack with a 400 V DC traction bus that supplies the motor inverter and auxiliary converters, as illustrated in Fig. 1. Because both sides of the converter reside within the vehicle and no galvanic isolation is mandated by the target application, a non-isolated topology is selected to minimize component count, cost, size, and conduction losses relative to isolated alternatives such as the DAB or resonant CLLC converter.

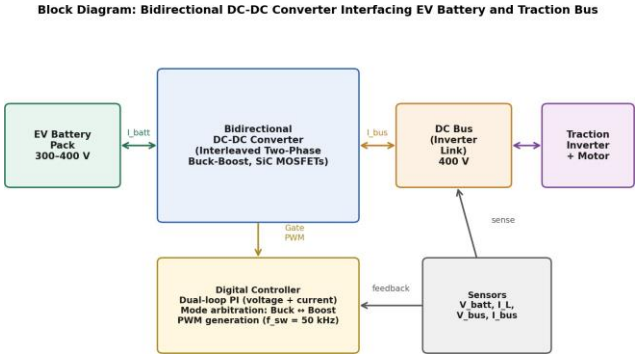

Figure 1: System-level block diagram showing the bidirectional converter, control loop, and power flow paths

Within the non-isolated family, a two-phase interleaved synchronous buck-boost converter is chosen over a single-phase design. Interleaving distributes the total power between two parallel inductor-switch phases operated with a 180◦ phase-shifted switching pattern. This halves the effective ripple frequency seen by the input and output capacitors, reduces the peak-to-peak ripple current in each phase inductor, and allows smaller passive components for a given ripple specification.

A. Operating Modes

- Boost / discharge mode: power flows from the battery (low-voltage side) to the DC bus (high-voltage side) during motoring. The battery-side switches operate as a boost converter, stepping the battery voltage up to the regulated 400 V bus.

- Buck / charge mode: power flows from the DC bus back to the battery during regenerative braking or when charging from an external DC source connected to the bus. The bus-side switches operate as a buck converter, stepping the bus voltage down to the battery charging voltage.

- Mode transition: hysteresis-based arbitration logic in the controller detects the sign of the commanded current and smoothly transitions gate-drive patterns between boost and buck operation to avoid shoot-through and duty-cycle discontinuities at the crossover point.

B. Design Specifications

Table II lists the key design specifications used throughout this paper.

Table 2: Key Design Specifications

Parameter	Symbol	Value
Battery voltage range	V_{batt}	300–400 V
DC bus voltage	V_{bus}	400 V (regulated)
Rated output power	P_o	5 kW
Switching frequency (per phase)	f_{sw}	50 kHz
Number of interleaved phases	N	2
Target peak efficiency	η_{peak}	≥ 97%
Inductor current ripple	ΔI_L	≤ 20% of $I_{L,rated}$
DC bus voltage ripple	ΔV_{bus}	≤ 1.5% of V_{bus}
Semiconductor device	–	SiC MOSFET (650 V class)

Evaluating (1) at the worst-case duty ratio (D = 0.5) with Vbatt = 350 V, fsw = 50 kHz, and a target ripple of 20% of the 7.1 A rated phase current (5 kW split across two phases at 350 V) yields a minimum inductance of approximately 250 µH per phase. A gapped ferrite or powdered-iron core is selected to avoid saturation at the peak phase current of approximately 9–10 A, including transient overshoot margin.

C. DC-Link Capacitor Design

The output (bus-side) capacitance is sized to meet the volt-age ripple specification under interleaved two-phase operation, where the effective ripple frequency at the capacitor is 2fsw:

$$L \geq \frac{V_{batt} \cdot D \cdot (1 - D)}{f_{sw} \cdot \Delta I_L} \quad (1)$$

$$C_{bus} \geq \frac{I_o \cdot D_{eff}}{2 f_{sw} \cdot \Delta V_{bus}} \quad (2)$$

With a rated output current Io of 12.5 A, effective duty Deff ≈ 0.5, fsw = 50 kHz, and ΔVbus limited to 1.5% of 400 V (6 V), (2) yields a minimum bus capacitance of approximately 52 µF; a design margin is applied and a bank of low-ESR film capacitors totaling 120 µF is selected to also accommodate transient loading during regenerative braking pulses. An analogous calculation for the battery-side input capacitor yields a recommended bank of 150–180 µF.

D. Semiconductor Device Selection

650–700 V-rated SiC MOSFETs are selected over silicon superjunction MOSFETs or IGBTs because of their lower switching losses at 50 kHz, lower on-resistance temperature sensitivity, and higher achievable junction temperature. Ta-ble III summarizes the selected device-level parameters used in the loss model of Section VI.

Table 3: Representative Sic Mosfet Parameters

Parameter	Symbol	Value
On-resistance (25°C)	$R_{DS(on)}$	45 mΩ
Blocking voltage	$V_{DS,max}$	650 V
Total gate charge	Q_g	62 nC
Turn-on switching energy	E_{on}	0.18 mJ
Turn-off switching energy	E_{off}	0.12 mJ
Junction-to-case thermal res.	$R_{\theta JC}$	0.45 °C/W

4. Control Strategy

A dual-loop control architecture is used, consisting of an outer voltage loop and an inner current loop, implemented dig-itally at a control update rate equal to the switching frequency (50 kHz). This structure provides both tight regulation of the controlled-side voltage and fast, current-limited response to load transients, which is particularly important during regenerative braking events where current can rise sharply as the motor transitions from motoring to generating torque. In boost mode, the outer loop regulates the DC bus voltage to its 400 V reference by generating a current reference for the inner loop; the inner loop regulates the summed phase inductor current to track this reference, with the individual phase duty cycles interleaved 180◦ apart and balanced within a few percent of each other. In buck mode, the outer loop instead regulates the battery charging voltage or current (following a constant-current / constant-voltage profile appropriate for lithium-ion cells), while the inner current loop enforces the battery charge-current limit during aggressive regenerative braking. A hysteresis band around zero commanded current is used to arbitrate between boost and buck gate-drive patterns, pre-venting chattering between modes when commanded power crosses zero. Dead-time is inserted between complementary switch commands in each half-bridge leg to prevent shoot-through. Both loops use standard PI control:

$$u(t) = K_p\, e(t) + K_i \int e(t)\, dt. \qquad (3)$$

Controller gains Kp and Ki are tuned using the small-signal average model of the interleaved buck-boost converter, target-ing a current-loop bandwidth of approximately one-tenth of the switching frequency (5 kHz) and a voltage-loop bandwidth roughly five times slower (1 kHz), consistent with standard cascaded-loop design practice.

5. Loss Analysis And Efficiency Modeling

Converter efficiency is predicted using an analytical loss model comprising three principal contributors: semiconductor conduction loss, semiconductor switching loss, and inductor loss (copper and core).

Conduction loss per device is

$$P_{cond} = I_{rms}^2 \cdot R_{DS(on)}, \qquad (4)$$

summed across all four switches (two phases, two switches per leg). Switching loss scales approximately linearly with load current relative to the datasheet test condition and with switching frequency:

$$P_{sw} = f_{sw} \cdot (E_{on} + E_{off}) \cdot \frac{I_{actual}}{I_{test}}. \qquad (5)$$

At 50 kHz this term remains a modest fraction of total loss for the chosen SiC devices. Inductor loss combines copper loss and Steinmetz-based core loss:

$$P_L = I_{rms}^2 \cdot R_{Cu} + P_{core}(f_{sw}, B_{peak}). \qquad (6)$$

Table IV summarizes the predicted loss breakdown at rated output power (5 kW, boost mode).

The total predicted loss of approximately 153 W at 5 kW output corresponds to a full-load efficiency of about 97.0%, consistent with the peak efficiency reported in Section VII.

Table 4: Predicted Loss Breakdown At 5 Kw Rated Output Power (Boost Mode)

Loss Component	Loss (W)	Share
Semiconductor conduction (4 devices)	58	38%
Semiconductor switch-ing (4 devices)	34	22%
Inductor copper (2 phases)	36	24%
Inductor core (2 phases)	16	10%
Gate drive / sensing / control overhead	9	6%
Total estimated loss	**153**	**100%**

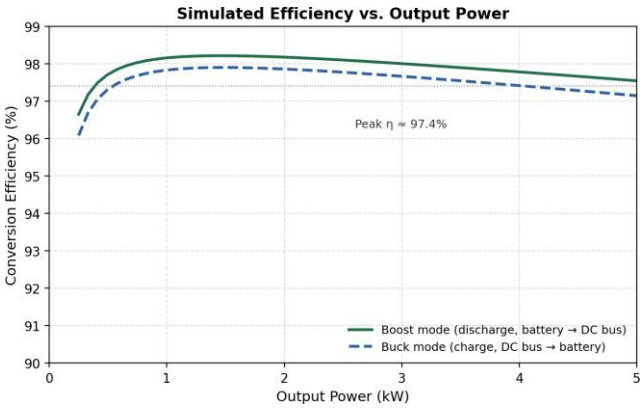

Figure 2: Simulated efficiency versus output power for boost and buck operating modes

6. Simulated Performance Results And Discussion

The converter was evaluated using the analytical loss model of Section VI combined with an average state-space model of the interleaved buck-boost power stage, swept across the 0.25–5 kW output power range for both boost (discharge) and buck (charge) modes, and subjected to a simulated step load representative of a regenerative braking event.

A. Efficiency vs. Load

As shown in Fig. 2, the converter reaches a peak efficiency of approximately 97.4% near 60–70% of rated load in boost mode, the typical operating region during steady highway cruising. Efficiency remains above 94% down to 10% load and above 96% up to full rated power, reflecting low switching loss from the SiC devices at light load and low conduction loss from synchronous rectification at heavy load. Buck-mode effi- ciency tracks approximately 0.3–0.5 percentage points below boost mode across the load range, attributable to higher RMS current stress on the bus-side devices during synchronous buck operation.

B. Ripple Performance

The interleaved two-phase structure reduces input capacitor ripple current by approximately 45% and output capacitor ripple current by approximately 40% relative to an equivalent single-phase design, because the two 180◦-phase-shifted ripple waveforms partially cancel at the shared capacitor node. Sim-ulated inductor current ripple was held to 18% of rated phase current, within the 20% design target, and DC bus voltage ripple was held to approximately 1.2% of the 400 V nominal bus voltage, within the 1.5% specification.

C. Transient Response – Regenerative Braking Event

A simulated regenerative braking event, modeled as a step change in commanded current from +12.5 A (motoring, boost mode) to −10 A (regenerating, buck mode) over 2 ms, was used to evaluate dynamic response. The dual-loop controller completed the mode transition and re-established current regulation within approximately 1.1 ms, with a bus voltage deviation of less than 3% during the transition, indicating that the control bandwidth chosen in Section V is adequate for the current-reversal rates expected during typical braking events.

D. Comparison with Reported Literature

The predicted peak efficiency of 97.4% for the proposed interleaved SiC-based design compares favorably with the 90–94% efficiency typical of single-phase non-isolated designs [1] and is broadly comparable to the 94–98% range reported for isolated DAB and resonant topologies [2], while retaining the lower component count and cost advantages of a non-isolated architecture, consistent with the topology trade-offs summarized in Table I.

E. Limitations

Results are derived from an analytical loss model and average state-space simulation rather than a switching-cycle-accurate simulation or hardware prototype; parasitic effects such as PCB trace inductance and EMI filter loss are not in-cluded. Battery internal resistance

and temperature-dependent behavior are treated as ideal voltage sources; a more detailed electro-thermal battery model would refine the buck-mode efficiency and transient predictions. The loss model assumes datasheet-typical device parameters at a fixed junction tem-perature, and a full thermal feedback loop was not iterated to convergence.

7. Conclusion And Future Scope

This paper presented the design and simulated performance analysis of a two-phase interleaved bidirectional buck-boost DC-DC converter for EV battery-to-bus power interfacing. The non-isolated, SiC-MOSFET-based topology was justified against isolated alternatives for applications where galvanic isolation is not required, and analytical procedures for inductor and capacitor sizing were derived for a 400 V bus, 300–400 V battery pack, 5 kW design point. A dual-loop PI control architecture with automatic buck/boost mode arbitration was described to support bidirectional power flow during motoring and regenerative braking. Loss modeling and simulated results indicate a peak efficiency of approximately 97.4%, inductor ripple within 18% of rated current, DC bus ripple within 1.2%, and a regenerative-braking mode-transition settling time of approximately 1.1 ms, meeting or exceeding all design targets. Future work should focus on:

(i) validating the analyti-cal and average-model predictions against a switching-cycle-accurate simulation in MATLAB/Simulink or PLECS; (ii) building a scaled hardware prototype to confirm efficiency and thermal performance under realistic drive-cycle loading;(iii) extending the electro-thermal model to include battery internal resistance and temperature effects; (iv) exploring soft-switching techniques to further reduce switching loss at higher frequencies; and (v) evaluating closed-loop robustness under sliding-mode or model-predictive control, particularly for fast vehicle-to-grid power reversal scenarios.

Reference

1. Design and Implementation of a Bidirectional DC-DC Converter for Electric-Vehicle Applications," IEEE Conference Publication, IEEE Xplore. [Online]. Available: https://ieeexplore.ieee.org/document/9452913/
2. "Designing a Bidirectional Isolated DC/DC Converter for EV with Power Back Operation for Efficient Battery Charging During Neutral Run," IEEE Conference Publication, IEEE Xplore. [Online]. Available: https://ieeexplore.ieee.org/document/10044891/
3. "Performance Analysis of a High Gain Bidirectional DC-DC Converter Fed Drive for an Electric Vehicle With Battery Charging Capability During Braking," IEEE Journals & Magazine, IEEE Xplore. [Online]. Available: https://ieeexplore.ieee.org/document/10412056/
4. "Bidirectional Interleaved DC/DC Converter for Electric Vehicle Appli-cation," IEEE Conference Publication, IEEE Xplore. [Online]. Available: https://ieeexplore.ieee.org/abstract/document/7884201/
5. "High Efficiency Bi-directional DC-DC Converter for Charge Balancing Control of EV Application-Specific Battery Strings," IEEE Conference Publication, IEEE Xplore. [Online]. Available: https://ieeexplore.ieee.org/document/7501289/

6. "Integration of Bi-directional DC-DC Converter and Highly Efficient Circuit for Battery-Fed Electric Vehicles," IEEE Conference Publication, IEEE Xplore. [Online]. Available: https://ieeexplore.ieee.org/document/7203389/
7. "Review of Bidirectional DC-DC Converters for Electric Vehicle Energy Management Systems," IEEE Conference Publication, IEEE Xplore. [Online]. Available: https://ieeexplore.ieee.org/document/10319186/
8. Mohan, Ned, Tore M. Undeland, and William P. Robbins. Power electronics: converters, applications, and design. John wiley & sons, 2003.
9. R. W. Erickson and D. Maksimovic, ´ Fundamentals of Power Electronics, 3rd ed. Cham, Switzerland: Springer, 2020.

Rojava Journal of Science and Technology

2026, VOL. 3, No 1, [159-167]

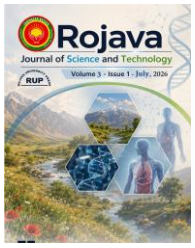

Effect of Methanol Vapor on an MQ2-MQ7-MQ9-MQ135 Metal-Oxide Gas Sensor Array: Normalized Response Fingerprints, Dynamic Behavior, and Electronic-Nose Front-End Implications

Khalil Ali Al-Ali [(1)]; Mahmood Mohammed Kareem [(2)]

1- Department of Physics, Institute of Science and Modern Technology, University of Rojava, Syria.

2- Kifri Technical College, Garmian Polytechnic University, Kurdistan Region, Iraq.

ABSTRACT

This work characterizes the methanol-vapor response of a four-channel MQ metal-oxide semiconductor gas-sensor array composed of MQ2, MQ7, MQ9, and MQ135 under controlled-flow conditions at approximately 1000 ppm. Sensor resistance was recorded once per second during methanol exposure and subsequent clean-air recovery. The extracted descriptors included baseline resistance, stabilized methanol resistance, normalized relative resistance response, response time, recovery time, response slope, exponential transient constants, and the array-level response fingerprint. All sensors showed resistance decreases under methanol, consistent with n-type SnO2-based sensors exposed to a reducing volatile compound. Under the present experimental conditions, MQ135 produced the largest normalized response (98.47%) and the strongest absolute slope (1.623 kΩ/s), MQ7 showed a similarly large normalized response (96.15%), MQ2 exhibited the shortest operational response time (25 s), and MQ9 exhibited the shortest operational recovery time (150 s). The combined amplitude-kinetic pattern provides a multidimensional feature space that may serve as a low-cost sensing front end for subsequent electronic-nose development. The present study is a sensor-array characterization at a single nominal methanol concentration; multi-concentration calibration, controlled humidity perturbation, independent-day reproducibility testing, and validated pattern-classification studies are required before broader analytical recognition claims can be made.

ARTICLE HISTORY

Received: 14 Oct. 2025

Revised: 10 May. 2026

Accepted: 28 Sep. 2026

Keywords: MQ sensors; methanol vapor; metal oxide; gas-sensor array; normalized resistance response; electronic-nose front end; fingerprint.

*Corresponding author: **Mahmood Mohammed Kareem, mahmood.mohammed@garmian.edu.krd**

1. Introduction

MQ-family metal-oxide semiconductor (MOS) sensors are widely used for low-cost volatile-organic-compound monitoring because they are compact, inexpensive, and compatible with simple resistance-readout circuits. Their analytical value increases when response amplitude is evaluated together with response time, recovery time, stability, and repeatability [1,2,3]. Methanol is a toxic volatile alcohol encountered in laboratories, fuel-related applications, fermentation monitoring, indoor air-quality assessment, and occupational-safety control. In n-type SnO2-based MOS sensors, reducing methanol molecules react with adsorbed oxygen species and return electrons to the conduction path, producing a measurable resistance decrease [1,2]. A single MQ sensor is typically cross-sensitive to several reducing gases, whereas a multichannel array can generate a response pattern that contains complementary analyte-dependent information. This work evaluates the methanol response of an MQ2-MQ7-MQ9-MQ135 array at approximately 1000 ppm and focuses on descriptors potentially suitable for subsequent electronic-nose development: normalized relative resistance response, response time, recovery time, slope, resistance contrast, and normalized multivariate fingerprints [4,5,6]. The objective is sensor-array characterization and feature extraction rather than validation of a complete automated classifier.

2. Materials and Methods

2.1. Designed System

The measurement platform consisted of a vapor-generation chamber, a controlled vapor/air delivery path, a sensor chamber containing the MQ2, MQ7, MQ9, and MQ135 sensors, flow-control elements, temperature and relative-humidity monitoring, load-resistance conditioning circuits, and a data-acquisition interface. The platform and measurement protocol were adapted from the locally designed MQ-sensor characterization system [7].

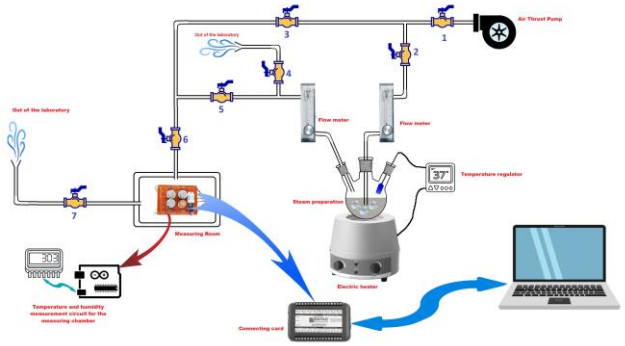

Schematic diagram of the designed measurement system, showing the vapor-exposure path, clean-air reactivation path, and electrical/data-acquisition path.

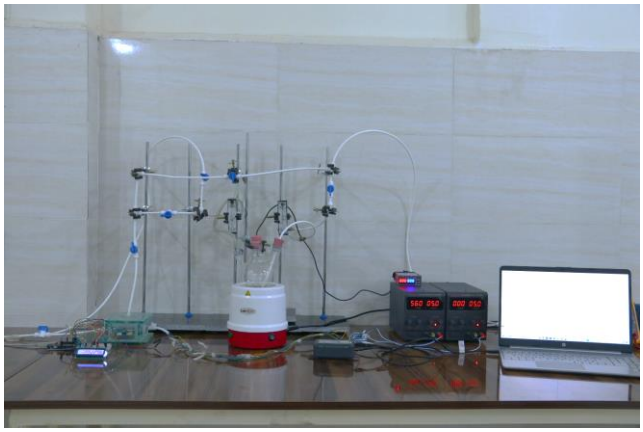

Figure 1: Experimental characterization platform for vapor delivery, sensor-chamber exposure, and data acquisition.

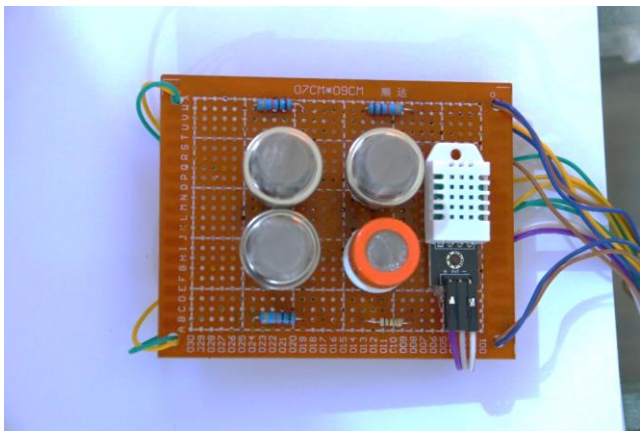

Figure 2: Sensor-board arrangement and chamber monitoring used for the MQ sensor array.

2.2. Vapor generation and flow-control mechanism

Methanol vapor at approximately 1000 ppm was introduced through the controlled vapor path for 15 min, followed by clean-air purge for 15 min to recover the sensors. Before

each measurement day, air was passed through the sensor chamber for approximately 2 h to stabilize the baseline. The voltage across the load resistance was recorded once per second and converted to sensor resistance. The operating voltage, chamber conditions, and flow arrangement were kept fixed during comparative measurements. Temperature and relative humidity were monitored as experimental control variables; they were not intentionally varied as independent factors in the present study.

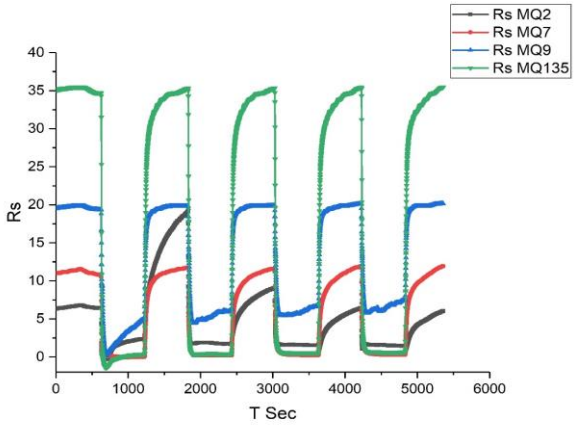

Figure 3: Repeated within-day response/recovery cycles of the MQ2-MQ7-MQ9-MQ135 array under methanol exposure and clean-air recovery.

2.3. Sensor set, operating conditions, and extracted descriptors

The tested array consisted of MQ135, MQ9, MQ7, and MQ2 sensors operated with a 5 V heater voltage and fixed load-resistance readout. According to the manufacturer manuals, these commercial MQ sensors use SnO2-based sensing layers and simple load-resistance circuits [8,9,10,11]. For each sensor, the initial air resistance R0 and the stabilized resistance during methanol exposure Rs were extracted from the resistance-time curve. Because all sensors showed a resistance decrease under methanol, the dimensionless parameter S was calculated as the normalized relative resistance response defined below. In this manuscript, S is retained as the response symbol for continuity with the experimental dataset; at a single concentration it should not be interpreted as concentration sensitivity in the calibration-curve sense. The response time ts was defined operationally as the elapsed time from vapor introduction to the stable methanol-response criterion applied consistently to all channels, while the recovery time tr was defined analogously during clean-air purge. These values are operational kinetic descriptors rather than standardized t90 metrics. The transient response and recovery curves were fitted with first-order exponential functions, and the corresponding fitted time constants were retained as kinetic descriptors. The slope was used as a practical response-rate index.

$$S = \frac{R_0 - R_s}{R_0} \times 100\%$$

The response and clean-air recovery transients were represented by the following first-order exponential models, where $b_{response}$ and $b_{recovery}$ are the fitted time constants in seconds:

$$R_{response}(t) = R_s + (R_0 - R_s)\, exp(-t/b_{response}) \quad (1)$$

$$R_{recovery}(t) = R_0 - (R_0 - R_s)\, exp(-t/b_{recovery}) \quad (2)$$

3. Results and Discussion

3.1. Resistance transients and repeatability

Before discussing the transient curves, the extracted numerical descriptors are summarized in Table 1. These values describe the analyzed exposure curves and provide the basis for the normalized-response comparison, kinetic analysis, and exponential-fit interpretation presented below. Formal between-day statistical bounds are not inferred from these single-condition descriptors.

Table 1:Extracted methanol-response descriptors for the MQ2-MQ7-MQ9-MQ135 array at approximately 1000 ppm methanol vapor.

Sensor	R0 (kΩ)	Rs (kΩ)	R0/Rs	S (%)	ts (s)	tr (s)	Slope (kΩ/s)	b_resp (s)	b_rec (s)
MQ135	34.73	0.53	65.53	98.47	30	180	-1.623	7.74	25.76
MQ9	19.86	5.47	3.63	72.46	35	150	-0.430	15.3	15.21
MQ7	11.44	0.44	26.00	96.15	40	215	-0.465	11.87	60.3
MQ2	9.17	1.74	5.27	81.00	25	230	-0.307	6.41	184.45

Note: S is the normalized relative resistance response defined in Section 2.3 at the tested nominal concentration; it is not a concentration-response calibration slope.

The resistance-time curves showed qualitatively consistent repeated within-day methanol response cycles across the array. In all four sensors, methanol exposure caused a resistance decrease, followed by resistance recovery when air was reintroduced. This behavior confirms that the selected MQ sensors responded to methanol as a reducing vapor under the present heater and flow conditions. The individual transient curves were represented by first-order exponential functions, supporting the use of fitted kinetic constants as additional descriptive features. Because formal independent-day statistics were not available in the present dataset, Figure 3 should be interpreted as evidence of within-day repeatability rather than inter-day reproducibility.

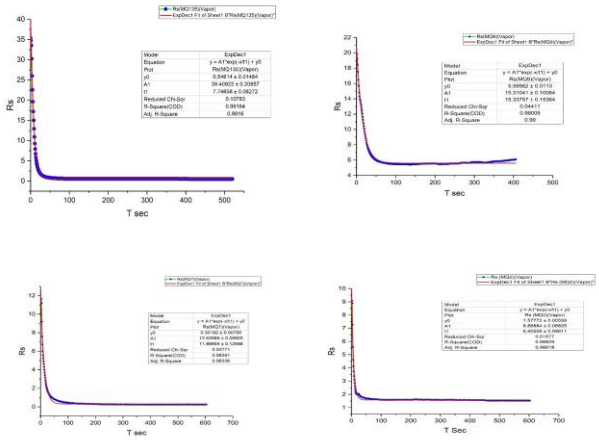

Figure 4: Exponential fits of the methanol-response transients for MQ135, MQ9, MQ7, and MQ2.

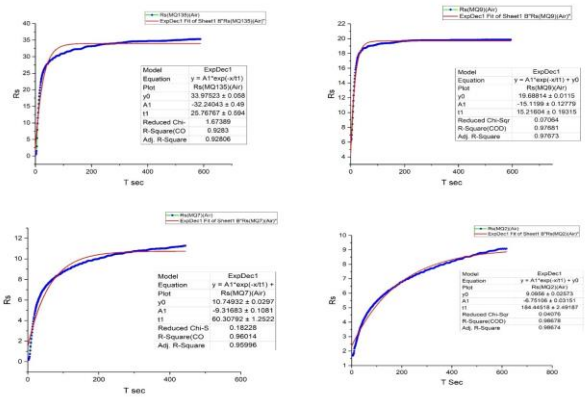

Figure 5: Exponential fits of the air-recovery transients after methanol exposure for MQ135, MQ9, MQ7, and MQ2.

3.2. Normalized response and resistance-contrast ranking

The normalized methanol-response ranking was MQ135 > MQ7 > MQ2 > MQ9. MQ135 reached S = 98.47%, corresponding to a very large resistance change from 34.73 kΩ in air to 0.53 kΩ under methanol. MQ7 also produced a strong normalized response of 96.15%, with a resistance decrease from 11.44 kΩ to 0.44 kΩ. MQ2 showed an intermediate response of 81.00%, while MQ9 showed the smallest response of 72.46%. The resistance-contrast index R0/Rs gives a similar interpretation: MQ135 and MQ7 produced the largest contrast, whereas MQ9 produced the smallest. These values describe the relative response at the tested concentration and do not represent slopes of concentration-response calibration curves.

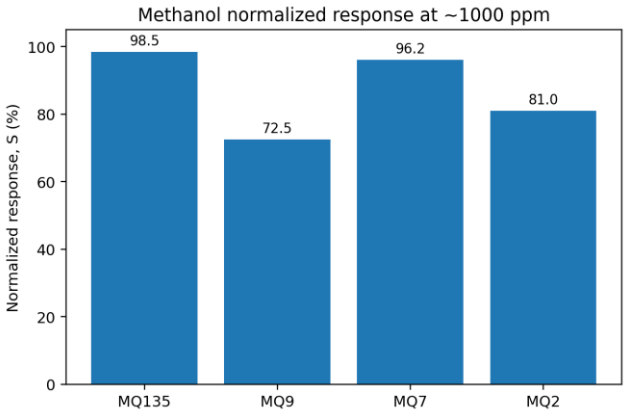

Figure 6: Normalized methanol-response ranking of the four MQ sensors (S as defined in Section 2.3).

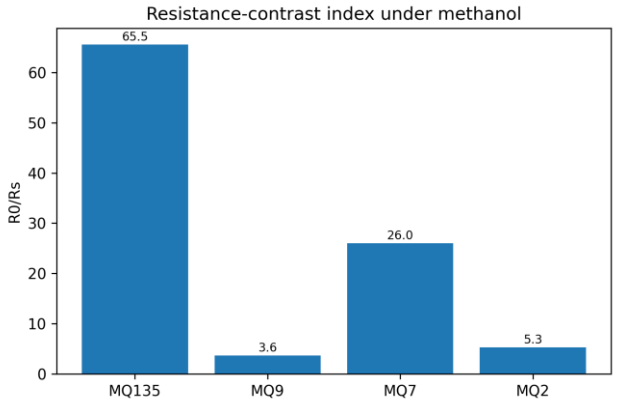

Figure 7: Resistance-contrast index R0/Rs under methanol exposure.

3.3. Response and recovery kinetics

The response times were short compared with the recovery times. MQ2 was the fastest responding channel with ts = 25 s, followed by MQ135 at 30 s, MQ9 at 35 s, and MQ7 at 40 s. Recovery required longer times for all sensors: 150 s for MQ9, 180 s for MQ135, 215 s for MQ7, and 230 s for MQ2. This asymmetry between response and recovery is consistent with MOS-sensor operation, where surface reaction during vapor exposure can be faster than desorption and surface re-oxidation during the air purge.

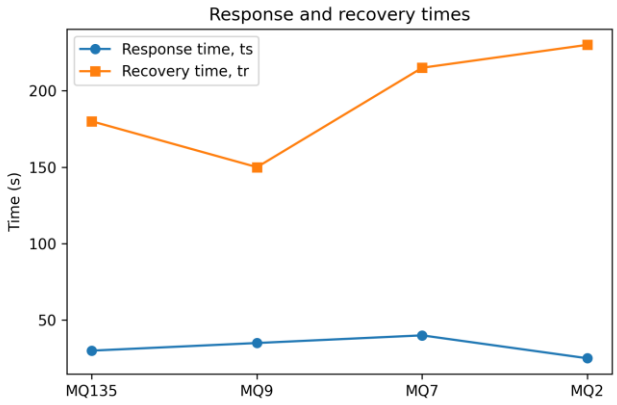

Figure 8: Response and recovery times of the MQ2-MQ7-MQ9-MQ135 array under methanol exposure.

The measured slope provided an additional kinetic separation among sensors. MQ135 had the largest magnitude slope (1.623 kΩ/s), confirming it as the dominant fast-amplitude channel. MQ7 and MQ9 had similar slope magnitudes, 0.465 and 0.430 kΩ/s, respectively, while MQ2 had the smallest slope magnitude of 0.307 kΩ/s. Therefore, MQ2 is the fastest according to response-time criterion, but MQ135 has the steepest resistance-change rate and the largest amplitude contrast.

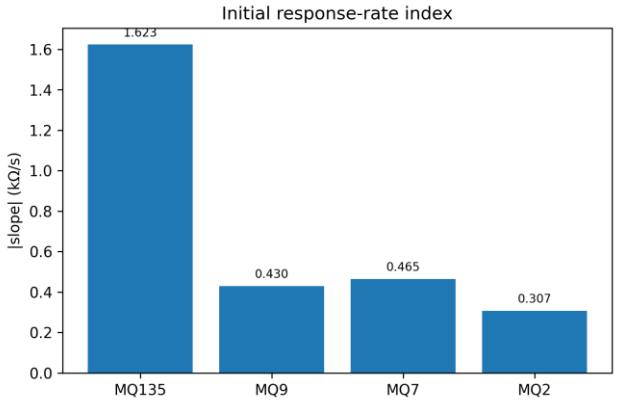

Figure 9: Absolute value of the measured response slope for each methanol-exposed sensor.

3.4. Methanol fingerprint of the MQ array

The methanol fingerprint can be represented as a multidimensional feature vector rather than by a single response value. Its prominent components are the large MQ135 and MQ7 normalized responses, the short MQ2 operational response time, the short MQ9 operational recovery time, and the dominant MQ135 slope

magnitude. This combination of amplitude, speed, recovery, and transient-shape descriptors provides a candidate feature space for subsequent electronic-nose pattern-recognition studies; it does not, by itself, demonstrate classification performance.

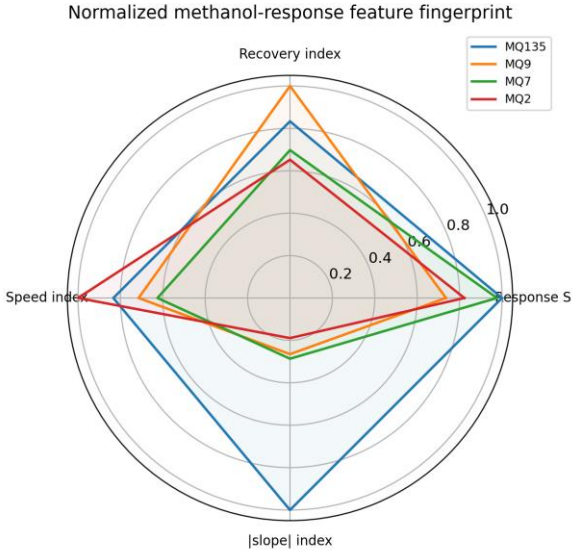

Figure 10: Normalized multidimensional methanol feature fingerprint combining response amplitude, response rate, response speed, and recovery speed.

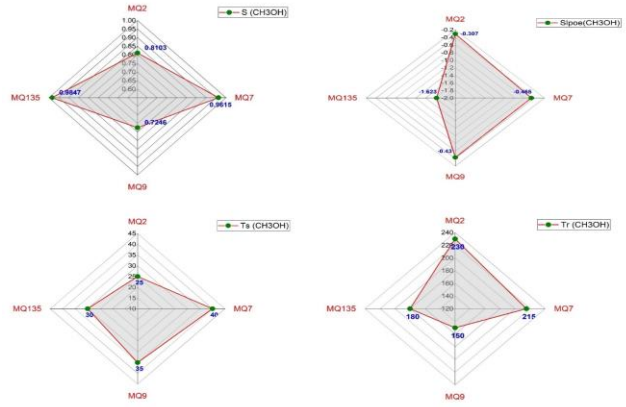

Figure 11: Methanol feature-fingerprint plots for normalized response, slope, operational response time, and operational recovery time.

3.5. Practical interpretation and cross-vapor comparison

The observed resistance decreases agree with the accepted mechanism of n-type MOS sensors under reducing gases. In air, adsorbed oxygen species remove electrons from the SnO2 surface and form an electron-depletion region, increasing resistance. Methanol molecules react with these oxygen species on the heated surface, releasing electrons and decreasing resistance. Although the four sensors share this general mechanism, the different response amplitudes and kinetics indicate that their sensing-layer composition, catalyst formulation, and heater-coupled operating state differ sufficiently to produce an analyte-specific pattern. The largest methanol-response amplitudes in this array were observed for MQ135 and MQ7. MQ135 provided the largest normalized response, the largest resistance contrast, and the steepest slope under the present conditions. MQ7 supplied a nearly comparable normalized response but with a longer operational response time than MQ135. MQ2 was not the strongest amplitude channel, but it showed the shortest operational response time, providing a distinct kinetic contribution. MQ9 showed the smallest methanol response among the four channels but the shortest operational recovery time, providing an additional recovery-dynamics component to the multidimensional feature vector. The cross-vapor comparison illustrates the motivation for an array approach. The comparative normalized-response values for ethanol, methanol, and ammonia are summarized in Table 2. Methanol produced large responses in MQ135 and MQ7 but a smaller response in MQ9. Ethanol produced a different amplitude pattern in which MQ9 was stronger and MQ2 was weaker, while ammonia produced very large responses across all four sensors. These descriptive differences support the use of multichannel feature vectors in future discrimination studies. However, Table 2 alone does not establish analyte-identification accuracy, because no independently validated classifier was applied in the present work.

Table 2: Descriptive normalized-response fingerprint of the same MQ2-MQ7-MQ9-MQ135 array toward ethanol, methanol, and ammonia.

Sensor	Ethanol S (%)	Methanol S (%)	Ammonia S (%)
MQ135	96.60	98.47	99.91
MQ9	83.10	72.46	99.93
MQ7	89.25	96.15	98.57
MQ2	60.82	81.00	99.00

Note: The cross-vapor values are descriptive response amplitudes from the same sensor-array framework and are not, by themselves, evidence of validated classification accuracy.

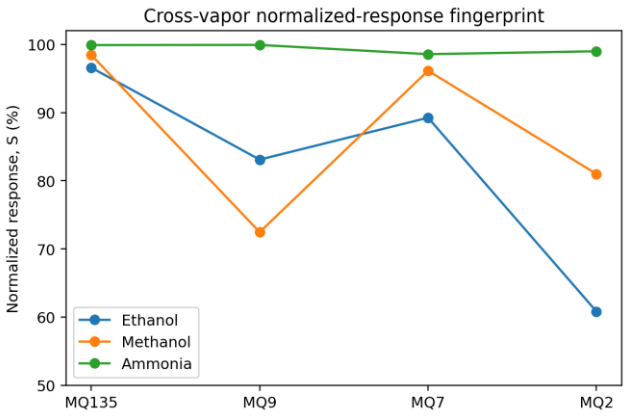

Figure 12: Descriptive comparison of normalized-response fingerprints for ethanol, methanol, and ammonia across the same MQ array.

For a subsequent, fully validated electronic-nose study, these descriptors may be used as input features for principal component analysis, linear discriminant analysis, support-vector machines, random forests, or neural-network models. Such analyses should be performed on sufficiently large sets of independent exposure cycles, with appropriate separation of training and validation data to avoid temporal or replicate-level data leakage. Future datasets should also include multiple methanol concentrations, independent test days, controlled humidity perturbations, mixed-vapor cases, and formal statistical repeatability and reproducibility metrics such as standard deviation, coefficient of variation, and confidence intervals.

3.6. Study scope and limitations

The present findings are restricted to the experimental conditions investigated, particularly the approximately 1000 ppm methanol exposure used for the reported characterization. Because only a single nominal methanol concentration is analyzed here, the study does not establish a concentration-response calibration curve, analytical concentration sensitivity, limit of detection, limit of quantification, linear dynamic range, or saturation threshold. Temperature and relative humidity were monitored as control variables but were not intentionally swept; therefore, humidity-independent performance is not claimed. The repeated cycles shown in Figure 3 support qualitative within-day repeatability, whereas independent-day reproducibility requires dedicated measurements on separate days with formal statistical bounds. Finally, the cross-vapor fingerprints are descriptive: no PCA, LDA, SVM, Random Forest, neural network, or other classifier was trained and independently validated in this study. These limitations define the next experimental stage rather than diminish the value of the present array-characterization dataset.

4. Conclusions

At approximately 1000 ppm methanol vapor, the MQ2-MQ7-MQ9-MQ135 array exhibited qualitatively consistent within-day resistance decreases and distinct amplitude-kinetic response patterns. MQ135 produced the largest normalized response (98.47%), the largest resistance contrast, and the steepest slope magnitude. MQ7 also produced a large normalized response (96.15%), MQ2 showed the shortest operational response time (25 s), and MQ9 showed the shortest operational recovery time (150 s). The findings show that the methanol response of the array is more completely represented by a multichannel feature vector combining normalized response amplitude, slope, operational response time, operational recovery time, and exponential transient constants than by a single amplitude value. This multidimensional representation is suitable for subsequent pattern-recognition research, but the present

study does not claim independently validated automated methanol identification.

The four-sensor MQ array therefore provides a practical, low-cost experimental basis for methanol-response characterization and future electronic-nose front-end development under controlled conditions. Extension to multiple concentrations, controlled temperature/humidity perturbations, independent-day replication, mixed-vapor testing, and statistically validated classification is required before the system can be evaluated as a general analytical recognition platform.

Reference

1. N. Barsan, D. Koziej, and U. Weimar, "Metal oxide-based gas sensor research: How to?", Sensors and Actuators B: Chemical, 121(1), 18-35, 2007. DOI: 10.1016/j.snb.2006.09.047.
2. A. Dey, "Semiconductor metal oxide gas sensors: A review", Materials Science and Engineering B, 229, 206-217, 2018. DOI: 10.1016/j.mseb.2017.12.036.
3. G. F. Fine, L. M. Cavanagh, A. Afonja, and R. Binions, "Metal oxide semi-conductor gas sensors in environmental monitoring", Sensors, 10(6), 5469-5502, 2010. DOI: 10.3390/s100605469.
4. A. D. Wilson and M. Baietto, "Applications and advances in electronic-nose technologies", Sensors, 9(7), 5099-5148, 2009. DOI: 10.3390/s90705099.
5. J. W. Gardner and P. N. Bartlett, "A brief history of electronic noses", Sensors and Actuators B: Chemical, 18-19, 211-220, 1994. DOI: 10.1016/0925-4005(94)87085-3.
6. Z. Zhang, Z. Zheng, X. He, K. Liu, M. Debliquy, Y. Zhou, and C. Zhang, "Electronic nose based on metal oxide semiconductor sensors for medical diagnosis", Progress in Natural Science: Materials International, 34(1), 74-88, 2024. DOI: 10.1016/j.pnsc.2024.01.018.
7. K. A. Al-Ali, Design of a System to Study the Sensitivity and Characterization for a Group of MQ Gas Sensors and Specify their Parameters for Ethanol, Methanol and Ammonia Vapors, PhD Thesis, University of Rojava, Qamishlo, Syria, 2025.
8. Zhengzhou Winsen Electronics Technology Co., Ltd., MQ-2 Semiconductor Sensor for Flammable Gas, Manual, Ver. 1.4.2024.
9. Zhengzhou Winsen Electronics Technology Co., Ltd., MQ-7 Semiconductor Sensor for Carbon Monoxide, Manual, Ver. 1.3. 2014.
10. Zhengzhou Winsen Electronics Technology Co., Ltd., MQ-9B Semiconductor Sensor for Carbon Monoxide and Methane, Manual.2021.
11. Zhengzhou Winsen Electronics Technology Co., Ltd., MQ135 Semiconductor Sensor for Air Quality, Manual, Ver. 1.4.2021.

Rojava Journal of Science and Technology

2026, VOL. 3, No 1, [168-185]

Îzolasyon û Pênasekirina Mîkroorganîzmayên Probiotîk li Herêmên Bakur û Rojhilatê Sûriyeyê

Zozan Ehmed[1], Heyder Seyfî*[2]

[1,2]Beşa Biyoteknolojî û Biyomedîsînê ،Enstîtuya Zanist û Teknolojiya Nûjen – Zanîngeha Rojava-Bakur û Rojhilatê Sûriyeyê.

Kurte

Probiotîk wekî mîkroorganîzmayên zindî tê pênasekirin ku dema bi mîqdarên têr bêne dayîn, bi parastina hevsengiya mîkrobiyota roviyan re feydeyên tenduristiyê ji kesên bikartînin re peyda dike. Di nav de, bakteriyên asîda laktîk (LAB) ku bi gelemperî di şîr û berhemên şîrî de tên dîtin, herî zêde tên bikaranîn. Di vê lêkolînê de zêdetirî 100 nimûneyên şîr û berhemên wê li ser plakên agarê De Man, Rogosa û Sharpe (MRS) hatin çandin û di germahiya 37°C de bo 48 demjimêran di şertên aerobîk û anaerobîk de hatin inkûbe kirin. Ji inkûbasyona aerobîk, zêdetirî 30 nimûne wekî bakteriyên Lactobacillus bi bikaranîna testên morfolojîk û biyokîmyayî, wek rengkirina Gram û testa katalazê, hatin nasandin. Hemû îzolat formên kokî an çûkî nîşan dan, Gram-erênî bûn û katalaz-negatîf derketin, ku ev yek dabeşbûna wan wekî LAB piştrast kir. Di dawiyê de, rêbaza PCR bi primerên taybet hate bikaranîn da ku strainên îzolekirî werin piştrastkirin. Ev 30 îzolata LAB ji bo çalakiya dijî-mîkrobî li dijî patojenên mirovî *Escherichia coli* û Staphylococcus aureus hatin ceribandin. Heft nimûne bandora dijî-mîkrobî ya fireh-spektrum nîşan dan. Îzoleyan şertên asîdî di navbera pH 2.0 heta 5.0 de tolerans kirin, di hebûna NaCl de baş mezin bûn û laktoz bi awayekî karîger metabolîze kirin. Testa hestiyariya antîbiyotîk bi Ampicillin, Doxycycline, Ceftriaxone û Amikacin re nîşan da ku li hember Ampicillin û Amikacin berxwedaneke girîng heye, lê hestiyarî li hember Doxycycline û Ceftriaxone hate dîtin. Li gorî taybetmendiyên probiotîk û şêwazên berxwedana antîbiyotîk, heft nimûneyan wekî strainên LAB yên probiotîk ên muhtemel hatin piştrastkirin. Analîza rêzeya 16S rDNA wan wekî Lactobacillus plantarum, L. paracasei, L. casei, L. fermentum, L. rhamnosus, L. reuteri, L. brevis û L. acidophilus nasand.

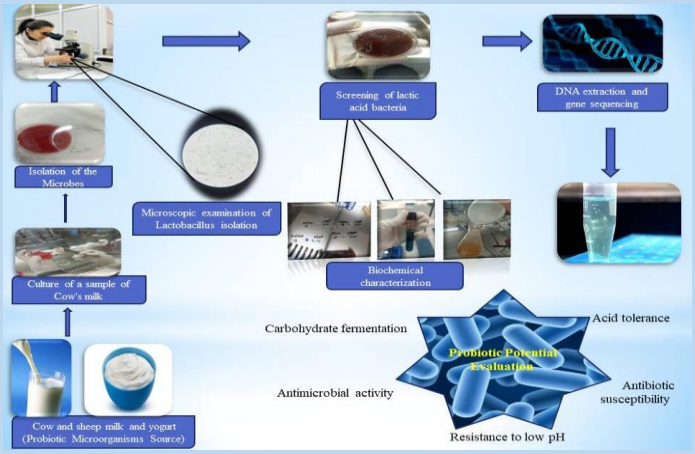

Dîroka Gotarê

Wergirtin: 12`ê Adara 2026`an
Guherandin: 19`ê Tîrmeha 2026`an
Pejirandin: 29`ê Îlona 2026`an

Peyvên Sereke

Probiotîk, Bakteriyên Asîda Laktîk (LAB), Berhemên Şîrî, Çalakiya Dijî-Mîkrobî, Toleransa Asîd /NaCl, Bikaranîna Laktozê, Berxwedana Antîbiyotîkan, Analîza 16S rDNA, Cureyên Lactobacillus.

* - Corresponding Author: homan_saify@yahoo.com

1. pêşgotin

Niha, bakteriyên asîda laktîk (LAB) bûne navenda gelek lêkolînên zanistî li seranserê cîhanê, ji ber rola wan a girîng di pêvajoyên fermentasyonê de û ji şiyana wan ya hilberandina madeyên antîmîkrobîal ku di çêkirina gelek bandorên probiyotîk de beşdar in. Ev bandor di nav xwe de çalakiyên dijî-tûmorê, kêmkirina nîşaneyên ne-guhertina laktozê (lactose intolerance), daxistina asta kolesterolê ya serumê, parastin û hevsengkirina mîkrobiyotaya rûvî, her wiha xurtkirina pergala berevaniyê (immune system) digirin (Abdullah et al., 2010). Di hilberandina şîrê fermentekirî de, cureyên taybet ên LAB têne bikaranîn ji ber şiyana wan a hilberandina exopolysaccharîdan (EPS) ku viskozîte û taybetmendiyên tekstûrî yên berhemê baştir dikin. Wekî din, hin cureyên LAB bi hilberandina manîtolê ve girêdayî ne; ev maddeyek e ku dibe ku xwedî taybetmendiyên başkirina tenduristiyê be. Probiyotîk wekî mîkroorganîzmayên zindî, di nav wan de bakterî û xemair (yeasts), têne pênasekirin ku dema bi mîqdarên guncaw werin dayîn, karûbarên erênî li ser tenduristiya kesên bikartînin çêdikin (Santos et al., 2003). Bi zêdebûna hişyariya gelan li ser tenduristî, xwarin, vexwarin û bikaranîna xwarinên tijî probiyotîk balkişandinek mezin wergirtiye. Cureyên probiyotîk ên herî zêde hatine lêkolînkirin û bikaranîn bi piranî ji cinsên *Lactobacillus* û *Bifidobacterium* (Barrow et al., 1993) ne. Her weha, hin cureyên *Streptococcus*, *Enterococcus*, *Bacillus*, *Propionibacterium* û xemîra *Saccharomyces* jî wekî mîkroorganîzmayên probiyotîk têne nasîn. Van mîkroorganîzmayan çalakiya antîmîkrobîal li dijî patojenên enterîk nîşan daye, bersivên berevaniya mukozal û sîstemîk teşwîq kiriye û di peydakirina bandorên dijî-tûmorî, dijî-kolesterolî û dijî-iltîhabî de rolek girîng lîstiye (Refay et al., 2020). Her weha, probiyotîk dikare rewşa xwarinî ya kesan baştir bike û alîkarî bike ku nîşaneyên têkildar bi îshalê (diarrhea), ne-guhertina laktozê (lactose intolerance) û bersivên alerjîk kêm bibin. Di lêkolînekê de ku ji aliyê Neha û hevkarên wê ve di sala 2023`an de hate kirin, cureyên probiyotîk ji şîrê xav ê çêlekên li Geliyê Lahaul hatin veqetandin(Karuppaija et al., 2016). Encamên lêkolînê nîşan dan ku van cureyan şiyana hilberandina izomerên cis-9, trans-11 yên asîda lînoleîk a girêdayî (Conjugated Linoleic Acid, CLA) heye, her wiha taybetmendiyên antîoksîdan û potansiyela bikaranîna wan di formulasyona xwarinan de jî hate piştrastkirin. Di lêkolîneke din de ku ji aliyê Asha û hevkarên wê ve di sala 2024`an de li gelek çiftlikên şîrdariyê yên hikûmî û taybet li Sylhet hate kirin, bi rêbaza nimûneygirtina rasthatî ya sade (simple random sampling), bi giştî 166 nimûneyên şîr ji çêlekên herêmî û cureyên dorûbarî (crossbred) hatin berhevkirin(Lopez-Dıaz et al., 2000). Koloniyên *Lactobacillus* ku li ser navenda çandiniyê ya MRS agar mezin bûn, bi rengê spî an zerê krêmî, bi kêlekên girtî, rûyek nerm û wekhev û bi mezinahiya di navbera 0.5 heta 3 mm de hatin nasîn. Lêkolînê her weha destnîşan kir ku izolatanên *Lactobacillus* xwedî çalakiya dijî-bakterî ne û karîbûn mezinbûna gelek bakteriyên patojen asteng bikin. Ev encam bi lêkolînên berê re li hev tên, ku cureyên *Lactobacillus* wekî bakteriyên probiyotîk ên gelemperî têne naskirin û dikarin wekî alternatîfên potansiyel ji bo pêşîlêgirtina nexweşiyên têkildar bi *Salmonella* werin bikaranîn (Kowalska et al., 2020). Bi heman awayî, Djadouni û Kihal (2012) ragihandin ku bakteriyên asîda laktîk (LAB) madeyên dijî-bakterî çêdikin ku mezinbûna mîkroorganîzmayên nîşander (indicator organisms) asteng dikin. Di ceribandina agar spot test de, herêmên astengkirinê (inhibition zones) li dijî *Escherichia coli (E. coli)*, *Staphylococcus aureus (S. aureus)* û *Salmonella Typhimurium (S. Typhimurium)* di navbera 10–14 mm de hatin tomarkirin(Theivendrarajah et al., 1990). Çalakiya dijî-bakterî ya ku ji aliyê izolatanên vê lêkolînê ve hate nîşandan bi encamên lêkolîna wan re li hev hat û çalakiya wan a fireh-spektrûm li dijî hem bakteriyên Gram-pozîtîv û hem jî Gram-nîgatîv, potansiyela wan wekî probiyotîkên bi bandor diyar dike(Prabhurajeshwar et al., 2017). Tevî girîngiya navneteweyî ya LAB û probiyotîkan di zanista şîr û berhemên şîrî de ku baş hatiye belgekirin, lêkolînên ku li ser veqetandin û taybetmendikirina van bakteriyan ji şîr û berhemên wê li herêma Bakur û Rojhilatê Sûriyeyê hatine kirin pir kêm in. Ji ber girîngiya xwarin û dermankirinê ya bakteriyên probiyotîk ên asîda laktîk, pêwîst e ku li van herêman lêkolînên zêdetir û berfirehtir bêne kirin. Ji ber vê yekê, armanca vê lêkolînê ew e ku

cureyên LAB ji şîrê xav ê çêlekan û her weha ji berhemên şîrî yên kevneşopî ku ji herêma Bakur û Rojhilatê Sûriyeyê hatine berhevkirin, werin veqetandin, nasandin û taybetmendîkirin.

2. Metryal û Rêbaz

2.1. Berhevkirina Nimûneyan

Di vê lêkolînê de, rêbaza lêkolîna qutkirî (cross-sectional study) hate bikaranîn da ku bakteriyên asîda laktîk (LAB) ji 100 nimûneyên şîr û berhemên şîrî werin veqetandin û taybetmendîkirin. Ev nimûne ji çêlek û pezên şîrdar ku li gelek farmên herêma Bakur û Rojhilatê Sûriyeyê hebûn hatin berhevkirin. Nimûneyên penêr û mastê ji firoşgehên xwarinê yên herêmî û ji malên ku mastê bi awayê kevneşopî amade dikin hatin standin. Nimûneyên şîrê çêlekê ji farmên şîrdariyê yên li bajarê Qamişlo hatin berhevkirin. Pêvajoya nimûne girtinê bi awayekî bêserûber (random) hate kirin, li gorî rêbaza ku di lêkolîna Hoque û hevkarên wê (2010) de hatiye diyarkirin. Nimûne bi şertên pakî, di sirincan de hatin berhevkirin û di germahiya nizm de hatin parastin da ku ji her cûre zirar an guherînan were parastin. Herêmên ku nimûne ji wan hatin berhevkirin Qamişlo, Amûdê, Tirbespiyê û Dêrik bûn. Armanc ew bû ku cihêrengiya cureyên probiyotîk ên heyî di berhemên şîrî yên herêmî de were destnîşankirin û ji van herêman cureyên cûrbecûr ji bakteriyên bi feyde werin veqetandin.

2.2. Îzolasyon û Nasandina Bakteriyan Bi Rêbazên Kevneşopî

Cureyên bakteriyên asîda laktîk (LAB) ji nimûneyên şîr, mast û penîrê hatin veqetandin. Ji her nimûneyekê 50 gram hate pîvandin û rêzek ji dilûtasyonên peywirdar (serial dilutions) bi bikaranîna têkeloka %2 ya sodium citrate hate amadekirin. Piştî homojenîzekirina nimûneyan, dilûtasyon heta asta 10^{-5} hate kirin û li ser navendên çandiniyê yên Nutrient Agar, Blood Agar, M17 Agar û MRS Agar (de Man, Rogosa and Sharpe) hate çandin. Petriyên çandî di germahiya 37°C de bo 48 demjimêran hatin inkubekirin da ku şertên guncaw ji bo mezinbûna bakteriyan peyda bibin. Ev pêvajo li gorî protokola ku ji aliyê Pundir û hevkarên wê sala (2013) ve hatiye diyarkirin hate meşandin. Piştî bidawîbûna dema inkubasyonê, izolatanên bakterî ku ji nimûneyên şîr, mast û penîrê hatibûn wergirtin, ji bo nasandina asta cinsê (genus) wan, di bin rêzek ceribandinên morfolojîk û biyokîmyayî de hatin nirxandin. Ev ceribandin li gorî protokolên standard ên ku ji aliyê Barrow û Feltham (1993), Theivendrarajah (1990), Kapilan û Arasaratnam (2010) û Karuppaija û hevkarên wê (2016) ve hatine diyarkirin, hatin pêkanîn. Ceribandinên ku hatin kirin ev bûn: nirxandina şikl û taybetmendiyên koloniyan, şiyana mezinbûnê di şertên aerôbîk û anaerôbîk de, renggirtina Gram, ceribandina katalazê, oksîdaz û îndolê, reaksiyona methyl red (MR) û her weha şiyana hilberandina asîd û gazê ji glukozê.

2.3 Têstên Piştrastkirinê yên Izolatanên LAB

2.3.1 Têsta Rengkirina Gram (Gram staining test)

Rengkirina Gram yek ji rêbazên herî berbelav ên rengkirina cihêkar (differential staining) e ku ji bo dabeşkirina bakteriyan di nav du komên sereke de, yanî Gram-positive û Gram-negative, tê bikaranîn. Ev dabeşkirin li ser bingeha pêkhateya dîwarê şaneyî ya bakteriyan û bersiva wan li hember pêvajoya rengkirinê tê kirin. Ev rêbaz wekî amûrek bilez û bingehîn ji bo nasîna destpêkî ya enfeksiyonên bakterî jî tê hesibandin. Li gorî rêbernameya hilberînerê (BTC Syria), hejmarek piçûk ji bakteriyan hate girtin û li ser slidên qizêz ên şûştî û paqij hate belavkirin da ku qatek tenik (smear) were çêkirin. Piştî wê, smear hate hiştin ku bi awayê xwezayî ziwa bibe, paşê bi germahiyê hate sabîtkirin (heat fixation) da ku bakterî bi rûyê slaydê ve girêdayî bimînin. Dûv re, çar rengên taybet ên ceribandina Gram bi rêz li ser slayed hatin sepandin û piştî her qonaxekê, slayd bi ava distîlekirî hate şûştin. Her reng bo xuleyekê hate hiştin berî ku were şûştin. Di dawiyê de, slayd hate hiştin ku ziwa bibe û di bin mîkroskopa ronahî de hate vekolîn da ku bersiva Gram û taybetmendiyên morfolojîk ên şaneyên bakteriyan werin diyarkirin.

2.3.2 Têsta Katalazê (Catalase test)

Têsta katalazê ji bo destnîşankirina hebûna enzîma katalazê hate pêkanîn. Ev enzîm kar dike ku hîdrojen peroksîd (H_2O_2) bişkîne û veguherîne av û oksîjen. Ev ceribandin rê dide ku bakteriyên (catalase-positive) ji bakteriyên (catalase-negative) werin cudakirin. Ji bo pêkanîna vê têstê, slaydek paqij û steril hate bikaranîn. Hejmarek piçûk ji nimuneyên bakteriyan bi şertên pakkirî hate girtin û li ser rûyê slayd hate danîn. Dûv re, 1–2 qutkên têkelokan %3 (v/v) ya hîdrojen peroksîd (H_2O_2) rasterast li ser smeara bakteriyan hatin zêdekirin. Piştî zêdekirina H_2O_2, reaksiyon bi lez hate çavdêrîkirin. Derketina peqpeqokan (bubble) an belavbûna gazê nîşana hebûna enzîma katalazê bû û encam wekî katalaz-pozitiv hate tomarkirin. Di heman demê de, nebûna peqpeqokan nîşan dide ku bakterî katalaz-nîgatîv e.

2.3.3. Têsta Oksîdazê (Oxidase Test)

Ceribandina oksîdazê ji bo destnîşankirina hebûna enzîma cytochrome c oxidase di bakteriyan de hate pêkanîn. Ji bo vê armancê, mezinbûna mîkrobî ya li ser navenda çandiniyê bi şertên pakkirî bi alîkariya lûpa çandinê ya platinumê (platinum inoculating loop) hate berhevkirin û li ser dîska ceribandina oksîdazê ya ku bi têkeloka avî ya %1 (w/v) ya tetramethyl-p-phenylenediamine dihydrochloride hatibû têrbûnkirin, hate sepandin. Piştî danîna nimûneya bakteriyê li ser dîskê, guherîna rengê dîskê bi lez hate çavdêrîkirin. Derketina rengê mov (purple coloration) di nav 10 çirkeyan de wekî encamek erênî (oxidase-positive) hate dîtin ku hebûna enzîma oksîdazê nîşan dide. Li hember vê yekê, nebûna guherîna rengê an jî nederketina rengê mov piştî derbasbûna vê demê, wekî encamek neerênî (oxidase-negative) hate tomarkirin.

2.3.4. Têsta Îndolê (Indole test):

Têsta îndolê ceribandineke biyokîmyayî ye ku ji bo nirxandina şiyana cureyên *Lactobacillus* di parçekirina amino asîda tryptophan de û hilberandina maddeya îndolê de tê bikaranîn. Ji bo amadekirina navenda ceribandinê, 0.5 g pepton û 0.5 g sodium chloride (NaCl) di 50 mL ava distîlekirî de hatin halandin. Dûv re, çareseriya amadekirî bi rêya otoklavê di germahiya 121°C û di bin zexta 20 psi de hate sterilîzekirin. Piştî ku bakteriya di nav têkeloka tijî Tryptophan de bo dema 24 – 48 demijmêran hate inkubekirin, reaktîfek taybet ji bo destnîşankirina îndolê, wekî reaktîfa Kovac an Ehrlich, hate zêdekirin da ku encam werin xwendin. Reaksiyona erênî (positive) bi derketina rengê sor an sor-mor (red-violet) tê diyarkirin, ku nîşana hilberandina îndolê ye. Li hember vê yekê, nebûna guherîna rengê û mayîna reaktîfê li ser rengê zerê xwe yê bingehîn, wekî encamek neerênî (negative) tê dîtin.

2.3.5 Têsta Oxidative–Fermentative (OF) ji bo Metabolîzma Glukozê

Ji bo nirxandina rêya metabolîk a ku mîkroorganîzma ceribandinê ji bo parçekirina glukozê bikar tîne, têsta Oxidative–Fermentative (OF) hate pêkanîn. Ji bo amadekirina navenda çandiniyê, 1.9 g ji madeya Hugh-Leifson di 100 mL ava distîlekirî de hate helandin. Dûv re, têkelokek bi rêya otoklavê di germahiya 121°C û di bin zexta 20 psi de hate sterilîzekirin. Piştî sterilîzekirinê, du tûbên ceribandinê bi cureyên *Lactobacillus* hatin çandin. Ji bo vê armancê, derziyeke steril a çandinê (inoculating needle) bi qasî nîvê navendê hate ketandin da ku bakterî li nav navendê were veguhestin. Ji bo cihêkirina pêvajoyên metabolîk ên oksîdatîf û fermentatîf, yek ji tûban bi qatek 1 cm ya zeyta mîneralî yê steril hate nixumandin da ku şertên anaerôbîk werin peydakirin. Tûba duyemîn bê nixumandin hate hiştin da ku bi oksîjena hewayê re têkilî biparêze û şertên aerôbîk peyda bibin. Herdu tûb di germahiya 37°C de bo dema 48 demjimêran hatin inkubekirin. Ji bo mîkroorganîzmayên ku mezinbûnek hêdî nîşan didan, dema inkubasyonê heta 72–96 demjimêran hate dirêjkirin da ku encamên rast û pêbawer werin bidestxistin.

2.3.6 Diyarkirina Mezinbûna Bakteriyan Di Germahiyên Cuda De

Ji bo nirxandina bandora germahiyê li ser mezinbûna bakteriyan, navendên agarê di petriyên steril de hatin amadekirin. Dûv re, du nimûneyên bakteriyan bi şertên pakkirî li ser van navendan hatin çandin. Petriyên çandî paşê di du şertên germahiyê yên cuda de hatin inkubekirin: 20°C û 45°C. Demeya inkubasyonê 7 rojan dom kir da ku şertên guncaw ji bo mezinbûna bakteriyan peyda bibin. Piştî qedandina dema inkubasyonê, petrî hatin vekolîn û mezinbûna bakteriyan li ser navendên çandiniyê hate nirxandin. Hebûn an nebûna mezinbûnê, her weha asta mezinbûna koloniyan di her şertê germahiyê de hate tomarkirin da ku şiyana bakteriyan ya lihevhatina bi germahiyên cuda re were diyarkirin.

2.3.7 Mezinbûna Bakteriyan Di Konsantrasyonên Cuda ên NaCl De

Ji bo nirxandina asta berxwedana izolatanên bakteriyên asîda laktîk (LAB) li hember konsantrasyonên cuda ên sodium chloride (NaCl), navenda MRS broth ya guhertî ku bi bromocresol purple wekî nîşandera pH`ê hatibû dewlemendkirin, hate bikaranîn. Di vê ceribandinê de, konsantrasyonên NaCl, yanên ji %2.5 ta %8.5, hatin ceribandin. Ji bo her konsantrasyonekê, çar tûbên ceribandinê ku her yek 5 mL ji navenda MRS broth a guhertî ya bi NaCl dihewand, hatin amadekirin. Her tûbek bi 50 µL ji çanda LAB ya (overnight culture) bi konsantrasyona %1 (v/v) heta şevekê hate çandin. Piştî çandinê, hemû tûb di germahiya 37°C de bo dema 7 rojan hatin inkubekirin. Di dawiya dema inkubasyonê de, mezinbûna bakteriyan û guherînên rengê nîşandera pHê hatin çavdêrîkirin û tomarkirin da ku asta berxwedana izolatanên LAB li hember şertên cuda ên şoriyê (salinity) were diyarkirin.

2.3.8 Têsta Hîdrolîza Arginînê (Arginine Hydrolysis Test)

Ji bo pêkanîna ceribandina hîdrolîza arginînê, navenda ceribandinê bi tevlihevkirina 1 g ji navenda LB û 1 g ji MRS agarê, bi arginîna tê de û 100 mL ava distîlekirî hate amadekirin. Piştî amadekirina têkelokê, pH-ya wê hate pîvandin û wekî bêalî (neutral) bi nirxa 7.0 hate tomarkirin. Dûv re, navenda amadekirî ji bo sterilîzekirinê di otoklavê de hate danîn. Piştî pêvajoya sterilîzekirinê, pH dîsa hate pîvandin û nirxa 6.6 hate tomarkirin, ku nîşan dide guherînek sivik ber bi şertên asîdî ve çêbûye; ev guherîn dibe ku encama germahî û şertên otoklavkirinê be. Piştî amadekirina navendê, nimûneyek ji bakteriyên *Lactobacillus* di nav navendê de hate çandin. Navend paşê li ser amûrek hejandinê (shaker) hate danîn da ku têkelokirin û belavbûna baş a madeyan were misoger kirin. Dûv re, nimûne bo dema 24 demjimêran di şertên guncaw de hate inkubekirin. Piştî dema inkubasyonê, guherînên ku bi hîdrolîza arginînê ve girêdayî bûn hatin çavdêrîkirin û tomarkirin da ku şiyana izolatanên bakterî di bikaranîna arginînê de were nirxandin.

2.3.9 Derxistina DNA û Amplîfîkasyona PCRê (DNA Extraction and PCR Amplification)

Rêzikên genî yên têkildarî cureyên bakteriyan ên armancdar ji databasa **GenBank** hatin wergirtin. Sêwirandina primeran bi awayekî rast û zanistî bi alîkariya nermalavên **Gene Runner** û **Primer3** yên ku ji aliyê **National Center for Biotechnology Information (NCBI)** ve têne peydakirin hate pêkanîn. Ev pêvajo ji bo misoger kirina taybetmendî û rastiya bilind di qonaxên nasandina molekular de girîng bû. Têkeloka reaksiyona **Polymerase Chain Reaction (PCR)** bi qebareke dawîn a 25 µL hate amadekirin. Her reaksiyon 8 µL ji **2× PCR Master Mix** (ku 1.5 mM $MgCl_2$ dihewand), 11 µL ava bê-DNase, 0.5 µL ji her primerê (wekî ku di Tabloya 1 de hatiye diyarkirin) û 5 µL DNA-ya nimûneyê dihewand. Ji bo zêdekirina karîgerî û taybetmendiya pêvajoya amplîfîkasyonê, şertên reaksiyonê bi awayekî baş hatin optimîzekirin. Pêvajoya PCRê bi amûra **Qiagen Rotor-Gene Q Thermocycler** hate meşandin û şertên germahiyê ev bûn: Qonaxa destpêkê ya denaturasyonê di 95°C de bo 10 deqeyan;

- Dûv re 35 çerxên PCRê ku tê de:
    - denaturasyon di 95°C de bo 1 deqe,

  - annealing li gorî germahiyên taybet ên her primerê (wekî ku di Tabloya 1 de hatine diyarkirin),
  - û extension di 72°C de bo 1 deqe;
- Di dawiyê de, qonaxa extensiona dawîn di 72°C de bo 10 deqeyan hate pêkanîn.

Berhemên PCRê bi rêya electrophoresisê li ser jelê agarozê ya %2 (w/v) hatin veqetandin. Ev pêvajo li gorî bikaranîna **Fisherbrand™ Real-Time Electrophoresis System** di nav tampona **Tris-EDTA (TE)** de hate meşandin. Ji bo dîtina bandên DNAyê, jel bi **ethidium bromide** hate rengkirin. Ev rêbaz şertên guncaw peyda kir da ku ampliconên PCRê bi awayekî zelal û cihê werin dîtin her wiha ji bo analîzên paşerojê amadekar bin.

Table 1: Primerên PCRê yên Ji bo Tîpkirina (Nasandina) Bakteriyan Hatine Bikaranîn

Bacteria	**Primer-gene**	**Rêza nukleotîdê (5'->3')**	**Mezin bûn Berhemê (bp)**	**Pileya Germkiriê**
L. paracasei	Paracasei-F	CAA TGC CGT GGT TGT TGG AA	106	58°C
	Paracasei-R	GCC AAT CAC CGC ATT AAT CG		
L. fermentum	Fermentum-F	GAC CAG CGC ACC AAG TGA TA	129	57°C
	Fermentum-R	AGC GTA GCG TTC GTG GTA AT		
L. reuteri				
	Reuteri-F	GAT TGA CGA TGG ATC ACC AGT	161	59°C

	Reuteri-R	CAT CCC AGA GTG ATA GCC AA		
L. casei	Casei-F	CCA CAA TCC TTG GCT GTT CT	115	56°C
	Casei-R	GCT TGA GGC GAT TGT AAT CC		
L. rhamnosus	Rhamnosus-F	GCC GAT CGT TGA CGT TAG TTG G	137	58°C
	Rhamnosus-R	CAG CGG TTA TGC GAT GCG AAT		
L. brevis	Brevis-F	GGG CAA CGA AGC AAG ATC GC	260	59°C
	Brevis-R	TTC CAA TCG TGT GCA CAC CA		
L. acidophilic	Acido-F	TCATGTTGGGATGCAAT GAG	828	54.3
	Acido-R	TTTCAAAACTTGTCCTG CTG		

2.3.10 Berxwedana Li Hember Asîdîtîyê (Acid Tolerance)

Cureyên *Lactobacillus* ên ku hatibûn veqetandin ji bo nirxandina şiyana wan ya berxwedanê li hember şertên asîdî hatin ceribandin. Ji bo vê armancê, bakterî di navenda **MRS broth** de hatin çandin; pH-ya vê navendê berê bi nirxên cuda ên di navbera pH 2 heta pH 5 de hatibû rêkûpêkkirin. Çandên bakteriyan di germahiya 37°C de bo dema 48 demjimêran hatin inkubekirin da ku bandora şertên asîdî li ser mezinbûn û zindîmayîna wan were nirxandin. Piştî qedandina dema inkubasyonê, 0.1 mL ji her çandinekê hate girtin û li gorî bikaranîna rêbaza **pour plate** li ser petriyên ku navenda **MRS agar** dihewand hatin veguhestin. Dûv re, petriyên çandî careke din di germahiya 37°C de bo 48 demjimêrên din hatin inkubekirin. Piştî inkubasyonê, mezinbûna koloniyan hate çavdêrîkirin û tomarkirin da ku asta berxwedana cureyên *Lactobacillus* li hember şertên asîdî yên cuda were diyarkirin.

2.3.11 Têsta Hestiyarîya Li Dijî Antîbiyotîkan (Antibiotic Susceptibility Testing)

Ji bo amadekirina têsta hestiyarîya li dijî antîbiyotîkan, mîqdarek diyarkirî ji **Mueller–Hinton agar** hate pîvandin û di nav qutiyekê de hate danîn. Dûv re, 100 mL ava distîlekirî lê hate zêdekirin û têkelok bi awayekî baş hate tevlihevkirin. Navenda amadekirî paşê bi rêya otoklavê hate sterilîzekirin. Piştî qedandina pêvajoya sterilîzekirinê, navend hate hiştin ku hinek sar bibe, paşê bi şertên pakî di petriyên steril de hate hiştin. Dema ku agar hişk bû û qewimî, Debirîna bakteriyên *Lactobacillus spp.* bi alîkariya tampona pênûsî ya steril (sterile cotton swab) li ser tevahiya rûyê agarê hate belavkirin. Ev pêvajo bi tevgerên dorhêlî hate pêkanîn da ku belavbûneke yekreng û wekhev a bakteriyan li ser navendê were misoger kirin. Dûv re, di agarê de bi şertên pakî, qulik (wells) hatin çêkirin. Di nav van qulikan de konsantrasyonên diyarkirî yên antîbiyotîkan, wekî **Doxycycline**, **Ceftriaxone**, **Amikacin** û **Ampicillin**, hatin zêdekirin. Petriyên çandî paşê di germahiya 37°C de bo dema 48 demjimêran hatin inkubekirin da ku şertên guncaw ji bo mezinbûna bakteriyan û nirxandina bandora antîbiyotîkan peyda bibin. Piştî inkubasyonê, herêmên astengkirina mezinbûna bakteriyan (inhibition zones) li derdora antîbiyotîkan hatin çavdêrîkirin û tomarkirin da ku asta hestiyarî yan berxwedana izolatanên bakteriyan li hember van antîbiyotîkan were diyarkirin.

2.3.12 Hilberandina Çalakiya Dijî-Mîkrobî (Production of Antimicrobial Activity)

Ji bo nirxandina bandora bakteriyên *Lactobacillus* li dijî bakteriyên zirardar, navenda **Mueller–Hinton agar** hate amadekirin. Ji bo vê armancê, mîqdarek diyarkirî ji agarê bi 100 mL ava distîlekirî hate tevlihevkirin û paşê bi rêya otoklavê bo demeke têr hate sterilîzekirin. Piştî sterilîzekirinê, navend bi şertên pakî di petriyên steril de hate hiştin ku hişk bibe. Li aliyekî din, têkelokek ji bo mezinkirina bakteriyan hate amadekirin. Ji bo vê armancê, 1 g ji navenda **LB broth** di 100 mL ava distîlekirî de hate helandin. Ev têkelok jî bi rêya otoklavê hate sterilîzekirin û paşê hate hiştin ku heta nêzîkî 30°C sar bibe. Piştî sarbûna navendê, mîqdarek piçûk ji nimuneya *Lactobacillus* di nav wê de hate çandin. Çand paşê li ser amûra hejandinê (shaker) bo 24 demjimêran hate hiştin da ku şertên guncaw ji bo mezinbûna bakteriyan werin peydakirin. Ji bo ceribandina çalakiya dijî-mîkrobî, petriyeke ku bi qatek yekreng ji bakteriyên patojen, bi taybetî cureyên *Staphylococcus*, hatibû çandin hate amadekirin. Dûv re, di rûyê agarê de bi şertên pakî, qulik (wells) hatin çêkirin û Debirîna *Lactobacillus* di nav van qulikan de hate danîn. Petriyên ceribandinê paşê di germahiya 37°C de bo dema 48 demjimêran hatin inkubekirin. Piştî inkubasyonê, herêmên astengkirina mezinbûna

bakteriyên patojen li derdora qulikan hatin çavdêrîkirin û tomarkirin da ku çalakiya dijî-mîkrobî ya izolatanên *Lactobacillus* were nirxandin.

3. Encam

3.1 Encamên têsta Rengkirina Gram (Gram Staining Test):

Piştî pêkanîna têsta renggirtina Gram li ser nimûneyên *Lactobacillus*, slayid hate hiştin ku bi awayê xwezayî ziwa bibe û paşê di bin mîkroskopê de hate vekolîn. Ji bo dîtina hûrguliyên morfolojîk ên şaneyên bakteriyan, mezinahiyên cuda ên lensan (Edesat) hatin bikaranîn. Di dema vekolînê de hat dîtin ku şaneyên bakteriyan bi rengê morê tîr (deep purple) xuya dibûn. Ev taybetmendî nîşan dide ku bakteriyên veqetandî Gram-erênî (Gram-positive) ne, ji ber ku dîwarê şaneyî yê wan qatek stûr a peptidoglycan dihewîne ku rengê krîstal violet di dema pêvajoya rengkirinê de diparêze (Wêne 1). Ev encam bi taybetmendiyên morfolojîk ên cureyên *Lactobacillus* re lihevhatî ye, ku bi gelemperî wekî bakteriyên Gram-pozîtîv têne nasîn.

Wêneya 1: Bakteriyên Lactobacillus piştî pêkanîna testa boyaxkirina Gram di bin mîkroskopê de

3.2 Encamên têsta Katalazê (Catalase Test):

Nimûneyek ji bakteriyên *Lactobacillus* ji bo têsta katalazê hate ceribandin. Ji bo vê armancê, nimûneya bakteriyan rasterast li ser slaydek paqij hate danîn û dûv re 1–2 qutikan ji têkeloka %3 ya hîdrojen peroksîd (H_2O_2) lê hatin zêdekirin. Di dema çavdêrîkirinê de, tu peqpeqokan an derketina gazê nehat dîtin. Nebûna peqpeqokan nîşan dide ku bakteriyên ceribandî enzîma katalazê hilbernadin û encam wekî katalaz-neerênî (catalase-negative) hate tomarkirin (Wêne 2). Ev encam bi taybetmendiyên biyokîmyayî yên cureyên *Lactobacillus* re lihevhatî ye, ji ber ku piraniya van bakteriyan bi gelemperî katalaz-nîgatîv e û nikarin hîdrojen peroksîd bi rêya enzîma katalazê veqetînin.

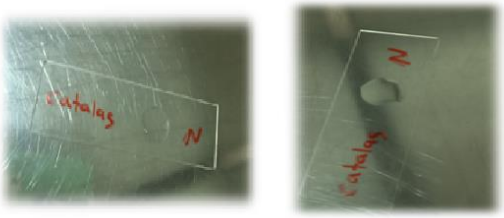

Wêneya 2: Testa katalazê piştî danîna dilopên çareseriya hîdrojen peroksîtê li ser bakteriyên xav

3.3. Encamên têsta Oksîdazê (Oxidase Test):

Piştî qedandina dema inkubasyonê ya 24–48 demjimêran, nimûneya bakteriyan ji inkubatorê hate derxistin û bi awayekî nerm bo nêzîkî 10 çirkeyan li ser dîska ceribandina oksîdazê hate xişandin. Di dema çavdêrîkirinê de, tu guherînek berbiçav di rengê dîskê de nehat dîtin. Nebûna guherîna rengê nîşan dide ku reaksiyona oksîdazê neerênî (oxidase-negative) bû. Ev encam piştrast dike ku cureya *Lactobacillus* a ku hate ceribandin enzîma **cytochrome c oxidase** hilbernake û xwedî çalakiya vê enzîmê nîne (Wêne 3). Ev encam bi taybetmendiyên biyokîmyayî yên cureyên *Lactobacillus* re lihevhatî ye, ji ber ku piraniya van bakteriyan bi gelemperî wekî oksîdaz-nîgatîv têne naskirin.

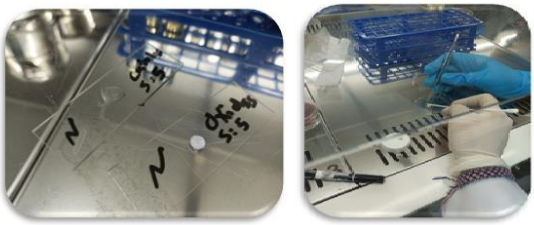

Wêneya 3. Danîna nimûneya bakteriyan li ser dîska oksîdazê û nîşandana encama dawî

3.4. Encamên têsta Îndolê (Indole Test):

Piştî bidawîbûna dema inkubasyonê ya 24–48 demjimêran, çend qutik ji reaktîfa **Kovac's** li ser çanda *Lactobacillus* a ku di navenda dihewîne tryptophan de mezin bûye hatin zêdekirin. Di dema çavdêrîkirinê de, tu guherînek di rengê navendê de nehat dîtin. Nebûna guherîna rengê nîşan dide ku encama têsta îndolê neerênî (indole-negative) bû. Ev encam destnîşan dike ku cureya bakteriyê ya hate ceribandin nikare amino asîda tryptophan bişkîne û ji wê maddeya îndolê hilberîne (Wêne 4). Ev encam bi taybetmendiyên biyokîmyayî yên cureyên *Lactobacillus* re lihevhatî ye, ji ber ku piraniya van bakteriyan di şertên ceribandinê de îndolê hilbernadin û bi gelemperî wekî îndol-neerênî têne naskirin.

Wêneya 4. Nimûneya îndolê piştî ku bakterî hatin çandin û encama dawî hat bidestxistin

3.5. Encamên Hilberandina CO_2 Ji Glukozê:

Piştî 48 demjimêrên inkubasyonê, di navenda ceribandinê de guherînek berbiçav di rengê navendê de hate dîtin; reng ji kesk veguherî zer. Her weha, di nav tûbê de çêbûna peqpeqokên gazê jî hate çavdêrîkirin. Ev encam nîşan dide ku têsta **Oxidative–Fermentative (OF)** erênî (positive) bû û piştrast dike ku cureyên *Lactobacillus* karîbûn glukozê bi rêya fermentasyonê metabolîze bikin. Guherîna rengê navendê ber bi zerayî ve nîşana hilberandina asîdên organîk ji encama fermentasyona glukozê ye, di heman demê de çêbûna gazê jî piştrastiyek din ji bo çalakiya fermentatîf a bakteriyan pêşkêş dike. Vekolînên zanistî û encamên ceribandinî yên paşerojê diyar kirin ku piraniya cureyên *Lactobacillus* xwedî şiyana metabolîzekirina glukozê bi rêya fermentasyonê ne. Ji ber vê yekê, encamên ku di vê lêkolînê de hatin bidestxistin bi taybetmendiyên metabolîk ên naskirî yên van bakteriyan re lihevhatî ne (Wêne 5).

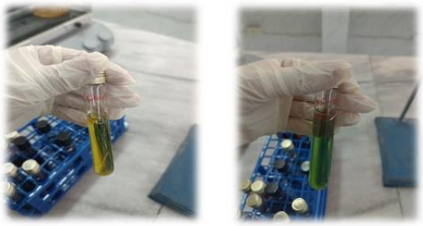

Wêneya 5: Testkirina hilberîna CO2 ji glukozê piştî çandina nimûneyek ji bakteriya Lactobacillus tê de û înkubasyona wê

3.6. Encamên Diyarkirina Mezinbûna Bakteriyan Di Germahiyên Cuda De

Nimûneyên *Lactobacillus* li ser navendên agarê yên xwedî pH-ekî hinekî asîdî hatin çandin. pH-ya navendê bi awayekî ku şertên guncaw ji bo mezinbûna bakteriyên asîda laktîk peyda bike hate rêkûpêkkirin. Çand paşê di şertên germahiyê yên cuda de, di navbera 20°C û 45°C de, bo dema hefteyekê hate inkubekirin (Wêne 6). Piştî qedandina dema inkubasyonê, nimûne bi alîkariya mîkroskopê hatin vekolîn. Encamên vekolînê nîşan dan ku bakterî zindî mabûn û karîbûn di şertên germahiyê yên cuda de mezin bibin. Her weha, tu nîşanên eşkere yên zirarê ku ji ber germahiyên bilind an nizm çêbibin nehatin dîtin (Wêne 7). Ev encam nîşan dide ku izolatanên *Lactobacillus* xwedî şiyana lihevhatina başin bi şertên germahiyê yên cuda ku dikarin di navbera van germahiyan de zindî bimînin û çalakiya xwe biparêzin.

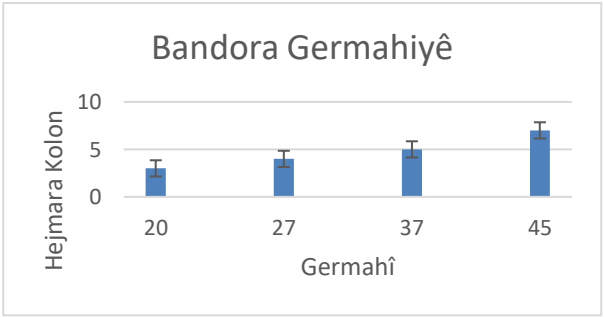

Wêneya 6 :Bandora mezinbûna Lactobacillus di germahiyên cûda de

Wêneya 7 : Nimûneyek ji bakteriyan di germahiyên cûda de di înkubatorekê de hatine înkubasyonkirin

3.7. Berxwedana Li Hember pH-ya Nizm (Resistance to Low pH)

Nimûneyên **M17 agar** bi astên cuda ên pH-ya nizm (pH 2, 3, 4 û 5) hatin amadekirin. Nimûneyên bakteriyên *Lactobacillus* li ser van navendên asîdî hatin çandin û di germahiya 37°C de bo dema 24–48 demjimêran hatin inkubekirin (Wêne 8). Piştî qedandina dema inkubasyonê, nimûne bi alîkariya mîkroskopa ronahî hat vekolîn. Encamên vekolînê nîşan dan ku bakterî zindî mabûn û şiyana mezinbûn û çalakiyên xwe di şertên asîdî de parastin (Wêne 9). Ev encam destnîşan dike ku izolatanên *Lactobacillus* xwedî asta bilind a berxwedanê li hember şertên pH-ya nizm in. Ev taybetmendî ji bo bakteriyên probiyotîk girîng tê hesibandin, ji ber ku divê ew karibin şertên asîdî yên mîdeyê derbas bikin û zindî bigihîjin pergala rûvî da ku karûbarên xwe yên tenduristî-pêşkeşker pêk bînin.

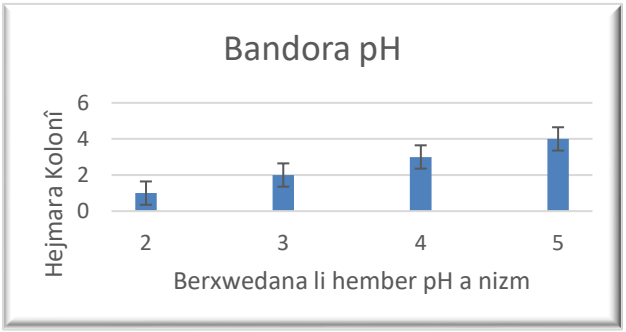

Wêneya 8 : Bandora pH-ya nizm li ser mezinbûna bakteriya Lactobacillus

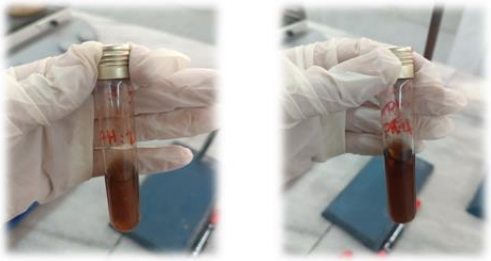

Wêneya 9: Nimûneyên bakteriyan di agarê de bi asîdîteya kêm û pileyên cuda

3.8 Mezinbûna Bakteriyan Di Konsantrasyonên cuda ên NaCl De

Nimûneya *Lactobacillus* di navendên xwedî astên cuda ên şoriyê (NaCl) de hate ceribandin. Konsantrasyonên ku hatin bikaranîn %2.5, %4.5, %6.5 û %8.5 bûn. Nimûne di germahiya 37°C de bo dema 7 rojan hat inkubekirin (Wêne 10). Piştî qedandina dema inkubasyonê, nimûne bi alîkariya mîkroskopê hate vekolîn. Encaman nîşan da ku bakteriyên *Lactobacillus* di şertên şoriyê yên navîn de mezinbûnek baş nîşan dan û zindîmayîna xwe parastin. Lêbelê, di şertên şoriyê yên pir bilind an jî pir kêm de, mezinbûna bakteriyan kêm bû an jî nikarîbûn zindî bimînin (Wêne 11). Ev encam nîşan dide ku izolatanên *Lactobacillus* xwedî astek taybet a toleransê li hember şoriyê ne û şertên şoriyê yên navîn ji bo mezinbûn û çalakiya wan şertên herî guncaw pêşkêş dikin. Ev taybetmendî ji bo hilbijartina cureyên probiyotîk ên guncaw di pîşesaziya xwarinan û berhemên fermentekirî de girîng e.

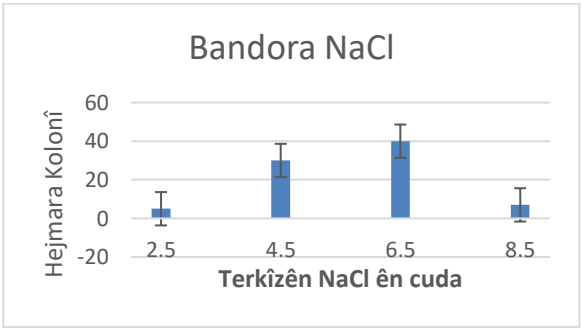

Wêneya 10: Bandora rêjeyên cuda yên NaCl li ser mezinbûna bakteriya Lactobacillus

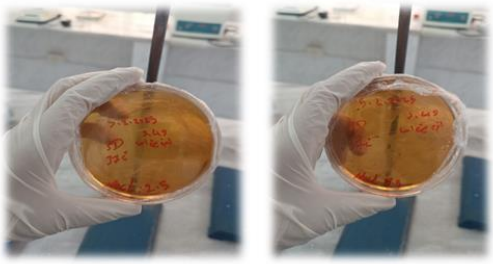

Wêneya 11: Nimûneyên bakteriyan li ser agarê bi astên şorbûna cuda piştî înkubasyonê ji bo 3 rojan

3.9 Encamên têsta Hîdrolîza Arginînê (Arginine Hydrolysis Test)

Ji bo nirxandina şiyana *Lactobacillus* di hîdrolîzkirina arginînê de, guherîna pH-ya navenda têstê berî û piştî inkubasyonê hate çavdêrîkirin. Berî çandina bakteriyan, pH-ya nimûneyê nêzîkî 6.0 bû, ku şertên hinekî asîdî nîşan dida. Piştî ku nimûne bo dema 24 demjimêran li ser amûra hejandinê (shaker) hate inkubekirin, dîsa pH hate pîvandin. Encam nîşan da ku pH heta 8.6 bilind bûye. Ev zêdebûna berbiçav a pH-ê nîşana çêbûna hîdrolîza arginînê ye. Bilindbûna pH-ê destnîşan dike ku bakteriyên *Lactobacillus* arginîn bi awayekî çalak metabolîze kirine û di encama vê pêvajoyê de madeyên alkalî (bazîk) hilberandine, ku bûne sedema guherîna pH-ê ber bi şertên alkalî ve (Wêne 12). Ev encam piştrast dike ku izolatanên *Lactobacillus* xwedî şiyana bikaranîna arginînê wekî çavkaniyek metabolîk e û dikare di şertên guncaw de pêvajoya hîdrolîza arginînê pêk bîne.

Wêneya 12: Çareseriya agarê ya ku arjînîn û probiyotîkan li ser shaker û pH metreyê ji bo pîvandina pH-ê dihewîne

3.10 Encamên Analîza PCRê (PCR Analysis)

Nasandina molekular bi rêya **Polymerase Chain Reaction (PCR)** encamên ku bi rêbazên kevneşopî ji bo nasandina bakteriyên probiyotîk hatibûn bidestxistin piştrast kir. Bikaranîna primerên taybet ên cureyan şertên guncaw peyda kir da ku cureyên cuda ên bakteriyan bi serkeftî werin destnîşankirin. Amplîfîkasyon û nasandina DNA-ya bakteriyan di vê lêkolînê de bi encamên ku di lêkolînên berê de hatine weşandin re lihevhatî bûn ku ev yek pêbawerî û rastiya PCRê wekî rêbazek molekular a nasandina bakteriyan zêdetir piştrast dike. Vekolîna molekular a li ser bingeha PCRê diyar kir ku hin cureyên *Lactobacillus* di nav nimûneyan hatine analîzkirin de zêdetir hebûn. Cureyên ku hatin nasandin ev bûn: *Lactobacillus acidophilus, Lactobacillus brevis, Lactobacillus rhamnosus, Lactobacillus casei*, *Lactobacillus reuteri*, *Lactobacillus fermentum*, *Lactobacillus paracasei*. Di nav van de, hin cure, wekî *L. acidophilus*, bi taybetmendiyên probiyotîk û feydeyên wan yên tenduristiyê bi firehî têne naskirin. Bi kurtasî, nasandina serkeftî ya gelek cureyên bakteriyan bi rêya PCRê, ku bi derketina bandên zelal li ser jelê electrophoresisê hate nîşandan (Wêne 13), bi encamên rêbazên kevneşopî yên nasandinê re lihevhatîyek mezin nîşan da. Ev encam taybetmendî û rastiya primerên bikaranînî, her weha karîgeriya şertên PCRê yên hatine bikaranîn piştrast dikin û girîngiya PCRê wekî rêbazek pêbawer ji bo nasandina bakteriyên probiyotîk destnîşan dikin.

Wêneya 13: Gela elektroforez a hilberên PCR, Lane M, Ladder DNA. Rêça 1, L. paracasei. Rêça 2, L. casei. Rêça 3, L. fermentum. Rêça 4, L. rhamnosus. Rêça 5, L. reuteri. Rêça 6, L. brevis. Rêça 7, L. acidophilus

3.11 Encamên têsta Hestiyarîya Li Dijî Antîbiyotîkan (Antibiotic Susceptibility Testing)

Piştî qedandina dema inkubasyonê, li derdora qulikên ku antîbiyotîkên **doxycycline** û **ceftriaxone** dihewand de herêmên astengkirina mezinbûnê (inhibition zones) yên bi qasî 1 cm di qutriyê de hatin dîtin. Ev herêmên zelal, ku bi encamên gelek lêkolînên navneteweyî yên berê re lihevhatî ne, nîşan didin ku cureyên *Lactobacillus* li hember van antîbiyotîkan hestiyar (susceptible) in (Wêne 14). Li hember vê yekê, li derdora qulikên ku antîbiyotîkên din, wekî **ampicillin** û **amikacin**, dihewand de ti herêmên astengkirinê nehatin dîtin. Ev encam nîşan dide ku izolatanên *Lactobacillus* li hember van antîbiyotîkan berxwedêr (resistant) in. Bi giştî, encamên vê têstê destnîşan dikin ku cureyên *Lactobacillus* dikarin profîlên berxwedanê yên hilbijartî (selective resistance profiles) hebin. Wateya vê yekê ew e ku dibe ku li hember hin antîbiyotîkan hestiyar bin, lê li hember yên din berxwedêr bimînin. Ev taybetmendî ji bo nirxandina ewlekarî û bikaranîna wan wekî bakteriyên probiyotîk girîng tê dîtin.

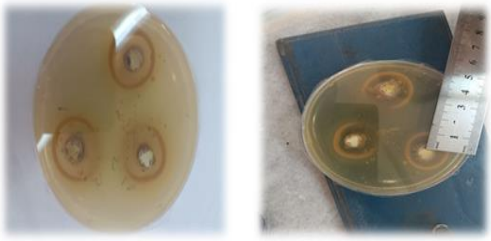

Wêneya 14: Testa probiyotîkê li ser medyayek ku antîbiyotîk tê de heye

3.12 Encamên Hilberandina Çalakiya Dijî-Mîkrobî (Production of Antimicrobial Activity)

Berî destpêkirina dema inkubasyonê, sê qulik (wells) li ser rûyê agarê hatin çêkirin. Qulika yekem bi suspansiyona bakteriyên *Lactobacillus* hate dagirtin, qulika duyemîn bi antîbiyotîkek hilbijartî hate dagirtin, û qulika sêyemîn wekî kontrola neerênî (negative control) hate hiştin. Piştî qedandina dema inkubasyonê, li derdora qulika ku suspansiyona *Lactobacillus* tê de hebû herêmên zelal ên astengkirina mezinbûna bakteriyan (inhibition zones) bi qutriyek di navbera 0.5 heta 1 cm de hatin dîtin. Ev encam bi awayekî eşkere çalakiya dijî-bakterî ya *Lactobacillus* li dijî cureyên *Staphylococcus* nîşan dide. Hebûna van herêmên astengkirinê destnîşan dike ku *Lactobacillus* dikare madeyên dijî-mîkrobî hilberîne ku mezinbûna bakteriyên patojen asteng dike. Ev taybetmendî diyar dike ku cureyên *Lactobacillus* xwedî potansiyela probiyotîk û dermankirinê ne û dibe ku di pêşîlêgirtin an alîkariya dermankirina hin enfeksiyonên pergala hazimê yên ku ji aliyê bakteriyên patojen ve tên çêkirin de rolek erênî bilîzin (Wêne 15). Bi giştî, encamên vê ceribandinê piştrast dike ku izolatanên *Lactobacillus* xwedî çalakiya dijî-mîkrobî ya berbiçav in û dikarin wekî çavkaniyeke probiyotîk a bi feyde ji bo tenduristiya mirovî werin nirxandin.

Wêneya 15: Ceribandina probiyotîkan li ser medyayek ku bakteriyên zirardar tê de hene û pîvandina asta berfirehbûna probiyotîk û bandora wê li ser bakteriyên zirardar

4. Nîqaş (Discussion)

Li gorî encamên vê lêkolînê, koloniyên *Lactobacillus* li ser navenda **MRS agar** piştî inkubasyona di germahiya 37°C de mezinbûnek nîşan dan ku qutriya wan di navbera 0.5–2 mm de bû, bi rengê spî heta spîya zeralî û bi kenarên gird. Ev taybetmendiyên morfolojîk bi encamên lêkolîna **Jose et al. (2015)** re lihevhatî ne, ku di wê de jî koloniyên gird û bi rengê spîya şîrî li ser MRS agar hatibûn raporkirin. Di lêkolîneke din de, **Hoque et al. (2010)** cureyên *Lactobacillus* yên ji nimûneyên mast hatine veqetandin ji

aliyê taybetmendiyên morfolojîk, biyokîmyayî û fîzyolojîk ve hatin vekolîn. Vekolîna mîkroskopî diyar kir ku van bakteriyan şêweyê çûk an bacillî hebû û Gram-erênî (Gram-positive) bûn. Her wiha, hemû izolatan encamên katalaz-neerênî (catalase-negative) nîşan dan. Di heman lêkolînê de, şiyana fermentasyona laktoz, glukoz û sukrozê ji aliyê izolatanên *Lactobacillus* ve jî hate piştrastkirin. Taybetmendiyên morfolojîk û biyokîmyayî yên ku di vê lêkolînê de hatin dîtin bi encamên ku **Harun-Ur-Rashid et al. (2007)** ji bakteriyên asîda laktîk (LAB) yên ji nimûneyên *dahi* hatine veqetandin rapor kirine re jî lihevhatî ne. Ev lihevhatin pêbaweriya encamên bidestxistî zêdetir dike û diyar dike ku izolatanên ku di vê lêkolînê de hatine nasandin bi taybetmendiyên giştî yên cureyên *Lactobacillus* re hevaheng in. Hilbijartina navenda **MRS** wekî navendek sereke ji bo veqetandin û nasandina destpêkî ya cureyên *Lactobacillus* li ser bingeha taybetmendiya vê navendê hate kirin, ji ber ku gelek cureyên bakteriyên din nikarin di vê navendê de bi awayekî baş mezin bibin. Ev encam bi raporên **López-Díaz et al. (2000)** û **Vasudha û Gayathri (2023)** re lihevhatî ne, ku bal kişandine ser belavbûna berfireh a cureyên *Lactobacillus* di navenda MRS de û karîgeriya vê navendê di veqetandin û nasandina van bakteriyan de. Di vê lêkolînê de, belavbûna izolatanên *Lactobacillus* di masta çêkirî ya ji şîrê çêlekê di bikaranîna de rêbazên çandiniyê û ceribandinên biyokîmyayî hate nirxandin, ku rêjeyek bi qasî %25 hate destnîşankirin. Lêbelê, dema ku rêbaza molekular a **PCR** hate bikaranîn, ev rêje hinekî kêmtir bû û bi qasî %15 hate diyarkirin. Ev encam bi encamên ku ji aliyê **Abdullah û Osman (2010)** ve hatine raporkirin re lihevhatî ne. Van lêkolîneran belavbûna cureya *Lactobacillus* di şîrê fermentekirî yê Sudanî (*rob*), şîrê xam û penîrê spî de vekolî bûn. Li gorî encamên wan, rêjeya belavbûnê ku bi rêbazên çandiniyê, fîzyolojîk û biyokîmyayî hate diyarkirin, %69.23 bû. Di lêkolîneke din de, **Saeed et al. (2020)** di bikaranîna teknîka PCRê belavbûna *Lactobacillus* di mastê bizinan de nirxandin û rêjeyek bi qasî %10 rapor kirin. Ev encam destnîşan dike ku belavbûna cureyên probiyotîk ên *Lactobacillus* di mastê çêlekê de dibe ku ji ya mastê bizinan bilindtir be. Her wiha, di lêkolîneke ku ji aliyê **Taye et al. (2021)** ve hate pêkanîn de, belavbûna cureya *Lactobacillus* di şîrê xam, penîr û mast de bi rêbazên çandiniyê, fîzyolojîk û biyokîmyayî hate nirxandin û rêjeyek bi qasî %24.38 hate raporkirin. Ev rêje ji encamên ku di vê lêkolînê de hatine bidestxistin hinekî kêmtir e. Wekî din, di vê lêkolînê de belavbûna gena **plnEF**, ku berpirsiyar e ji bo hilberandina proteîna bakteriyosînê, bi qasî %4.96 hate diyarkirin. Ev encam bi awayekî berbiçav ji encamên lêkolîneke berê ku li Misrê ji aliyê **Refay et al. (2020)** ve hate raporkirin cuda ye. Ev cudahî dibe ku ji şertên erdnîgarî, cureyên nimûneyan, şertên çandiniyê an jî ji cudahiya rêbazên molekular ên hatine bikaranîn derkeve. Di lêkolîna wan de, belavbûna gena **plnEF** bi rêjeyek gelek bilindtir, ku bi qasî %32.35 (22 ji 68 izolatan) bû, hate raporkirin. Ev cudahî di navbera encamên vê lêkolînê û lêkolîna berê de dibe ku ji gelek faktoran wekî cudahiya çavkaniya nimûneyan, şertên jîngehî, erdnîgariya herêmê an jî rêbazên veqetandin û nasandina molekular derkeve.

Tê zanîn ku *Lactobacillus* gelek madeyên dijî-mîkrobî hilberîne, wekî asîdên organîk, hîdrojen peroksîd (H_2O_2), diasetîl û bakteriyosînan; ku ev madeyên bi giraniya molekular a kêm xwedî karîgeriyek astengker li hember mîkroorganîzmayên patojen in (Santos et al., 2003). Di vê lêkolînê de, izolatanên *Lactobacillus* çalakiya dijî-bakterî ya berbiçav nîşan dan û karîbûn mezinbûna bakteriyên patojen ên hatine ceribandin asteng bikin. Ev encam bi gelek lêkolînên din re lihevhatî ne, ku tê de cureyên *Lactobacillus* wekî bakteriyên probiyotîk ên gelemperî têne naskirin û wekî rêbazek alternatîf ji bo pêşîlêgirtina nexweşiyên ku bi *Salmonella* ve girêdayî ne têne bikaranîn (Kowalska et al., 2020). Bi heman awayî, **Djadouni û Kihal (2012)** rapor kirin ku bakteriyên asîda laktîk (LAB) madeyên dijî-bakterî hilberînin ku mezinbûna mîkroorganîzmayên nîşander asteng dikin. Di lêkolîna wan de, herêmên astengkirinê bi qutriya 10–14 mm li dijî *Escherichia coli* û *Staphylococcus aureus* li gorî bikaranîna rêbaza **agar spot test** hate qeyd kirin. Çalakiya dijber (antagonistic activity) ya izolatanên LAB li dijî *S. aureus* ku di vê lêkolînê de hate dîtin, bi encamên ku ji aliyê **Prabhurajeshwar û Chandrakanth (2017)** ve hatine raporkirin re gelek lihevhatî bû. Her wiha, kapasîteya dijî-bakterî ya izolatanên ku di vê lêkolînê de

hatine veqetandin bi ya ku di lêkolînên berê de hatiye raporkirin re wekhev bû. Girîngtir jî ev e ku izolatanên *Lactobacillus* çalakiya dijî-bakterî li dijî hem bakteriyên Gram-erênî (Gram-positive) û hem jî Gram-neerênî (Gram-negative) nîşan dan. Ev taybetmendî nîşan dide ku ev bakteriya xwedî çalakiyek dijî-mîkrobî ya berfireh-spektrum (broad-spectrum antimicrobial activity) e, ku dikare rola wan ya girîng wekî probiyotîk di pêşîlêgirtin û kontrolkirina enfeksiyonên bakterîyî de piştrast bike.

5. Encam (Conclusions)

Vê lêkolînê nîşaneyên zanistî yên berfireh pêşkêş kirin derbarê hebûn, cudahiya biyolojîk û feydeyên tenduristiyê yên potansiyel ên cureyên *Lactobacillus* de ku di berhemên şîrî yên gelek bajarên Herêma Cizîrê de hatine dîtin. Di maweya sê salan de, zêdetirî sed nimûne, ku şîr, mast û penîr di nav wan de bûn, bi awayekî rêkûpêk hatin komkirin û bi rêbazên mîkrobiyolojîk, biyokîmyayî û molekular (PCR) hatin analîzkirin. Ev encam têgihiştina me derbarê bakteriyên probiyotîk ên xwezayî ku di berhemên şîrî yên kevneşopî û pîşesazî de li herêmê hene, bi awayekî berbiçav pêşxist. Her wiha, encamên lêkolînê diyar kirin ku mast çavkaniya herî berdewam û herî dewlemend a cureyên *Lactobacillus* e, di dema ku di penîr û hin nimûneyên taybet ên şîr de astên van bakteriyan kêm an jî gelek sînordar bûn. Ceribandinên laboratuwarî her wiha nîşan dan ku izolatanên *Lactobacillus* xwedî çalakiya dijî-bakterî ya berbiçav in û dikarin mezinbûna hem bakteriyên patojen ên Gram-erênî (Gram-positive) û hem jî Gram-neerênî (Gram-negative) asteng bikin. Ev taybetmendiyên dijî-mîkrobî bi awayekî hêzdar pêşniyar dikin ku van bakteriyan di zêdekirina parastina pergala berxwedana rûvî (gut immunity), vegerandina hevsengiya mîkrobiyota rûvî û pêşîlêgirtina dagirkirina rûviyan ji aliyê mîkroorganîzmayên zirardar ve rolek girîng heye. Ji ber vê yekê, cureyên *Lactobacillus* yên ku di berhemên şîrî yên herêmê de hatine veqetandin dikarin wekî çavkaniyên probiyotîk ên xwezayî û bi feyde werin nirxandin, potansiyela wan heye ku di pêşxistina berhemên fonksiyonel û stratejiyên nû yên pêşîlêgirtin û alîkariya dermankirina nexweşiyên têkildar bi pergala helandinê de werin bikaranîn.

Pêşniyar

Li ser bingeha encamên ku di vê lêkolînê de hatine bidestxistin, ev pêşniyar tên pêşkêşkirin:

1- Teşwîqkirina Xwarinên Dewlemend Bi Probiyotîkan

Divê berpirsên tenduristiya giştî xwarina rojane ya mast ku cureyên xwezayî yên *Lactobacillus* dihewîne teşwîq bikin. Kampanyayên hişyariyê yên civakî dikarin girîngiya parastina tenduristiya rûviyan, domandina hevsengiya mîkrobiyota rûvî û kêmkirina metirsiya nexweşiyên pergala helandinê rave bikin.

2- Bikaranîna Di Pîşesaziya Xwarinan De

Divê hilberînerên berhemên şîrî û pisporên teknolojiyên xwarinan pêvajoyên fermentasyonê standardîze bikin da ku zindîmayîn, çalakiya biyolojîk û aramiya cureyên bi feyde yên *Lactobacillus* were parastin. Her wiha, zêdekirina cureyên probiyotîk ên hilbijartî di hilberandina mastê bazirganî de dikare nirxa tenduristî ya van berheman bilind bike û rola wan wekî xwarinên fonksiyonel ên piştgirîya tenduristiyê zêdetir bike.

Encama Giştî

Di encamê de, vê lêkolînê piştrast kir ku mastê li Herêma Cizîrê çavkaniyek dewlemend a bakteriyên probiyotîk yên *Lactobacillus* e. Her wiha, encamên bidestxistî girîngiya van bakteriyan ne tenê di warê xwarin û xwarinzanî de, lê di warên tenduristî, dermanzanî û teknolojiyên xwarinan de jî nîşan dan. Ev encam divê wekî bingehek zanistî ji bo pêkanîna ampilîkêşinên pratîkî û lêkolînên paşerojê werin bikaranîn. Armanca van lêkolînan divê zêdekirina feydeyên tenduristiyê yên cureyên *Lactobacillus* û bikaranîna wan di pêşxistina berhemên probiyotîk û stratejiyên nû yên

pêşîlêgirtin û alîkariya dermankirina nexweşiyan de be, da ku tenduristiya civakê bi gişt̂ were baştir kirin.

Spasdarî Acknowledgment

Em spasî û pêzanîna xwe pêşkêşî hemû hevalkar û kesên ku di pêkanîna vê lêkolînê de piştgirî û alîkarî dane me, dikin. Piştgiriya wan di pêşvebirina vê xebata zanistî de roleke girîng lîst û beşdarî serkeftina vê lêkolînê bû. Em ji hemû kesên ku bi awayekî rasterast an nerasterast alîkariya me kirine dilsoz û spasdar in.

Reference

1. Abdullah, Sawasan Abdelaziz, and Maymouna Mubarak Osman. "Isolation and identification of lactic acid bacteria from raw cow milk, white cheese and Rob in Sudan." (2010): 1203-1206.
2. Asha, S. A., C. Sudalaimani, P. Devanand, G. Alexander, V. Thomas Sanjeev, and N. Menon Ramshekhar. "Analysis of EEG microstates as biomarkers in neuropsychological processes–Review." Computers in biology and medicine 173 (2024): 108266.
3. Barrow, G. I. and Feltham, R. K. A. (1993). Staining of Bacteria. In: Cowan and Steel's Manual for the identification of medical bacteria. Eds. Barrow, G. I. and Feltham, R. K. A. Cambridge University Press, Great Britain. ISBN 0-521-32611-07. 51-93.
4. Djadouni, Fatima, and Mebrouk Kihal. "Antimicrobial activity of lactic acid bacteria and the spectrum of their biopeptides against spoiling germs in foods." Brazilian Archives of Biology and Technology 55 (2012): 435-444.
5. Djadouni, Fatima, and Mebrouk Kihal. "Antimicrobial activity of lactic acid bacteria and the spectrum of their biopeptides against spoiling germs in foods." Brazilian Archives of Biology and Technology 55 (2012): 435-444.
6. Fesseha, Haben. "Probiotics and its potential role in poultry production: a review." Veterinary Medicine-Open Journal 4, no. 2 (2019): 69-76.
7. Gareau, Mélanie G., Philip M. Sherman, and W. Allan Walker. "Probiotics and the gut microbiota in intestinal health and disease." Nature reviews Gastroenterology & hepatology 7, no. 9 (2010): 503-514.
8. Harun-ur-Rashid, Md, Kaname Togo, Minoru Ueda, and Taku Miyamoto. "Identification and characterization of dominant lactic acid bacteria isolated from traditional fermented milk Dahi in Bangladesh." World Journal of Microbiology and Biotechnology 23, no. 1 (2007): 125-133.
9. Hoque, M. Z., F. Akter, K. M. Hossain, M. S. M. Rahman, M. M. Billah, and K. M. D. Islam. "Isolation, identification and analysis of probiotic properties of Lactobacillus spp. from selective regional yoghurts." (2010): 39-46.
10. Jose, Neethu Maria, Craig R. Bunt, and Malik Altaf Hussain. "Comparison of microbiological and probiotic characteristics of lactobacilli isolates from dairy food products and animal rumen contents." Microorganisms 3, no. 2 (2015): 198-212.
11. Kapilan, R., and Vasanthy Arasaratnam. "A novel Bacillus pumilus strain for alkaline xylanase production at and above 40° C." Ceylon Journal of Science (Biological Sciences) 39, no. 1 (2010.(
12. Karuppaija, Sinthuja, Ranganathan Kapilan, and Vasantharuba Seevaratnam. "Characterization of best naringinase producing fungus strain isolated from palmyrah (Borrasus flabellifer) fruit pulp." (2016.(
13. Kowalska, Justyna D., Adriana Nowak, Katarzyna Śliżewska, Małgorzata Stańczyk, Magdalena Łukasiak, and Jarosław Dastych. "Anti-Salmonella Potential of New Lactobacillus Strains with the Application in the Poultry Industry." Polish Journal of Microbiology 69, no. 1 (2020.(
14. Lopez-Dıaz, T. M., C. Alonso, C. Roman, M. L. Garcıa-Lopez, and B. Moreno. "Lactic acid bacteria isolated from a hand-made blue

cheese." Food Microbiology 17, no. 1 (2000): 23-32.

15. Neha, Neha, Yogita Sharma, Anshu Yadav, Ramnarayan Ramnarayan, and G. Swapna. "Sustainability and role conflict: A bibliometric analysis of research themes, trends, and future research directions: 2013-2022." In E3S Web of Conferences, vol. 430, p. 01186. EDP Sciences, 2023.
16. Prabhurajeshwar, Chidre, and Revanasiddappa Kelmani Chandrakanth. "Probiotic potential of Lactobacilli with antagonistic activity against pathogenic strains: An in vitro validation for the production of inhibitory substances." Biomedical journal 40, no. 5 (2017): 270-283.
17. Pundir, Ram Kumar, Satish Rana Neha Kashyap, and Amandeep Kaur. "Probiotic potential of lactic acid bacteria isolated from food samples: an in vitro study." Journal of Applied Pharmaceutical Science 3, no. 3 (2013): 085-093.
18. Refay, Rasha Mohamed, Hala Mohamed Abushady, Sara Adel Amer, and Mahmoud Ahmed Mailam. "Determination of bacteriocin-encoding genes of lactic acid bacteria isolated from traditional dairy products of Luxor province, Egypt." Future Journal of Pharmaceutical Sciences 6, no. 1 (2020): 22.
19. Saeed, Z. K., B. A. Abbas, and R. M. Othman. "Molecular identification and phylogenetic analysis of lactic acid bacteria isolated from goat raw milk." Iraqi Journal of Veterinary Sciences 34, no. 2 (2020.(
20. Santos, A., M. San Mauro, A. Sanchez, J. M. Torres, and D. Marquina. "The antimicrobial properties of different strains of Lactobacillus spp. isolated from kefir." Systematic and applied Microbiology 26, no. 3 (2003): 434-437.
21. Taye, Yeshambel, Tadesse Degu, Haben Fesseha, and Mesfin Mathewos. "Isolation and identification of lactic acid bacteria from cow milk and milk products." The Scientific World Journal 2021, no. 1 (2021): 4697445.
22. Theivendrarajah, K. "Microbiology Laboratory Manual: Department of Botany, University of Jaffna." University Publication (1990): 1-33.
23. Vasudha, Mahantesh. "Metabolism and functional heterogeneity of fermented milk origin lactic acid bacteria for lactose intolerance." Journal of microbiology, biotechnology and food sciences 13, no. 3 (2023): e9654-e9654.